Micropaleontological applications in coastal geoarchaeology

Micropaleontological and μXRF applications in coastal geoarchaeological studies

By
RILEY ELAINE STEELE, B.SC., M.SC.

A Thesis Submitted to the School of Graduate Studies
in the Partial Fulfillment of the Requirements for the Degree of

Doctor of Philosophy
in
Earth and Environmental Sciences

McMaster University
Hamilton, Ontario

Doctor of Philosophy (2023)
School of Earth, Environment, & Society
McMaster University
Hamilton, Ontario, Canada

TITLE: Micropaleontological and μXRF applications in coastal geoarchaeological studies

AUTHOR: Riley Elaine Steele, B.Sc., M.Sc.

SUPERVISOR: Dr. Eduard Reinhardt

NUMBER OF PAGES: xvii, 183

Abstract

The development of tools and techniques used in paleoenvironmental studies is important for the advancement of geoarchaeological research. Geoarchaeological studies of ancient harbours involve the integration of paleoenvironmental data with archaeological findings, allowing for a more comprehensive understanding of site development and regional maritime trade. This dissertation highlights and/or explores novel applications of microfossils and micro-X-ray fluorescence (μXRF) core scanning data in paleoenvironmental reconstructions within three ancient harbour studies.

Foraminifera, diatom, pollen, μXRF, carbon stable isotope, and radiocarbon dating results from underwater cave sediments on the eastern coast of the Yucatán Peninsula indicate that the region's wetlands developed between 1157 BCE and 312 CE. Continued sea-level rise after ~312 CE allowed canoe access through a channel from the Caribbean Sea to Muyil, a Classic Maya maritime port site. Development of the wetlands may have implications for increased maritime trade on the Yucatán's eastern coast during the Postclassic (925–1550 CE). This study demonstrates the importance of karst cave systems for obtaining paleoenvironmental records and provides a first assessment of the diatom community that has been transported into the sampled cave system.

The novel application of epiphytic foraminifera as biostratigraphic indicators was investigated at Caesarea, Israel. Benthic foraminifera assemblages indicated that the emplacement of hard harbour structures along the sandy coast between 21–10 BCE altered the environmental conditions and impacted the nearby ecological communities. Epiphytic foraminifera, in particular *Pararotalia calcariformata*, were found to be useful indicators for the timing of harbour construction at Caesarea. μXRF and magnetic susceptibility results also supported the presence of increased harbour material (i.e., kurkar and volcanic ash) in offshore sediments over time. This study demonstrates that epiphytic foraminifera can be cost-effective biostratigraphic indicators in geoarchaeological studies. Results also confirm that *P. calcariformata* is endemic to Israel and is not a recent arrival following the opening of the Suez Canal.

Foraminifera, testate amoebae, μXRF, and radiocarbon dating results from sediment cores collected from two lagoons, Khor Al Balid and Khor Rori, on the southern coast of Oman indicate that the lagoons closed off from the sea between the 12th and 15th centuries CE. Prior to lagoon formation, these two sites formed natural harbours that were the locations of major maritime trade ports. Progressive siltation and sand accumulation along the coastline after the 15th century likely impacted shipping activities, contributing to abandonment of the city near Khor Al Balid. Evidence of a marine overwash event across most cores from both sites dating to the 18th–19th century CE suggests that an extreme wave event (e.g., tsunami or large tropical cyclone) may have also contributed to the decline of the city. The results of this study provide an important paleoenvironmental context for previous archaeological findings.

Acknowledgements

I'd like to thank my supervisor, Dr. Eduard Reinhardt, for his support and assistance throughout my Ph.D. and for sharing his interest in geoarchaeology. I am forever grateful for the opportunity to experience exciting field work and environmental research. Thanks to my committee members, Dr. Joseph Boyce, Dr. Sang-Tae Kim, and Dr. Henry Schwarcz, and the external reviewer for their suggestions, guidance, and knowledge that has helped me put together this thesis.

For the past few years I've been able to study three very interesting geoarcheological sites, though I was not able to participate in as much field work as planned because of the global pandemic. I'd like to thank everyone involved in collecting my samples during previous field work seasons. Thanks also to everyone who assisted with various analyses throughout the past few years, especially Dr. Brian Cumming and Matthew Marshall for their help with diatom methods, and Martin Knyf for help with stable isotope work. Thanks to the undergraduate students who contributed to this thesis, including Juliet Zhu for her work on the Boca Paila manuscript and Meghan Burchell and Andrew Kingston for their work on the Caesarea foraminifera analysis. Thanks to Marcia Reid for all of the SEM work.

I'm grateful to the members of the Reinhardt laboratory for their support over the years. I can't thank Jeremy Gabriel enough for all of his assistance with R and geochemistry methods. Thanks also to the staff members of the School of Earth, Environment, and Society for all of their help over the years. I am sincerely thankful for the SEES Department Scholarships and the Ontario Graduate Scholarship (OGS) that have supported me during my Ph.D. Lastly, I'm very grateful for my family and friends who have always supported my love of learning and encouraged me to find work that I enjoy. Special thanks to my mother for acting as my own personal technical writing editor for my entire academic career.

Contents

List of Figures

List of Tables

List of Abbreviations and Symbols

BCE: Before the Common Era
CE: Common Era
ITCZ: Intertropical Convergence Zone
mbsl: Meters below sea level
MeWM: Meteoric water mass
MaWM: Marine water mass
MSZ: Makran Subduction Zone
NMDS: Non-metric multidimensional scaling
OFZ: Owen Fracture Zone
OM: Organic matter
RSL: Regional sea level
SDI: Shannon-Weaver diversity index
SEM: Scanning electron microscope
μ**XRF:** Micro-X-ray fluorescence
yr BP: Years before present
δ^{13}**C:** Delta Carbon 13
δ^{15}**N:** Delta Nitrogen 15

Preface

This dissertation contains three research papers as chapters that have been published in, submitted to, or prepared for peer reviewed journals. Each chapter was formatted as per the specific journal requirements and reproduction permission was obtained for published manuscripts. Due to the style of dissertation, there is some overlap in content within the background and methods sections of the three research papers. Contributions of co-authors to each paper are outlined below. In all cases, the dissertation author was the main contributor, Dr. Eduard Reinhardt assisted with research direction and interpretation of results, and all authors contributed towards reviewing and editing of the individual manuscripts.

Chapter 2:

Steele, R.E., Reinhardt, E.G., Devos, F., Meacham, S., LeMaillot, C., Gabriel, J.J., Rissolo, D., Vera, C.A., Peros, M.C., Kim, S-T, Marshall, M., Zhu, J. (2023) Evidence of recent sea-level rise and the formation of a classic Maya canal system inferred from Boca Paila cave sediments, Sian Ka'an biosphere, Mexico. Quaternary Science Reviews, 310(108117).
https://doi.org/10.1016/j.quascirev.2023.108117.

Sediment core samples from Boca Paila cave were collected by Dr. Eduard Reinhardt, Frederic Devos, Sam Meacham, and Chris LeMaillot. Dr. Jeremy Gabriel assisted with the μXRF statistical chemofacies analysis. Dr. Dominique Rissolo provided resources and information on Maya history/geoarchaeology. Cesar Arturo Vera and Dr. Matthew Peros performed the pollen analysis. Dr. Sang-Tae Kim assisted with the stable isotope analysis. Matthew Marshall provided resources and information on diatom analysis. Juliet Zhu assisted with the original draft manuscript. The dissertation author performed all foraminifera, diatom, μXRF, and stable isotope analyses as well as data compilation and analysis, figure creation, and manuscript writing.

Chapter 3:

Steele, R.E., Reinhardt, E.G., Boyce, J., Goodman-Tchernov, B., Gabriel, J.J., Burchell, M., Kingston, A. (*submitted*) Anthropogenic structure emplacement and sediment transport at King Herod's harbour, Israel: ED-μXRF (Itrax) data and foraminifera *Pararotalia calcariformata* as proxies of coastal development over millenia. Submitted to Marine Geology Sept 2023.

Sediment core samples were collected by Dr. Eduard Reinhardt and Dr. Beverly Goodman-Tchernov. Dr. Joseph Boyce assisted with magnetic susceptibility analysis. Dr. Jeremy Gabriel assisted with the μXRF statistical chemofacies analysis. Meghan Burchell and Andrew Kingston performed the foraminifera analysis. The dissertation author performed all μXRF, and magnetic susceptibility work, as well as data compilation and analysis, figure creation, and manuscript writing.

Chapter 4:

Steele, R.E., Reinhardt, E.G., Boyce, J., Gabriel, J.J., Vosmer, T. (*to be submitted*) Closure of Khor Al Balid and Khor Rori with coastal uplift and aridity in the 12th – 15th c. CE and evidence for an extreme overwash event in 18th – 19th c. CE: implications for ancient port sites in southern Oman. In preparation for submission to a peer-reviewed journal.

Sediment core samples were collected by Dr. Eduard Reinhardt and Dr. Joseph Boyce. Dr. Reinhardt also performed the microfossil analysis and provided draft figures. Dr. Jeremy Gabriel assisted with the μXRF statistical chemofacies analysis. The dissertation author performed all μXRF work as well as data compilation and analysis, figure creation, and manuscript writing.

Chapter 1

Introduction

Geoarchaeology has become a well-established field of research over the past several decades (Goldberg & Macphail, 2006; Marriner et al., 2010; Marriner & Morhange, 2007; Rapp, 1987). Integrating paleoenvironmental data with archaeological findings leads to a more comprehensive understanding of the interactions between human populations and their environmental settings. Coastal environments are particularly complex as shorelines shift relatively rapidly due to erosion, tectonism, sea-level fluctuations, storms, etc. and often no longer resemble the settings that were originally occupied (Goldberg & Macphail, 2006; Marriner & Morhange, 2007). Ancient harbour sites often contain long-term (e.g., Holocene) records of both coastal morphological changes and human activity related to harbour construction, use, and decline (Marriner et al., 2010; Marriner & Morhange, 2006, 2007; Morhange & Marriner, 2015; Salomon et al., 2016). Geoarchaeological research is a constantly evolving field with respect to the methods and techniques applied. Modern studies typically involve the collection of field data such as sediment cores from harbour basins, geophysical measurements (e.g., magnetometry, ground penetrating radar), and site observations (e.g., the presence of raised beaches, platforms, erosional notches, wetlands, estuaries, sand barriers, etc.) followed by laboratory analyses of multiple environmental proxies (e.g., microfossils, pollen, geochemistry, etc.; Goiran et al., 2022; Goldberg & Macphail, 2006).

Assessing the abundance of microfossils (e.g., foraminifera, ostracods, diatoms, testate amoebae) throughout sediment records is especially useful in coastal reconstructions, as these taxa are abundant in aquatic settings, preserve well in sediments over time, and have varying tolerances to environmental conditions (salinity, water depth, substrate type, sunlight availability, etc.; Armstrong & Brasier, 2005; Charman et al., 2010; Marriner & Morhange, 2007; Murray, 2006). Changes in assemblages of microfossil species throughout a sediment record can therefore be used to indicate how open or closed a body of water is to the ocean over time, which is useful for reconstructing periods of harbour construction, use, and/or demise (e.g.,Goiran et al., 2022; Reinhardt et al., 1994; Reinhardt & Raban, 1999). Foraminifera and ostracods have been applied in this manner during coastal geoarchaeological studies in France (Morhange et al., 2003), Germany (Daniel et al., 2019), Greece (Finkler et al., 2018; Riddick et al., 2021; Vött et al., 2007), Israel (Giaime et al., 2021; Reinhardt et al., 1994), Italy (Aiello et al., 2020; Amato et al., 2020; Di Bella et al., 2011; Goiran et al., 2014; Mazzini et al., 2011), Lebanon (Marriner et al., 2005), Mexico (Jaijel et al., 2018), and Turkey (Algan et al., 2011; Bony et al., 2012; Goodman et al., 2009; Kraft et al., 2003; Pint et al., 2015; Riddick et al., 2022a, 2022b; Stock et al., 2013, 2016). Diatoms and testate amoebae also have the potential to provide valuable paleoenvironmental data in geoarchaeological studies, but are less commonly used (possibly due to taxonomic challenges and salinity requirements, respectively; Goiran et al., 2022; Marriner & Morhange, 2007). Another unexplored application of microfossils in geoarchaeology relates to biostratigraphy. Microfossil biozones (e.g., the appearance and extinction of certain species over time) are typically used to correlate rocks and sediments belonging to periods of geological time (Mcgowran, 2005). This concept has also been applied over shorter timescales, with various fossil taxa. Ragweed pollen horizons, for instance, have been shown to be useful sediment dating biomarkers of major deforestation events related to European settlement (e.g., Brush, 2001). Microfossils may similarly be helpful for studying site formation processes and dating of sediments related to the construction of harbour structures, which can significantly alter coastal environments.

Microfossil results are often interpreted alongside lithology (e.g., changes in colour, grain size, and other sediment characteristics) and geochemistry results (Goldberg & Macphail, 2006; Marriner & Morhange, 2007). Organic content, carbonate content, and stable isotopes related to pollution levels (e.g., lead; Véron et al., 2006) as well as water mass variability (e.g., carbon, oxygen; Riddick et al., 2021) are common geochemical analyses in coastal geoarchaeological studies. Analysis of the elemental composition of sediments, however, is not yet widely applied. Elemental analysis methods such as micro-X-ray fluorescence (μXRF, through core scanning or portable methods) and inductively coupled plasma optical emission spectroscopy (ICP-OES) have only been used in a few geoarchaeological harbour studies (Aiello et al., 2020; Finkler et al., 2018; Pint et al., 2015; Riddick et al., 2021; Riddick et al., 2022a, 2022b; Seeliger et al., 2013, 2014; Stock et al., 2013, 2016). μXRF analysis is non-destructive and can rapidly provide high-resolution (200 μm) information on the relative abundance of elements from Aluminum to Uranium (Rothwell & Croudace, 2015). Chemofacies results interpreted from μXRF data (i.e., lithologically and biologically derived elements from terrestrial and marine sources) are a valuable addition to geoarchaeological studies worldwide (Goiran et al., 2022).

1.1 Dissertation structure

This dissertation contributes to geoarchaeological and maritime trade research by exploring the use of non-conventional sediment sources for environmental proxies (i.e., underwater cave systems), applying a wider range of microfossil taxa including diatoms and testate amoebae, and/or applying μXRF elemental chemofacies methods in three coastal harbour studies. The following three chapters present research projects that are individual advances in the field and involve the reconstruction of paleoenvironmental landscapes of ancient port sites.

Chapter two investigates the timing of wetland development along the eastern coast of the Yucatán Peninsula. Samples were collected from an underwater cave system, an underutilized source of well-preserved environmental records common along this coastal region. Environmental proxies including foraminifera, diatom, pollen, elemental composition, and stable carbon isotopes were used to infer the timing of coastal flooding and canal formation between Muyil, a Maya port site, and the Caribbean Sea. Results may have important implications for maritime trade patterns throughout the region. This study also incorporates the first assessment of diatom species within the regional cave system providing initial data for future research in the area.

Chapter three investigates a novel geoarchaeological application of epiphytic foraminifera as biostratigraphic indicators at Sebastos, an ancient, submerged, Israeli harbour that has well-documented environmental and archaeological histories. Abundances of the foraminifer *Pararotalia calcariformata*, μXRF elemental data, and magnetic susceptibility data obtained from sediment cores were useful for correlating sediments associated with harbour construction and deterioration. The study highlights previously unused applications of benthic foraminifera in coastal geoarchaeological settings and confirms that *P. calcariformata* is an epiphytic foraminifer endemic to the Israeli coast and is not a Lessepsian arrival, as mistakenly proposed in previous studies (Schmidt et al., 2015; Zenetos et al., 2012).

Chapter four focuses on the formation of two lagoons, Khor Al Balid and Khor Rori, at two ancient port sites along the southern coast of Oman. Archaeological information is abundant in this region; however, paleoenvironmental information is very limited, inhibiting a full understanding of maritime trade activity, and harbour development and decline at the sites (D'Andrea, 2021). Foraminifera, testate amoebae, and μXRF elemental trends were analyzed to determine the timing of lagoon siltation and sand barrier formation. Results indicate that natural shoreline changes and/or an extreme wave event (a tsunami or large tropical cyclone) are likely key contributing factors towards the decline and abandonment of the two ancient harbour sites.

Chapter 2

Evidence of recent sea-level rise and the formation of a classic Maya canal system inferred from Boca Paila cave sediments, Sian Ka'an biosphere, Mexico

The content of this chapter is a published manuscript under the following citation:

Steele, R.E., Reinhardt, E.G., Devos, F., Meacham, S., LeMaillot, C., Gabriel, J.J., Rissolo, D., Vera, C.A., Peros, M.C., Kim, S-T, Marshall, M., Zhu, J. (2023) Evidence of recent sea-level rise and the formation of a classic Maya canal system inferred from Boca Paila cave sediments, Sian Ka'an biosphere, Mexico. Quaternary Science Reviews, 310(108117). https://doi.org/10.1016/j.quascirev.2023.108117.

Evidence of recent sea-level rise and the formation of a classic Maya canal system inferred from Boca Paila cave sediments, Sian Ka'an biosphere, Mexico

Riley E. Steele[a*], Eduard G. Reinhardt[a], Frederic Devos[b], Samuel Meacham[b], Chris LeMaillot[b], Jeremy J. Gabriel[a], Dominique Rissolo[c], Cesar Arturo Vera[d], Matthew C. Peros[e], Sang-Tae Kim[a], Matthew Marshall[f], Juliet Zhu[a]

[a] *School of Earth, Environment, and Society, McMaster University, 1280 Main St. W, Hamilton, Ontario, L8S 4L8, CA*
[b] *Centro Investigador Del Sistema Acuifero De Quintana Roo A.C. (CINDAQ), 77733, Puerto Aventuras, Quintana Roo, Mexico*
[c] *Jacobs School of Engineering, University of California, San Diego, 9500 Gilman Drive, La Jolla, California, 92093, USA*
[d] *Université de Sherbrooke, 2500 boulevard de l'Université, Sherbrooke, Québec, J1K 2R1, CA*
[e] *Department of Environment and Geography, Bishop's University, 2600 College Street, Sherbrooke, Québec, J1M 1Z7, CA*
[f] *Department of Earth Sciences, Carleton University, 1125 Colonel By Drive, Ottawa, Ontario, K1S 5B6, CA*
[*] *Corresponding author: steelr3@mcmaster.ca*

Abstract

Cave sediments along the eastern coast of the Yucatán Peninsula contain important records of paleoenvironmental change that have not been fully explored. Reconstructing environmental changes in Boca Paila lagoon reveals details about sea level, flooding of the Sian Ka'an Biosphere, and the timeline of occupation at Muyil, an important Classic Maya maritime trading site. Three sediment cores (BP1, BP2, and BP3) were collected from a cave system beneath Boca Paila lagoon in the Sian Ka'an Biosphere. Radiocarbon dating, geochemical (X-Ray Fluorescence Core Scanning, δ^{13}C, C/N), and microfossil (foraminifera, diatoms, pollen) analyses were performed. The combined results show three distinct phases of coastal evolution. Phase 1 (1157 BCE or earlier), an upland area with mangrove associate Conocarpus erectus, grasses, and ferns, is characterised by: organic-rich detrital peat; a relative absence of foraminifera and diatoms; organic geochemistry results within terrestrial ranges (δ^{13}C values of -28 ‰ to -26 ‰); and low Sr/Ca, Si/Ti, and Ti/K ratios. These indicate dry conditions at the karst surface. Phase

2 (1157 BCE – 312 CE), a shallow wetland, is represented by: an increase in weathering products (Ti/K) and diatom productivity (Si/Ti); more positive δ^{13}C values (-27 ‰ to -22 ‰) and decreasing C/N ratios; and increased marine foraminifera (e.g., *Ammodiscus* sp.). These indicate more open water conditions. Phase 3 (>312 CE), a wetland/lagoon environment, is characterized by: carbonate-rich marl; a greater diversity of foraminifera (*Ammonia* spp., *Elphidium* spp., *Rosalina* spp., and *Bolivina* spp.), diatoms (*Cyclotella meneghiniana*, *Craticula* spp., *Amphora* spp., *Hyalosynedra laevigata*, and *Grammatophora* spp.) and pollen (from mangroves, ferns, grasses, palms, and pine); increased Si/Ti and Sr/Ca values; and mixed marine and terrestrial organic geochemistry values (δ^{13}C values of -22 ‰ to -20 ‰). These indicate increased input of marine organic sediment during sea-level rise. Sea-level and climate records support the interpretation of a dry upper karst environment prior to ∼1157 BCE, with sea-level rise forming shallow (<50 cm) wetlands by ∼312 CE. Previous archaeological analysis estimates that the first settlers arrived at Muyil ∼350 BCE, but that population expansion and construction of most structures occurred during the Postclassic (925–1550 CE). Sea-level rise would have been an important factor in the expansion of coastal settlements and trade routes; continued sea-level rise after ∼312 CE allowed for the formation of deeper lagoons and channels connecting the coast to Muyil and other inland sites which would likely not have been navigable prior to the Early Classic period (250–600 CE) as they would be too shallow. This study highlights the impacts of environment on society, as well as the importance of karst cave systems for obtaining paleoenvironmental records.

Keywords: *Holocene, Sea Level Changes, North America, Yucatán Peninsula, Coastal geomorphology, Geoarchaeology, Cave sediments, Micropaleontology, µXRF*

2.1 Introduction

Circum-peninsular maritime trade networks are thought to have been integral to Maya economies across the Yucatán Peninsula, but only beginning during the Terminal Classic period (800–925 CE; Glover et al., 2011). Despite multiple lines of evidence for long-distance trade from Veracruz to the Gulf of Honduras, there remain questions surrounding Maya maritime trade activity and why it only developed and expanded in later periods (Andrews, 1993; Biar, 2017; Clark, 2016; Jaijel et al., 2018; McKillop, 2010; Sabloff & Rathje, 1975; Thompson, 1949). Coastal communities are thought to have developed a lifestyle less reliant on agriculture compared to inland communities, focusing more on available marine resources and trade across Mesoamerica (Andrews, 1993; Glover et al., 2011, 2018). Although inland populations declined and many major cities were abandoned during the Terminal Classic period, many coastal communities continued to thrive up until the Spanish conquest in the 16th century (Clark, 2016; Glover et al., 2011; Sabloff & Rathje, 1975). Archaeological research has revealed remains of port settlements along coasts of the entire Yucatán Peninsula (Clark, 2016), models and depictions of dugout canoes (Biar, 2017), and a wooden oar from a Late Classic saltworks site in Belize (McKillop, 2005). Most of the information gathered on Maya port sites on the eastern coast relates to the Late Postclassic period (1000–1550 CE), though there is evidence of sea trade activity as early as the Preclassic period in the western and northern coasts of the Peninsula (2000 BCE – 250 CE; Andrews, 1993; Biar, 2017; Clark, 2016; Sabloff & Rathje, 1975; Witschey, 1988, 1993). The Yucatán's eastern coast has the highest concentration of Postclassic sites in the Maya Lowlands (Andrews, 1993). Coastal sites are often spaced ~30–40 km apart (ideal daily distances for canoe travel: Glover et al., 2018) and are located next to natural harbours near lagoons, islands, or rivers that offer shelter from adverse weather conditions (Andrews, 1993). The wetlands that currently extend along the eastern coast, providing sheltered canoe routes for maritime trade, did not always exist in their current form and their developmental history remains largely undocumented.

Holocene sea-level rise (~2 m in the past 3000 years; Khan et al., 2017; Milne & Peros, 2013; Toscano & Macintyre, 2003) would have caused progressive flooding and encroachment of marine environments into the Yucatán's interior, resulting in the current groundwater-fed wetlands along the eastern coast (Platt & Wright, 2022). These changes in coastal landscapes likely had an impact on nearby human activity. Reconstructing coastal evolution with subrecent sea-level rise (i.e., the past 3000 yrs) provides important environmental context for understanding cultural changes and is particularly relevant in low-relief karst terrains (epikarst) where small changes in sea level may cause large shifts in the shoreline and coastal habitats. The formation of wetlands and protected embayments would provide navigable waterways for small craft (e.g., dugout canoes) and the extent of these environments is largely determined by sea level and epikarst relief. Despite the importance of these environments for maritime trade in the Yucatán, there are few studies that have purposefully examined coastal evolution from an archaeological context, with most of the research concentrating on north and western portions of the peninsula (e.g., Vista Alegre, Jaijel et al., 2018; Celestun Lagoon, Hardage et al., 2022). Lagoon/wetland sediment records are typically used for coastal reconstructions; however, these sediments can present issues with stratigraphic continuity in terms of physical and biological reworking (i.e., wave action and currents, bioturbation). Cave sediments have not been studied extensively; however, they typically have little or no bioturbation and may contain more coherent temporal records. Our results from the Boca Paila Cave System in the Sian Ka'an Biosphere provide further context for understanding Terminal Classic to Postclassic maritime trade further south on the peninsula and demonstrate the potential of undisturbed cave sediments for studying sea-level change and coastal evolution in karst terrains.

Paleoenvironmental proxies within the Yucatán's submerged coastal cave sediments have not yet been fully explored. These systems are often suboxic to anoxic, typically have low groundwater flow, and contain few benthic taxa to disturb the sediments (e.g., Collins et al., 2015a, 2015b). Geochemical data from cave sediment records have been useful for inferring climate and weather events, phytoplankton productivity, and water mass changes (Kovacs et al., 2017a, 2018; McNeill-Jewer et al., 2019). Measuring the relative content of elements within sediment samples through scanning X-ray fluorescence (XRF) is advantageous because it is non-destructive and provides high-resolution (200 μm) geochemical data compared with other conventional methods. Lithologically derived and biologically influenced elements from cave sediments have been useful indicators of climate patterns in the Yucatán Peninsula (McNeill-Jewer et al., 2019) and have potential for reconstructing coastal landscape changes. Organic matter geochemistry (δ^{13}C, C/N) can help to infer changes in the source of organic carbon in coastal settings (Douglas et al., 2016; Lamb et al., 2006). In the Yucatán Peninsula, analyses have been useful for reconstructing sea-level changes and coastal cave flooding events (Gabriel et al., 2009; van Hengstum et al., 2010). Because minimal organic matter is generated in cave settings, the accumulation of organic matter that has been transported into the cave system can be used to indicate environmental changes on the karst surface. Foraminifera and diatoms are useful environmental proxies for inferring sea level and flooding histories (e.g., Gabriel et al., 2009; van Hengstum et al., 2009, 2010, 2011). They are abundant in aquatic environments, preserve well in sediment over time, and are sensitive to various environmental variables (Armstrong & Brasier, 2005; Murray, 2006). Because diatoms are photosynthetic, their presence in cave sediments can only be the result of taphonomic transport; therefore, changes in assemblages will reflect conditions on the sunlit environments of the epikarst. Both foraminifera and diatoms taxa display varying tolerances to salinity (Armstrong & Brasier, 2005; Smol & Stoermer, 2010), making them useful for inferring changes from marine to brackish mangrove habitats associated with lagoon development. Pollen analysis is also a useful indicator of vegetation and environmental change on the epikarst surface, which is often related to climate or land-use (Douglas et al., 2016). Pollen assemblages have previously been used in cave and cenote settings to help document vegetation changes due to sea-level rise and flooding events, especially related to mangroves (i.e., Rhizophora mangle; Gabriel et al., 2009), and can help confirm the formation of wetlands on the eastern coast of the Yucatán Peninsula.

Multiproxy sediment studies have provided information on past environmental conditions for some areas of the eastern coastline including the northeastern tip (Jaijel et al., 2018) and the region between Playa del Carmen and Tulum (Shaw, 2016). The modern northeastern tip near Vista Alegre, a Maya port site, is characterized by mangrove islands, tidal flats, hypersaline ponds, and flooded forests (Jaijel et al., 2018). A period of increased site occupation ∼2000–1550 yr BP (50 BCE to 400 CE) corresponds to the flooding of nearby bays with sea-level rise which would have created more open space for maritime activity and canoe access (Glover et al., 2011; Jaijel et al., 2018). The northeastern coastline becomes rocky headlands with bays and crescent shaped beaches between Playa del Carmen and Tulum (Shaw, 2016). The rocky headlands are underlain by fossilized coral reefs dating to the late Pleistocene (122,000–2000 yr BP), and the modern bays and beaches occupy the low-elevation areas of the ancient coastline (Shaw, 2016). A coastal berm stretches 50 km along this area of the coastline. Its features indicate that an anomalously extreme event, such as a tsunami or mega-hurricane, struck the coast around 1500 yr BP (450 CE; Shaw & Benson, 2015). Further south, the Yucatán's eastern coastal terrain is close to sea level and transitions back into shallow brackish and freshwater lagoons, mangroves, and flooded wetland environments. These wetlands extend further south into the Belize coast (e.g., ~100 km; Luzzadder-Beach & Beach, 2009), preserve many ancient Maya port sites, and contain underlying cave systems that can reveal past environmental records. Previous studies on carbon accumulation (Adame et al., 2021), sedimentation in caves (Collins et al., 2015c), and vegetation changes (Torrescano & Islebe, 2006) in the Yucatán's eastern coastal region provide estimates of 3040–3800 yr BP (1850–1090 BCE) for the timing of initial mangrove peat accumulation related to rising sea-level.

This study focusses on Muyil, a Maya port site within the wetlands on the Yucatán's southeastern coast. Previous archaeological studies have revealed information on the timing of human activity at this Classic–Postclassic port site (Witschey, 1988, 1993). Past coastal reconstruction is a useful addition to this archaeological study, providing a more comprehensive understanding of Muyil's history. The purpose of this study is to reconstruct around 3000 years of environmental changes. Three sediment cores from within the cave passages beneath Boca Paila lagoon were analyzed using geochemical and microfossil methods. The paleoenvironmental results will help to determine the timing of wetland development and canoe accessibility to Muyil from the sea and elsewhere along the Yucatán's coast. This study contributes to geoarchaeological research by highlighting the potential implications of environmental change on the increased maritime activity observed on the Yucatán's eastern coast during the Postclassic. Results also demonstrate the effectiveness of cave sediments as a source of paleoenvironmental proxies.

2.2 Regional Setting

2.2.1 Yucatán Peninsula

The Yucatán Peninsula's tropical climate has seasonal trends in temperature and rainfall: a cool, dry season from December to April, and a warm, wet season from May to November (Kovacs et al., 2017b). The average winter temperature is 25 °C and 28 °C in summer, with an average yearly precipitation of 1500 mm in the northeast to 500 mm in the northwest (Beddows et al., 2016; Collins et al., 2015b). Variation in precipitation is largely controlled by the Intertropical Convergence Zone (ITCZ; Hodell et al., 2007).

The Yucatán Peninsula is an extensive, partially emergent Cretaceous–Cenozoic limestone/dolostone platform (Bauer-Gottwein et al., 2011; Smart et al., 2006; Ward et al., 1985). The topography is relatively flat, with a maximum elevation of ∼250 m in the central area of the platform gradually decreasing towards the margins and northeastern region (Bauer-Gottwein et al., 2011). The limestone has been extensively eroded due to a combination of precipitation, mixing-zone hydrology, glacio-eustatic sea-level change, and littoral processes (Smart et al., 2006). Precipitation quickly infiltrates through the porous limestone, so there are very few surface waterbodies (Beddows et al., 2016). There are, however, many cenotes (sinkholes) that connect to the aquifer (Perry et al., 2003). The aquifer is density stratified, with a Meteoric Water Mass (MeWM; <1–7 ppt, ∼25 °C) overlying a warmer Marine Water Mass (MaWM; >30 ppt, ∼27 °C) penetrating from the coast (Beddows, 2004). The halocline is the transition between these water masses and can be diffuse (i.e., a brackish layer) or sharp. It is undersaturated with respect to calcite ($CaCO_3$) resulting in limestone dissolution near coastal outlets and the formation of subterranean cave systems throughout the region (Perry et al., 2003; Smart et al., 2006). Many cave passages are hydrologically connected to one another, as well as the ocean; they extend up to ∼12 km inland and are continuing to expand with exploration efforts (Smart et al., 2006).

2.2.2 The Sian Ka'an Biosphere, Boca Paila lagoon, and Muyil

The Sian Ka'an Biosphere Reserve is a 4000 km2 UNESCO World Heritage Site on the east coast of the Yucatán Peninsula (Figure 2.1; Arellano-Guillermo, 2003; Claudino-Sales, 2019). The biosphere extends 40–50 km inland and ∼120 km along the coast. It protects the biodiversity of tropical forests, wetlands, and coastal and marine ecosystems, each around one-third of the total area (Arellano-Guillermo, 2003). The tropical forests are dominated by evergreen trees, shrubs, palms, and other woody vegetation. The wetlands contain islands of mangroves (mainly Rhizophora mangle) and tropical forest taxa, while the coastal dune vegetation often includes low, non-woody plants (Islebe et al., 2015). The Sian Ka'an area illustrates relatively early transgressive phase environments. Rising sea level has resulted in the progressive encroachment of shallow marine environments into the platform interior as well as the formation of groundwater-dependent freshwater wetlands further inland (Platt & Wright, 2022). Due to faults and the interaction between fresh and marine groundwater, the coastal region is characterized by cenotes, caves, and crescent shaped beaches (Claudino-Sales, 2019).

Boca Paila is a large (∼0.5–2 km x ∼5.5 km) coastal lagoon ∼20 km south of Tulum, within Sian Ka'an. The lagoon is variable in depth but shallow with an average depth of 3 m. Sand and seagrass (Thalassia testudinum) cover the karstified limestone bottom (Lara & González, 1998). There are numerous vents discharging groundwater into the lagoon, and the Boca Paila Cave System is one of these vents that has undergone extensive exploration and mapping by CINDAQ. Karst elevation (sill height) at the entrance to the cave is very shallow at ∼1-1.5 m water depth. The lagoon water is brackish and turbulent due to incoming waves from the Caribbean through a break in the offshore reef/dune barrier and groundwater discharge into the lagoon. On the landward side, Boca Paila is bound by seasonally flooding wetlands and mangrove forests (Claudino-Sales, 2019; Witschey, 1988).

Very little is known of the aquifer hydrology of the Sian Ka'an biosphere. The Yax Chen Cave System, ∼10 km north of Boca Paila, experiences low flow in the MeWM (Coutino et al., 2017; Kovacs et al., 2017). Based on cave diver observations, Boca Paila experiences strong reversing flow in and out of the cave passage close to the entrance of the lagoon. This has not been instrumentally measured but is likely tidal in origin. Instrumental monitoring of Campechen Lagoon (adjacent to Boca Paila) shows a semidiurnal to diurnal tidal cycle and overall (seasonal) water level varied by ∼30 cm over the 4-month period of measurement (August to December, 2019; Coutino et al., 2021).

Cayo Venado, a channel ∼3–6 m wide and 1–2 m deep, meanders westward ∼10 km inland from Boca Paila to Chunyaxche lagoon (Matthews, 1995; Platt & Wright, 2022). This freshwater lagoon is ∼5 km long, 2.5 km wide, and contains multiple cenote areas (Platt & Wright, 2022). Muyil canal, a short (550 m) waterway, leads from Chunyaxche lagoon to Muyil lagoon, a smaller (1.8 km diameter; Platt & Wright, 2022) freshwater source. Located at the edge of Muyil lagoon, 12 km inland, is the ancient Maya port settlement of Muyil, one of several Maya settlements found within Sian Ka'an (Arellano-Guillermo, 2003; Witschey, 1993).

Archaeological excavations of Muyil were conducted between 1987 and 1991 by Walter Witschey (Witschey, 1988, 1993). Ceramic and architectural evidence suggests that the site was occupied as early as 350 BCE, during the Preclassic (2000 BCE – 250 CE), and functioned as a coastal port until the Spanish conquest in 1500 CE (Witschey, 1993). During early occupation, the site was relatively small, as ceramics were the only evidence of inhabitants. The earliest evidence of temples, pyramids, and sacbes (raised causeways) leading from the lagoon to the structures of the site date to the Classic period (250–800 CE). Ceramic evidence suggests increased trade with Belize and nearby island sites, and a more established settlement during this time. Muyil continued to expand into the Postclassic period (925–1550 CE); population grew by an estimated 25–75%, as evidenced by the types and distribution of ceramics as well as by the construction of new temples, pyramids, sacbes, and field walls (Witschey, 1993).

2.3 Materials and Methods

2.3.1 Sediment core retrieval

Three push cores were collected by SCUBA divers in the cave passage under the Boca Paila lagoon (Figure 2.1; entrance: 20°0.480'N, 87°29.480'W). BP1 (length 58 cm) was collected ∼186 m from the cave entrance at a water depth of 14 m relative to sea level, and BP2 (length 73 cm) was collected ∼212 m from the entrance at a depth of 16 m. Both sample sites were collected from soft substrates along the cavern bottom. BP3 (length 47 cm) was retrieved ∼148 m from the entrance at a depth of 10 m, from an eroded bank of peat that outcropped (∼50 cm high) on the side of the cave passage. After collection, cores were split in half and stored at ∼4 °C.

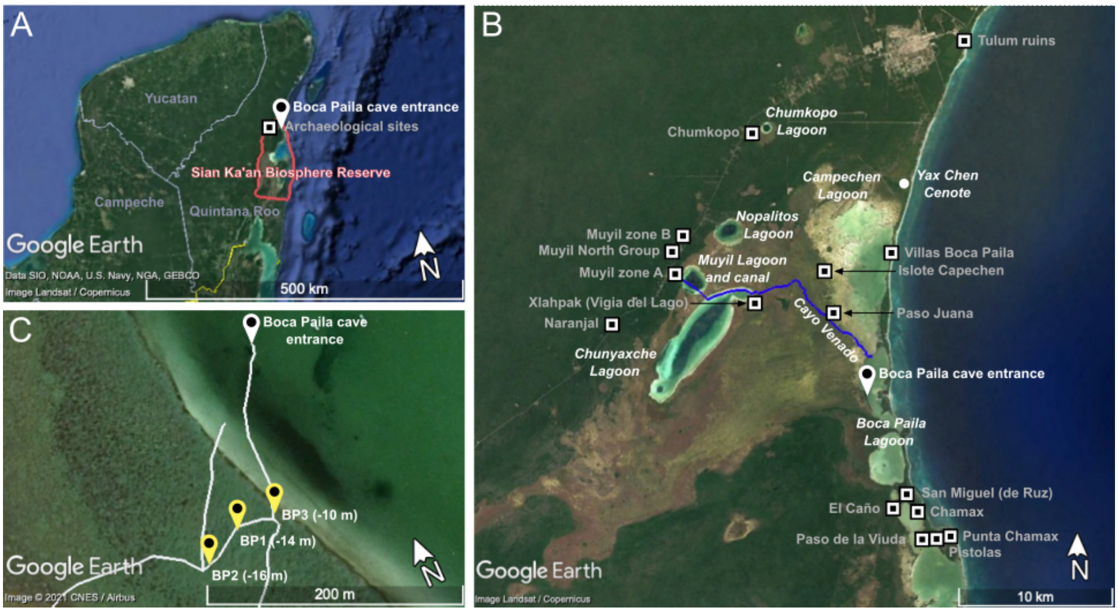

FIGURE 2.1: (a, b) Location of Boca Paila within the Sian Ka'an Biosphere Reserve, nearby archaeological sites, the sea-route leading to the Maya port site Muyil, and (c) three sediment cores collected from the Boca Paila Cave System. Maps Data: (a) Google, Data SIO, NOAA, U.S. Navy, NGA, GEBCO, Image Landsat/Copernicus; (b) Google, Image Landsat/Copernicus; (c) Google©2021 CNES/Airbus.

To provide an additional radiocarbon age for the timing of platform flooding and mangrove development, a small grab sample of basal mangrove peat (fibrous) on karstified limestone (1 m water depth) was collected at the southeastern side of Yax Chen Cenote (YCP1; 20°7.874'N, 87°27.994'W; Figure 2.1). The landowners had previously cut back the mangrove peat to expose a shallow limestone platform for swimmers. The basal peat (YCP1) sample was collected from the innermost portion of a core pressed into the exposed balk wall (∼20 cm penetration).

2.3.2 Water column measurements

Water mass characteristics of the Boca Paila lagoon and cave were taken using a Hydrolab MS5a multiparameter mini sonde on June 5th, 2009 by SCUBA divers near the core collection sites for approximately two hours (2:00 PM–4:00 PM).

Measurements of depth (±0.05 cm), temperature (±0.05 °C), conductivity (±0.05 mS/cm), salinity (±0.05 ppt), pH (±0.05), oxidation-reduction potential (ORP; ±0.5 mV), and dissolved oxygen (DO) content (±0.05%) were taken around every 30 seconds at various depths in the water column.

2.3.3 Radiocarbon dating

Nine subsamples from Boca Paila and one sample of basal (1 m depth; YCP1; Table 2.1) mangrove peat from Cenote Yax Chen (∼12 km north of Boca Paila lagoon) were analyzed for radiocarbon by DirectAMS through Accelerated Mass Spectrometry. Seven samples were selected from BP2 because it was the most complete core in terms of lithology. The other two samples included bulk sediment and a twig from BP3, targeting detrital peat deposits for estimated dates of platform flooding and mangrove development. The depths of samples from BP3, which was composed entirely of Detrital Peat (DP), were adjusted to the estimated depths within the DP layer of BP2 (Table 2.1), assuming that the top of BP3 (0 cm) represents the contact between DP and the Peat-Marl Transition (PMT) in PB2 (∼23 cm). This was done so that all radiocarbon results could be incorporated into a composite age-depth model to illustrate taphonomic processes (reworking) during deposition of the DP.

Dates were calibrated using IntCal20 Northern Hemisphere Radiocarbon Age Calibration Curve (Reimer et al., 2020). Ages were calibrated for two scenarios: (i) no reservoir correction, and (ii) a brackish reservoir correction for the upper laminated marl sediments (Table 2.1). Reservoir correction scenarios were considered because the bulk sediment samples may contain older or younger carbon (through incorporation of dissolved CO_2 or HCO_3^- from older limestone or shells, or organic matter from younger mangrove roots) which can lead to inaccuracies in the calibrated radiocarbon dates (Strunk et al., 2020). Kovacs et al. (2017a) found an average hard water offset of ∼1300 ^{14}C years BP (similar to other nearby values of 1200–1300 yr BP; Curtis et al., 1996) between the raw radiocarbon ages of terrestrial plant seeds and coeval calcite raft samples from the Sac Actun Cave System, ∼35 km north of Boca Paila. The average local marine reservoir correction is 135 ±77 yr BP, based on the ten closest data points from Boca Paila in the

Marine Reservoir Correction Database (http://calib.org/marine/). Using both the average hard water (∼1 ppt salinity) and the average local marine reservoir offset values (∼35 ppt), a reservoir correction ratio for brackish salinities based on the ∼17 ppt salinity of Boca Paila was calculated to be ∼736 yr BP[1]. This offset was not applied to the terrestrial peat samples. Because the Organic Matter (OM) from within the upper marl samples was derived from the brackish lagoon, these samples were included in age calibration scenario (ii). Age-depth models were constructed for the two age calibration scenarios using the R statistical software package Bacon (Version 2.5.8; Blaauw & Christen, 2011).

2.3.4 μXRF elemental analysis

Elemental analysis of the sediment cores was conducted with a Cox Analytical ITRAX X-Ray Fluorescence Core Scanner (μXRF) at the McMaster University Core Scanning Laboratory (MUCS Lab). Each core was analyzed using the Chromium heavy element (Cr-HE) X-Ray source with 30 kV, 29 mA, 200 μm resolution, and 15 second exposure time. The elements of interest for this study include strontium (Sr), calcium (Ca), titanium (Ti), potassium (K), and silicon (Si), which are valuable proxies for records of past fluctuations in rainfall and sea level (Kovacs et al., 2017a; Krywy-Janzen et al., 2019; McNeill-Jewer et al., 2019). A common source of Sr is from the weathering of limestone which is found throughout the Yucatán Peninsula and in groundwater (Kovacs et al., 2017a; Skougstad & Horr, 1963). Sr is found in reef-forming corals and other taxa that build their skeletons or shells with aragonite, which contains more Sr compared to calcite (Marshall & McCulloch, 2002). Thus, elevated Sr/Ca acts as an indicator of reefal sediment sources (Rothwell & Croudace, 2015). In the Yucatán, Ti and K originate from limestone weathering, and because Ti has a lower dissolution rate than K, an increase in Ti/K corresponds to greater lithological weathering and rainfall input (Lo et al., 2016). K is also biologically influenced by mangroves and primary productivity in cenotes and has a delayed response to precipitation (McNeill-Jewer

[1]This value was calculated by plotting the two known offset points according to their source salinity values (-135 cal yr BP at 35 ppt and -1267 cal yr BP at 1.1 ppt). The resulting trendline (y=33.392x-1303.7) was used to calculate an age offset at 17 ppt.

et al., 2019). Si is also a product of weathering and a useful indicator of precipitation patterns; however, Si is also related to biogenic silica (i.e., diatom abundance). The contribution from biogenic silica can be isolated from terrigenous inputs using a Si to Ti ratio. Because both Si and Ti are weathering products from limestone at relatively the same rate, and siliciclastic are scarce in the region, a greater Si/Ti ratio indicates greater diatom productivity (McNeill-Jewer et al., 2019; Peinerud, 2000).

Statistical identification of geochemically distinct zones across all three cores were determined by constrained cluster analysis of the μXRF results. The elemental data was standardized (column-centered with mean=0, sd=1), elemental proxies of importance for the coastal geological setting were selected (Al, Si, S, Cl, K, Ca, Ti, V, Mn, Fe, Ni, Cu, Zn, As, Br, Rb, Sr, Zr, Sb, Ba, and U; Rothwell & Croudace, 2015), and samples were clustered using a Self-Organizing Map (SOM; "SOMbrero" package, Olteanu & Villa-Vialaneix, 2015). This method assesses the similarity of observations (each 0.2 mm of core), through Ward's method of hierarchical clustering, using Euclidean distance as a measure of dissimilarity. Clusters were then grouped into 6 higher order clusters (superclusters) to help identify stratigraphic sequences of distinct elemental composition. The three cores were then correlated based on lithology and chemofacies results.

2.3.5 Stable isotope organic geochemistry

Thirty-four bulk sediment samples were analyzed for carbon and nitrogen isotopes and their elemental concentrations (δ^{13}C $\pm$0.07 ‰, δ^{15}N $\pm$0.17 ‰, C $\pm$0.2 %, N $\pm$0.2 %; precision values are standard deviations from the standards used). The samples were treated with a 10 % hydrochloric acid solution for 24 hours to remove carbonate material, rinsed several times with deionized water, then dried at room temperature. The remaining material was ground into a fine powder, and approximately 2.5-mg subsamples were combusted using Costech Elemental Combustion System ECS 4010, carried in a helium stream to a Thermo Finnigan ConFlo III, and measured on a Thermo Finnigan DELTAplus XP continuous-flow isotope ratio mass spectrometer. Results were compared against several standards (USGS 24, USGS 40, IAEA 600, IAEA C-3, IAEA N-2, IAEA CH-7, and ANU

Sucrose). Carbon isotopic ratios were expressed as standard delta notation (δ) in per mil (‰) with respect to Vienna PeeDee Belemnite (VPDB) and nitrogen isotopic ratios were expressed similarly with respect to atmospheric nitrogen (Air-N_2).

2.3.6 Microfossil analysis

Twelve samples (~1 cm intervals) from BP2 were collected for analysis of foraminifera. Subsamples (~3.7 cm3) were wet sieved through 45 μm and 300 μm mesh to remove both fine and coarse material. Samples were wet split if required, and foraminifera were identified and enumerated wet in a petri dish using an Olympus SZX12 binocular microscope (60–100X magnification). A least 300 specimens per sample were counted when possible. For samples with <300 specimens, the entire sample was analyzed, and the maximum number of foraminifera were counted. Identification was completed with reference to well-illustrated publications (Gabriel et al., 2009; Poag, 2015; van Hengstum et al., 2008; van Hengstum & Scott, 2011). Ostracods were enumerated, although not identified further. Where the estimated standard error for the taxa identified was greater than the abundance in all samples, the taxa was deemed statistically insignificant and omitted from further analysis (Patterson & Fishbein, 1989). The Shannon-Weaver diversity index (SDI; Shannon, 1948) was used as a measure of foraminifera diversity for each sample as outlined in van Hengstum et al. (2008). SDI values >2.5 indicate stable conditions for ecological assemblages, while values 1.5–2.5 suggest transitional conditions and values ~<1.5–0.5 indicate unfavorable conditions (Magurran, 1988; Patterson & Kumar, 2002).

Twenty-three samples (~1 cm intervals) from BP2 were collected for analysis of diatoms. Subsamples (~0.5 g) were treated with a 10 % hydrochloric acid solution for 24 hours to remove excess carbonate material and 35 % hydrogen peroxide for several weeks to remove excess organic material. Microspheres were then added to each sample to allow for calculation of approximate diatom concentrations. Samples were mounted on slides with Naphrax®, and diatoms were identified and enumerated using Differential Interference Contrast microscopy (DIC; Nikon Optiphot binocular microscope) and 100x oil immersion magnification. At least

300 specimens per sample were counted where available. Identification was completed to genus, or species level, using well-illustrated references, databases, and published lists of diatoms found in Mexico, the Gulf of Mexico, and the nearby Caribbean region (Krayesky et al., 2009; Licea et al., 2016; Lopez-Fuerte et al., 2010; Merino-Virgilio et al., 2013; Sánchez et al., 2002; Smol & Stoermer, 2010; Spaulding et al., 2021; The Periphyton Group, 2022). Phytoliths were enumerated but not identified. Statistically insignificant diatom taxa were omitted from further analysis, and the SDI was used as a measure of diatom diversity for each sample, as explained above for foraminifera.

Eleven subsamples (~1.25 cc) from BP2 were analyzed for fossil pollen using standard processing procedures (Faegri & Iversen, 1990). One tablet of Lycopodium was added to each subsample to calculate pollen concentration. Subsamples were treated with 10 % HCl to remove carbonate material, then boiled in 10 % KOC for 15 minutes to break down humic acids. Subsamples were sieved at 125 and 10 μm to concentrate the pollen and then boiled in hydrofluoric acid for 10 minutes to remove silicate material. The subsamples were then washed in glacial acetic acid (GAA) followed by acetolysis treatment to remove plant cellulose. A second GAA wash was performed before washing the subsamples in water. Subsamples were then treated with tert-Butyl alcohol and mixed with silicone oil as a mounting medium, before being mounted on slides. Pollen was identified and enumerated using a Zeiss Axio Lab A.1 microscope at 400X magnification. The pollen counts per slide were low (<100 grains per sample) and were therefore summarized semi-quantitatively. Although samples from the central portion of the core (27–37 cm) were processed, the high mineral content of these samples meant that little pollen was extracted and the residue itself was unable to be used to make slides (i.e., it was highly sticky after processing).

2.4 Results

2.4.1 Hydrological conditions

Boca Paila groundwater is distinctly stratified, with a salinity of ~15–18 ppt in the MeWM above the halocline (~16 m deep) and 35 ppt below the halocline in the MaWM (Figure 2.2). Water temperature and pH follow a similar trend: temperatures were 26.25–26.50 °C with a pH of ∼7.0 above 16 m and reached 27.40 °C with a pH of 7.6 at the halocline. Surficial water in the lagoon was warmer (∼26.5 – 27.3 °C) than the MeWM. DO saturation values in the lagoon ranged from 12.5–43 % in the upper ∼2.5 m and became anoxic in the cave entrance and within the MeWM and MaWM (Figure 2.2). During measurement (June 5th, 2009), SCUBA divers noted (unmeasured) high flow in the cave passage proximal to the entrance but lower flow in the distal upstream areas.

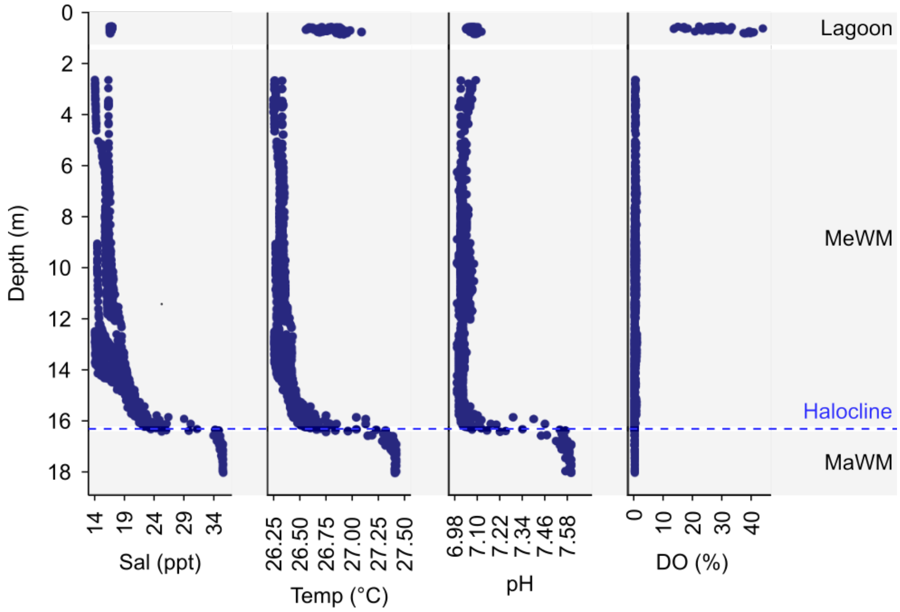

FIGURE 2.2: Hydrological (salinity, temperature, pH, and dissolved oxygen) profiles of the Boca Paila Cave System, showing the halocline, the Marine Water Mass (MaWM), the Meteoric Water Mass (MeWM), and the lagoon surface.

2.4.2 Lithology and core chronology

The base of BP1 and BP2 and the entirety of BP3 consists of dark Detrital Peat (DP) interval that tends to be structureless with some intervals of subtle bedding (Figure 2.3). In BP1 and BP2, the DP is followed by a Peat-Marl Transition (PMT) interval. The PMT is relatively lower in organic matter (OM) content, as evidenced by the X-ray radiograph, and is finely laminated. The contact between the DP and PMT is sharp in BP2 (∼23 cm) and more gradual in BP1 (32 cm). Above the PMT in cores BP1 and BP2 lies finely Laminated Marl (LM).

The radiocarbon results (Table 2.1) and the age-depth models (Figure 2.4) show that the DP sediments span a few thousand years (∼3484–1157 BCE). In BP2, these DP ages contain reversals likely related to the input of older carbon sources from the surface and/or erosion and redeposition of sediment within the cave passage. The two ages in BP3 are in chronological order and include the youngest age (∼1157 BCE) for the DP sediments. The lower section of the PMT in BP2 dates to ∼2462 BCE, while the upper PMT dates to ∼682 BCE (Table 2.1). The lower PMT date is an outlier on age-depth curve which likely reflects older carbon sources (Figure 2.4). The LM sediments are much younger than the underlying units, dating to ∼312 and ∼480 CE with no reservoir correction and to ∼1070 CE and ∼1206 CE with a brackish reservoir correction. The basal mangrove peat from the shallow (∼1 m) edge of Cenote Yax Chen dated to ∼711 CE (Table 2.1).

2.4.3 Geochemistry results

Geochemical trends from the μXRF data (Figure 2.3) and the supercluster analysis (Figure 2.5) show distinct zones that correspond to visual changes in lithology. The DP units of BP2 and BP3 contain layers of shell fragments (visible as white specs and as alternating light and dark banding in the radiograph) that correlate with spikes in Sr and Ca. This pattern is most apparent in BP3 ∼20–25 cm. Concentrations of both Sr and Ca begin to increase in the PMT units of cores BP1 and BP2. In the LM units of BP1 and BP2, Sr counts continue to increase notably, while Ca counts decrease. Ti, K, and Si counts increase sharply at the top of the DP units of all three cores and into the PMT of cores BP1 and BP2 (Figure 2.3). Both above and below this transition, Ti counts remain relatively low (∼<1000) in BP1 and BP2. K and Si counts continue to increase slightly up-core in the LM sediments, especially in BP2. The inc/coh values, related to the porosity/density of sediment and therefore OM content, due to its high porosity relative to carbonate sediment. The inc/coh decreases in the PMT units in BP1 and BP2 and the radiograph also shows higher sediment density in this interval.

TABLE 2.1: Radiocarbon results for BP2, BP3, and isolated plant material from Yax Chen basal mangrove peat (YC), showing estimates with no reservoir correction and a brackish correction (736 yr BP, within dashed boxes) for LM samples. (S=bulk sediment, LM=Laminated Marl, PMT=Peat-Marl Transition, DP=Detrital Peat, MP=Mangrove Peat).

Core	Core Depth (cm)	Adjusted* Depth (cm)	Sample type & Lithology	Fraction of modern		Radiocarbon age		Cal BCE/CE (+)	Cal BCE/CE (-)	Prob-ability	Cal CE/BCE Mid	Error ±
				pMC	1σ error	BP	1σ error					
BP2	10.5	10.5	S, LM	81.94	0.24	1600	24	420	540	95%	480	60
								1156	1255	95%	1206	50
BP2	20.5	20.5	S, LM	80.45	0.24	1747	24	242	382	95%	312	70
								991	1148	95%	1070	79
BP2	31.5	31.5	S, PMT	72.79	0.24	2551	26	-800	-564	95%	-682	118
BP2	35.5	35.5	S, PMT	61.02	0.19	3968	25	-2573	-2351	95%	-2462	111
BP2	54.5	54.5	S, DP	64.52	0.22	3520	27	-1929	-1751	95%	-1840	89
BP2	40.5	40.5	S, DP	55.87	0.25	4676	36	-3601	-3366	95%	-3484	118
BP2	69.5	69.5	S, DP	66.61	0.23	3264	28	-1613	-1454	95%	-1534	80
BP3	12.5	44	S, DP	69.25	0.2	2952	23	-1258	-1055	95%	-1157	102
BP3	36	57	Twig, DP	67.79	0.19	3123	23	-1448	-1302	95%	-1375	73
YCP1	1 m		Plant, MP	84.66	0.29	1338	28	647	774	95%	711	64

* Sample depths for BP3 adjusted to Peat-Marl Transition in BP2 for composite age model in Figure 4.
Dashed boxes = age estimates with brackish correction of 736 yr BP

BP3 has relatively high inc/coh ratio values throughout, reflecting the organic-rich DP composition (Figure 2.3).

The correlation between cores and the trends in Sr/Ca, Si/Ti, and Ti/K ratios are presented in Figure 2.6. The LM and the PMT facies are represented in cores BP1 and BP2. The DP facies is found in all three cores and contains relatively low Sr/Ca values with intermittent spikes. The Sr/Ca ratio values decrease in the PMT, then steadily increase upwards throughout the LM units. Si/Ti ratio values are low throughout the DP, then oscillate between high and low values in the PMT and the LM sediments. The Ti/K ratio values increase in variability throughout the PMT sediments and remain relatively low in the DP and LM units in all cores (Figure 2.6).

The $\delta^{13}C$ values from the DP unit of BP2 range from -28.2 ‰ to -26.2 ‰ (mean= -27.2 ‰). Values increase in range in the PMT unit (-26.3 ‰ to -23.0 ‰, mean= -25.3 ‰), and further increase in the LM (-22.4 ‰ to -20.2 ‰, mean= -21.5 ‰). The average $\delta^{15}N$ values increase slightly upcore, with 7.3 ‰ in the DP, 8.2 ‰ in the PMT, and 8.2 ‰ in the LM. The C/N ratios are variable throughout the core, with mean values of 10.7 in the DP unit, 10.8 in the PMT unit, and 9.6 in the LM unit (Figure 2.7; Appendix A1).

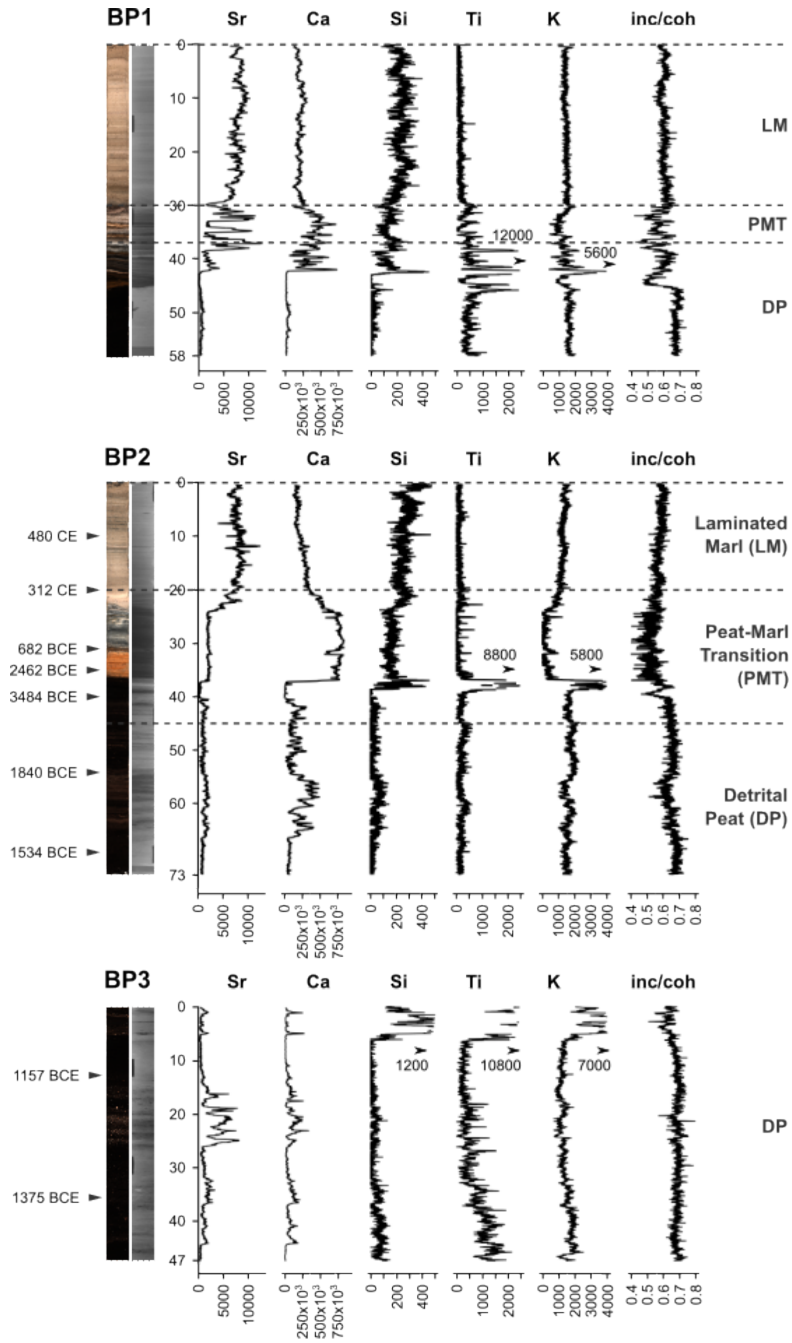

FIGURE 2.3: Optical and radiograph images of cores BP1, BP2, and BP3, with μXRF results for elements of interest, radiocarbon dates plotted in relation to core depth, and chemofacies divisions based on supercluster results (see Figure 2.5).

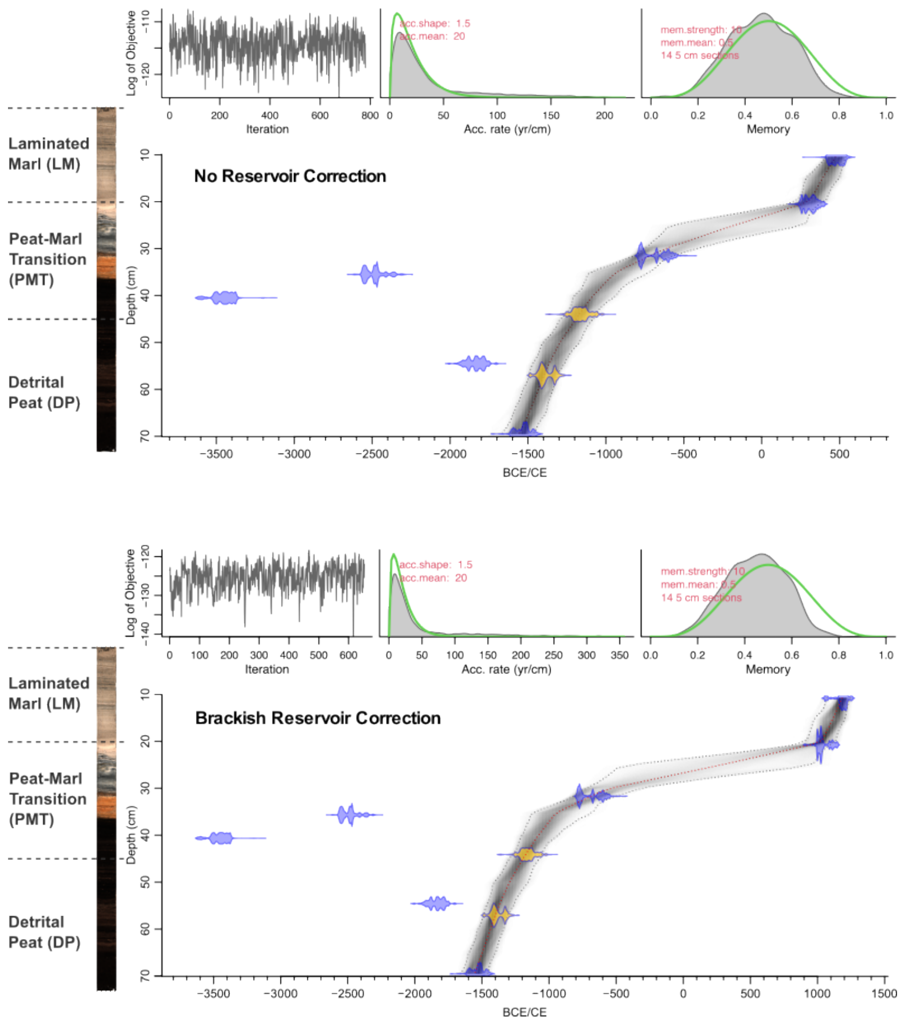

FIGURE 2.4: Composite age-depth models of BP2 (blue) and BP3 (yellow) radiocarbon results for no reservoir correction and a brackish reservoir correction using Bacon (R), with chemofacies divisions based on the supercluster results (see Figure 2.5).

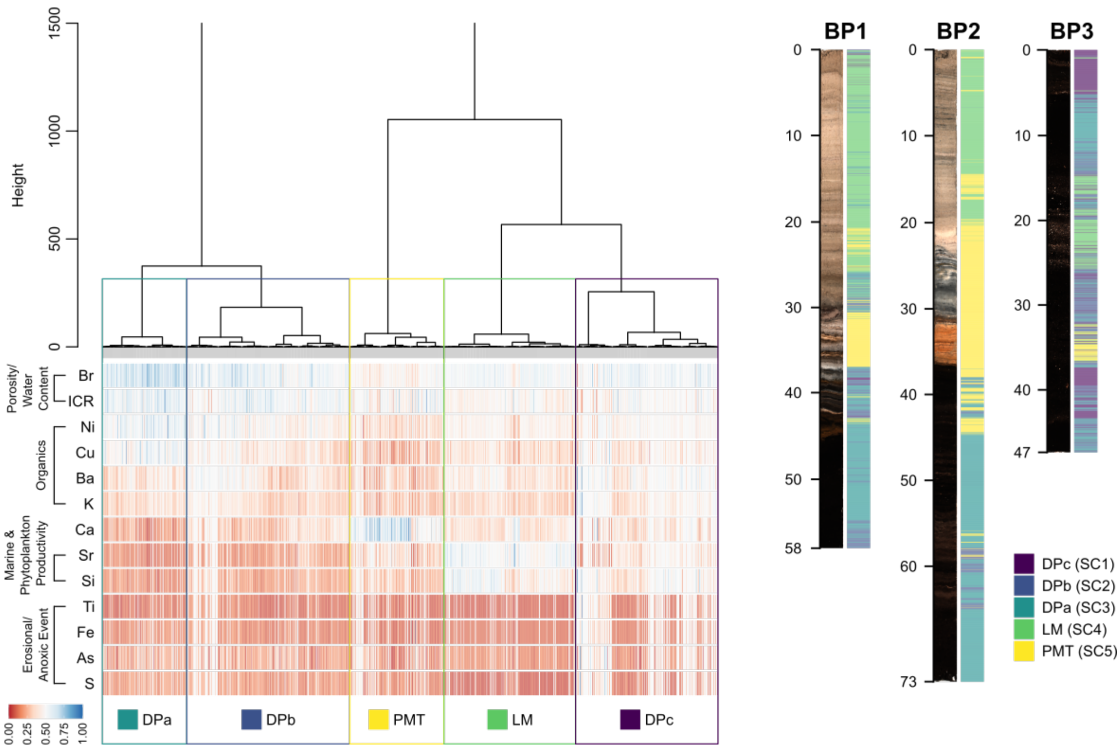

FIGURE 2.5: Chemofacies superclusters (DP= Detrital Peat, PMT = Peat Marl Transition, LM = Laminated Marl) of μXRF data from cores BP1, BP2, and BP3, with heatmap of elemental trends.

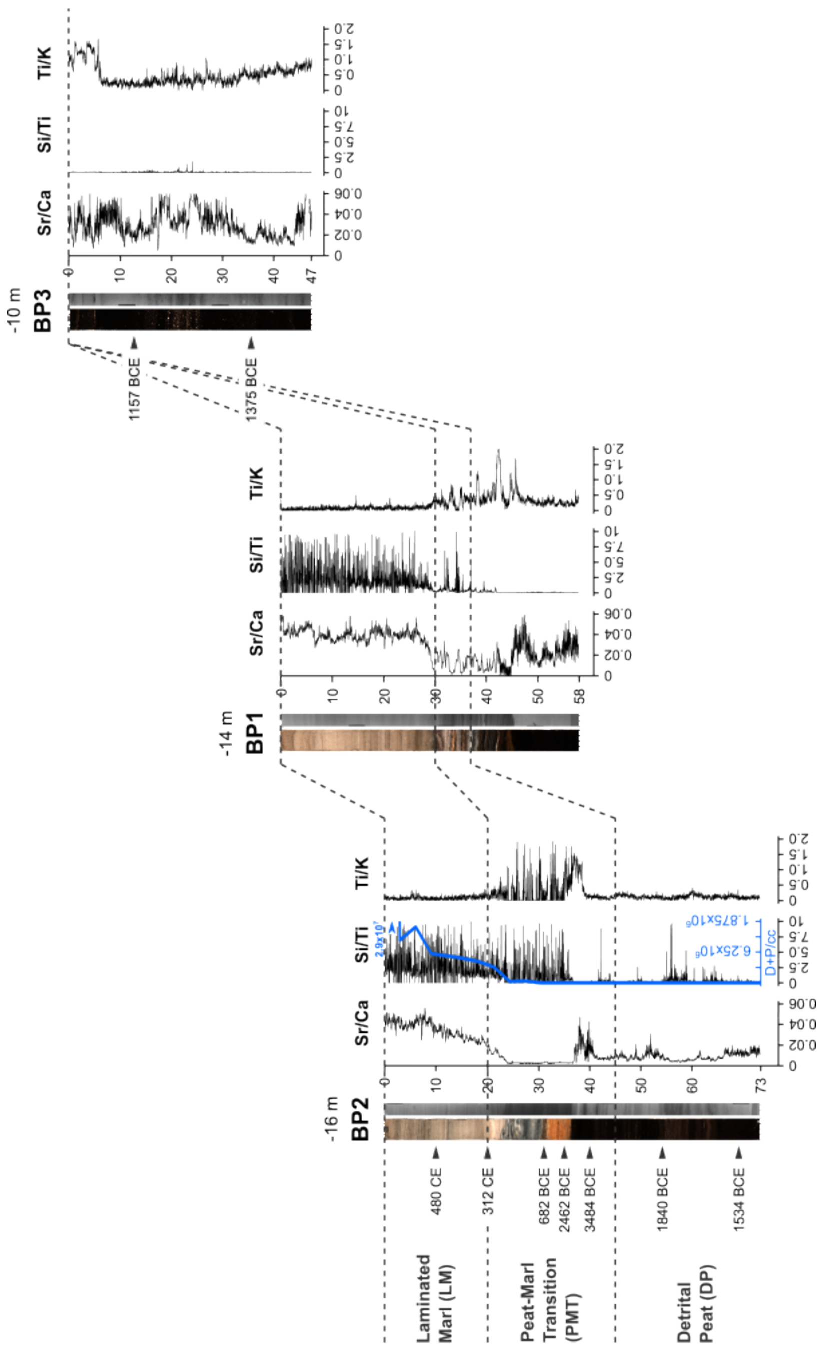

FIGURE 2.6: Correlation between cores BP1, BP2, and, BP3 based on relative water depth, chemofacies (see Figure 2.5), and elemental ratios, with diatom and phytolith (D+P/cc) concentration results compared to Si/Ti trends in BP2.

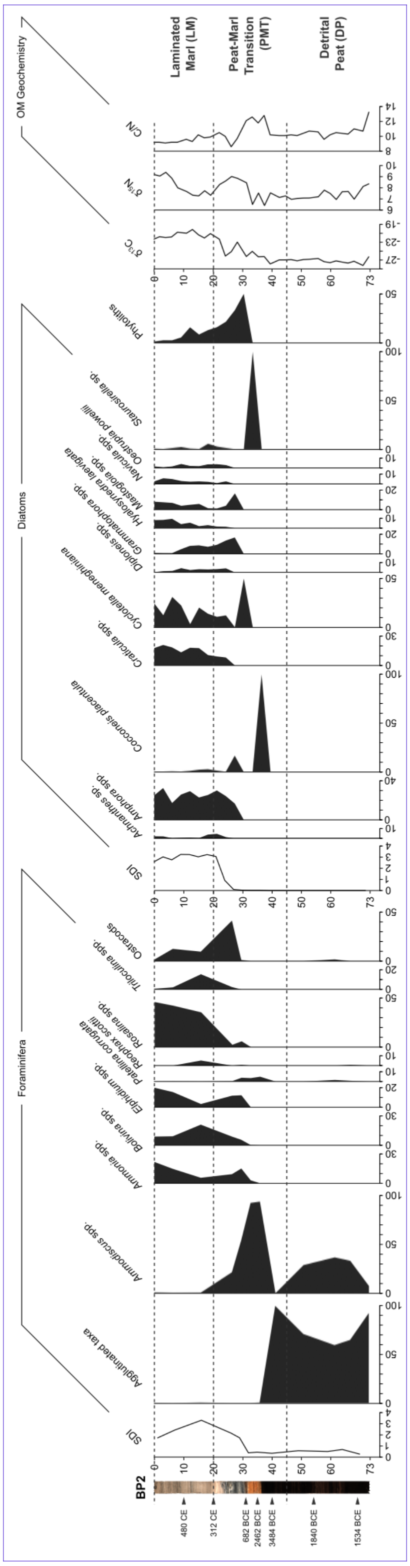

FIGURE 2.7: Shannon Diversity Index (SDI) values, relative abundances (%) of dominant micro-fossils, and organic geochemistry results for core BP2 with chemofacies divisions (see Figure 2.5).

Table 2.2: Pollen counts in 8 samples from core BP2.

Depth (cm)	**1**	**5**	**14**	**23**	**38**	**47**	**56**	**71**
Individuals/cc	1784	2203	2970	1262	1918	4710	1379	2878
Sum	38	31	66	9	19	191	12	97
Mangroves								
Rhizophora	6	12	25	2	6	40	-	20
Conocarpus					9	88	10	54
Ferns								
Monolete spores	6	3	1	-	-	3	-	1
Trilete spores	-	-	-	1	-	3	-	-
Grass								
Poacaea (monoporate)	2	4	-	1	-	9	1	3
Chenopodiaceae	3	1	3	-	-	2	-	-
Asteraceae	2	-	7	-	-	8	-	1
Anacardinaceae (Spondias-type)	-	-	-	2	-	-	-	-
Palms								
Arecaceae	-	5	16	-	-	-	-	-
Myrica	4	-	-	-	-	-	-	-
Fig family								
Moraceae (2-pores)	-	3	-	-	-	19	-	-
Moraceae (3-pores)	-	-	-	-	-	-	-	12
Moraceae (4-pores)	-	-	-	-	-	-	-	4
Pine								
Pinus	6	2	7	3	1	-	-	-
Solanaceae	-	-	-	-	-	-	-	1
Unidentified pollen spores	9	1	7	-	3	19	1	1

2.4.4 Microfossil results

2.4.4.1 Foraminifera

Eighteen statistically significant foraminifera taxa were identified from the 12 BP2 samples, and results vary closely with lithology (Figure 2.7, Appendix A2). The five samples from the DP section at the base of the core contain very few specimens (9–80 per cc), including agglutinated taxa (∼60–100 % relative abundance, with proportions of ∼85 % *Trochammina inflata* and ∼15 % *Jadammina macrescens*) with some *Ammodiscus* spp. (∼7–37 %) and *Patellina corrugata* (∼1–2 %). Diversity is very low, with SDI values ranging from 0.25–0.67. The four samples from the PMT show increasing concentrations of foraminifera (from 88 to 307 counts/cc) with increasing diversity (0.37 to 2.15 SDI). *Ammodiscus* spp. (22–94 %), *P. corrugata* (∼1–5 %), and *Siphonina reticulata* (∼1 %) characterize this unit, with higher abundances of *Elphidium* spp. (∼12 %) and *Ammonia parkinsoniana* (3–11 %) towards the upper half of the section. The three LM samples contain high abundances (497-1365/cc; mean = 870/cc) and diversity (SDI 1.70-3.29; mean = 2.47) of foraminifera. Major species include *Rosalina* spp. (∼33–42 %), *Elphidium* spp. (∼3–20 %), *A. parkinsoniana* (∼3–16 %), *Bolivina variabilis* (∼6–13 %), and *Ammonia tepida* (∼2–9 %; Figure 2.7, Appendix A2).

2.4.4.2 Diatoms

Thirty-two statistically significant diatom taxa were identified from the 34 BP2 samples. There were no diatoms observed in the DP unit, and very few specimens observed in the PMT unit (Figure 2.7, Appendix A3). The dominant taxa in the transition include *Cyclotella meneghiniana* (∼12–50 %), *Grammatophora* spp. (∼14–17 %), *Amphora proteus* (∼12–17 %), *Craticula* spp. (∼8 %), *Amphora ostrearia* (∼5 %), and *Diploneis suborbicularis* (∼4 %). Abundances are low (5.7×10^2–4.4×10^4/cc; mean = 1.7×10^4/cc) with extremely low diversity (SDI 0.02–0.92; mean = 0.22). The LM sediments contain higher diversity (SDI 2.77–3.46, mean = 3.22) and increasing concentrations up core (from 4.1×10^5 to 3.1×10^7/cc; mean = 4.7×10^6/cc). Dominant diatom taxa in the LM unit include *C. meneghiniana* (∼3–24 %), *Craticula* spp. (∼9–21 %), *Amphora immarginata* (∼2–11 %), *A. proteus* (∼2–10 %), *Hyalosynedra laevigata* (∼2–9 %), and *Grammatophora* spp. (∼1–9 %; Figure 2.7, Appendix A3).

2.4.4.3 Pollen

Eight of the 11 samples collected for pollen analysis yielded results whereas the three samples from the middle of the core (27–28, 32–33, and 36–37 cm intervals from BP2) were not processable using standard methods as they produced sticky, mineral-rich sediment that did not allow them to be counted. Pollen concentrations were low in each sample and thus are qualitative in terms of their utility (<5000 grains/cc, compared to ∼40,000 grains/cc found at Cenote Aktun Ha; Gabriel et al., 2009). This is expected, due to the location of core samples ∼212 m from the entrance of a submerged cave system, as opposed to a surface-exposed location (e.g., Cenote Aktun Ha). Though the pollen analysis did not produce key results, the data is still supportive of overall findings. The DP contained relatively high abundances of buttonwood mangrove pollen (*Conocarpus*), red mangrove (*Rhizophora*), and fig family pollen (Moraceae). The upper LM samples contained relatively lower counts, but a wider variety compared to the DP, including *Rhizophora*, pine, ferns, grass, and palms (Table 2.2).

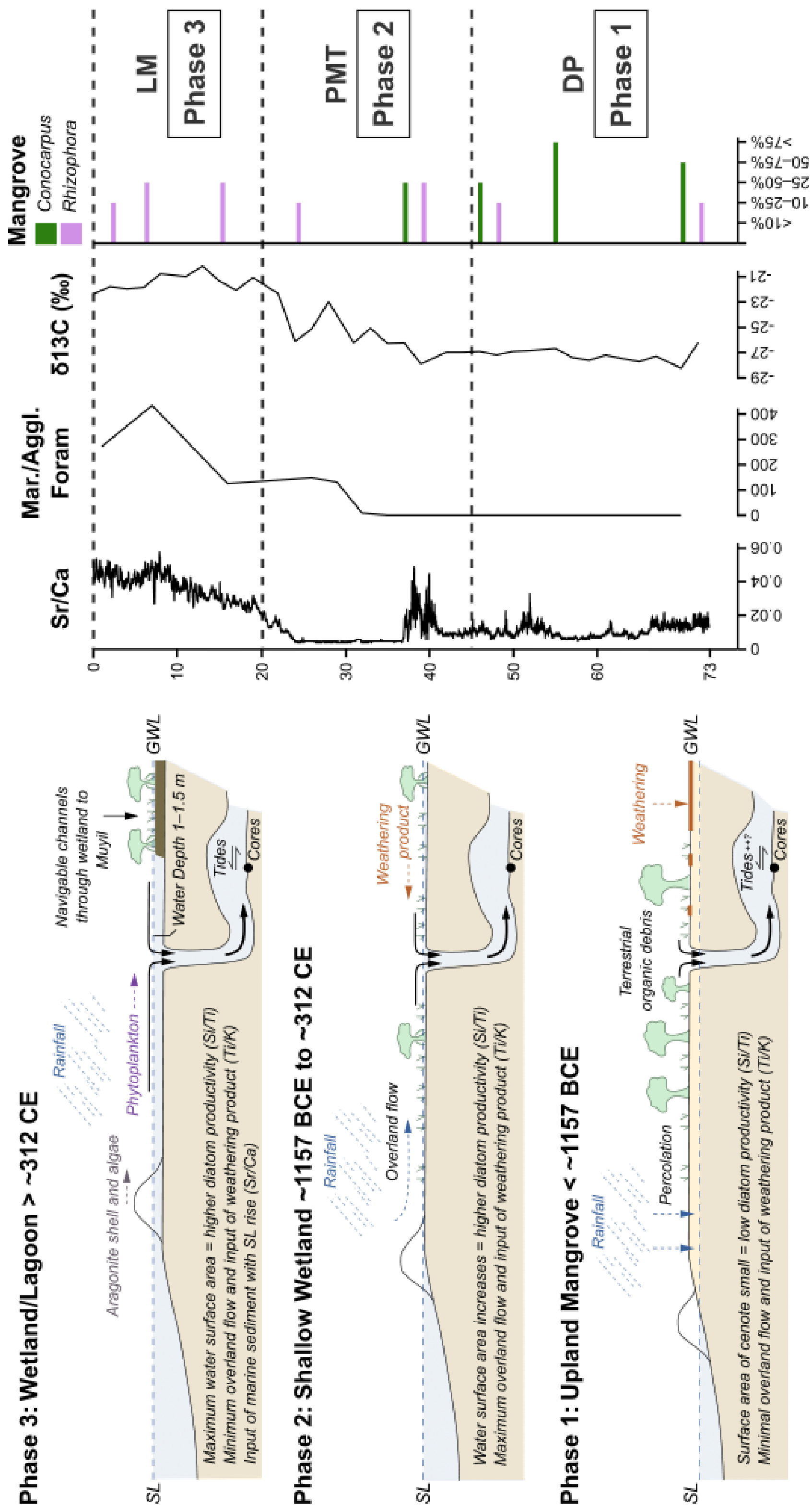

Figure 2.8: ~3000-year interpretation of coastal environmental changes near Boca Paila Lagoon, with results from μXRF (Sr/Ca, chemofacies), foraminifera (marine/agglutinated taxa), and pollen (mangrove) analyses. SL: Sea Level; GWL: Ground Water Level.

2.5 Discussion

The combined results from lithology, radiocarbon dating, and analysis of elemental and stable isotope geochemistry, foraminifera, diatoms, and pollen indicate three distinct periods of sediment deposition. The observed trends were compared to regional environmental records and sea-level curves, and a sequence of environmental history was reconstructed for the Boca Paila area, spanning the past 3000 years. The inferred reconstruction includes three phases of coastal landscape evolution: Phase 1, upland isolated mangroves and mangrove associates; Phase 2, a shallow wetland environment; and Phase 3, flooded wetlands/mangroves with lagoon development (Figure 2.8). The following discussion of environmental phases will focus on core BP2, as it contains the most complete record.

2.5.1 Phase 1: Upland Mangrove Environment

The dark DP unit at the base of all three cores, containing age reversals in the radiocarbon dates, is likely related to the transport of older OM (i.e., older plant material) into the cave from the surface as well as transport and reworking of OM from upstream locations in the cave passage itself. The down cutting and erosion of the OM is evidenced by the exposed scarp of peat on the side of the cave passage (i.e., the location of BP3). To account for this age uncertainty, the estimated age of the DP units was approximated by the youngest age obtained, ∼1157 BCE, from BP3. Prior to this age, the upper karst environment was likely dry/moist, which is reflected in the results from this study and is corroborated by climate and sea level studies from the area (e.g., Carrillo-Bastos et al., 2010; Gischler & Storz, 2009; Khan et al., 2017; Metcalfe et al., 2000; Webster et al., 2007).

The elemental geochemistry results from the DP indicate high porosity and OM content (high inc/coh), minimal input of weathering products (low Ti/K), and low phytoplankton productivity (low Si/Ti; Figure 2.3, Figure 2.6; Lo et al., 2016; McNeill-Jewer et al., 2019; Peinerud, 2000). Low terrigenous weathering product input during this phase is expected because rainfall would percolate directly to the aquifer through cracks and fissures in the limestone (McNeill-Jewer et al., 2019). Relatively dry surface conditions and low phytoplankton productivity are also supported by the lack of diatoms observed in Phase 1 sediments (Figure 2.7). Foraminifera observed here are largely *T. inflata* and *J. macrescens*, agglutinated species that are often associated with coastal brackish to fresh water and high/mid marsh conditions as well as mangrove peats (Khan et al., 2019; Appendix A2 and A4), suggesting moist conditions nearby. The organic carbon isotope results mainly fall within terrestrial ranges (δ^{13}C = -28.2 ‰ to -26.2 ‰; Lamb et al., 2006) and are similar to the δ^{13}C value of mangrove roots in the region (-28 ‰; Adame et al., 2021). The pollen signal during this phase likely reflects the taxa growing in the immediate vicinity. The presence of *Conocarpus* pollen supports the hypothesis that the cave entrance was located in a relatively dry area further inland from the coastline (DeYoe et al., 2020).

According to Adame et al. (2021), mangrove peat began to accumulate ∼3220 ±30 cal yr BP (1270 BCE) at the base (6 m) of Casa Cenote (30 km north of Boca Paila, 50 m from the coast) and ∼3040 ±30 cal yr BP (1090 BCE) at the base (5 m) of Cenote Yax Chen (∼12 km north of Boca Paila, 350 m from the coast). Collins et al. (2015c)'s study of Cenote Yax Chen cave sediments suggested that flooding of the upper karst terrain and initial mangrove development occurred ∼3800 cal yr BP (1850 BCE), which is similar to Torrescano and Islebe (2006)'s estimate from El Palmar, ∼200 km south of Boca Paila, 23km from the coast. Therefore, with the water table ∼3-4 m from the upper limestone, Rhizophora/Conocarpus mangroves would have been localized in Boca Paila itself, but also in cenotes and depressions in upstream areas which would have transported detrital OM into the cave during this phase. Extant mangroves have been documented in inland areas of the Yucatán, but also in sediment cores from Carwash Cenote (also known as Aktun Ha) which showed mangroves inhabiting the base of the sinkhole when sea level was lower (∼7 ka; Aburto-Oropeza et al., 2021; Gabriel et al., 2009; Meacham, 2012). There appears to be an erosional event towards the end of Phase 1, observed through the eroded peat outcrop at the location of BP3. Evidence of this event is shown when comparing the elevation and depth of the DP facies of the three cores as well as the spikes in the elemental counts (Ca, Ti, K, and Si) near the top of the DP units (Figure 2.3 and 2.6). The western Caribbean basin is tectonically stable with no recorded historical earthquakes or tsunamis (Shaw & Benson, 2015), although the eastern portions do experience seismicity (Moreno & Calais, 2021). Recently, on January 28, 2020 (2:10 p.m.; UTC-5), a M 7.7 earthquake occurred in the Caribbean Sea to the south of Cuba and northwest of Jamaica (https://earthquake.usgs.gov/earthquakes/eventpage/us60007idc/executive). Although no tsunami was produced, unusually large currents were reported in Cenote Akalche (Ox Bel Ha Cave System ~20 km north of Boca Paila) as well as other nearby cenotes. During the event, cenote water level rose and fell (±1 m) several times and currents became so strong that the divers had to hold on to rocks (See Appendix A5). The event was not instrumentally recorded and was not widespread. It is possible that a similar seismic or unknown flow event caused the observed erosion in Boca Paila sometime between ~1157 BCE and ~312 CE. The berm described by Shaw and Benson (2015) ~50 km north of Boca Paila records two or three large waves that struck the coast ~470 CE and more closely resembles the deposits of a tsunami than a mega-hurricane. The estimated age of the berm was based on the presence of Late Postclassic Maya structures built on top of the deposits (1200–1517 CE), the formation of the modern coastline (~2000 BCE), and two radiocarbon dated peat samples from a nearby underlying sediment unit (~1500 cal yr BP or ~470 CE; Shaw & Benson, 2015). This nearby anomalous storm event is estimated to have occurred later than the events recorded here in Boca Paila; however, considering radiocarbon dating uncertainties, as well as the constraints used to estimate the age of the berm, it is possible that both the berm deposit and the cave sediment erosion were caused by the same extreme flow event. A more probable process, however, is a hurricane, which is a regular occurrence on the coast of the Yucatán Peninsula. A recent study on the hurricane record at Cenote Muyil (Chunyaxche Lagoon) suggested a statistically significant period of local major hurricane activity between around 250 BCE and 100 CE (Sullivan et al., 2022). Anomalous hurricane activity during this time could have caused local flooding, washing a mix of terrestrial and marine material into the cave systems, and creating abnormal tides within some caverns including Boca Paila.

2.5.2 Phase 2: Shallow Wetland

The transition between DP and LM sediments occurs sometime between ~1157 BCE and ~312 CE or ~1070 CE, depending on whether reservoir corrections are applied to the marl samples (see 5.4.2 and 5.4.3 for discussion on age-depth model selection). The radiocarbon age obtained from the lower section of this unit (2462 BCE) likely reflects the input of older OM that had accumulated on the karst surface or from the underlying DP. During this phase, the cave opening had become a flooded cenote with the nearby environment transitioning into shallow, flooded wetlands (Figure 2.8). Increased input of weathering products from the previously exposed epikarst (higher Ti/K, Ca, Si counts) into the cave during this period was caused by precipitation, and overland flow with rainfall events into the cave (Lo et al., 2016; McNeill-Jewer et al., 2019). Because the groundwater level was at or slightly above the epikarst, large rainfalls would raise the water level and would entrain weathering product into the cave as the water receded (McNeill-Jewer et al., 2019). Shallow open-water conditions, which were increasing in area and depth, are supported by an inferred increase in phytoplankton activity represented by increased Si/Ti values and the presence of diatoms during the latter half of Phase 2 (Figures 2.6 and 2.7; McNeill-Jewer et al., 2019; Peinerud, 2000). The few diatom taxa observed here are often associated with fresh to brackish water and mangroves (*C. meneghiniana* and *Craticula* spp.) or nearshore marine environments (*Grammatophora* spp., *A. proteus*, *A. ostrearia*, and *D. suborbicularis*), indicating increased marine sediment input into the cave environment (Appendix A4). Foraminifera abundance and diversity increase throughout this phase and suggest a "transitional" environment towards more optimal salinity conditions (Appendix A2; Patterson & Kumar, 2002). The dominant foraminifera species observed during this period are often associated with marine inner shelf and brackish lagoon environments (*Ammodiscus* spp., *Ammonia* spp., and *Elphidium* spp.; Appendix A4). The organic carbon isotope results overlap both terrestrial and marine ranges (-26.3 ‰ to -23.0 ‰), suggesting mixed sources of sediment in the cave passage during this period (Lamb et al., 2006).

2.5.3 Phase 3: Flooded wetlands with lagoon development

Carbonate-rich sediments began to accumulate in the cave system by ~312 CE with no reservoir correction, or by 1070 CE with a brackish reservoir correction (see further discussion in sections 2.5.4.2 and 2.5.4.3). By Phase 3, the region was likely characterized by deeper wetlands and lagoons similar to the modern coastline, which occurred between 312–1070 CE based on the two dating scenarios.

Elemental geochemistry results indicate increased water surface area and phytoplankton productivity (high Si/Ti) as well as input of shallow offshore marine sediments (high Sr/Ca values; Figure 2.6; McNeill-Jewer et al., 2019; Rothwell & Croudace, 2015). The decrease in Ti/K values during this phase is attributed to the weathering products being preferentially deposited in the fringing wetlands and mangroves surrounding the open water lagoon that was forming. This would be a more diffuse input of weathering product into the cave versus the direct overland flow in Phase 2. Deeper water conditions and increased marine influence are supported by the increase in abundance and diversity of foraminifera and diatoms (Figure 2.7, Appendix A2 and A3). Dominant species include a wider variety of more marine taxa compared to previous phases, with observations of foraminifera *Rosalina* spp. and *Bolivina* spp., diatoms *A. immarginata* and *H. laevigata*, and other taxa typically found in Caribbean lagoons (Gregory et al., 2015; Hardage et al., 2022; Appendix A4). The δ^{13}C values fall within marine range, while the C/N values suggest mixed input from marine and terrestrial sources (Lamb et al., 2006). The δ^{15}N values (average 8.2 ‰) could also reflect mixed input from terrestrial (e.g., plants ∼-7 to +7 ‰, photosynthetic organisms ∼0 ‰, animals/excrement ∼+5 to +20 ‰) and marine (e.g., ocean POM ∼+3 to +18 ‰) sources (Samper-Villarreal, 2020; Sharp, 2017). The presence of a more diverse assemblage of pollen taxa observed in the laminated marl sediments, including grains of *Rhizophora*, ferns, grasses, palms, and pine (Table 2.2), may indicate the rise in the groundwater level closer to the surface, allowing root access for terrestrial plants. The higher abundance of *Rhizophora* and the absence of *Conocarpus* pollen supports the interpretation of widespread mangrove development in the area during this last phase (DeYoe et al., 2020). As water level increased with sea-level rise, flooded wetlands and brackish lagoons dominated, with *Rhizophora* as the main mangrove species growing around the fringes of Boca Paila as they are today.

2.5.4 Age-depth scenarios and Muyil trade activity: An archaeological perspective

2.5.4.1 Phase 1: <∼1157 BCE

Rise in the sea level and regional groundwater level facilitated marine trade around the Yucatán Peninsula. The proposed Maya route connecting Muyil with the Caribbean Sea would only have been functional if water was deep enough to accommodate a dugout canoe, a transport vessel widely believed to be used by ancient Maya (Biar, 2017; McKillop, 2010). Regional sea-level curves suggest that sea level was ∼2 meters below present level by the end of Phase 1 (Khan et al., 2017; Milne & Peros, 2013; Toscano & Macintyre, 2003). With modern lagoon water depths of ∼1–1.5 m near the Boca Paila cave opening, the upper karst surface would have been dry, but groundwater level would have been near the upper limestone surface (∼1 m). Topographically depressed areas to the east would have been flooded, as the current average depth of the lagoon is ∼3 m. Prior to ∼1157 BCE, the extensive wetlands that currently characterise the southeastern coast of the Yucatán Peninsula may not have existed because groundwater levels were too low; however, variations in limestone topography may have allowed more localized wetlands to form. There was most likely little to no sea-route access to Muyil at this time (Figure 2.8).

2.5.4.2 Phase 2: ∼1157 BCE to ∼312 CE

People are estimated to have arrived at Muyil by sea no later than 350–300 BCE (Witschey, 1993). The estimated founding of Muyil corresponds well with the end of Phase 2 under radiocarbon age correction scenario (i), no reservoir correction, at ∼312 CE (Table 2.1; Figure 2.4). According to regional estimates, sea level would have been at or near the elevation (∼1.5 m) of the Boca Paila cave opening ∼1000 BCE (Figure 2.9; Khan et al., 2017; Milne & Peros, 2013; Toscano & Macintyre, 2003), which matches our ∼700 BCE mid-date for this phase under reservoir correction scenario (i). This supports the theory that the cave opening was transitioning into a flooded, open-water cenote throughout this time and was occasionally connected to a larger water body during rainfalls, with the development of mangroves and shallow wetlands on the nearby karst surface. Water depth was still likely not sufficient for canal access to Muyil from the Caribbean Sea until closer toward the end of Phase 2, as sea level continued to rise. Early versions of the Cayo Venado and Muyil canals that connect Boca Paila to Muyil may have existed, especially towards the end of Phase 2. During his excavation, Witschey (1993) concluded that these canals are naturally formed outflow channels, but that Muyil canal may have been dredged, reinforced, straightened, or otherwise maintained for easier access. Human intervention may have been necessary due to relatively lower water levels during early occupation of the site.

When considering the ages calibrated with a brackish reservoir correction (scenario (ii); Table 2.1), deposition of the lagoonal Laminated Marl sediments would have begun more recently ∼1070 CE. In this scenario, the transition between a shallow wetland environment and deeper wetlands with lagoons and flooded canals would not have occurred until the Postclassic, when maritime trade routes around the Peninsula are thought to have already been well established (Andrews, 1993; Glover et al., 2011). The corrected age also does not fit well with regional sea-level curve estimates, which indicate that sea level would have been close to present depths by ∼1070 CE (Figure 2.9). Boca Paila, like most lagoons, receives both freshwater and seawater, but is not continuously flushed. The most significant source of organic matter to lagoon sediments is likely autochthonous (e.g., in situ plankton, terrestrial plants; Lamb et al., 2006), and therefore may contain atmosphere-related radiocarbon requiring minimal reservoir correction (Strunk et al., 2020). The carbon isotope results from the LM sediments support this possibility, with δ^{13}C values that fall within marine range but still within range of terrestrial values (Lamb et al., 2006). Uncorrected ages of ∼1157 BCE to ∼312 CE for Phase 2 were deemed to be most reliable based on the balance of evidence in this study; however, we cannot dismiss the range of ∼1157 BCE to 1070 CE for this phase. The uncorrected ages correspond better with previous archeological and sea level data, and further research may better constrain the age for this environmental transition.

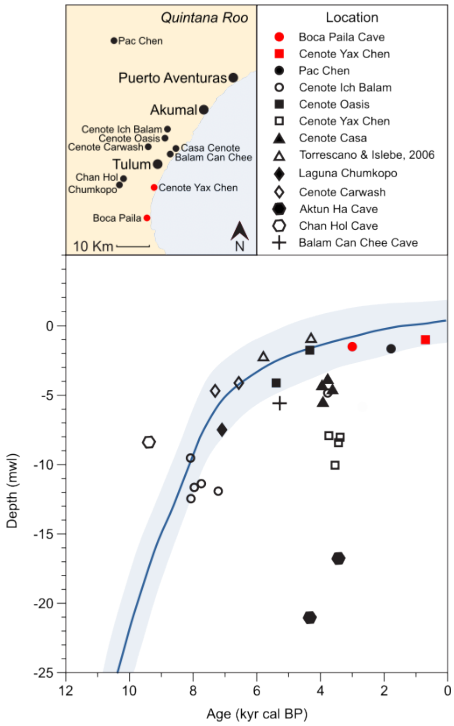

FIGURE 2.9: Relative mean sea level estimate (m $\pm 2\sigma$) for the Yucatán Peninsula based on Khan et al., (2017) and indicators from locations in the inset list and map (Brown et al., 2014; Collins et al., 2015a; Gabriel et al., 2009; Krywy-Janzen et al., 2019; Moseley et al., 2015; Stinnesbeck et al., 2017; Torrescano & Islebe, 2006; van Hengstum et al., 2010). Modified from Krywy-Janzen et al. (2019).

2.5.4.3 Phase 3: >~312 CE

Site expansion and increased trade with Belize and nearby islands during the Classic period (250–800 CE), as well as the significant estimated population growth and construction of infrastructure during the Postclassic (925–1550 CE; Witschey, 1993), coincide well with a continued sea-level rise and flooding of the wetlands, lagoons, and canal system throughout Phase 3 under radiocarbon age correction scenario (i), no reservoir correction (>~312 CE). Radiocarbon age calibration scenario (ii) does not fit well with the estimated timeline of activity at Muyil, because major site expansion and growth would have had to occur in shallow wetlands with minimal access to sea routes.

According to regional estimates, sea level was likely within 1 m of modern depths ∼312 CE (Khan et al., 2017; Milne & Peros, 2013; Toscano & Macintyre, 2003) which is supported by estimated ages of mangrove growth from nearby Yax Chen (Khan et al., 2017; Milne & Peros, 2013; Toscano & Macintyre, 2003) and the age of the basal mangrove peat obtained in this study (711 CE) from the shallow (∼1 m peat depth) limestone of Cenote Yax Chen. Considering that average water depths across the entire lagoon are ∼3 m (Lara & González, 1998), Boca Paila was likely significantly flooded by this time. The current canal system, which rests on the upper limestone and connects the Caribbean to Muyil through Cayo Venado (currently ∼1.8 m deep) and Muyil canal (currently 0.5–1.2 m deep), would have also likely been partially flooded (∼0–1 m deep) and canoe-navigable by the onset of Phase 3 (Matthews, 1995; Witschey, 1993). By the Late Postclassic, Muyil would have been well situated along circum-peninsular trade routes in a sheltered area protected from the Caribbean Sea.

Nearby port sites along the coast (Figure 2.1) were likely experiencing similar changes in coastal morphology, because the wetlands surrounding Boca Paila extend further into the Sian Ka'an Biosphere, as well as southwards into Belize at comparable elevation (Luzzadder-Beach & Beach, 2009). The formation of flooded wetlands throughout this geographical region may have facilitated maritime trade during the Postclassic by providing sheltered canoe-accessible routes. Further research along these coastal wetlands can provide more information on the timing of wetland development and more evidence to confirm the possibility that wetland formation provided increased opportunities for Maya circum-peninsular trade on the eastern coast of the Yucatán Peninsula during the Early Postclassic–Late Postclassic period.

2.6 Conclusion

Three sediment cores were collected from a cave system beneath Boca Paila lagoon, located on the eastern Yucatán Peninsula coast. Three distinct depositional phases were defined following radiocarbon dating, geochemical (μXRF, δ^{13}C, C/N), and microfossil (foraminifera, diatom, and pollen) analyses. Prior to ∼1157

BCE (Phase 1), the coast was likely characterised by an upland mangrove environment. Organic-rich detrital peat sediments contain indicators (Ti/K, Si/Ti, δ^{13}, C/N) of relatively dry surface conditions with low terrestrial weathering, low phytoplankton productivity, and terrestrial organic carbon sources. Regional sea-level curves, along with the observed absence of diatoms, the presence of a few brackish foraminifera (i.e., *T. inflata* and *J. macrescens*), and the landward mangrove taxa *Conocarpus*, suggest that the bottom of the Boca Paila cave passage had flooded by this time, but that the upper karst environment was still relatively dry. Between ∼1157 BCE and ∼312 CE (Phase 2), sea level had likely reached the elevation of the Boca Paila cave opening, forming a flooded cenote surrounded by shallow wetlands. Detrital peat–laminated marl transition sediments contain geochemical and biotic indicators (Ti/K, Si/K, δ^{13}C, C/N, mangrove/nearshore marine diatoms and foraminifera taxa) of increased surface weathering input and phytoplankton productivity related to an inferred increased flooding, sunlit, and open-water conditions. Deeper wetlands and lagoons appear to have formed after ∼312 CE (Phase 3) with continued sea-level rise of ∼1 m over the past 2000 years. Geochemical indicators (Sr/Ca, δ^{13}, C/N) within the carbonate-rich laminated marl sediments suggest increased input from marine sources. Notably higher concentrations of brackish and marine foraminifera (e.g., *Ammonia* spp., *Elphidium* spp., *Rosalina* spp., and *Bolivina* spp.), diatoms (e.g., *C. meneghiniana*, *Craticula* spp., *A. immarginata*, *A. proteus*, *H. laevigata*, and *Grammatophora* spp.), and a wider variety of pollen taxa (from nearby mangroves, ferns, grasses, palms, and pine) also indicate fully flooded conditions similar to the modern coastline. Our results suggest that the sea-route to Muyil could have been navigable by canoe toward the end of Phase 2, roughly corresponding with a previous estimate for the time that settlers first appeared at the site. Archaeological evidence of the site's population expansion during the Postclassic coincides with the formation of deeper lagoons and canal system during Phase 3. Deeper wetlands across the southeastern coast of the Yucatán Peninsula may have provided more opportunities for canoe travel and could have contributed to the observed increase in sea trade along the eastern coast during the Postclassic period. Further research and spatial coverage in the biosphere wetlands will better constrain the timing of paleoenvironmental evolution and may elucidate further patterns and relationships with coastal Maya trade. This study highlights the dynamics between human activity and changing coastal morphology and shows the importance of karst cave systems for obtaining paleoenvironmental records.

Acknowledgments

We would like to thank El Centro Investigador del Sistema Acuífero de Quintana Roo A.C. (CINDAQ A.C.) and the Comisión Nacional de Áreas Naturales Protegidas, Reserva de la Biosfera de Sian Ka'an. We also gratefully acknowledge Prof. Dr. Brian Cumming (Queen's University at Kingston) for assistance with diatom identification and for reviewing and editing the manuscript. Funding: This work was financially supported by Natural Sciences and Engineering Research Council (NSERC) Discovery Grant (EGR), as well as the Canada Foundation for Innovation (CFI) and NSERC grants (CAV and MCP).

Data availability

Data will be made available upon request.

References

Aburto-Oropeza, O., Burelo-Ramos, C. M., Ezcurra, E., Ezcurra, P., Henriquez, C. L., Vanderplank, S. E., & Zapata, F. (2021). Relict inland mangrove ecosystem reveals Last Interglacial sea levels. Proc. Natl. Acad.Sci., 118(41), 1–8. https://doi.org/10.1073/pnas.2024518118.

Adame, M. F., Santini, N. S., Torres-Talamante, O., & Rogers, K. (2021). Mangrove sinkholes (cenotes) of the Yucatan Peninsula, a global hotspot of carbon sequestration. Biol. Lett., 17(5), rsbl.2021.0037. https://doi.org/10.1098/rsbl.2021.0037.

Andrews, A. P. (1993). Late Postclassic lowland Maya archaeology. J. World Prehist., 7(1), 35–69. https://doi.org/10.1007/BF00978220.

Arellano-Guillermo, A. (2003). Site management and partnerships: the Sian Ka'an Biosphere Reserve experience. In E. de Merode, R. Smeets, & C. Westrik (Eds.), Linking universal and local values: managing a sustainable future for world heritage (pp. 136–141). UNESCO World Heritage Centre.

Armstrong, H., & Brasier, M. (2005). Microfossils (Second). Blackwell Publishing Ltd.

Bauer-Gottwein, P., Gondwe, B. R. N., Charvet, G., Marín, L. E., Rebolledo-Vieyra, M., & Merediz-Alonso, G. (2011). Review: The Yucatán Peninsula karst aquifer, Mexico. Hydrogeol. J., 19(3), 507–524. https://doi.org/10.1007/s10040-010-0699-5.

Beddows, Patricia A., Glover, J. B., Rissolo, D., Carter, A. M., Jaijel, R., Smith, D. M., & Goodman-Tchernov, B. (2016). The Proyecto Costa Escondida: Recent interdisciplinary research in search of freshwater along the North Coast of Quintana Roo, Mexico. Wiley Interdiscip. Rev. Water, 3(5), 749–761. https://doi.org/10.1002/wat2.1161.

Beddows, Patricia Anne. (2004). Groundwater Hydrology of a Coastal Conduit Carbonate Aquifer: Caribbean Coast of the Yucatán Peninsula, México. University of Bristol.

Biar, A. (2017). Prehispanic Dugout Canoes in Mexico: A Typology Based on a Multidisciplinary Approach. J.Marit. Archaeol., 12(3), 239–265. https://doi.org/10.1007/s11457-017-9188-5.

Blaauw, M., & Christen, J. A. (2011). Flexible paleoclimate age-depth models using an autoregressive gamma process. Bayesian Analysis, 6(3), 457–474. https://doi.org/10.1214/11-BA618.

Brown, A. L., Reinhardt, E. G., van Hengstum, P. J., & Pilarczyk, J. E. (2014). A Coastal Yucatan Sinkhole Records Intense Hurricane Events. J.Coast.Res., 294(2), 418–428. https://doi.org/10.2112/JCOASTRES-D-13-00069.1.

Carrillo-Bastos, A., Islebe, G. A., Torrescano-Valle, N., & González, N. E. (2010). Holocene vegetation and climate history of central Quintana Roo, Yucatán Península, Mexico. Rev. Palaeobot. Palynol., 160(3–4), 189–196. https://doi.org/10.1016/j.revpalbo.2010.02.013.

Clark, D. J. (2016). The Residential Spaces, Social Organization and Dynamics of Isla Cerritos, an Ancient Maya Port Community [Harvard University]. https://search.proquest.com/docview/1787194513?accountid=9645.

Claudino-Sales, V. (2019). Coastal World Heritage Sites. In Coastal World Heritage Sites (Vol. 28). Springer Netherlands. https://doi.org/10.1007/978-94-024-1528-5.

Collins, S. V., Reinhardt, E. G., Rissolo, D., Chatters, J. C., Nava Blank, A., & Luna Erreguerena, P. (2015). Reconstructing water level in Hoyo Negro, Quintana Roo, Mexico, implications for early Paleoamerican and faunal access. Quat. Sci. Rev., 124, 68–83. https://doi.org/10.1016/j.quascirev.2015.06.024.

Collins, S. V., Reinhardt, E. G., Werner, C. L., Le Maillot, C., Devos, F., & Meacham, S. S. (2015). Regional response of the coastal aquifer to Hurricane Ingrid and sedimentation flux in the Yax Chen cave system (Ox Bel Ha) Yucatan, Mexico. Palaeogeogr. ,Palaeoclimatol., Palaeoecol., 438, 226–238. https://doi.org/10.1016/j.palaeo.2015.07.030.

Collins, S. V., Reinhardt, E. G., Werner, C. L., Le Maillot, C., Devos, F., & Rissolo, D. (2015). Late Holocene mangrove development and onset of sedimentation in the Yax Chen cave system (Ox Bel Ha) Yucatan, Mexico: Implications for using cave sediments as a sea-level indicator. Palaeogeogr. ,Palaeoclimatol., Palaeoecol., 438, 124–134. https://doi.org/10.1016/j.palaeo.2015.07.042.

Coutino, A., Stastna, M., Kovacs, S., & Reinhardt, E. (2017). Hurricanes Ingrid and Manuel (2013) and their impact on the salinity of the Meteoric Water Mass, Quintana Roo, Mexico. J. Hydrol., 551, 715–729. https://doi.org/10.1016/j.jhydrol.2017.04.022.

Coutino, A., Stastna, M., McNeill-Jewer, C., & Reinhardt, E. G. (2021). Inland Tidal Oscillations Within the Yucatan Peninsula. Geophysi. Res. Lett., 48(9), 1–9. https://doi.org/10.1029/2020GL092091.

Curtis, J., Hodell, D., & Brenner, M. (1996). Climate Variability on the Yucatan Peninsula (Mexico) during the Past 3500 Years , and Implications for Maya Cultural Evolution. Quat. Res., 47, 37–47.

DeYoe, H., Lonard, R. I., Judd, F. W., Stalter, R., & Feller, I. (2020). Biological Flora of the Tropical and Subtropical Intertidal Zone: Literature Review for Rhizophora mangle L. J. Coast. Res., 36(4), 857. https://doi.org/10.2112/JCOASTRES-D-19-00088.1.

Douglas, P. M. J., Brenner, M., & Curtis, J. H. (2016). Methods and future directions for paleoclimatology in the Maya Lowlands. Glob. Planet. Change, 138, 3–24. https://doi.org/10.1016/j.gloplacha.2015.07.008.

Faegri, K., & Iversen, J. (1990). Textbook of Pollen Analysis. Hafner Press. https://www.jstor.org/stable/4109011?origin=crossref.

Gabriel, J. J., Reinhardt, E. G., Peros, M. C., Davidson, D. E., van Hengstum, P. J., & Beddows, P. A. (2009). Palaeoenvironmental evolution of Cenote Aktun Ha (Carwash) on the Yucatan Peninsula, Mexico and its response to Holocene sea-level rise. J. Paleolimnol., 42(2), 199–213. https://doi.org/10.1007/s10933-008-9271-x.

Gischler, E., & Storz, D. (2009). High-resolution windows into Holocene climate using proxy data from Belize corals (Central America). Palaeobiodivers. and Palaeoenviron., 89(3–4), 211–221. https://doi.org/10.1007/s12549-009-0011-7.

Glover, J. B., Hruby, Z. X., Rissolo, D., Ball, J. W., Glascock, M. D., & Shackley, M. S. (2018). Interregional interaction in Terminal Classic Yucatan: Recent obsidian and ceramic data from Vista Alegre, Quintana Roo, Mexico. Lat. Am. Antiq., 29(3), 475–494. https://doi.org/10.1017/laq.2018.22.

Glover, J. B., Rissolo, D., & Mathews, J. P. (2011). The Hidden World of the Maritime Maya: Lost Landscapes Along the North Coast of Quintana Roo, Mexico. In The Archaeol. of Marit. Landsc. (pp. 195–216). https://doi.org/10.1007/978-1-4419-8210-0_11.

Gregory, B. R. B., Peros, M., Reinhardt, E. G., & Donnelly, J. P. (2015). Middle–late Holocene Caribbean aridity inferred from foraminifera and elemental data in sediment cores from two Cuban lagoons. Palaeogeogr. ,Palaeoclimatol., Palaeoecol., 426, 229–241. https://doi.org/10.1016/j.palaeo.2015.02.029.

Hardage, K., Street, J., Herrera-Silveira, J. A., Oberle, F. K. J., & Paytan, A. (2022). Late Holocene environmental change in Celestun Lagoon, Yucatan, Mexico. J. Paleolimnol., 67(2), 131–162. https://doi.org/10.1007/s10933-021-00227-4.

Hodell, D. A., Brenner, M., & Curtis, J. H. (2007). Climate and cultural history of the Northeastern Yucatan Peninsula, Quintana Roo, Mexico. Climatic Change, 83(1–2), 215–240. https://doi.org/10.1007/s10584-006-9177-4.

Islebe, G. A., Schmook, B., Calmé, S., & León-Cortés, J. L. (2015). Introduction: Biodiversity and Conservation of the Yucatán Peninsula, Mexico. In Biodiversity and Conservation of the Yucatán Peninsula (pp. 1–5). Springer International Publishing. https://doi.org/10.1007/978-3-319-06529-8_1.

Jaijel, R., Glover, J. B., Rissolo, D., Beddows, P. A., Smith, D., Ben-Avraham, Z., & Goodman-Tchernov, B. (2018). Coastal reconstruction of Vista Alegre, an ancient maritime Maya settlement. Palaeogeogr. ,Palaeoclimatol., Palaeoecol., 497(May 2017), 25–36. https://doi.org/10.1016/j.palaeo.2018.02.003.

Khan, N. S., Ashe, E., Horton, B. P., Dutton, A., Kopp, R. E., Brocard, G., Engelhart, S. E., Hill, D. F., Peltier, W. R., Vane, C. H., & Scatena, F. N.

(2017). Drivers of Holocene sea-level change in the Caribbean. Quat. Sci. Rev., 155, 13–36. https://doi.org/10.1016/j.quascirev.2016.08.032.

Khan, N. S., Vane, C. H., Engelhart, S. E., Kendrick, C., & Horton, B. P. (2019). The application of δ^{13}C, TOC and C/N geochemistry of mangrove sediments to reconstruct Holocene paleoenvironments and relative sea levels, Puerto Rico. Marine Geol., 415(January), 105963. https://doi.org/10.1016/j.margeo.2019.105963.

Kovacs, S. E., Reinhardt, E. G., Chatters, J. C., Rissolo, D., Schwarcz, H. P., Collins, S. V., Kim, S.-T., Nava Blank, A., & Luna Erreguerena, P. (2017). Calcite raft geochemistry as a hydrological proxy for Holocene aquifer conditions in Hoyo Negro and Ich Balam (Sac Actun Cave System), Quintana Roo, Mexico. Quat. Sci. Rev., 175, 97–111. https://doi.org/10.1016/j.quascirev.2017.09.006.

Kovacs, S. E., Reinhardt, E. G., Stastna, M., Coutino, A., Werner, C., Collins, S. V., Devos, F., & Le Maillot, C. (2017). Hurricane Ingrid and Tropical Storm Hanna's effects on the salinity of the coastal aquifer, Quintana Roo, Mexico. J. Hydrol., 551, 703–714. https://doi.org/10.1016/j.jhydrol.2017.02.024.

Kovacs, S. E., Reinhardt, E. G., Werner, C., Kim, S. T., Devos, F., & Le Maillot, C. (2018). Seasonal trends in calcite-raft precipitation from cenotes Rainbow, Feno and Monkey Dust, Quintana Roo, Mexico: Implications for paleoenvironmental studies. Palaeogeogr. ,Palaeoclimatol., Palaeoecol., 497(February), 157–167. https://doi.org/10.1016/j.palaeo.2018.02.014.

Krayesky, D., del Castillo, E. M., Zamudio, M. E., Norris, J. N., & Fredericq, S. (2009). Diatoms (Bacillariophyta) of the Gulf of Mexico. In D. L. Felder & D. K. Camp (Eds.), Gulf of Mexico–Origin, Waters, and Biota. Biodiversity. Texas A&M University Press.

Krywy-Janzen, A., Reinhardt, E., McNeill-Jewer, C., Coutino, A., Waltham, B., Stastna, M., Rissolo, D., Meacham, S., & van Hengstum, P. (2019). Water-level change recorded in Lake Pac Chen Quintana Roo, Mexico infers connection with the aquifer and response to Holocene sea-level rise and Classic Maya droughts. J. Paleolimnol., 62(4), 373–388. https://doi.org/10.1007/s10933-019-00094-0.

Lamb, A. L., Wilson, G. P., & Leng, M. J. (2006). A review of coastal palaeoclimate and relative sea-level reconstructions using δ^{13}C and C/N ratios in organic material. Earth Sci. Rev., 75(1–4), 29–57. https://doi.org/10.1016/j.earscirev.2005.10.003.

Lara, E. N., & González, E. A. (1998). The relationship between reef fish community structure and environmental variables in the southern Mexican Caribbean. J. Fish Biol., 53(Supplement A), 209–221. https://doi.org/10.1006/jfbi.1998.0829.

Licea, S., Moreno-Ruiz, J. L., & Luna, R. (2016). Checklist of Diatoms (Bacillariophyceae) from the Southern Gulf of Mexico: Data-Base (1979-2010) and New Records. J. Biodivers. Endanger. Species, 04(03). https://doi.org/10.4172/2332-2543.1000174.

Lo, F.-L., Chen, H.-F., & Fang, J.-N. (2016). Discussion of Suitable Chemical Weathering Proxies in Sediments by Comparing the Dissolution Rates of Minerals in Different Rocks. J. Geol., 125(1), 83–99. https://doi.org/10.1086/689184.

Lopez-Fuerte, F. O., Siqueiros-Beltrones, D. A., & Navarro, J. N. (2010). Benthic diatoms associated with mangrove enviroments in the northwest region of México (V. P. e Imprenta (ed.)).

Luzzadder-Beach, S., & Beach, T. (2009). Arising from the Wetlands: Mechanisms and Chronology of Landscape Aggradation in the Northern Coastal Plain of Belize. Annals of the Assoc. of Amer. Geogr., 99(1), 1–26. https://doi.org/10.1080/00045600802458830.

Magurran, A. E. (1988). Ecological Diversity and Its Measurement. Springer Netherlands. https://doi.org/10.1007/978-94-015-7358-0.

Marshall, J. F., & McCulloch, M. T. (2002). An assessment of the Sr/Ca ratio in shallow water hermatypic corals as a proxy for sea surface temperature. Geochim. Cosmochim. Acta, 66(18), 3263–3280. https://doi.org/10.1016/S0016-7037(02)00926-2.

Matthews, D. (1995, September). Four Faces of Mexico; In the Yucatan, a Wild and Seldom-Visited Wetland. The Washington Post.

McKillop, H. (2010). Ancient Maya canoe navigation and its implications for Classic to Postclassic Maya economy and sea trade: a view from the south coast of Belize. J. Caribb.Archaeol., Special Publication 3, 93–105. https://flmnh.ufl.edu/jca/McKillop.pdf.

McKillop, Heather. (2005). Finds in Belize document Late Classic Maya salt making and canoe transport. Proc. Natl. Acad.Sci., 102(15), 5630–5634. https://doi.org/10.1073/pnas.0408486102.

McNeill-Jewer, C. A., Reinhardt, E. G., Collins, S., Kovacs, S., Chan, W. M., Devos, F., & LeMaillot, C. (2019). The effect of seasonal rainfall on nutrient input and biological productivity in the Yax Chen cave system (Ox Bel Ha), Mexico, and implications for μXRF core studies of paleohydrology. Palaeogeogr. ,Palaeoclimatol., Palaeoecol., 534(July), 109289. https://doi.org/10.1016/j.palaeo.2019.109289.

Meacham, S. S. (2012). Using Landsat 5 TM Data to Identify and Map Areas of Mangrove in Tulum, Quintana Roo, Mexico [University of New Hampshire]. https://scholars.unh.edu/thesis.

Merino-Virgilio, F. del C., Okolodkov, Y. B., Aguilar-Trujillo, A. C., & Herrera-Silveira, J. A. (2013). Phytoplankton of the northern coastal and shelf waters of the Yucatan Peninsula, southeastern Gulf of Mexico, Mexico. Check List, 9(4), 771. https://doi.org/10.15560/9.4.771.

Metcalfe, S. E., O'Hara, S. L., Caballero, M., & Davies, S. J. (2000). Records of Late Pleistocene-Holocene climatic change in Mexico - A review. Quat. Sci. Rev., 19(7), 699–721. https://doi.org/10.1016/S0277-3791(99)00022-0.

Milne, G. A., & Peros, M. (2013). Data–model comparison of Holocene sea-level change in the circum-Caribbean region. Glob. Planet. Change, 107, 119–131. https://doi.org/10.1016/j.gloplacha.2013.04.014.

Moreno, B., & Calais, E. (2021). Evidence of Correlation between High Frequency Geomagnetic Variations and Seismicity in the Caribbean. Open J. of Earthq. Res., 10(02), 30–41. https://doi.org/10.4236/ojer.2021.102003.

Moseley, G. E., Richards, D. A., Smart, P. L., Standish, C. D., Hoffmann, D. L., ten Hove, H., & Vinn, O. (2015). Early–middle Holocene relative sea-level oscillation events recorded in a submerged speleothem from the Yucatán Peninsula, Mexico. Holocene, 25(9), 1511–1521. https://doi.org/10.1177/0959683615585832.

Murray, J. W. (2006). Ecology and Applications of Benthic Foraminifera. In Ecology and Applications of Benthic Foraminifera. Cambridge University Press. https://doi.org/10.1017/CBO9780511535529.

Myers, E. H. (1935). The life history of Patellina Corrugata Williamson, a foraminifer (pp. 355–392).

Olteanu, M., & Villa-Vialaneix, N. (2015). On-line relational and multiple relational SOM. Neurocomputing, 147(1), 15–30. https://doi.org/10.1016/j.neucom.2013.11.047.

Patterson, R. T., & Fishbein, A. (1989). Re-examination of the statistical methods used to determine the number of point counts needed for micropaleontological quantitative research. J.Paleontol., 63, 245–248.

Patterson, R. T., & Kumar, A. (2002). A review of current testate rhizopod (thecamoebian) research in Canada. Palaeogeogr. ,Palaeoclimatol., Palaeoecol., 180(1–3), 225–251.

Peinerud, E. K. (2000). Interpretation of Si concentrations in lake sediments: three case studies. Environ. Geol., 40(1), 64–72.

Perry, E., Velazquez-Oliman, G., & Socki, R. A. (2003). Hydrogeology of the Yucatán Peninsula. In The lowland Maya area: three millenia at the human-wildland interface (pp. 115–138). Free Products Press.

Platt, N. H., & Wright, V. P. (2022). Flooding of a carbonate platform: the Sian Ka'an Wetlands, Yucatán, Mexico – a model for the formation and evolution of palustrine carbonate factories around the modern Caribbean Sea and in the depositional record. The Depos. Rec., December. https://doi.org/10.1002/dep2.217.

Poag, C. W. (2015). Benthic Foraminifera of the Gulf of Mexico: Distribution, Ecology, Paleoecology. Texas A&M University Press.

Reimer, P. J., Austin, W. E. N., Bard, E., Bayliss, A., Blackwell, P. G., Bronk Ramsey, C., Butzin, M., Cheng, H., Edwards, R. L., Friedrich, M., Grootes, P. M., Guilderson, T. P., Hajdas, I., Heaton, T. J., Hogg, A. G., Hughen, K. A., Kromer, B., Manning, S. W., Muscheler, R., … Talamo, S. (2020). The IntCal20 Northern Hemisphere Radiocarbon Age Calibration Curve (0–55 cal kBP). Radiocarb., 62(4), 725–757. https://doi.org/10.1017/RDC.2020.41.

Rothwell, R. G., & Croudace, I. W. (2015). Twenty Years of XRF Core Scanning Marine Sediments: What Do Geochemical Proxies Tell Us? In I. W. Croudace & R. G. Rothwell (Eds.), Micro-XRF Studies of Sediment Cores: Applications of a Non-destructive Tool for the Environmental Sciences (Vol. 17, pp. 25–102). Springer Netherlands. https://doi.org/10.1007/978-94-017-9849-5.

Sabloff, J. A., & Rathje, W. L. (1975). The Rise of a Maya Merchant Class. Sci. Am., 233(4), 72–82. https://doi.org/10.1038/scientificamerican1075-72.

Samper-Villarreal, J. (2020). Strengths and challenges of δ^{15}N to identify anthropogenic nutrient loading in coastal systems. Isot. in Environ. and Health Studies, 56(5–6), 700–712. https://doi.org/10.1080/10256016.2020.1809389.

Sánchez, M., Alcocer, J., Escobar, E., & Lugo, A. (2002). Phytoplankton of cenotes and anchialine caves along a distance gradient from the northeastern coast of Quintana Roo, Yucatan Peninsula. Hydrobiologia, 467, 79–89. https://doi.org/10.1023/A:1014936714964.

Shannon, C. E. (1948). A mathematical theory of communication. Bell Syst. Tech. J., 27, 379–423 and 623–656.

Sharp, Z. (2017). Chapter 9: Nitrogen. In Principles of Stable Isotope Geochemistry (Second). https://doi.org/https://doi.org/10.25844/h9q1-0p82.

Shaw, C. E. (2016). Late Pleistocene Bays and Reefs: Ancestors to the Modern Caribbean Coast, Yucatán Península, México. J.Coast.Res., 32(2), 280. https://doi.org/10.2112/JCOASTRES-D-14-00083.1.

Shaw, C. E., & Benson, L. (2015). Possible Tsunami Deposits on the Caribbean Coast of the Yucatán Peninsula. J.Coast.Res., 316(6), 1306–1316. https://doi.org/10.2112/JCOASTRES-D-14-00084.1.

Skougstad, M. W., & Horr, C. A. (1963). Chemistry of strontium in natrual water: Occurrence and distribution of strontium in natural water. In Geological survey water-supply paper 1496–D. https://pubs.er.usgs.gov/publication/wsp1496D.

Smart, P. L., Beddows, P. A., Coke, J., Doerr, S., Smith, S., & Whitaker, F. F. (2006). Cave development on the Caribbean coast of the Yucatan Peninsula, Quintana Roo, Mexico. In Perspectives on Karst Geomorphology, Hydrology, and Geochemistry - A Tribute Volume to Derek C. Ford and William B. White (Vol. 404, Issue 10, pp. 105–128). Geological Society of America. https://doi.org/10.1130/2006.2404(10).

Smol, J. P., & Stoermer, E. F. (2010). The Diatoms (J. P. Smol & E. F. Stoermer (eds.); Second). Cambridge University Press. https://doi.org/10.1017/CBO9780511763175.

Spaulding, S. A., Potapova, M. G., Bishop, I. W., Lee, S. S., Gasperak, T. S., Jovanoska, E., Furey, P. C., & Edlund, M. B. (2021). Diatoms.org: supporting taxonomists, connecting communities. Diatom Res., 36(4), 291–304. https://doi.org/10.1080/0269249X.2021.2006790.

Stinnesbeck, W., Becker, J., Hering, F., Frey, E., González, A. G., Fohlmeister, J., Stinnesbeck, S., Frank, N., Terrazas Mata, A., Benavente, M. E., Avilés Olguín, J., Aceves Núñez, E., Zell, P., & Deininger, M. (2017). The earliest settlers of Mesoamerica date back to the late Pleistocene. PLOS ONE, 12(8), e0183345. https://doi.org/10.1371/journal.pone.0183345.

Strunk, A., Olsen, J., Sanei, H., Rudra, A., & Larsen, N. K. (2020). Improving the reliability of bulk sediment radiocarbon dating. Quat. Sci. Rev., 242, 106442. https://doi.org/10.1016/j.quascirev.2020.106442.

Sullivan, R. M., van Hengstum, P. J., Donnelly, J. P., Tamalavage, A. E., Winkler, T. S., Little, S. N., Mejia-Ortiz, L., Reinhardt, E. G., Meacham, S., Schumacher, C., & Korty, R. (2022). Northeast Yucatan hurricane activity during the Maya Classic and Postclassic periods. Sci. Rep., 12(1), 20107. https://doi.org/10.1038/s41598-022-22756-2.

The Periphyton Group, F. I. U. (2022). Diatom Image Database. Florida Coastal Everglades LTER, Florida International University. https://fce-lter.fiu.edu/data/database/diatom/.

Thompson, J. E. S. (1949). Canoes and Navigation of the Maya and Their Neighbours. J. R. Anthropol. Inst. G. B. Irel., 79(1/2), 69–78.

Torrescano, N., & Islebe, G. A. (2006). Tropical forest and mangrove history from southeastern Mexico: a 5000 yr pollen record and implications for sea level rise. Veg. Hist. Archaeobotany, 15(3), 191–195. https://doi.org/10.1007/s00334-005-0007-9.

Toscano, M. A., & Macintyre, I. G. (2003). Corrected western Atlantic sea-level curve for the last 11,000 years based on calibrated 14C dates from Acropora palmata framework and intertidal mangrove peat. Coral Reefs, 22(3), 257–270. https://doi.org/10.1007/s00338-003-0315-4.

van Hengstum, P.J, Reinhardt, E., Beddows, P., Huang, R., & Gabriel, J. (2008). Thecamoebians (testate amoebae) and foraminifera from three anchialine cenotes in Mexico: low salinity (1. 5–4. 5 psu) faunal transitions. J. Foraminifer. Res, 38(4), 305–317.

van Hengstum, Peter J., Reinhardt, E. G., Beddows, P. A., & Gabriel, J. J. (2010). Linkages between Holocene paleoclimate and paleohydrogeology preserved in a Yucatan underwater cave. Quat. Sci. Rev., 29(19–20), 2788–2798. https://doi.org/10.1016/j.quascirev.2010.06.034.

van Hengstum, Peter J., & Scott, D. B. (2011). Ecology of foraminifera and habitat variability in an underwater cave: Distinguishing anchialine versus submarine cave environments. J. Foraminifer. Res, 41(3), 201–229. https://doi.org/10.2113/gsjfr.41.3.201.

van Hengstum, Peter J., Scott, D. B., Gröcke, D. R., & Charette, M. A. (2011). Sea level controls sedimentation and environments in coastal caves and sinkholes. Mar.Geol., 286(1–4), 35–50. https://doi.org/10.1016/j.margeo.2011.05.004.

van Hengstum, Peter J., Scott, D. B., & Javaux, E. J. (2009). Foraminifera in elevated Bermudian caves provide further evidence for +21 m eustatic sea level during Marine Isotope Stage 11. Quat. Sci. Rev., 28(19–20), 1850–1860. https://doi.org/10.1016/j.quascirev.2009.05.017.

Ward, W. C., Weide, A. E., & Back, W. (1985). Geology and Hydrogeology of the Yucatan and Quaternary Geology of the Northeastern Yucatan Peninsula (p. 86). New Orleans Geological Society.

Webster, J. W., Brook, G. A., Railsback, L. B., Cheng, H., Edwards, R. L., Alexander, C., & Reeder, P. P. (2007). Stalagmite evidence from Belize indicating significant droughts at the time of Preclassic Abandonment, the Maya Hiatus, and the Classic Maya collapse. Palaeogeogr. ,Palaeoclimatol., Palaeoecol., 250(1–4), 1–17. https://doi.org/10.1016/j.palaeo.2007.02.022.

Witschey, W. R. T. (1988). Recent Investigations at the Maya Inland Port City of Muyil (Chunyaxche), Quintana Roo, Mexico. Mexicon, 10(6), 111–117.

Witschey, W. R. T. (1993). The archaeology of Muyil, Quintana Roo, Mexico: A maya site on the east coast of the Yucatan Peninsula. Tulane University.

Chapter 3

Anthropogenic structure emplacement and sediment transport at King Herod's harbour, Israel: ED-μXRF (Itrax) data and foraminifera *Pararotalia calcariformata* as proxies of coastal development over millenia

This chapter is a manuscript that has been submitted to Marine Geology:

Steele, R.E., Reinhardt, E.G., Gabriel, J.J., Boyce, J., Burchell, M., Kingston, A., Goodman-Tchernov, B. (submitted) Anthropogenic structure emplacement and sediment transport at King Herod's harbour, Israel: ED-μXRF (Itrax) data and foraminifera *Pararotalia calcariformata* as proxies of coastal development over millenia. Marine Geology.

Anthropogenic structure emplacement and sediment transport at King Herod's harbour, Israel: ED-μXRF (Itrax) data and foraminifera *Pararotalia calcariformata* as proxies of coastal development over millenia

Riley E. Steele[a*], Eduard G. Reinhardt[a], Jeremy J. Gabriel[b], Joe Boyce[a], Meghan Burchell[c], Andrew Kingston[d], Beverly Goodman-Tchernov[b]

[a] *School of Earth, Environment, and Society, McMaster University, 1280 Main St. W, Hamilton, Ontario, L8S 4L8, CA*
[b] *Department of Marine Geosciences, Leon Charney School of Marine Sciences, University of Haifa*
[c] *Memorial University, Department of Archaeology, St. John's, NL A1C 5S7 CA*
[d] *Geological Survey of Canada, Natural Resources Canada, 3303 33 Street Northwest, Calgary, Alberta T2L 2A7*
[*] *Corresponding author: steelr3@mcmaster.ca*

Abstract

The construction of harbours along high energy nearshore environments, which commonly include the emplacement of hard structures both as central features (e.g., piers, jetties) as well as protective measures (e.g., wave breakers, coastal armouring), can alter coastlines in a multitude of ways. These include reconfiguring the coast's morphology, introducing or redistributing exogenous and endogenous materials, and changing localized environmental substrate and structural conditions, and, as a result, impact the associated ecological communities. With growing coastal populations and associated coastal development, concerns over the long-term consequences of such projects are of global interest. Caesarea Maritima, a large-scale, artificially constructed ancient harbour built between 21–10 BCE, provides a rare opportunity to address these impacts and investigate its fingerprint on the landscape over 2000 years. To approach this, representative sediment samples were isolated and analyzed from two sediment cores (C1, C2), an excavated trench (W), and a sample of ancient harbour construction material (aeolianite sandstone and hydraulic concrete; COF). Geochemical (Itrax μXRF, magnetic susceptibility) and foraminifera analyses were conducted and results from both methods were statistically grouped into significantly similar clusters. Results demonstrated the increased presence of aeolianite-associated elemental contributions only after the construction of Caesarea as well as in particularly high concentrations following previously proposed tsunami events, during which shallower and deeper materials would have been transported and redeposited. The foraminifera data shows the appearance and eventual abundance dominance of *Pararotalia calcariformata* as an indicator of coastal hardening. Results suggest that they are an especially well-suited species to demonstrate changing environmental conditions existing today. In previous studies, this species was mistakenly presented as a recent lessepsian arrival from the Red Sea, when in fact it has had a long history of co-existence in the Mediterranean with humans and their harbour buildings habits. Specimens of *P. calcariformata*, therefore, are useful indicators for the timing of harbour construction at Caesarea and may be used as rapid and cost-effective biostratigraphic indicators on sandy nearshore coastline in future geoarchaeological studies. This has implications for future studies along the Israeli coast, including both paleoenvironmental and modern ecological assessments.

Keywords: *King Herod's harbour, Caesarea, hydraulic concrete, epiphytic foraminifera, Pararotalia calcariformata, μXRF*

3.1 Introduction

Ancient harbour sediments and stratigraphy are often studied because they contain evidence of past environmental change including climate, sea-level, and anthropogenic activity (Blackman, 1982a, 1982b; Marriner & Morhange, 2007; Reinhardt et al., 1994; Riddick et al., 2021; Riddick et al., 2022a, 2022b; Salomon et al., 2016). The analysis and interpretation of environmental proxies (e.g., microfossils, geochemistry, lithology, etc.) can be more straightforward in cases of shoreline progradation, where relative sea-level changes, siltation, and/or high input of river sediments have resulted in landlocked marine structures (i.e., within lagoons or estuaries). Sediments in these cases often record transitions from marine to more brackish/freshwater conditions associated with construction of harbour structures and/or natural barriers that are identifiable through changes in microfossil assemblages, sediment grain size and geochemistry, and other environmental indicators (e.g., Amato et al., 2020; Finkler et al., 2018; Pint et al., 2015; Stock et al., 2013, 2016).

The environmental evolution (i.e., site formation) of ancient harbour sites on high-energy, sandy coasts is more challenging to assess. Sediments from within a harbour basin can record geoarchaeological information (e.g., ancient harbour parasequences, changes in microfossil assemblages, archaeological material, etc.; Marriner & Morhange, 2006; Reinhardt et al., 1994; Riddick et al., 2021; Riddick et al., 2022a, 2022b); however, correlating stratigraphy in a harbour region can often be hindered by sediment reworking with waves and storms and by the absence of significant lithological changes in the sandy stratigraphy, with the exception of tsunamis or other large storm events (Goodman-Tchernov et al., 2009). The emplacement of ancient harbours (i.e., artificial hard substrates) on naturally soft-bottomed, sandy shorelines, significantly alters the local seascape resulting in sediment erosion and accumulation as well as the formation of a hard and stable substrate (Leys & Mulligan, 2011).

Past research on ancient harbour sediments (e.g., Marriner et al., 2005; Reinhardt et al., 1994; Salomon et al., 2016) has focused on analysis of harbour muds, recognizable by their muddy-appearance (finer particle size distribution; 'muds'; Hohlfelder, 2000), higher organic content, and increased concentrations of artifacts. In those studies, various bioindicator proxies, in particular gastropods, molluscs, ostracods, and foraminifera, were used to recognize harbour stratigraphy and related changing conditions connected to construction, destruction, and/or functionality (Marriner et al., 2005; Reinhardt & Raban, 1999). Amongst marine biomarkers, benthic foraminifera are especially popular as environmental proxies due to their known ecological preferences and tolerances, their rapid response to environmental change, and their durability in the sediment record over time (Holbourn et al., 2013; Murray, 2014). Generally, research to date on ancient harbour assemblage changes were linked to the increased presence of fine-grained sediment preferring species (e.g., Bolivinids) as well as shifting relative abundances of the more dominant Ammonia species (Goodman et al., 2009; Marriner et al., 2005; Reinhardt et al., 1994; Reinhardt & Raban, 1999). This agrees with the more general understanding that substrate is a major controlling factor in foraminifera assemblages (Langer, 1993). We hypothesize here that while the harbour muds introduce new conditions for a changing benthic foraminifera assemblage, so too can the increased presence of hard materials related to harbour construction and coastal development. These hard surfaces are especially influential on attached, epiphytic taxa. These taxa, therefore, will record a response to the introduction of artificial hard substrates, even beyond the more protected sediments of the harbour muds, and can act as biostratigraphic indicators of pre- and post- harbour sediments, a concept that has not previously been tested or applied.

Previously collected samples from a previously excavated trench area (W; Reinhardt et al., 2006), two sediment cores (C1, C2; Goodman-Tchernov et al., 2009), and a piece of harbour mole material (COF; Reinhardt et al., 2001) were included in this study (Figure 3.1). Seven samples (5-cm intervals) were available from W (-11.4 to -13.4 meters below sea level (mbsl), ~0.60 km from the coast; Reinhardt et al., 2006). Nineteen samples (1-cm intervals) from the upper 126 cm were available from C1 (233 cm in length, 15.5 mbsl, ~0.82 km from the coast) and 14 samples (1-cm intervals) were available from C2 (174 cm in length, 20.3 mbsl, ~1.25 km from the coast; Goodman-Tchernov et al., 2009). Radiocarbon and/or pottery dating methods were previously conducted on W, C1, and C2 samples. See Goodman-Tchernov et al. (2009) and Reinhardt et al. (2006) for further details on dating methods used. Geochemical ((μXRF, magnetic susceptibility) and foraminifera methods were applied here. The use of benthic foraminifera as biostratigraphic indicators to help correlate sediments in archaeological contexts is still a developing area of research (McGowran, 2009). The application of benthic foraminifera in this manner will be useful for future geoarchaeological studies as a rapid and cost-effective method for correlating sediments across an ancient harbour site, especially in high energy sandy shoreface settings. Results also have implications for understanding sediment transport in and around coastal structures, as well as for modern studies involving the monitoring and/or predicting of ecological changes in response to coastal anthropogenic activity.

3.2 Background

3.2.0.1 Regional geology and geochemistry

The Israeli Mediterranean coastline (Figure 3.1) is mostly characterized by unconsolidated sands and Pleistocene aeolian sandstone ridges (‘kurkar’). These

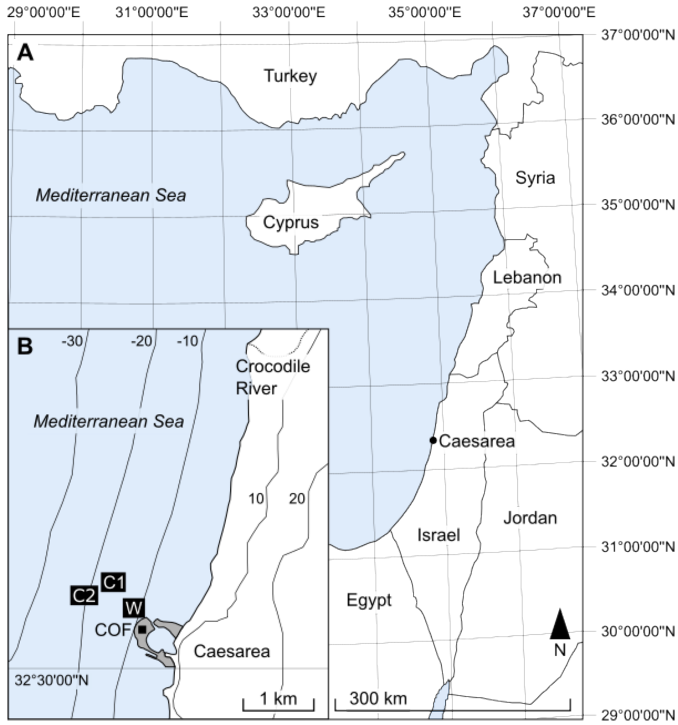

FIGURE 3.1: A) Location of Caesarea along the Israeli coastline. B) Location of sediment samples (cores C1 and C2, and excavated trench area W), and a harbour concrete sample (COF) offshore of Caesarea harbour (shaded in grey). Bathymetry contours are shown in meters. See Goodman-Tchernov et al., 2009, Reinhardt et al., 2006, and Reinhardt, Raban, and Goodman, 2001 for detailed information on sampling locations.

thick calcareous-cemented sand beds accumulated cyclically between thin layers of iron-rich paleosols ('hamra') and currently run parallel to the coast, both on and offshore (Almagor et al., 2000; Ronen, 2018). Located towards the northern extent of the Nile Littoral Cell, offshore sediments near Caesarea are predominantly transported from the south through wave-induced long-shore currents (Emery & Neev, 1960; V. Goldsmith & Golik, 1980; Golik, 1993, 1997; Schattner et al., 2015; Zviely et al., 2007). Prior to the construction of the Aswan Dam in the 1960s, approximately 100,000 m^3/yr of clastic sediments reach the coasts of Caesarea, largely sourced from Central Africa and the Ethiopian Highlands (Nir, 1984). These sediments are dominated by silica (quartz), alumina, and trivalent iron oxides (e.g., aluminosilicates) with minor amounts of heavy minerals (Goldsmith et al., 2001; Inman & Jenkins, 1984; Nir, 1984). The majority of heavy minerals include hornblende, augite, and epidotes, as well as minor amounts of resistant (e.g., zircon, tourmaline, rutile) and metamorphic minerals (e.g., sillimanite, staurolite, kyanite; Stanley, 1989). Local sources (i.e., eroded kurkar, onshore sediments, marine productivity) contribute some calcareous sediment to the nearshore environment (Goldsmith et al., 2001; Inman & Jenkins, 1984; Nir, 1984; see Appendix B1 for more details on dominant minerals, compositions, and sources). Sand-sized sediment extends 3–5 km from the shore to water depths of $\sim$25 m, while increasing amounts of silt and clay (mainly smectite, with minor kaolinite and illite) are found further offshore in slightly deeper water (30–50 m depths; Almagor et al., 2000; Emery & Neev, 1960; Nir, 1984; Sandler & Herut, 2000). The siliclastic sands, which characterize most of the nearshore, transition into more carbonate-rich sediments with higher instances of rocky substrates north of Haifa Bay (Almagor et al., 2000; Avnaim-Katav et al., 2015; Hyams-Kaphzan et al., 2014; Nir, 1984).

3.2.1 Historical and geological background on installations at Caesarea

The historical site of Caesarea Maritima is located 40 km south of Haifa, on the Israeli Mediterranean coast (34°53.5'E 32°30.5'N). Over six decades of research have provided details on the construction and deterioration of its harbour, also referred to as Sebastos, the largest artificial open-sea Mediterranean harbour of its time (Brandon, 2008; Hohlfelder et al., 2007). The harbour was constructed between 21 and 10 BCE using local kurkar and imported volcanic material (Vola et al., 2011; Votruba, 2007). Local kurkar is characterized by well-sorted quartz with calcite and minor amounts of feldspar, biotite, heavy minerals (e.g., hornblende, augite, zircon, rutile, tourmaline, magnetite, garnet, etc.), and allochems (Wasserman, 2021). Volcanic material has been used in concrete by the Romans since the 2nd century BCE (Oleson, 1988), often sourced from the Bay of Naples Neopolitan Yellow Tuff (NYT) deposits. Pozzolanic tuff-ash from this region was used in hydraulic concrete to form the breakwaters and foundations for harbour moles at Sebastos (Vola et al., 2011; Votruba, 2007). The mixture of lime, pozzolana, and aggregate provided a strong concrete that could set underwater. At Caesarea, the dominant coarse aggregates in the hydraulic concrete are kurkar sandstone and limestone (4 mm–20 cm in size; Vola et al., 2011). The mortar contains high proportions of pozzolanic material (yellow brown tuff ash/aggregates, lava fragments) with dominant minerals identified as sanidine, clinopyroxene, analcime, and phillipsite. The cementitious binding matrix contains similar material (calcite, tobermorite, ettringite, Calcium–Aluminum–Silicate–Hydrate) and was likely produced by the reaction between powdered pozzolanic material, lime, and seawater. Non-pozzolanic portions include white lime clasts, kurkar sandstone aggregates, ceramics, and wood fragments, with dominant minerals identified as tobermorite, quartz, illite, anthophyllite, ettringite, halite, bassanite, and sjogrenite (Vola et al., 2011; Appendix B1).

The chronology of Sebastos has been well-studied, with detailed research into the timing of deterioration and harbour use throughout antiquity (Boyce et al., 2009; Galili et al., 2021; Goodman-Tchernov & Austin, 2015; Hohlfelder, 2000; Raban, 1992, 1996; Reinhardt et al., 2006; Reinhardt & Raban, 1999). The location of Sebastos on a high-energy, mostly sandy coastline, as well as the previously established chronology of harbour construction, makes this an ideal site to assess the use of benthic foraminifera as biostratigraphic indicators of anthropogenic structure emplacement. The distribution of benthic foraminifera along the Israeli coast has been well-documented, providing a strong basis for interpreting trends within sediment samples offshore of Caesarea.

3.2.2 Benthic foraminifera of the Israeli Mediterranean coastline

Studies of both living and dead benthic foraminifera assemblages along the Israeli coast of the Mediterranean Sea indicate that substrate type (linked to bathymetry), food availability, and seasonality are the main factors controlling the distribution of species (Arieli et al., 2011; Avnaim-Katav et al., 2013, 2015, 2016, 2020, 2021; Hyams-Kaphzan et al., 2008, 2009, 2014). Certain taxa such as *Ammonia* *parkinsoniana* and *Buccella* spp. are highly abundant in the shallow (3–20 m), sandy nearshore settings. Others including *Ammonia inflata*, *Ammonia tepida*, *Elphidium* spp., *Porosononion* spp., and Milliolids are often observed in slightly deeper (20–40 m), silty to clayey environments further offshore on the inner Israeli shelf (Avnaim-Katav et al., 2013, 2015, 2016a, 2016b, 2017, 2020, 2021; Hyams-Kaphzan et al., 2008, 2009, 2014). Epiphytic taxa, which live on roots, stems, and leaves of plants (Langer, 1993), are highly associated with the micro- and macroalgal-covered hard substrates along the Israeli Mediterranean coast, especially the carbonate-rich rocky settings along the northern coast (Arieli et al., 2011; Avnaim-Katav et al., 2013, 2015, 2021; Hyams-Kaphzan et al., 2008, 2014). Coralline red algae (e.g., *Galaxuara rugosa* and *Jania rubens*) are highly abundant along the Israeli coast, along with other types of red (e.g., *Centroceras* sp., *Ceramium* sp., *Bangia* sp., *Halopteris scoparia*, *Laurencia* sp., *Neosiphonia* sp., and *Polysiphonia* sp.), brown (e.g., *Dictyora* sp., and *Ectocarpus* sp.), and green algae (*Codium* sp. and *Ulva* sp.; Arieli et al., 2011; Bresler & Yanko, 1995a, 1995b; Emery & Neev, 1960; Hyams-Kaphzan et al., 2014; Schmidt et al., 2015). Some of the most common epiphytic foraminifera taxa observed here include *Amphistegina lobifera*, *Lachlanella* spp., *Heterostegina depressa*, *Pararotalia calcariformata*, *Rosalina globularis*, *Textularia agglutinans*, and *Tretomphalus bulloides*, (Arieli et al., 2011; Hyams-Kaphzan et al., 2014). Many of these larger, symbiont bearing foraminifera are widely assumed to be more recently introduced Lessepsian species, a term used to describe Red Sea/Indian Ocean tropical species that have arrived after the construction of the Suez Canal (1869 CE). While some have been linked genetically and morphologically with their Red Sea communities, others, such as *P. calcariformata* (Schmidt et al., 2015; Zenetos et al., 2012) still have not.

3.2.2.1 *Pararotalia calcariformata*

Specimens of *P. calcariformata* McCulloch, 1977 were originally identified as *P. spinigera* (Le Calvez, 1949) on the Israeli coast, in particular within dated, stratigraphically discreet underwater archaeological excavations and geological collections (e.g., in Reinhardt et al. (1994, 2003), Reinhardt & Raban (1999)). Schmidt et al. (2015)'s initial error occurred when they mistook the date of the first publication that reported them on this coastline for the timing of their first observation (see reference to Reinhardt et al., 1994 in introduction of Schmidt et al., 2015). In fact, the *P. calcariformata* in that study were firmly positioned in sediments dating to at least 1500 years ago.

P. calcariformata is a well-documented epiphyte, found in highest abundances near hard substrates (up to 96% in shallow rocky habitats) of the Israeli coast (Hyams-Kaphzan et al., 2014; Reinhardt et al., 2003), usually living on calcareous algae and other seaweeds (e.g., *Jania rubens*, *Halimeda*, *Sargassum*, *Cystoseira*; Arieli et al., 2011; Bresler & Yanko, 1995a, 1995b; Emery & Neev, 1960; Schmidt et al., 2015, 2018). It is observed less frequently (up to 20% relative abundances) in shallow, soft-bottomed, sandy sediments (Avnaim-Katav et al., 2017, 2020; Hyams-Kaphzan et al., 2008, 2009). Recent work on this species explores its microalgal symbionts (Schmidt et al., 2015, 2018) and its high heat tolerance (Schmidt et al., 2016; Titelboim et al., 2016, 2017). These studies predict that warming sea temperatures will play a role in expanding populations of *P. calcariformata* along the Mediterranean.

3.3 Material and methods

3.3.1 Geochemical analyses

Forty samples from across W, C1, and C2 were analyzed in a sequential sample reservoir (Gregory et al., 2017) using the Cox Analytical ITRAX energy-dispersive micro-X-Ray Fluorescence Core Scanner (μXRF) at the McMaster University Core Scanning Laboratory (MUCS Lab). The kurkar/hydraulic concrete sample (COF) was also analyzed using the μXRF ITRAX machine. Analysis was conducted using the Chromium X-Ray source at 40 kV, 10 mA, 200–500 μm sampling interval, and 15 second exposure time. Elements of interest include Ca, Si, Ti, Fe, and Sr, all of which are likely to be found in relatively high abundance in the coastal Israeli sands based on the various sources of sediment (i.e., the Nile, kurkar bedrock, aeolian dust, marine productivity, and Sebastos harbour structures; Appendix A1). Ratios of Sr/Ca were used as an indicator of aragonite, because many marine taxa, including coralline algae, build their skeletons with aragonite which contains higher proportions of strontium (Sr) compared to calcite (Marshall & McCulloch, 2002; Rothwell & Croudace, 2015). Ratios of Zr+Ti/Ca and Zr+Ti/Si were used as indicators of heavy minerals. Zirconium- and Ti- rich minerals (e.g., zircon, rutile) are found as accessory minerals in many igneous rocks (Hasan et al., 2022; Rothwell & Croudace, 2015). They are typically dense, highly resistant to weathering, and have been used as indicators of volcanic sourced sediment (Konfirst et al., 2011; Marsh et al., 2007; Rothwell & Croudace, 2015; Westerhold et al., 2009). Ti and Zr are also found in the heavy mineral fraction of Israel's coastal sands (Appendix B1); however, the ratio of these elements against Ca or Si (the most dominant elements in Israeli sands) is expected to provide a proxy for heavy minerals sourced from the volcanic pozzolana material of Sebastos harbour.

Constrained cluster analysis of the µXRF results was used to identify statistically distinct geochemical zones across the sediment sampling areas (W, C1, C2) and COF. The data were row-centered (mean=0, sd=1), elements of interest were selected (Zr, Ca, Si, Ti, Fe, and Sr), and samples were clustered using a Self-Organizing Map (SOM; Kohonen, 2013) with the R "SOMbrero" package (Olteanu & Villa-Vialaneix, 2015). The similarity of observations (each 0.2 or 0.5 mm of sediment) was assessed through Ward's hierarchical clustering, using Euclidean distance. Clusters were further grouped into higher order "superclusters" to help identify zones with distinct elemental composition.

Volume magnetic susceptibility measurements (κ) of available sediment samples were obtained using a Barrington MS2E surface probe. Repeat surface measurements were taken and average values were reported.

3.3.2 Foraminifera analysis

Thirty-five samples from across W, C1, and C2 were subsampled for analysis of foraminifera in spring of 2006. Shelly/coarse grained layers and the intervening sands directly above and below them were targeted for analysis. Subsamples (0.9–15 cc) were wet sieved through 63 and 500 μm mesh to remove both fine and coarse material. Subsamples were dried and added to tetrachloroethylene to separate less dense foraminifera from terrigenous silicious and carbonate components. Subsamples were dried and subdivided for analysis using a dry splitter (Scott et al., 2001). Foraminifera were identified and enumerated (at least 300 specimens per sample) using an Olympus SX12 binocular microscope (100–400X magnification). Where the estimated standard error for the taxa identified was greater than the abundance in all samples, the taxa was deemed statistically insignificant and omitted from further analysis (Patterson & Fishbein, 1989). Specimens of *P. calcariformata* were imaged through Scanning Electron Microscopy at the Canadian Centre for Electron Microscopy (CCEM).

Identification of samples with statistically similar foraminifera assemblage compositions, and the statistical significance of the groups, was performed using the R statistical software package PVClust (Suzuki et al., 2022) with Ward's Minimum variance method (Ward, 1963) and Euclidean distances. Two types of p-values are computed with this package; Approximately Unbiased (AU) p-values are computed by multiscale bootstrap resampling and are more accurate than Bootstrap Probability (BP) p-values (Suzuki et al., 2022). Clusters with high AU values (e.g., 95%, equivalent to alpha=0.95 or 2σ significance) were considered as distinct biofacies throughout W, C1, and C2. Non-Metric Multidimensional Scaling (NMDS; Ramette, 2007), was used to analyse the spatial patterns of significant clusters in two-dimensional ordination space, using Euclidean distances.

3.4 Results

3.4.1 Core lithology and chronology

W is described in Reinhardt et al. (2006), while C1 and C2 are described in Goodman-Tchernov et al. (2009). W (∼2 m of excavated sediment) contains two main shell layers: (i) a poorly sorted mix of *Glycymeris* spp. and pebbles from ∼107–165 cm, with convex-up oriented fragments in the top portion, and (ii) a heterogeneous layer of shell fragments, ship ballast, and pottery shards from ∼39–59 cm. The intervening units consist of massive, homogeneous, medium-grained sand with isolated articulated and fragmented bivalve shells and/or pebbles. The upper ∼0–39 cm also contains thin layers of shells and pebbles (Figure 3.2). The upper 126 cm of C1 contains two shell layers: (i) a poorly sorted mix of *Glycymeris* spp. and pebbles, with fragments of worn pottery from 85–94 cm, and (ii) poorly sorted, convex-up oriented *Glycymeris* spp. and pebbles from 28–42 cm. The intervening units are massive, tan/grey, fine-grained sand, some with isolated bivalves and/or pebbles. (Figure 3.2). C2 (174 cm) similarly contains two shell layers: (i) framework supported, convex-up oriented *Glycymeris* spp. fragments from 132–138 cm, and (ii) convex-up oriented *Glycymeris* spp. fragments from 29–43 cm. The intervening units are massive, tan/gray, fine-grained sand with some silt and isolated bivalves.

The chronology of W, C1, and C2 has been previously described (Goodman-Tchernov et al., 2009; Reinhardt et al., 2006), and units have been correlated to age ranges (radiocarbon and pottery; Table 3.1) and identified events (i.e., tsunami deposits; Figure 3.2). W, C1, and C2 were found to capture similar event layers dating to ∼1492–100 BCE (pre-harbour), 92 BCE–418 CE (containing the 115 CE Roman tsunami event), 327 BCE–408 CE, ∼300–1280 CE (containing the 551/749 CE Late Byzantine/Early Islamic tsunami events), and ∼1280 CE–present (Table 3.1, Figure 3.2).

Table 3.1: Radiocarbon and pottery dating results for W, C1, and C2 based on previous studies.

Core/Area	Depth (cm)	Analysis	Conventional Radiocarbon (BP)	Cal BP	BCE/CE	Reference
1	30 cm	AMS	1420 ±40	Cal BP 1152–670*	798–1280 CE*	1
1	~35 cm	Pottery	-	-	4th – 6th c. CE	1
1	90 cm	AMS	3610 ±40	Cal BP 3763–3177*	1814–1228 BCE*	1
2	130 cm	AMS	3640 ±40	Cal BP 3805–3224*	1856–1275 BCE*	1
W7	11.6 m	Pottery	-	-	6th c. CE – present	2
W7	12.0 m	Pottery	-	-	4th – 6th c. CE	2
W7	12.3 m	Radiocarbon	2330±100	Cal BP 2276 – 1543*	327 BCE – 408 CE*	1, 2
W7	12.6 m	Radiocarbon	2310±80	Cal BP 2208 – 1533*	259 BCE – 418 CE*	1,2
W7	12.9 m	Radiocarbon	2370±70	Cal BP 2281–1640*	332 BCE – 311 CE*	2
W7	13.1 m	Pottery	-	-	1st/2nd c. CE	2
W7	13.4 m	Radiocarbon	4740±100	Cal BP 5298 – 4538*	3349 – 2589 BCE*	2

[1] Goodman-Tchernov, B.N., Dey, H.W., Reinhardt, E.G., McCoy, F., & Mart, Y. (2009). Tsunami waves generated by the Santorini eruption reached Eastern Mediterranean shores. *Geology*, *37*(10), 943–946. https://doi.org/10.1130/G25704A.1.

[2] Reinhardt, E.G., Goodman, B.N., Boyce, J.I., Lopez, G., van Hengstum, P., Rink, W., J., Mart, Y., & Raban, A. (2006). The tsunami of 13 December A.D., 115 and the destruction of Herod the Great's harbour at Caesarea Maritima, Israel. *Geology*, *34*(12), 1061–1064. https://doi.org/10.1130/G22780A.1.

*Recalibrated using Marine20 at 95.4% with Delta R=-94±94 (average of 10 nearest Marine Reservoir Correction data points to Caesarea; http://calib.org/marine/).

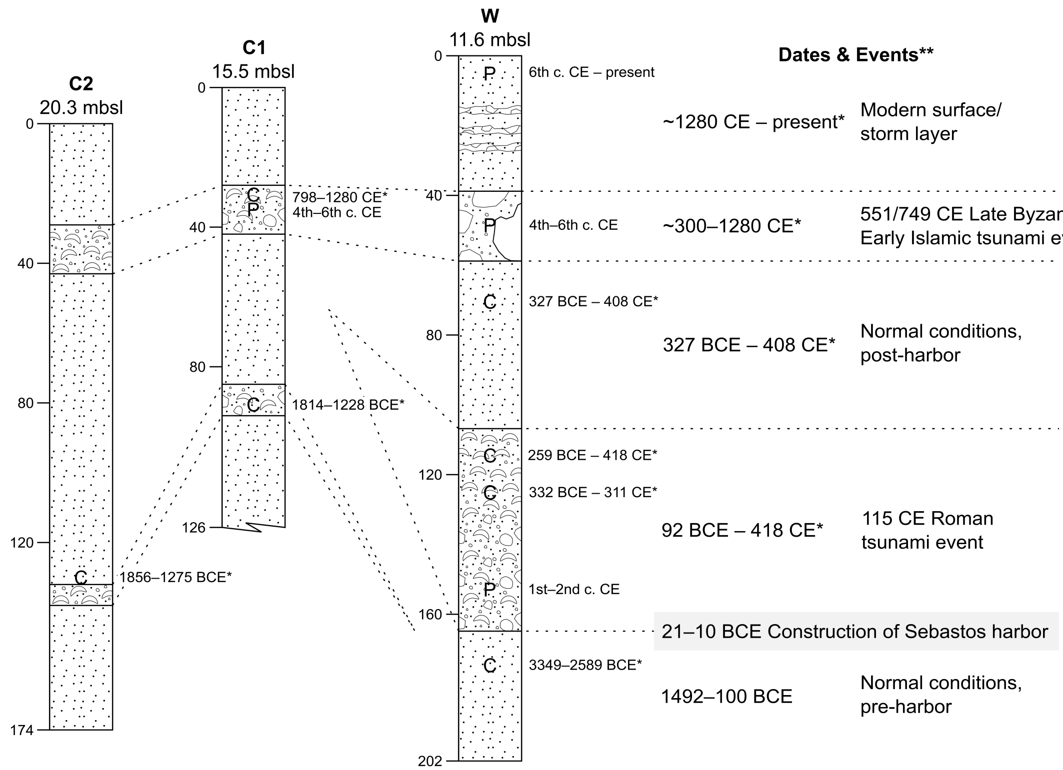

FIGURE 3.2: Correlation between C1, C2, and the summarized stratigraphy of W. Layers of shells, pottery, and ballast material with intervening sands, as well as radiocarbon (C) and pottery (P) dates with summarized ages and interpreted events for each horizon are shown. Modified from Goodman-Tchernov et al., 2009 and Reinhardt et al., 2006. *Age ranges using re-calibrated dates. **Based on Goodman-Tchernov et al., 2009 and Reinhardt et al., 2006 using radiocarbon, optically stimulated luminescence, and pottery results for four additional cores/sample sites than were included in this study. See Table 3.1 for more details on dates.

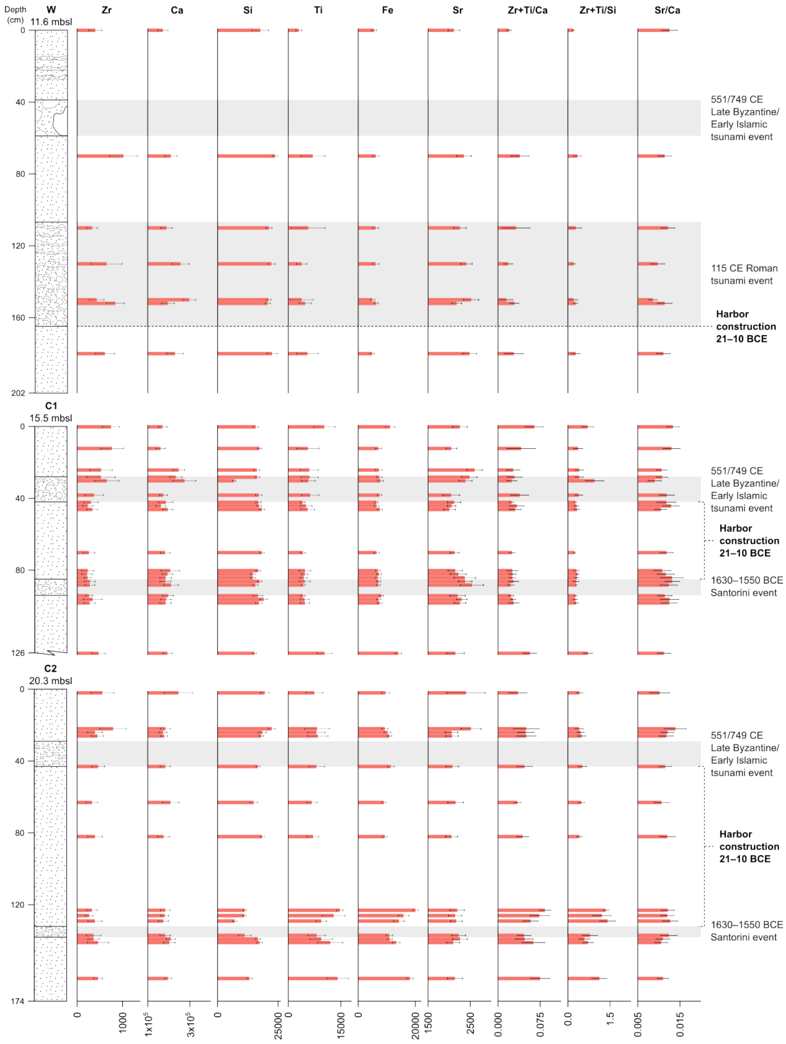

FIGURE 3.3: μXRF results (mean counts and standard deviations) for elements of interest in samples from W, C1, and C2, showing estimated interval for the time of harbour construction. See Figure 3.2 for dates and events.

3.4.2 Geochemical results

Elemental (μXRF) results are shown in Figure 3.3 and Appendix B2. Average counts of Zr increase upcore in each sampling area, with uppermost values ~2–3 times higher than those at the base (~700–1000 compared to 200–400; Figure 3.3, Appendix B2). Ca is highly variable throughout all sampling areas, with some peaks up to 1.7x higher (~300,000) in shell layers than in sandy samples. Counts of Si remain relatively high (∼17,000) throughout time, with some decreases up to 1.5–2.5x lower in shell layers. Average Ti values are variable through time (∼6000) with some spikes up to 2x higher at the top and bottom of C1 and surrounding the bottom shell layer of C2. Fe follows similar trends to Ti, with values ∼2x higher near the top and bottom of C1 and the darker sandy sediments of C2 (161–123 cm) compared to the intervening sandy samples (counts of ∼6000–7000). Counts of Sr remain quite constant throughout all sampling areas over time (∼2000), with a slight increasing trend in the upper portions of C1 and C2 (values up to ∼1.3x; Figure 3.3, Appendix B2).

Ratio results of Zr+Ti/Ca and Zr+Ti/Si are variable throughout time in W (values 0.02–0.04 and 0.20–0.34) and C2 (0.03–0.08 and 0.4–1.4), especially within tsunami event layers, though results show no clear increasing/decreasing trends over time. In C1, these ratios show a distinct increasing trend through the upper half of the core (Zr+Ti/Ca: from 0.02 up to 0.06; Zr+Ti/Si: 0.3 up to 0.7). Sr/Ca values remain relatively consistent in all coring areas (∼0.10), with minor variation surrounding shell layers (Figure 3.3, Appendix B2).

Sample COF shows distinct variation in elemental composition between kurkar and hydraulic concrete (Figure 3.4). On average, counts of Zr and Ti are over 10x higher in the hydraulic concrete than the kurkar. Counts of Fe are also higher in the hydraulic concrete by a factor of ∼8. Ca shows the opposite trend, with counts 5x higher in the kurkar than the hydraulic concrete. Counts of Si were variable throughout both materials but were slightly higher in the hydraulic concrete. Sr peaked in the kurkar and decreased moving into the hydraulic concrete, with some variability associated with the aggregate material (Figure 3.4). Ratio results for Zr+Ti/Ca are ∼94x higher in the hydraulic concrete than in the kurkar, while Zr+Ti/Si values are almost 2x higher. Sr/Ca are ∼4x higher in the hydraulic concrete than in the kurkar (Figure 3.4).

The cluster analysis of W, C1, C2, and COF results displayed seven superclusters (SC1–SC7; Figure 3.5). SC1 and SC2 are highly similar, though SC1 contains relatively higher counts of Si and lower counts of Ti and Fe than SC2. SC2 appears more frequently in samples from the upper halves of the cores, while SC1 appears more frequently in deeper and older contexts (Figure 3.5). SC3 and SC4 appear

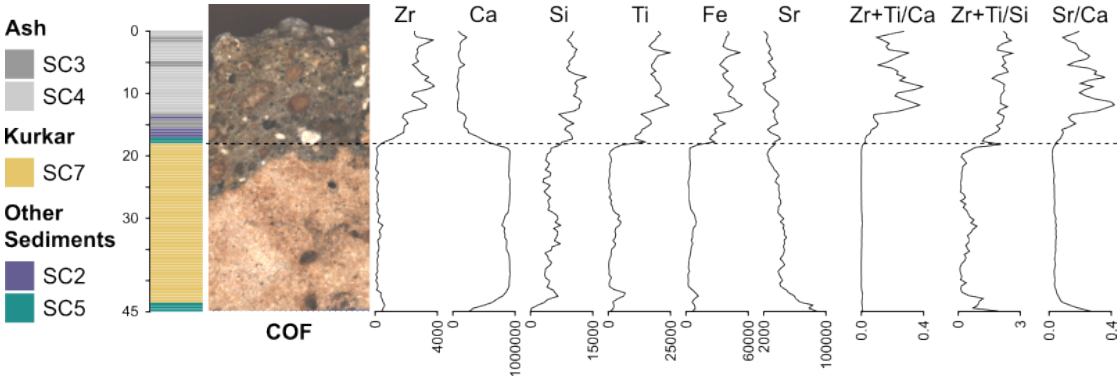

FIGURE 3.4: μXRF results (counts) for elements of interest in sample COF with chemofacies results (see Figure 3.5).

only in the ash-rich portion of COF. SC5 is highly similar to SC1, with some peaks in Zr and Sr compared to SC1, appears mainly in the sandy units of cores, and reflects the general sedimentary background of the coast. SC6 contains very few samples and is analogous to SC5. SC7 is characterized by relatively high counts of Ca and Si and is predominantly associated with the kurkar portion of COF, with some samples from tsunami layers of W and C1, and with the uppermost sand layers of C2 (Figure 3.5).

The magnetic susceptibility of sediments remains relatively low throughout all samples (Table 3.2). Aside from a peak (27.8x10-6 SI) at the top of C1, values range between 5.2–10.4x10-6 SI in C1, 8.9–13.5x10-6 SI in C2, and 2.6–7.1x10-6 SI in W, with no distinct trends over time (Table 3.2).

TABLE 3.2: Magnetic susceptibility for W, C1, and C2 sediment samples.

Sample	Depth (cm)	n	Mean Susc. κ (10^{-6} SI)	Standard Dev. (10^{-6} SI)
W	0–5	4	5.2	0.47
	70–75	4	3.5	0.19
	110–115	4	4.8	0.17
	130–135	7	4.4	1.48
	150–155	4	4.3	0.39
	152–157	4	7.1	0.43
	180–185	6	2.6	0.66
C1	0–1	4	27.8	0.72
	12–13	4	9.3	0.49
	26–27	4	8.1	0.37
	28–29	4	9.9	0.05
	30–31	4	7.3	0.08
	38–39	4	8.1	0.17
	42–43	4	5.2	0.22
	44–45	4	6.9	0.57
	46–47	4	9.8	0.51
	70–71	4	10.4	0.58
	80–81	4	6.7	0.29
	82–83	4	6.9	0.13
	84–85	4	9.0	0.15
	86–87	4	7.6	0.49
	88–89	4	7.4	0.39
	94–95	4	8.1	0.25
	96–97	4	6.9	0.14
	98–98	4	7.5	0.67
	126–127	4	9.9	0.13
C2	2–3	-	-	-
	22–23	4	10.0	0.20
	24–25	4	13.5	0.14
	26–27	4	12.3	0.14
	43–44	4	9.8	0.26
	63–64	4	8.9	0.16
	82–83	4	10.5	0.24
	123–124	4	13.4	1.13
	126–127	4	10.9	0.51
	129–130	4	11.5	0.54
	137–138	4	10.3	0.05
	139–140	4	10.6	0.34
	141–142	4	10.5	0.22
	161–162	4	11.9	0.14

- insufficient sample for analysis

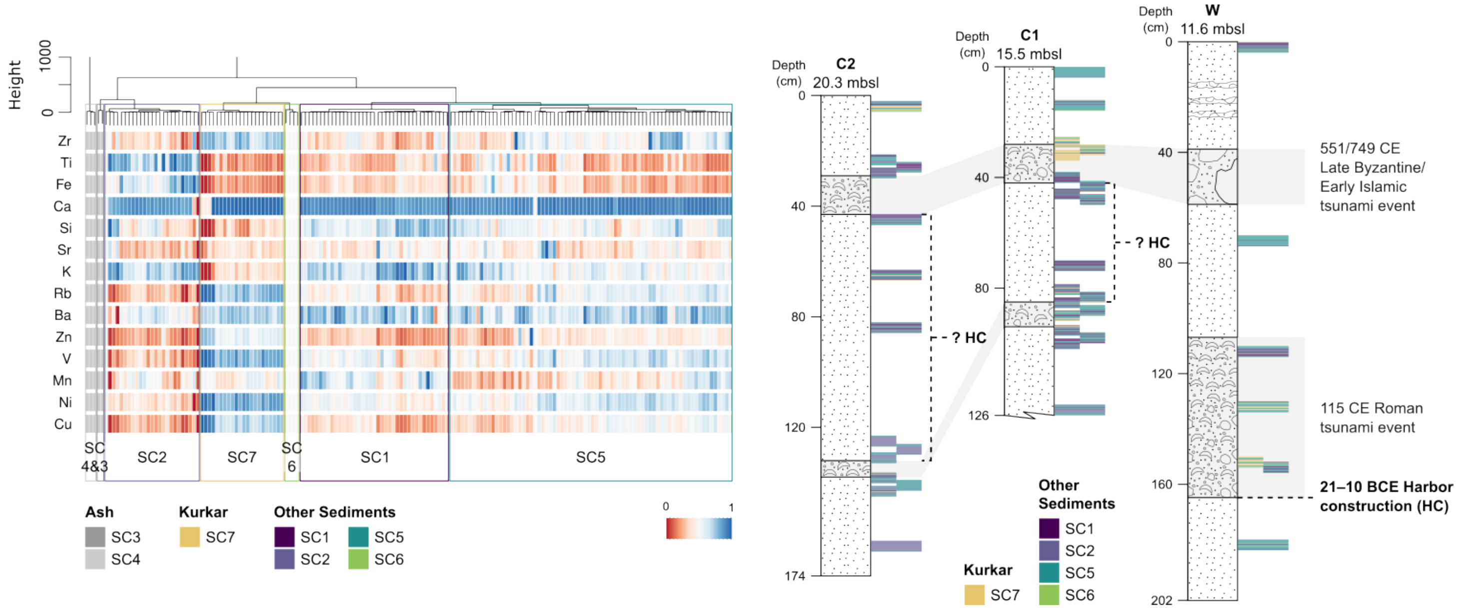

FIGURE 3.5: Chemofacies superclusters for elemental data within samples from W, C1, and C2, showing relative proportions for elements of interest. Complete Sequential Sampling Reservoir (SSR) clustering data is shown for each sample (note that sample thicknesses are exaggerated to show clustering variation within each sample).

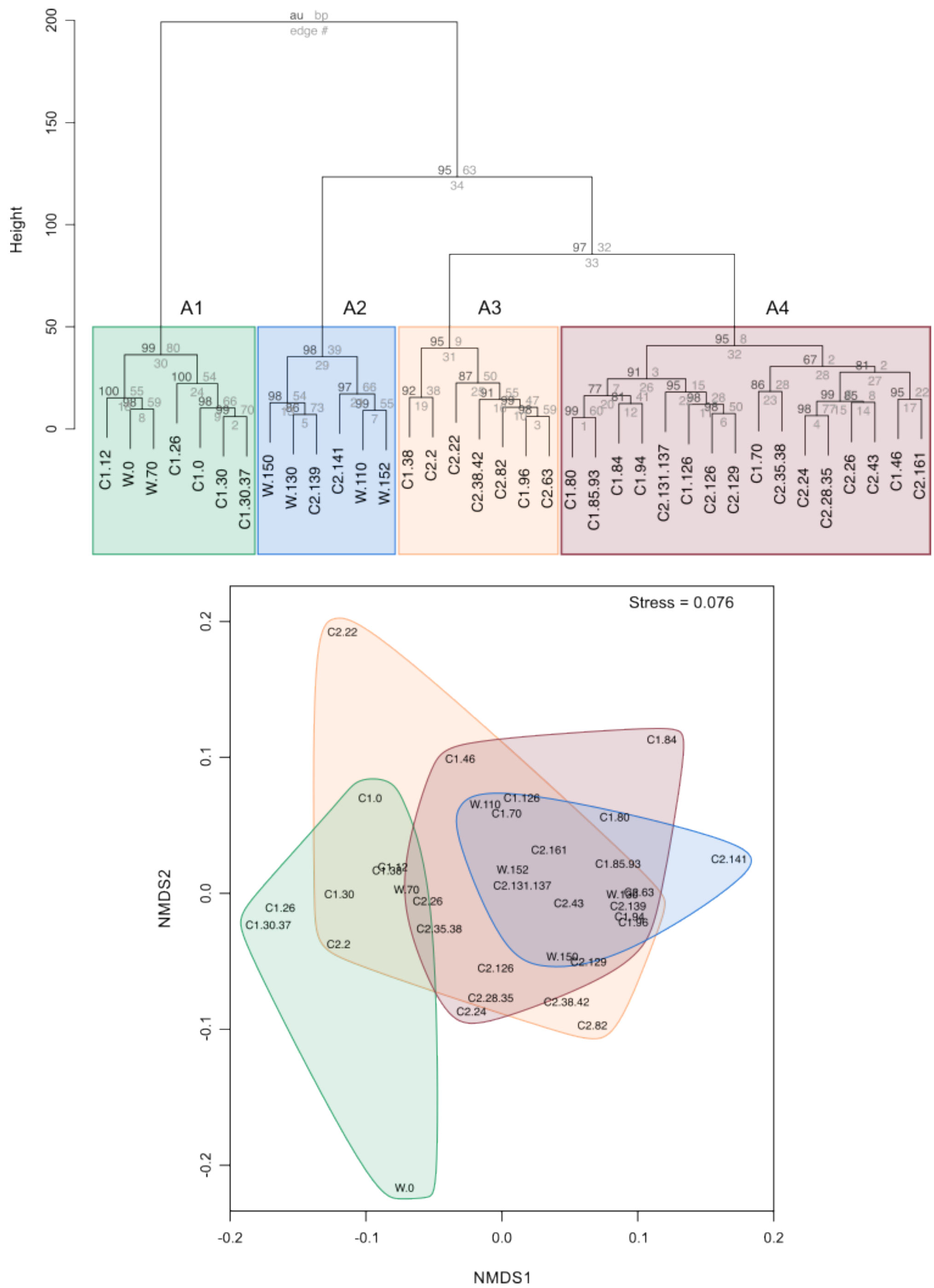

FIGURE 3.6: Clustering and NMDS results for W, C1, and C2 foraminifera data, showing biofacies A1, A2, A3, and A4.

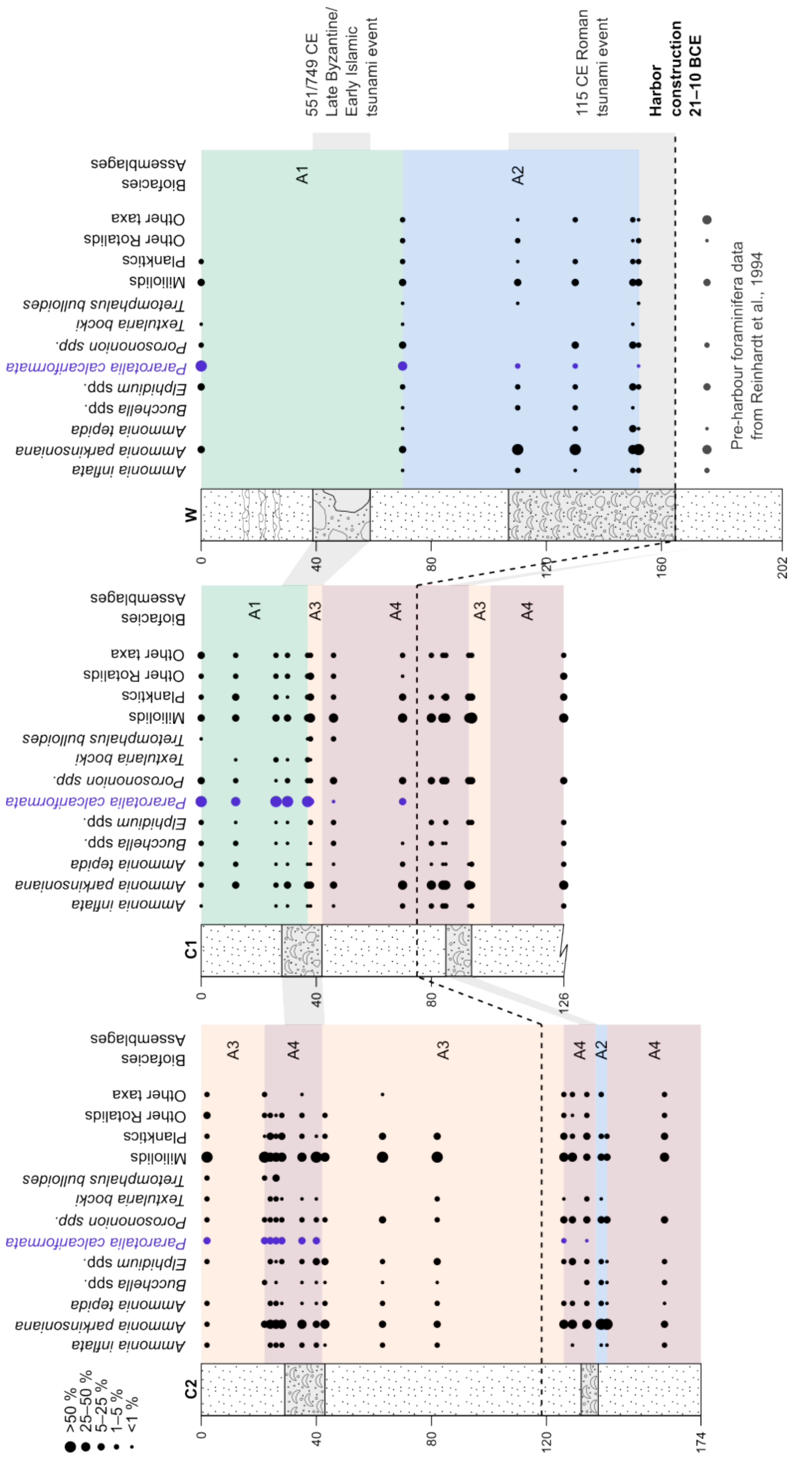

FIGURE 3.7: Relative abundance (%) of foraminifera within samples from C1, C2, and W, showing biofacies assemblages (see Figure 3.6).

3.4.3 Foraminifera results

Thirteen statistically significant foraminifera taxa were identified across W, C1, and C2, and the cluster analysis revealed four significant (au >95%) assemblages (A1, A2, A3, A4; Figure 3.6 and 3.7, Appendix B3). The NMDS showed that the four assemblages overlapped, especially A2, A3, and A4, suggesting that samples within these assemblages were quite similar despite grouping distinctly (Figure 3.6). A1 contains only samples from the tops of W and C1. This assemblage is dominated by *A. parkinsoniana* (∼3–21%), *P. calcariformata* (∼43–74%), and Miliolids (∼13–20%; Figure 3.7; Appendix B3). A2 contains samples from the sand and lower shell layers of W, as well as the lower shell layer of C2. Assemblage A2 is dominated by *A. parkinsoniana* (∼46–70%), *Porosononion* spp. (∼0–19%), and Miliolids (∼12–22%). Assemblage A3 contains samples from the top and middle shell layers of C1, as well as the top sand, middle sand and shell layers of C2. Dominant specimens within this assemblage include *A. parkinsoniana* (∼4–23%), *P. calcariformata* (∼0–19%), *Porosononion* spp. (∼2–11%), and Miliolids (∼42–69%). A4 contains samples from the middle sand layers of C1, as well as the middle sand, and bottom shell and sand layers of C2 (Figure 3.7). This assemblage is dominated by *A. parkinsoniana* (∼20–44%), *P. calcariformata* (∼0–21%), *Porosononion* spp. (∼1–17%), Miliolids (∼21–46%), and planktics (∼0–15%; Figure 3.7; Appendix B3).

Increasing abundances of *P. calcariformata* (Appendix B4) over time were observed in all three sampling locations. In W, this species was relatively abundant (0.38–51.74%) and was observed in all samples except for 150–155 cm. *P. calcariformata* was observed at highest abundances (0.91–73.68%) in the top 0–71 cm of C1, and at lowest abundances (6.25–20.79%) in the top 0–42 cm of C2. This species was also observed at relatively low abundances towards the bottom of C2 (1.19% at 126–127 cm and 0.71% at 131–137 cm).

3.5 Discussion

3.5.1 Pre-harbour nearshore sediment composition and distribution

Prior to the construction of Sebastos, the shoreline at Caesarea was characterised by a soft-bottomed, unconsolidated sandy beach overlying regional kurkar ridges (Figure 3.8; Almagor et al., 2000; Reinhardt et al., 1994; Ronen, 2018). This is reflected in both foraminifera and geochemistry results in C2 and the lower two thirds of C1 and W (Figure 3.3, Figure 3.7). Biofacies A2, A3, and A4 (pre-harbour), characterized by relatively higher proportions of *A. parkinsoniana*, Milliolids, and *Porsononion* spp., are consistent with Reinhardt et al. (1994)'s pre-harbour foraminiferal faunal results (Figure 3.7). These taxa are typically associated with shallow and mid-depth (3–20 m, and 20–40 m) Nilotic sands and silty–clayey sediments of the Israeli inner shelf (Avnaim-Katav et al., 2013, 2015, 2016, 2017, 2019, 2020, 2021; Hyams-Kaphzan et al., 2008, 2009, 2014). The minor presence of *P. calcariformata* at the bottom of C2 and in pre-harbour sediments is associated with the coarse shell unit of the Santorini tsunami (Goodman-Tchernov et al., 2009). This event transported shallow marine sediment offshore including the epiphytic *P. calcariformata*, likely from the kurkar hard grounds (Reinhardt et al., 2003).

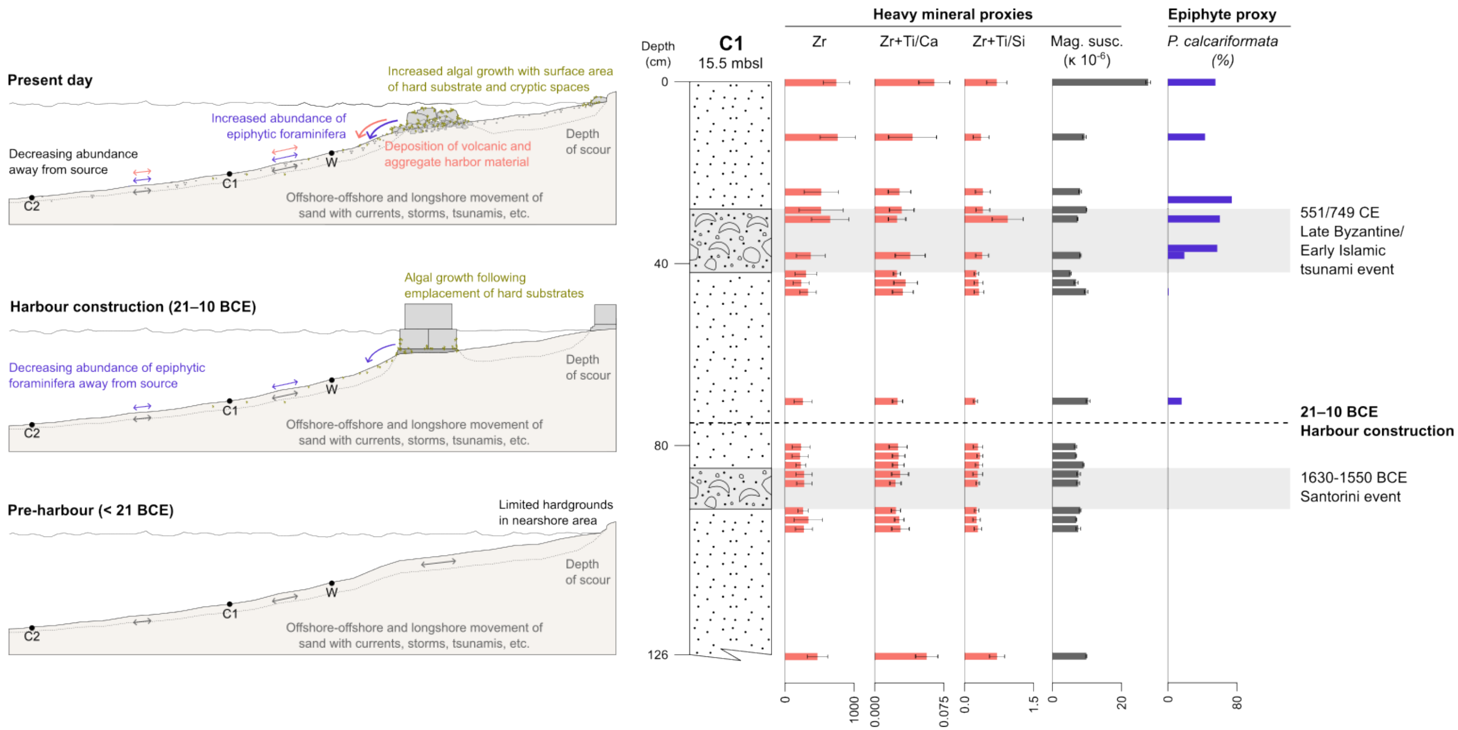

FIGURE 3.8: Interpretation of coastal change at Sebastos Harbour, showing relative abundances (%) of *Pararotalia calcariformata*, Zr, Zr+Ti/Ca and Zr+Ti/Si ratios, and magnetic susceptibility results for C1, alongside a simplified diagram of pre-harbour, newly constructed harbour (modified from Reinhardt et al. (2006)), and recent coastal settings.

The relative consistency in average counts of Ca, Si, Ti, and Fe through time within the sandy units of each of the three sampling areas suggests that there is virtually no difference in abundance of these elements in pre-and post-harbour sediments (Figure 3.3; Appendix B2). This reflects the pre-harbour (and post-harbour) regional geology (local carbonate-rich kurkar), marine productivity (e.g., shells), and Nile sediment sources (aluminosilicate minerals within the shoreline's sands, silts, and clays, as well as the minor amounts of heavy minerals; Appendix B1 and B2). In pre-harbour sediments, slight variations in counts for Ca, Si, Ti, and Fe (increases or decreases in average counts by factors of ∼1.1–1.8) predominantly surround the Santorini event (Figure 3.3). This is expected, as high-energy events typically result in abnormal deposition (e.g., shell material, rip-up clasts, archaeological material, beach-derived pebbles) that would be reflected in geochemical results (Goodman-Tchernov et al., 2009).

The cluster analysis of elemental data shows very slight variation in sediment composition based on sample location, especially between W and C2 (Figure 3.5), which could be the result of natural nearshore sediment transport patterns (Almagor et al., 2000; Emery & Neev, 1960; Quick, 1991). Onshore-offshore sediment transport is mainly wind-driven and is controlled by several forces related to incoming waves, sediment size, and beach slope (Quick, 1991). During summer months on the Israeli coast, relatively calm northwesterly winds generate waves and currents that cause sands to move shoreward (Almagor et al., 2000; Emery & Neev, 1960; Quick, 1991). During winter months, strong southwesterly storm winds result in offshore sand transport. Since waves break at an angle to the Israeli shoreline, onshore-offshore sediment movement occurs in a slightly oblique direction, with net transport northwards (Almagor et al., 2000; Emery & Neev, 1960). Because the amount of sediment carried through longshore currents decreases northward, and beach accretion along the coasts largely does not take place, researchers have concluded that sediment must be lost (e.g., moved seawards or blown landwards) along the way (Almagor et al., 2000; Emery & Neev, 1960). Through a study on sand balance, Almagor et al. (2000) estimated that roughly 450,000 m^2 per year of sediment is lost to seaward escape between Gaza and Haifa. Sands are actively deposited within a gently sloping (0.5–0.8°)

nearshore zone extending 3–5 km offshore (∼40 m water depth), near the easternmost drowned kurkar ridge (Almagor et al., 2000). Sands that escape past this point are mixed with increasing amounts of silts and clays that accumulate on a relatively flat seabed (Almagor et al., 2000; Nir, 1984; Sandler & Herut, 2000). All sampled areas in this study are within this zone of active sedimentation, though each site was sampled at different depths and distances from shore, so we would expect to see some natural variation in composition.

3.5.2 Post-harbour nearshore sediment composition and distribution

3.5.2.1 Geochemical indicators of harbour deterioration

The chemofacies results reflect coastal development, mainly through SC1, SC2, and SC7. SC1 is a coarser grain version of sediments that cluster with SC2. SC1 replaces SC2 in the upper portion of all three cores. The reduction in clays (indicated by Ti) and increase in silica within this shift in chemofacies suggests slight grain coarsening over time, while the increase in Ba indicates an increase in productivity. This slight shift over time may represent natural changes in sediment sources (e.g., variations in White and Blue Nile sediments, terrestrial inputs, etc.) and/or anthropogenic influence (Kalman et al., 2022). SC7, which relates to the kurkar component of sediments (Figure 3.4 and 3.5), appears much more frequently post-harbour and with tsunami influence. Kurkar was heavily used in the construction of the harbour (Vola et al., 2011; Votruba, 2007), and tsunamis transported and deposited this material further offshore. The slight presence of SC7 in the Santorini event layer (C1, Figure 3.5) reflects this process occurring pre-harbour, with natural kurkar deposits along the coast.

Heavy minerals including zircon and rutile exist in Israeli sands in minor abundances (Lin et al., 1974; Pomerancblum, 1966; Stanley, 1989), as demonstrated by the presence of Zr (∼300) and Ti (∼5,000) throughout the pre-harbour sediment samples. These minerals come from several sources including Nile sediments, local onshore terrains, aeolian dust, and reworked sedimentary bedrock (Appendix B1).

On the Israeli coast and other high-energy, sandy shorelines, heavy minerals become naturally concentrated due to mechanical sorting (Stanley, 1989). Through waves and currents, denser mineral grains typically settle out of suspension and accumulate at the bottom of the swash zone while lighter grains are carried back towards shore to the wave zone (Dinis & Soares, 2007; Hou et al., 2017). Abundances along the Israeli coast are still relatively low (∼0.1–0.5%; Lin et al., 1974). Differences along the coast due to varying local sources of sediment (e.g., nearby wadis/rivers) are minor, and any significant changes in heavy mineral abundances would require vast amounts of sand inputs (Boenigk & Neber, 2005). The increase in Zr+Ti/Ca and Zr+Ti/Si values from pre- to post-harbour sediments (by factors of 3 and 2.3, respectively), and the observed increasing trend within post-harbour sediments is therefore not likely to be caused by natural sources and is most likely related to harbour deterioration. Although Zr was not reported in Vola et al. (2011)'s bulk chemical and petrographic analysis of Sebastos concrete and TiO_2 was only a minor component of the mortar (0.2–0.3%), we observed distinctly higher values of Zr and Ti throughout the hydraulic concrete portion of COF (avg Zr+Ti/Ca: 0.187; avg Zr+Ti/Si: 2.02) compared to the kurkar portion (avg Zr+Ti/Ca: 0.002; avg Zr+Ti/Si: 1.27). This suggests the presence of trace amounts of (or mineral impurities including) Zr and Ti within the aggregate material and the fine-grained matrix of the concrete. Our results suggest that the foreign volcanic material contains a much larger proportion of heavy minerals compared to local kurkar sources of sediment.

Magnetic susceptibility results are comparable to previous studies of Caesarea. Boyce et al. (2004, 2009) found a range of 0.1 to 8.7 x10^{-5} SI for harbour bottom sands and muds, which is similar to most sediments in this study (2.6 to 13.5 x10^{-5} SI; Table 3.2). The relatively extreme value observed at the top of C1 (27.8 x10^{-5} SI) more closely aligns with values of pozzolana (22.7 to 175.2x10^{-6} SI; Boyce et al., 2004) than the quartz sands and harbour muds. The presence of eroded hamra material (κ = 88.0x10^{-5} SI; Boyce et al., 2004), eroded igneous or metamorphic ballast stones (κ = >90 to >200x10^{-5} SI; Boyce et al., 2009) or eroded clay fragments (κ = 133.7x10^{-5} SI; Boyce et al., 2004) could also be influencing the higher value at the top of C1. Any of these sources could indicate increased presence of harbour material in recent offshore sediments (Figure 3.8).

Additional sediment samples, especially throughout the top portion of W and C1 would help to confirm the observed trends in magnetic susceptibility.

Observable changes in heavy minerals following harbour construction occur within sediments between the Santorini event (1630–1550 BCE) and the Late Byzantine/Early Islamic tsunami events (551/749 CE); however, correlating a more precise estimated depth for the timing of harbour construction remains a challenge solely with the XRF results (Figure 3.3). The benthic foraminifera results, however, can be used to further refine these estimates.

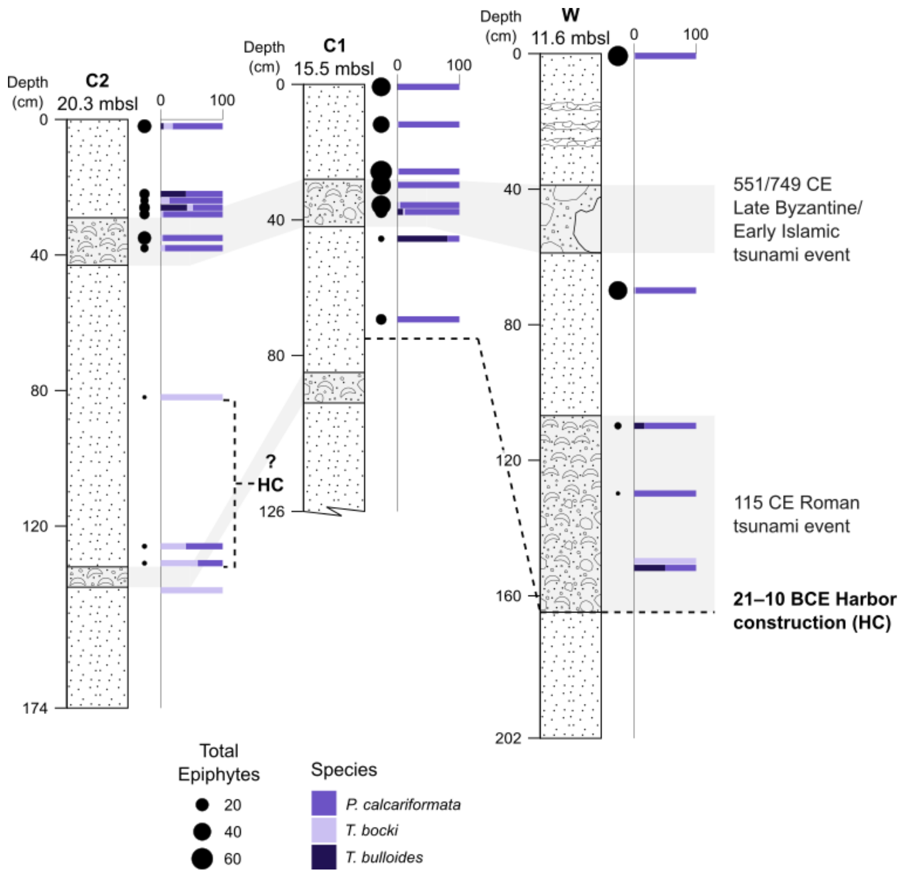

FIGURE 3.9: Total and relative proportions of the three epiphytic species (*Pararotalia calcariformata*, *Textularia bocki*, and *Tretomphalus bulloides*) observed in W, C1, and C2.

3.5.2.2 Epiphytic foraminifera as biostratigraphic indicators of artificial substrate change

The effect of harbour emplacement on benthic foraminifera populations is evident in A1, at the tops of W and C1 (Figure 3.7). This assemblage contains distinctly higher abundances of *P. calcariformata* (Figure 3.9; Appendix B4), a common epiphytic species usually found in association with calcareous algae in rocky areas of the Israeli inner shelf (Arieli et al., 2011; Bresler & Yanko, 1995a, 1995b; Emery & Neev, 1960; Hyams-Kaphzan et al., 2014; Reinhardt et al., 2003; Schmidt et al., 2015, 2018). As harbour structures progressively deteriorated over time, increasing amounts of cryptic spaces would have formed, providing increasing amounts of surface area for algal growth. Ratio values for Sr/Ca do not seem to vary significantly over time, suggesting a continuous presence of aragonitic organisms (shells, calcareous algae, etc.). In C1, values slightly increase over time following a drop during the Late Byzantine tsunami event (Figure 3.3) which may be related to an increase in calcareous algal growth on harbour ruins. Increased sample resolution would help to confirm this trend. Hard substrates (i.e., submerged harbour structures) with algal growth are optimal settings for *P. calcariformata*, and increased populations of this species after harbour construction are recorded in all three sampling areas. After death, these specimens would have detached from the algal-covered harbour and been transported to the nearby sediments by onshore-offshore transport mechanisms discussed above (section 5.1), especially by strong storm waves during winter months (Figure 3.8; Almagor et al., 2000; Quick, 1991). Higher abundances are recorded in deposits close to the site (i.e., W and C1), though their presence is still observed 800 m from the harbour structures (C2; Figure 3.7).

Other epiphytic species are present in low abundances throughout the sampling areas (Figure 3.9) but do not show significant trends over time, likely due to their preferred habitats. *T. bocki* and *T. bulloides* are more often associated with the northern coast of Israel beyond the Nile littoral cell; *T. bocki* is usually found in deeper (30–100 m), silty-clayey sediments (Avnaim-Katav et al., 2013, 2015, 2020, 2021), while *T. bulloides* has been observed in shallow rocky areas surrounding Haifa (Arieli et al., 2011; Hyams-Kaphzan et al., 2014). These foraminifera results demonstrate the importance of understanding the distribution and habitat preferences for the taxa of a specific region when considering using epiphytic species as indicators of substrate changes.

The benthic foraminifera result here, especially *P. calcariformata*, provide information to help further correlate the timing of harbour construction within C1 and C2 (Figure 3.7). Results also show that *P. calcariformata* is not a recent invasive species as previously thought (Schmidt et al., 2015; Zenetos et al., 2012). In all three cores, *P. calcariformata* was observed in sediments follow construction of Sebastos harbor, and in C2, specimens were observed in two samples dating to the Santorini event bed (1630–1550 BCE; Figure 3.7; Appendix B3). This supports Reinhardt et al. (1994)'s observations of this species in historical sediments and suggests that this species has been living on the eastern Mediterranean coast since around the Late Bronze Age. Recent studies involving *P. calcariformata* discuss possible future range expansions of this species along the Mediterranean, especially northwards through longshore current transport (Schmidt et al., 2015, 2016, 2018; Titelboim et al., 2016, 2017). The samples of *P. calcariformata* used in these previous studies were collected from algae and sediments on hard substrates. Although Schmidt et al. (2015) briefly mention that there is some substrate control on this species, estimations of range expansions were based on solar radiance, turbidity, and temperature. These variables are proven to be important controls on this species; however, substrate conditions are equally important habitat controls on *P. calcariformata* populations as shown in this study. While studying the foraminiferal response to pollution sources, (Yanko et al., 1994) found distinctly higher abundances of *P. calcariformata* (identified as *Eponides repandus*; Schmidt et al., 2015) in proximity to the coal-contaminated site of Hadera compared to the control site, which had similar water depth and substrate conditions (0–15.1% compared to 0–0.3%). Although increased sea temperatures from the cooling water discharge at the power plant is a key factor, this trend could be due to the presence of extensive hardgrounds at the power station (harbour structures and numerous pilings) and algal coverage on the long pier that extends 2 km from the shoreline. Nearby substrates, including artificial structures such as harbours or pilings, should be considered in future research involving the distribution of benthic foraminifera along the eastern Mediterranean (e.g., studies monitoring the effects of anthropogenic activity or climate change on coastal ecosystem health).

3.5.3 Implications for sediment transport and site formation

Based on the distribution pattern of *P. calcariformata* observed here, alternative applications of epiphytic foraminifera along high energy sandy shoreface settings could include long-term studies on sediment dynamics (e.g., tracking sediment transport in and around coastal structures, the extent of onshore-offshore sand movement, tracking the extent of the storm weather wave base over time, etc.). Understanding sediment dynamics is important for coast engineering projects (Leys & Mulligan, 2011). Fluorescent tracers are often used to assess onshore-offshore sediment transport and sediment accumulation patterns around marinas; however, these methods only provide data spanning several months (Klein et al., 2007). Because the main source of *P. calcariformata* in high energy sandy shoreface settings is the submerged surface of harbour structures (anthropogenic hard grounds), these microfossils can provide long-term data on onshore-offshore transport trends, sediment accumulation patterns around the harbor itself, and on longshore transport patterns along the coast. This could enhance studies using fluorescent tracers as it provides more long-term information.

Sediment reworking (vertical movement) during storms and tsunamis plays a major role in the stratigraphic distribution of *P. calcariformata*. As discussed in Reinhardt & Raban (2016), the sands within the active sediment layer are regularly reworked. Storms and tsunami waves often cause scour and erosion of the seabed as well as removal of fine sand particles from around larger, heavier, rubble material. This results in vertical transport of the rubble material downwards, producing an “armoured” layer that resists further erosion (Reinhardt & Raban, 2016). Foraminifera and larger sand particles within the active sediment layer would be reworked through this winnowing action as well, with larger storms having a greater effect on transport, especially closer to shore. This mechanism of sediment reworking would occur offshore up to the storm weather wave base, though to a lesser extent. Significant abundances of *P. calcariformata* would likely not be transported much further offshore and therefore provide recognition of the storm wave base through time. Our three cores show this trend with *P. calcariformata*, found at ∼0–30 cm at 20 m water depth (C2, ∼0–60 cm at 15 m (C1), and ∼0–150 cm at 10 m (W). This shows that shallow marine sands are being transported at least ∼2 km offshore with larger storms. The presence/absence of *P. calcariformata* provides an efficient low-cost method for determining pre- and post-harbour sediment which can be difficult to identify in these sandy high-energy settings, especially if the sands contain no material culture (e.g., pottery).

3.6 Conclusion

This study shows that anthropogenically altered coastlines, in particular hard coastal structures, leave a fingerprint on their environment not only through changed elemental composition but also biomarkers such as epiphytic foraminifera. These changes are present and recognizable in the ancient harbour context at Caesarea Maritima. There, an excavated trench area (W), two sediment cores (C1, C2), and a piece of harbour material (COF) were analyzed through elemental (μXRF, magnetic susceptibility) and/or foraminifera analyses. Heavy mineral proxies (Zr+Ti/Ca, Zr+Ti/Si, magnetic susceptibility) indicate that particulate matter offshore, originating as part of or due to the harbour structures have increased since the construction of the harbour ∼2000 years ago. Benthic foraminifera assemblages A3, and A4 reflect the shallow and mid-depth (3–40 m) sandy to sandy silt substrates that characterised much of the nearshore Israeli coast prior to harbour construction. Post-construction assemblages (e.g., A1, A2) include increasing abundances of epiphytic species, especially *P. calcariformata.* This species was successfully used as a biostratigraphic indicator for the timing of harbour construction as it is present in significant abundances only after the harbour and city are established around 2000 years ago. *P. calcariformata* was recently erroneously assumed to be a recent invasive species, increasing in population along the Israeli coast following the opening of the Suez Canal in 1869. Results from this study suggest that this species is endemic to the Israeli coast, observed here in coastal sediments pre-dating the canal opening by thousands of years. The recent attention on this species as a marker of changing environments and climate, suggested due to its current proliferation along the coastline and heat tolerance, is not an error and is worthy of continued study. We add here, in agreement, that it is a harbinger of anthropogenic change and thrives on the increased coarsening and hardening of the coastline and shallow shelf, outcomes of post-Aswan Dam decreases in the delivery of fine sediments (Kalman et al., 2022), coastal armouring, and general development.

This study demonstrates that the analysis of epiphytic foraminifera, such as *P. calcariformata*, can be implemented as rapid and cost-effective biostratigraphic indicators in future geoarchaeological studies at Caesarea or in similar settings elsewhere. The results have implications for the role of *P. calcariformata* in modern studies of benthic foraminifera on the eastern Mediterranean, mainly that it is not a recent invader, but rather a species that has thrived on the changing substrate conditions created by human activity for millennia.

Acknowledgments

Funding: This work was financially supported by the Natural Sciences and Engineering Research Council of Canada Discovery Grant (EGR—RGPIN-2020-06861) and the Canadian Foundation for Innovation (EGR—105-04523). Support for this research was also provided by N. Krischer and by A. Weil of EcoOcean and the Mediterranean Explorer. We also thank D. Schafer, M. Artzy, S. Breitstein, A. Yurman, Y. Turkaspa, and the staff at the Recanati Institute for Maritime Studies. The funding sources were not involved in study design; in the collection, analysis, and interpretation of data; in the writing of the report; or in the decision to submit the article for publication.

Data availability

Data is available in supplementary material.

References

Aiello, G., Amato, V., Barra, D., Caporaso, L., Caruso, T., Giaccio, B., Parisi, R., & Rossi, A. (2020). Late Quaternary benthic foraminiferal and ostracod response to palaeoenvironmental changes in a Mediterranean coastal area, Port of Salerno, Tyrrhenian Sea. Reg. Stud. Mar. Sci., 40, 101498. https://doi.org/10.1016/j.rsma.2020.101498.

Almagor, G., Gill, D., & Perath, I. (2000). Marine Sand Resources Offshore Israel. Mar. Georesources Geotechnol., 18(1), 1–42. https://doi.org/10.1080/10641190009353781.

Amato, V., Aiello, G., Barra, D., Caporaso, L., Caruso, T., Giaccio, B., Parisi, R., & Rossi, A. (2020). Holocene paleogeographic evolution of an ancient port city of the central Mediterranean area: Natural and anthropogenic modifications from Salerno city, southern Italy. Geoarchaeology, 35(3), 366–383. https://doi.org/10.1002/gea.21774.

Arieli, R. N., Almogi-Labin, A., Abramovich, S., & Herut, B. (2011). The effect of thermal pollution on benthic foraminiferal assemblages in the Mediterranean shoreface adjacent to Hadera power plant (Israel). Mar. Pollut. Bull., 62(5), 1002–1012. https://doi.org/10.1016/j.marpolbul.2011.02.036.

Avnaim-Katav, S., Agnon, A., Sivan, D., & Almogi-Labin, A. (2016). Calcareous assemblages of the southeastern Mediterranean low-tide estuaries — Seasonal dynamics and paleo-environmental implications. J. Sea Res., 108, 30–49. https://doi.org/10.1016/j.seares.2015.12.002.

Avnaim-Katav, S., Almogi-Labin, A., Agnon, A., Porat, N., & Sivan, D. (2017). Holocene hydrological events and human induced environmental changes reflected in a southeastern Mediterranean fluvial archive. Palaeogeogr. ,Palaeoclimatol., Palaeoecol., 468, 263–275. https://doi.org/10.1016/j.palaeo.2016.12.021.

Avnaim-Katav, S., Almogi-Labin, A., Herut, B., Kanari, M., & Guy-Haim, T. (2021). Benthic foraminifera from the Southeastern Mediterranean shelf: Dead assemblages and living-dead comparisons recording consequences of Nile River damming. Mar. Micropaleontol., 164(March), 101977. https://doi.org/10.1016/j.marmicro.2021.101977.

Avnaim-Katav, S., Almogi-Labin, A., Kanari, M., & Herut, B. (2020). Living benthic foraminifera of southeastern Mediterranean ultra-oligotrophic shelf habitats: Implications for ecological studies. Estuar. Coast. Shelf Sci., 234(January), 106633. https://doi.org/10.1016/j.ecss.2020.106633.

Avnaim-Katav, S., Almogi-Labin, A., Sandler, A., & Sivan, D. (2013). Benthic foraminifera as palaeoenvironmental indicators during the last million years in the eastern Mediterranean inner shelf. Palaeogeogr. ,Palaeoclimatol., Palaeoecol., 386, 512–530. https://doi.org/10.1016/j.palaeo.2013.06.019.

Avnaim-Katav, S., Almogi-Labin, A., Schneider-Mor, A., Crouvi, O., Burke, A. A., Kremenetski, K. V., & MacDonald, G. M. (2019). A multi-proxy shallow marine record for Mid-to-Late Holocene climate variability, Thera eruptions and cultural change in the Eastern Mediterranean. Quat. Sci. Rev., 204, 133–148. https://doi.org/10.1016/j.quascirev.2018.12.001.

Avnaim-Katav, S., Hyams-Kaphzan, O., Milker, Y., & Almogi-Labin, A. (2015). Bathymetric zonation of modern shelf benthic foraminifera in the Levantine Basin, eastern Mediterranean Sea. J. Sea Res., 99, 97–106. https://doi.org/10.1016/j.seares.2015.02.006.

Avnaim-Katav, S., Milker, Y., Schmiedl, G., Sivan, D., Hyams-Kaphzan, O., Sandler, A., & Almogi-Labin, A. (2016). Impact of eustatic and tectonic processes on the southeastern Mediterranean shelf during the last one million years: Quantitative reconstructions using a foraminiferal transfer function. Mar. Geol., 376, 26–38. https://doi.org/10.1016/j.margeo.2016.03.010 Blackman, D. J. (1982a). Ancient harbours in the Mediterranean. Part 1. Int. J. Naut. Archaeol., 11(2), 79–104. https://doi.org/10.1111/j.1095-9270.1982.tb00079.x.

Blackman, D. J. (1982b). Ancient harbours in the Mediterranean. Part 2. Int. J. Naut. Archaeol., 11(3), 185–211. https://doi.org/10.1111/j.1095-9270.1982.tb00079.x.

Boenigk, W., & Neber, A. (2005). Temporal and Spatial Variations in the Heavy Mineral Spectra of Coastal Dunes Along the Israeli Coastal Plain. Journal of The Israel Prehistoric Society, 35, 19–43.

Boyce, J. I., Reinhardt, E. G., & Goodman, B. N. (2009). Magnetic detection of ship ballast deposits and anchorage sites in King Herod's Roman harbour, Caesarea Maritima, Israel. J. Archaeol. Sci., 36(7), 1516–1526. https://doi.org/10.1016/j.jas.2009.03.007.

Boyce, J. I., Reinhardt, E. G., Raban, A., & Pozza, M. R. (2004). Marine Magnetic Survey of a Submerged Roman Harbour, Caesarea Maritima, Israel. Int. J. Naut. Archaeol., 33(1), 122–136. https://doi.org/10.1111/j.1095-9270.2004.00010.x.

Brandon, C. (2008). Roman Structures in the Sea: Sebastos , the Herodian Harbor of Caesarea. Mem. Am. Acad. Rome, Supplementary Volumes, 6(The Maritime World of Ancient Rome), 245–254.

Bresler, V., & Yanko, V. (1995a). Acute toxicity of heavy metals for benthic epiphytic foraminfiera Pararotalia spinigera (Le Calvez) and influence of seaweed-derived DOC. Environ. Toxicol. and Chem., 14(10), 1687–1695.

Bresler, V., & Yanko, V. (1995b). Chemical ecology; a new approach to the study of living benthic epiphytic Foraminifera. J. Foraminiferal Res., 25(3), 267–279. https://doi.org/10.2113/gsjfr.25.3.267.

Dinis, P. A., & Soares, A. F. (2007). Stable and ultrastable heavy minerals of alluvial to nearshore marine sediments from Central Portugal: Facies related trends. Sediment. Geol., 201(1–2), 1–20. https://doi.org/10.1016/j.sedgeo.2007.04.004.

Emery, K. O., & Neev, D. (1960). Mediterranean beaches of Israel. In Isr. Geol. Surv. Bull. 26.

Finkler, C., Fischer, P., Baika, K., Rigakou, D., Metallinou, G., Hadler, H., & Vött, A. (2018). Tracing the Alkinoos Harbor of ancient Kerkyra, Greece, and reconstructing its paleotsunami history. Geoarchaeology, 33(1), 24–42. https://doi.org/10.1002/gea.21609.

Galili, E., Salamon, A., Gambash, G., & Zviely, D. (2021). Archaeological and Natural Indicators of Sea-Level and Coastal Changes: The Case Study of the Caesarea Roman Harbor. Geosciences, 11(8), 306. https://doi.org/10.3390/geosciences11080306.

Goldsmith, S. ., Krom, M. ., Sandler, A., & Herut, B. (2001). Spatial trends in the chemical composition of sediments on the continental shelf and slope off the Mediterranean coast of Israel. Cont. Shelf Res., 21(16–17), 1879–1900. https://doi.org/10.1016/S0278-4343(01)00027-9.

Goldsmith, V., & Golik, A. (1980). Sediment transport model of the southeastern Mediterranean coast. Mar. Geol., 37(1–2), 147–175. https://doi.org/10.1016/0025-3227(80)90015-8.

Golik, A. (1993). Indirect evidence for sediment transport on the continental shelf off Israel. Geo-Mar. Lett., 13(3), 159–164. https://doi.org/10.1007/BF01593189.

Golik, A. (1997). Dynamics and management of sand along the Israeli coastline by. CIESM, Sci. Ser. 3, 18(Transformations and evolution of the Mediterranean coastline), 97–110.

Goodman-Tchernov, B. N., & Austin, J. A. (2015). Deterioration of Israel's Caesarea Maritima's ancient harbor linked to repeated tsunami events identified in geophysical mapping of offshore stratigraphy. J. Archaeol. Sci.: Rep., 3, 444–454. https://doi.org/10.1016/j.jasrep.2015.06.032.

Goodman-Tchernov, B. N., Dey, H. W., Reinhardt, E. G., McCoy, F., & Mart, Y. (2009). Tsunami waves generated by the Santorini eruption reached Eastern Mediterranean shores. Geology, 37(10), 943–946. https://doi.org/10.1130/G25704A.1.

Goodman, B. N., Reinhardt, E. G., Dey, H. W., Boyce, J. I., Schwarcz, H. P., Sahoğlu, V., Erkanal, H., & Artzy, M. (2009). Multi-proxy geoarchaeological study redefines understanding of the paleocoastlines and ancient harbours of Liman Tepe (Iskele, Turkey). Terra Nova, 21(2), 97–104. https://doi.org/10.1111/j.1365-3121.2008.00861.x.

Gregory, B. R. B., Reinhardt, E. G., Macumber, A. L., Nasser, N. A., Patterson, R. T., Kovacs, S. E., & Galloway, J. M. (2017). Sequential sample reservoirs for Itrax-XRF analysis of discrete samples. J. Paleolimnol., 57(3), 287–293. https://doi.org/10.1007/s10933-017-9944-4.

Hasan, A. S. M. M., Hossain, I., Rahman, M. A., Zaman, M. N., Biswas, P. K., & Alam, M. S. (2022). Chemistry and mineralogy of Zr- and Ti-rich minerals sourced from Cox's Bazar beach placer deposits, Bangladesh: Implication of resources processing and evaluation. Ore Geol. Rev., 141, 104687. https://doi.org/10.1016/j.oregeorev.2021.104687.

Hohlfelder, R. L. (2000). Anastasius I, Mud, and Foraminifera: Conflicting Views of Caesarea Maritima's Harbor in Late Antiquity. Bull. Am. Schools Orient. Res., 317(317), 41–62. https://doi.org/10.2307/1357483.

Hohlfelder, R. L., Brandon, C., & Oleson, J. P. (2007). Constructing the Harbour of Caesarea Palaestina, Israel: New Evidence From the ROMACONS Field Campaign of October 2005. Int. J. Naut. Archaeol., 36(2), 409–415. https://doi.org/10.1111/j.1095-9270.2007.00156.x.

Holbourn, A., Henderson, A. S., & MacLeod, N. (2013). Atlas of Benthic Foraminifera. In Atlas of Benthic Foraminifera. Wiley. https://doi.org/10.1002/9781118452493.

Hou, B., Keeling, J., & Van Gosen, B. S. (2017). Geological and Exploration Models of Beach Placer Deposits, Integrated from Case-Studies of Southern Australia. Ore Geol. Rev., 80, 437–459. https://doi.org/10.1016/j.oregeorev.2016.07.016.

Hyams-Kaphzan, O., Almogi-Labin, A., Benjamini, C., & Herut, B. (2009). Natural oligotrophy vs. pollution-induced eutrophy on the SE Mediterranean shallow shelf (Israel): Environmental parameters and benthic foraminifera. Mar. Pollut. Bull., 58(12), 1888–1902. https://doi.org/10.1016/j.marpolbul.2009.07.010.

Hyams-Kaphzan, O., Almogi-Labin, A., Sivan, D., & Benjamini, C. (2008). Benthic foraminifera assemblage change along the southeastern Mediterranean inner shelf due to fall-off of Nile-derived siliciclastics. Neues Jahrbuch Für Geologie Und Paläontologie - Abhandlungen, 248(3), 315–344. https://doi.org/10.1127/0077-7749/2008/0248-0315.

Hyams-Kaphzan, O., Grossowicz, L. P., & Almogi-Labin, A. (2014). Characteristics of benthic foraminifera inhabiting rocky reefs in northern Israeli Mediterranean shelf. In GSI Report ES-20-14: Vol. 36/2014.

Inman, D. L., & Jenkins, S. A. (1984). The Nile Littoral Cell and Man's Impact on the Coastal Zone of the Southeastern Mediterranean. Coast. Eng. Proc., 1(19), 109. https://doi.org/10.9753/icce.v19.109.

Kalman, A., Goodman-Tchernov, B., Hill, P., Everhardt, C., Mathalon, A., & Katz, T. (2022). Anthropogenic changes in waterways produce "drought-like" layers in shelf sediments. Elem. Sci. Anth., 10(1), 1–19. https://doi.org/10.1525/elementa.2021.00039.

Klein, M., Zviely, D., Kit, E., & Shteinman, B. (2007). Sediment Transport along the Coast of Israel: Examination of Fluorescent Sand Tracers. J. Coast. Res., 236(6), 1462–1470. https://doi.org/10.2112/05-0488.1.

Kohonen, T. (2013). Essentials of the self-organizing map. Neural Netw., 37, 52–65. https://doi.org/10.1016/j.neunet.2012.09.018.

Konfirst, M. A., Kuhn, G., Monien, D., & Scherer, R. P. (2011). Correlation of Early Pliocene diatomite to low amplitude Milankovitch cycles in the ANDRILL AND-1B drill core. Mar. Micropaleontol., 80(3–4), 114–124. https://doi.org/10.1016/j.marmicro.2011.06.005.

Langer, M. R. (1993). Epiphytic foraminifera. Mar. Micropaleontol., 20(3–4), 235–265. https://doi.org/10.1016/0377-8398(93)90035-V.

Leys, V., & Mulligan P., R. (2011). Modelling Coastal Sediment Transport for Harbour Planning: Selected Case Studies. In Sediment Transport (Issue 1). InTech. https://doi.org/10.5772/15007.

Lin, I. J., Rohrlich, V., & Slatkine, A. (1974). Surface microtextures of heavy mineralsfrom the Mediterranean coast of Israel. J. Sediment. Petrol., 44(4), 1281–1295.

Marriner, N., & Morhange, C. (2006). The 'Ancient Harbour Parasequence': Anthropogenic forcing of the stratigraphic highstand record. Sediment. Geol., 186(1–2), 13–17. https://doi.org/10.1016/j.sedgeo.2005.12.001.

Marriner, N., & Morhange, C. (2007). Geoscience of ancient Mediterranean harbours. Earth-Sci. Rev., 80(3–4), 137–194. https://doi.org/10.1016/j.earscirev.2006.10.003.

Marriner, N., Morhange, C., Boudagher-Fadel, M., Bourcier, M., & Carbonel, P. (2005). Geoarchaeology of Tyre's ancient northern harbour, Phoenicia. J. Archaeol. Sci., 32(9), 1302–1327. https://doi.org/10.1016/j.jas.2005.03.019.

Marsh, R., Mills, R. A., Green, D. R. H., Salter, I., & Taylor, S. (2007). Controls on sediment geochemistry in the Crozet region. Deep Sea Research Part II: Topical Studies in Oceanography, 54(18–20), 2260–2274. https://doi.org/10.1016/j.dsr2.2007.06.004.

Marshall, J. F., & McCulloch, M. T. (2002). An assessment of the Sr/Ca ratio in shallow water hermatypic corals as a proxy for sea surface temperature. Geochim. Cosmochim. Acta, 66(18), 3263–3280. https://doi.org/10.1016/S0016-7037(02)00926-2.

McGowran, B. (2009). The biostratigraphy of fossil microplankton. In Biostratigraphy (pp. 19–46). Cambridge University Press. https://doi.org/10.1017/CBO9780511610653.003.

Murray, J. W. (2014). Ecology and Palaeoecology of Benthic Foraminifera. Routledge. https://doi.org/10.4324/9781315846101.

Nir, Y. (1984). Recent sediments of the Israeli Mediterranean continental shelf and slope. University of Goteburg, Sweden.

Oleson, J. P. (1988). The technology of Roman harbours. Int. J. Naut. Archaeol., 17(2), 147–157. https://doi.org/10.1111/j.1095-9270.1988.tb00635.x.

Olteanu, M., & Villa-Vialaneix, N. (2015). On-line relational and multiple relational SOM. Neurocomputing, 147(1), 15–30. https://doi.org/10.1016/j.neucom.2013.11.047.

Patterson, R. T., & Fishbein, A. (1989). Re-examination of the statistical methods used to determine the number of point counts needed for micropaleontological quantitative research. J.Paleontol., 63, 245–248.

Pint, A., Seeliger, M., Frenzel, P., Feuser, S., Erkul, E., Berndt, C., Klein, C., Pirson, F., & Brückner, H. (2015). The environs of Elaia's ancient open harbour – a reconstruction based on microfaunal evidence. J. Archaeol. Sci., 54, 340–355. https://doi.org/10.1016/j.jas.2014.06.011.

Pomerancblum, M. (1966). The distributionof heavy minerals and their hydraulic equivalents in sediments of the Mediterranean continental shelf of Israel. J. Sediment. Petrol., 36(1), 162–174.

Quick, M. C. (1991). Onshore-offshore sediment transport on beaches. Coastal Engineering, 15(4), 313–332. https://doi.org/10.1016/0378-3839(91)90014-8.

Raban, A. (1992). Sebastos: the royal harbour at Caesarea Maritima-a short-lived giant. Int. J. Naut. Archaeol., 21(2), 111–124. https://doi.org/10.1111/j.1095-9270.1992.tb00353.x.

Raban, A. (1996). The Inner Harbor Basin of Caesarea: Archaeological Evidence for its Gradual Demise. In A. Raban & K. G. Holum (Eds.), Caesarea Maritima: A Retrospective after Two Millenia (pp. 628–666). Documenta et Monumenta Orientis Antiqui 21. Leiden: Brill.

Ramette, A. (2007). Multivariate analyses in microbial ecology. FEMS Microbiology Ecology, 62(2), 142–160. https://doi.org/10.1111/j.1574-6941.2007.00375.x.

Reinhardt, E. G., Fitton, R. J., & Schwarcz, H. P. (2003). ISOTOPIC (Sr, O, C) INDICATORS OF SALINITY AND TAPHONOMY IN MARGINAL MARINE SYSTEMS. J. Foraminiferal Res., 33(3), 262–272. https://doi.org/10.2113/33.3.262.

Reinhardt, E. G., Goodman, B. N., Boyce, J. I., Lopez, G., van Hengstum, P., Rink, W. J., Mart, Y., & Raban, A. (2006). The tsunami of 13 December A.D. 115 and the destruction of Herod the Great's harbor at Caesarea Maritima, Israel. Geology, 34(12), 1061. https://doi.org/10.1130/G22780A.1.

Reinhardt, E. G., Patterson, R. T., & Schroeder-Adams, C. J. (1994). Geoarchaeology of the ancient harbor site of Caesarea Maritima, Israel; evidence from sedimentology and paleoecology of benthic foraminifera. J. Foraminiferal Res., 24(1), 37–48. https://doi.org/10.2113/gsjfr.24.1.37.

Reinhardt, E. G., & Raban, A. (1999). Destruction of Herod the Great's harbor at Caesarea Maritima, Israel—Geoarchaeological evidence. Geology, 27(9), 811. https://doi.org/10.1130/0091-7613(1999)027<0811:DOHTGS>2.3.CO;2.

Reinhardt, E. G., & Raban, A. (2016). Site formation and stratigraphic development of Caesarea's ancient harbor. In G. Holum, Kenneth, A. Stabler, Jennifer, & E. G. Reinhardt (Eds.), Caesarea Reports and Studies: Excavations 1995–2007 within the Old City and the Ancient Harbor (pp. 155–181). BAR Publishing.

Reinhardt, E. G., Raban, A., & Goodman, B. (2001). Caesarea Harbor Excavations - 2001 Season Report.

Riddick, N. L., Boyce, J. I., Krezoski, G. M., Şahoğlu, V., Erkanal, H., Tuğcu, İ., Alkan, Y., Gabriel, J. J., Reinhardt, E. G., & Goodman-Tchernov, B. N. (2022a). Palaeoshoreline reconstruction and underwater archaeological potential of Liman Tepe: A long-occupied coastal prehistoric settlement in western Anatolia, Turkey. Quat. Sci. Rev., 276, 107293. https://doi.org/10.1016/j.quascirev.2021.107293.

Riddick, N. L., Boyce, J. I., Reinhardt, E. G., Rothaus, R. M., Chomicki, K. M., & McCarthy, F. M. G. (2021). Multi-proxy palaeoenvironmental record of coastal tectonic uplift and abandonment (ca. 6th c. CE) of Lechaion's inner harbour, ancient Corinth, Greece. Quat. Sci. Rev., 267, 107080. https://doi.org/10.1016/j.quascirev.2021.107080.

Riddick, N. L., Boyce, J. I., Şahoğlu, V., Erkanal, H., Tuğcu, İ., Alkan, Y., Reinhardt, E. G., & Goodman-Tchernov, B. N. (2022b). Coastal palaeoenvironmental record of Late Bronze to Iron Age harbour development at Liman Tepe-Clazomenae, western Anatolia, Turkey. Mar. Geol., 450(June), 106842. https://doi.org/10.1016/j.margeo.2022.106842.

Ronen, A. (2018). Quaternary sedimentology and prehistory on the Mediterranean coastal plain of Israel. Quat. Int., 464, 315–326. https://doi.org/10.1016/j.quaint.2017.10.027.

Rothwell, R. G., & Croudace, I. W. (2015). Twenty Years of XRF Core Scanning Marine Sediments: What Do Geochemical Proxies Tell Us? In I. W. Croudace & R. G. Rothwell (Eds.), Micro-XRF Studies of Sediment Cores: Applications of a Non-destructive Tool for the Environmental Sciences (Vol. 17, pp. 25–102). Springer Netherlands. https://doi.org/10.1007/978-94-017-9849-5.

Salomon, F., Keay, S., Carayon, N., & Goiran, J.-P. (2016). The Development and Characteristics of Ancient Harbours—Applying the PADM Chart to the Case

Studies of Ostia and Portus. PLOS ONE, 11(9), e0162587. https://doi.org/10.1371/journal.pone.0162587.

Sandler, A., & Herut, B. (2000). Composition of clays along the continental shelf off Israel: contribution of the Nile versus local sources. Mar. Geol., 167(3–4), 339–354. https://doi.org/10.1016/S0025-3227(00)00021-9.

Schattner, U., Gurevich, M., Kanari, M., & Lazar, M. (2015). Levant jet system—effect of post LGM seafloor currents on Nile sediment transport in the eastern Mediterranean. Sediment. Geol., 329, 28–39. https://doi.org/10.1016/j.sedgeo.2015.09.007.

Schmidt, C., Morard, R., Almogi-Labin, A., Weinmann, A. E., Titelboim, D., Abramovich, S., & Kucera, M. (2015). Recent Invasion of the Symbiont-Bearing Foraminifera Pararotalia into the Eastern Mediterranean Facilitated by the Ongoing Warming Trend. PLOS ONE, 10(8), e0132917. https://doi.org/10.1371/journal.pone.0132917.

Schmidt, C., Morard, R., Romero, O., & Kucera, M. (2018). Diverse Internal Symbiont Community in the Endosymbiotic Foraminifera Pararotalia calcariformata: Implications for Symbiont Shuffling Under Thermal Stress. Front. Microbiol., 9(SEP), 1–11. https://doi.org/10.3389/fmicb.2018.02018.

Schmidt, C., Titelboim, D., Brandt, J., Herut, B., Abramovich, S., Almogi-Labin, A., & Kucera, M. (2016). Extremely heat tolerant photo-symbiosis in a shallow marine benthic foraminifera. Sci. Rep., 6(1), 30930. https://doi.org/10.1038/srep30930.

Scott, D. B., Medioli, F. S., & Schafer, C. T. (2001). Chapter 2: Methodological Considerations. In Monitoring in Coastal Environments Using Foraminifera and Thecamoebian Indicators (pp. 10–27). Cambridge University Press. https://doi.org/10.1017/CBO9780511546020.

Stanley, D. J. (1989). Sediment transport on the coast and shelf between the Nile delta and Israeli margin as determined by heavy minerals. J. Coast. Res., 5(4), 813–828.

Stock, F., Knipping, M., Pint, A., Ladstätter, S., Delile, H., Heiss, A. G., Laermanns, H., Mitchell, P. D., Ployer, R., Steskal, M., Thanheiser, U., Urz, R., Wennrich, V., & Brückner, H. (2016). Human impact on Holocene sediment dynamics in the Eastern Mediterranean - the example of the Roman harbour of Ephesus. Earth Surf. Process. Landf., 41(7), 980–996. https://doi.org/10.1002/esp.3914.

Stock, F., Pint, A., Horejs, B., Ladstätter, S., & Brückner, H. (2013). In search of the harbours: New evidence of Late Roman and Byzantine harbours of Ephesus. Quat. Int., 312, 57–69. https://doi.org/10.1016/j.quaint.2013.03.002.

Suzuki, R., Terada, Y., & Shimodaira, H. (2022). Hierarchical Clustering with P-Values via Multiscale Bootstrap Resampling (p. 14). CRAN.

Titelboim, D., Almogi-Labin, A., Herut, B., Kucera, M., Schmidt, C., Hyams-Kaphzan, O., Ovadia, O., & Abramovich, S. (2016). Selective responses of benthic foraminifera to thermal pollution. Mar. Pollut. Bull., 105(1), 324–336. https://doi.org/10.1016/j.marpolbul.2016.02.002.

Titelboim, D., Sadekov, A., Almogi-Labin, A., Herut, B., Kucera, M., Schmidt, C., Hyams-Kaphzan, O., & Abramovich, S. (2017). Geochemical signatures of benthic foraminiferal shells from a heat-polluted shallow marine environment provide field evidence for growth and calcification under extreme warmth. Glob. Chang. Biol., 23(10), 4346–4353. https://doi.org/10.1111/gcb.13729.

Vola, G., Gotti, E., Brandon, C., Oleson, J. P., & Hohlfelder, R. L. (2011). Chemical, mineralogical and petrographic characterization of Roman ancient hydraulic concretes cores from Santa Liberata, Italy, and Caesarea Palestinae, Israel. Period. Di Mineral., 80(2), 317–338. https://doi.org/10.2451/2011PM0023.

Votruba, G. F. (2007). Imported Building Materials of Sebastos Harbour, Israel. Int. J. Naut. Archaeol., 36(2), 325–335. https://doi.org/10.1111/j.1095-9270.2007.00152.x.

Ward, J. H. (1963). Hierarchical Grouping to Optimize an Objective Function. J. Am. Stat. Assoc., 58(301), 236–244. https://doi.org/10.1080/01621459.1963.10500845.

Wasserman, R. (Irena). (2021). Deterioration of Sandstone in the Historical and Contemporary Sea Walls upon the Impact of the Natural and Man-Made Hazards. Appl. Sci., 11(15), 6892. https://doi.org/10.3390/app11156892.

Westerhold, T., Röhl, U., McCarren, H. K., & Zachos, J. C. (2009). Latest on the absolute age of the Paleocene–Eocene Thermal Maximum (PETM): New insights from exact stratigraphic position of key ash layers + 19 and - 17. Earth Planet. Sci. Lett., 287(3–4), 412–419. https://doi.org/10.1016/j.epsl.2009.08.027.

Yanko, V., Kronfeld, J., & Flexer, A. (1994). Response of benthic Foraminifera to various pollution sources; implications for pollution monitoring. J. Foraminiferal Res., 24(1), 1–17. https://doi.org/10.2113/gsjfr.24.1.1.

Zenetos, A., Gofas, S., Morri, C., Rosso, A., Violanti, D., Garcia Raso, J. E., Cinar, M. E., Almogi-Labin, A., Ates, A. S., Azzurro, E., Ballesteros, E., Bianchi, C. N., Bilecenoglu, M., Gambi, M. C., Giangrande, A., Gravili, C., Hyams-Kaphzan, O., Karachile, P. K., Katsanevakis, S., . . . Veriaque, M. (2012). Alien species in the Mediterranean Sea by 2012. A contribution to the application of European Union's Marine Strategy Framework Directive (MSFD). Part 2. Introduction trends and pathways. Mediterr. Mar. Sci., 13(2), 328. https://doi.org/10.12681/mms.327.

Zviely, D., Kit, E., & Klein, M. (2007). Longshore sand transport estimates along the Mediterranean coast of Israel in the Holocene. Mar. Geol., 238(1–4), 61–73. https://doi.org/10.1016/j.margeo.2006.12.003.

Chapter 4

Closure of Khor Al Balid and Khor Rori with coastal uplift and aridity in the 12th – 15th c. CE and evidence for an extreme overwash event in 18th – 19th c. CE: implications for ancient port sites in southern Oman

This chapter is a manuscript that has been prepared for submission to a peer-reviewed journal:

Steele, R.E., Reinhardt, E.G., Boyce, J., Gabriel, J.J., Vosmer, T. (to be submitted) Closure of Khor Al Balid and Khor Rori with coastal uplift and aridity in the 12th – 15th c. CE and evidence for an extreme overwash event in 18th – 19th c. CE: implications for ancient port sites in southern Oman. In preparation for submission to a peer-reviewed journal.

Closure of Khor Al Balid and Khor Rori with coastal uplift and aridity in the 12th – 15th c. CE and evidence for an extreme overwash event in 18th – 19th c. CE: implications for ancient port sites in southern Oman

Riley E. Steele[a*], Eduard G. Reinhardt[a], Joe Boyce[a], Jeremy J. Gabriel, Tom Vosmer[b]

[a] *School of Earth, Environment, and Society, McMaster University, 1280 Main St. W, Hamilton, Ontario, L8S 4L8, CA*
[b] *School of Social Sciences, University of Western Australia, (M257), 35 Stirling Highway, 6009 Perth, AU*
[*] *Corresponding author: steelr3@mcmaster.ca*

Abstract

Ancient maritime trading ports along the southern coast of Oman have been the target of archaeological excavations for several decades. Though historical chronologies are well-researched, information from a paleoenvironmental perspective is lacking and can provide a more complete understanding of site development. This study investigates the timing of coastal sand barrier accumulation in the natural harbours at Khor Al Balid and Khor Rori, which had considerable effects on the populations at the ancient cities of al–Balīd and Sumhuram. Six cores from Khor Al Balid and four cores from Khor Rori were analyzed using sedimentological, microfossil (foraminifera and testate amoebae), geochemical (μXRF), and radiocarbon dating methods. Marine proxies (e.g., *Amphistegina* spp., *C. pseudolobatulus*, *E. lebatum*, Sr, Ca/Si) and lagoon proxies (e.g., *T. macrescens*, *T. inflata*, *C. constricta* and *C. aculeata*, Ti/Ca, Fe/Ca) were used to identify Marine Sand, Brackish Lagoon/Marsh, and Freshwater facies. Results indicate that the eastern arm of Khor Al Balid closed off from the sea around the 12th century CE and that the western arm closed around the 15th century CE. Siltation of harbours and the formation of sand barriers may have contributed towards site abandonment. Previous archaeological findings suggest that al-Balīd was able to continue with maritime trade activities along the southern seaside edge of the city for several centuries after siltation of Khor Al Balid, possibly with the help of dredging. An extreme overwash event was recorded in almost all cores across both sampling sites, suggesting that a very large cyclone or a tsunami hit the southern Oman coast sometime around the 18th–19th century CE. This event, as well as

continuous coastal sand accumulation, may have contributed to the decline and abandonment of Khor Al Balid and highlights the impacts that large storm/wave events have on archaeological site preservation.

Keywords: *Khor Al Balid, al–Balīd, Khor Rori, foraminifera, testate amoebae, μXRF, Coastal geomorphology, Lagoon development, Geoarchaeology*

4.1 Introduction

Over seven decades of archaeological work on the ancient port sites at Khor Al Balid and Khor Rori have revealed information on major periods of site occupation and aspects on international trade in the region; however, there remain questions about the foundation, development, and decline of the settlements (D'Andrea et al., 2021). The ancient port city at Khor Rori, known as Sumhuram, is located ~1 km inland at the edge of the Wadi Darbat-fed estuary and was an important trade outpost for frankincense (Cremaschi & Negrino, 2002; Degli Esposti & Pavan, 2020). The city was first occupied during the 3rd century BCE and was abandoned during the 5th century CE. Archeological investigations have revealed information on site layout and activities including two "Monumental Buildings", several smaller buildings, and areas for metalworking, dyeing, storage, and residences (Degli Esposti & Pavan, 2020; Ribechini et al., 2016). The abandonment of the city is thought to be linked to environmental factors, specifically the accumulation of a sand barrier at the mouth of the estuary (Hoorn & Cremaschi, 2004), first proposed by Reinhardt (2000).

Following the abandonment of Sumhuram, a nearby port city at Khor Al Balid was established during the 10th century CE (or as early as the 6th century CE; Newton & Zarins, 2014). The ancient city, known as Zafār during early occupation, became an important center for international trade and export of horses, incense, and sardines (Costa, 1979; D'Andrea, 2021; Fusaro, 2020; Zarins, 2007). The site, a roughly rectangular shape spanning ~64 ha, reached peak maritime trade activity between the 13th to 15th centuries and was abandoned during the 18th century (D'Andrea, 2021; Pavan & Visconti, 2023). Archaeological excavations at Al Balid since the 1950's have involved several different teams of researchers focused on specific areas and landmarks over the years (e.g., the citadel, great mosque, city-wall, gates, towers, etc.; see D'Andrea (2021) for a detailed summary). The western side of the city contains important buildings (i.e., the citadel or husn, the Grand Mosque) as well as evidence of a bridge or causeway, suggesting that the northern arm of the lagoon was extended into an artificial channel on the western side of the city and that the city was surrounded on all sides by water (Costa, 1979; D'Andrea, 2021; Pavan & Visconti, 2023). The central area of the city contains evidence of houses and mosques, while the eastern side of the city was likely used for stocking, loading, and unloading trade items (Connan et al., 2023; Pavan & Visconti, 2023). The main city was fortified by a wall, with several towers, and excavation along the seaside (southern) wall indicate the presence of 17 towers, five gates, and four jetties that were part of early construction phases (D'Andrea, 2021). Five main phases of construction in the city between 450 CE and 1700 CE have been proposed, based on building materials, masonry techniques, pottery, and other small finds (D'Andrea, 2021; Fusaro, 2019; Lischi et al., 2020; Newton & Zarins, 2014; Pavan & Al Kathiri, 2021; Zarins, 2007). The documented decline of the city during the 16th and 17th centuries is thought to have been caused by combination of political, economic, military, and environmental factors (Costa, 1979; Hoorn & Cremaschi, 2004; Newton & Zarins, 2019; Pavan & Visconti, 2023; Zarins, 2007). Invasions by the Portuguese and Turks, as well as bans on horse, incense, and sardine trading, had a major impact on harbor activity (Newton & Zarins, 2019). Climate and weather events, and siltation of the lagoon are thought to have contributed to the city's decline (D'Andrea, 2021; Hoorn & Cremaschi, 2004), but the paleoenvironmental setting of the site has not been extensively documented.

The site's chronology has been well studied through a historical perspective; however, information from a paleoenvironmental perspective is limited and hiders a full understanding of the site's history (D'Andrea, 2021; Newton & Zarins, 2019). A paleoenvironmental study focusing on pollen changes at Khor Al Balid and Khor Rori indicate that the estuaries were open to the Arabian Sea between ∼750–390 BCE and 270–420 CE, when wetter climate conditions may have resulted in increased runoff of freshwater from the Oman mountains into the khors (Hoorn &

Cremaschi, 2004). After ∼270–420 CE, the authors suggest that more arid conditions prevailed, and that the estuaries became increasingly blocked by sand barriers due to lower input of freshwater runoff (Hoorn & Cremaschi, 2004). Another pollen study at Khor Rori indicates that the shift to reduced freshwater habitats was not continuous (i.e., conditions alternated between wet/dry during a general trend of increasing aridity; Lippi et al., 2011). Paleoenvironmental data for the region is limited, and there is no available date associated with the accumulation of sand barriers and the closure of estuaries at Khor Al Balid and Khor Rori, which may have important implications for the development and decline of the regions' ancient port sites. Here we present new results which indicate that changing morphology of the coastline may have contributed to or caused the abandonment of the sites.

4.1.1 Regional sea-level and climate trends

Changes in sea-level throughout the Holocene have influenced the coastal landscapes of the Arabian Peninsula (Zerboni et al., 2020). Sea level data for Oman is relatively scarce, in part due to limited reference water levels and to differential movement of the lithosphere (Decker et al., 2020). The current global rate of eustatic sea level rise is 3.1 mm/year (Cazenave, 2018; Dieng et al., 2017), though differential uplift/subsidence rates due to glacial isostatic adjustment and tectonics affect Regional Sea Level (RSL) along the Oman coast (Khanna et al., 2021). Khanna et al. (2021) constructed RSL curves for several zones around the Arabian Peninsula spanning the mid-Holocene to the present, taking into account eustatic, isostatic, and tectonic factors within each coastal zone. Their study suggests that transgression occurred along the majority of the Arabian Peninsula shorelines during the mid-Holocene (7.5 and 6.5 ka BP). In the southeastern zone, including the Dhofar region, there was a continuous sea level highstand until a few hundred years ago, with levels ∼3 m above present ∼3–5 ka BP and levels ∼1 m above present ∼1 ka PB (Khanna et al., 2021). This zone is currently affected by eustacy and glacial isostatic adjustment (Milne & Mitrovica, 2008) and has shown little to no signs of tectonic uplift or subsidence since the mid-Holocene (Hoffmann et al., 2013c). This contrasts with most other zones, which are affected by tectonic uplift (e.g., 0.15 mm/year and 0.68 mm/year near the Gulf of Aqaba and the Red

Sea, up to 1 mm/year along the eastern coasts of Oman; (Khanna et al., 2021; Lambeck et al., 2011; Moraetis et al., 2018).

Landscape changes along the southern coast of Oman have also been driven by changes in climate. The climate of the Dhofar region is predominantly affected by the Indian Ocean monsoon, the African summer monsoon, and the location of the Intertropical Convergence Zone (ITCZ; (Woor et al., 2022; Zerboni et al., 2020). Because paleoclimate data for southwestern Oman is limited, records from the wider Arabian Peninsula region as well as East and North Africa have been used to help infer changing conditions in Dhofar throughout the Holocene (Decker et al., 2020; Hoorn & Cremaschi, 2004; Zerboni et al., 2020). Generally, records from the early to middle Holocene (∼8000–6000 BCE) indicate a period of increased humidity/rainfall in the Arabian region related to monsoon strength and/or a northward displacement of the ITCZ (Cremaschi et al., 2015; Cremaschi & Negrino, 2005; Fleitmann et al., 2003, 2007; Lézine et al., 2010; Zerboni et al., 2020). From the Middle to Late Holocene (i.e., ∼6000 BCE to present), there is evidence of increasing aridity and a continuous decrease in monsoon precipitation associated with a southward migration of the ITCZ and decreased summer insolation (Burns et al., 1998; Cremaschi et al., 2015; Fleitmann et al., 2003, 2007). During the general trend of declining precipitation throughout the late Holocene, climate records indicate fluctuating conditions. The northeastern Arabian Sea records high summer monsoon activity between 3050–1950 BCE transitioning into more arid conditions until ∼50–250 BCE and back to increased monsoon precipitation between 50 BCE–450 CE (Lückge et al., 2001). Wet conditions between 2050–1550 BCE, 550 BCE–450 CE and 950–990 CE were also recorded in Ethiopia (Gasse & Van Campo, 1994; Machado et al., 1998) and Mount Kenya (∼350 BCE–450 CE; (Rietti-shati et al., 1998). Wider global trends of wetter conditions during the Medieval Warm Period that transition into a drier environment throughout the Little Ice Age (∼1310–1660 CE) were also recorded in Southern Oman (Fleitmann et al., 2004). Following these time periods, relatively higher rainfall periods were recorded between 1660–1760 CE and 1800–1950 CE, with drier intervening periods (Fleitmann et al., 2004). Recent reduction of precipitation has been observed through the increased erosion, reduced vegetation cover (e.g., mangrove forests; Lézine et al., 2002), and inactive speleothems within the Jebel Qara (Cremaschi & Negrino, 2005). These trends in climate are also thought to have led to increased sediment accumulation in estuaries along the southern coast, through reduced outflow from wadi systems (Hoorn & Cremaschi, 2004).

4.1.2 The use of testate amoebae and foraminifera in harbour studies

Testate amoebae and foraminifera are well-established paleoenvironmental proxies, as they are abundant in aquatic environments, preserve well in the sediment record over time, and respond rapidly to environmental change (Charman et al., 2010; Gehrels, 2006; Marriner & Morhange, 2007). Different groups of taxa have specific ecological preferences (e.g., salinity, substrate, temperature) and modes of life (e.g., epifaunal, infaunal, free living) that make them important indicators of coastal change (Murray, 2014; Poag, 2015). Certain benthic foraminifera species, for instance, live in association with reefs and sediments of shallow (0–130 m) marine shelf habitats (e.g., large, symbiont-bearing species such as *Amphistegina* spp.; Langer & Mouanga, 2016; Murray, 2014; Uthicke & Nobes, 2008; Weinmann et al., 2013). Other taxa prefer more brackish settings in the muddy sands of inner shelves and lagoons (e.g., *Ammonia* spp., *Trochammina inflata*, *Trochammina macrescens*; Murray, 2014; Poag, 2015). Though testate amoebae are freshwater protozoans, certain species (e.g., *Centropyxis aculeata* and *Centropyxis constricta*) are slightly brackish-tolerant and can be useful indicators in coastal lagoons/marshes (Gehrels, 2006; Vázquez Riveiros et al., 2007). Assemblages of microfossils have been used in previous harbour studies to identify transitions from high energy marine settings to lower energy and more brackish/fresh conditions associated with the construction of harbour structures and/or the formation of natural barriers (e.g., Amato et al., 2020; Finkler et al., 2018; Goodman et al., 2009; Pint et al., 2015; Reinhardt et al., 1994; Riddick et al., 2021; Riddick et al., 2022a, 2022b; Stock et al., 2013, 2016). The aim of this study is to reconstruct the environmental history of Khor Al Balid and Khor Rori through the analysis of microfossils (testate amoebae and foraminifera) and geochemistry within ten sediment cores collected from across the two sites. Results will be compared to the previous environmental findings as well as climate and sea-level data from the region. The geomorphological history constructed in this study will provide a paleoenvironmental perspective to help improve the understanding of lagoon development and harbour decline at Khor Al Balid and Khor Rori.

4.2 Regional setting

4.2.1 The Dhofar Governate

The Dhofar region, located along the southwestern coast of Oman, includes the Salalah Coastal Plain (55 km long, 15 km wide) and the Jebel Qara mountains which range 65 km east-west (up to 2000 meters high; Hoorn & Cremaschi, 2004; Shammas & Jacks, 2007; Zerboni et al., 2020). This area has a semi-arid climate with mean annual temperatures ∼18–29 ºC and average precipitation of 110 mm/yr in the plain and 230–450 mm/yr near the Jebel Qara (Al-Kindi et al., 2023; Kwarteng et al., 2009; Shammas & Jacks, 2007). Precipitation (a drizzle known as khareef, as well as rain, mist, and fog) occurs predominantly (>80%) between July and September due to the Indian summer monsoon (southwesterly winds; (Fleitmann et al., 2004; Shammas & Jacks, 2007). Yearly rainfall onto the Jebel Qara and the plain penetrates into permeable bedrock. This replenishes the groundwater supply which lies within an underground karst aquifer system and often emerges from the bedrock in permanent pools, sinkholes, and small springs (Costa, 1979; Zerboni et al., 2020). The fresh groundwater supports nearby populations and agriculture, as well as the region's forests, grasslands, and shrublands (Al-Kindi et al., 2023; Galletti et al., 2016; Zerboni et al., 2020).

A Late Cretaceous to Neogene limestone plateau underlies the Dhofar region (Shammas & Jacks, 2007). The plateau slopes slightly towards the north and contains several fault systems and escarpments related to tectonic activity (Cremaschi & Negrino, 2005; Hoffmann et al., 2013c; Zerboni et al., 2020). Rifting of the African and Arabian plates after formation of the Hadramhaut group, for instance, resulted in down faulting of the Salalah plain (Shammas & Jacks, 2007), while tectonism during the Neogene resulted in uplift of ∼300–400 m asl in the south (Zerboni et al., 2020). The fault systems and the karst formations influence the draining processes in the region. The plateau has been extensively eroded over time, with many bare outcropping and dendritic valleys cut into the limestone bedrock. The convergence of several alluvial fans descending from the plateau through dry valleys or wadis form the relatively uniform surface of the Salalah plain, which contains predominantly Pleistocene-age gravel-sized sediment (Zerboni et al., 2020). Many Pleistocene marine terraces up to ∼10 m high are observed in the western area along with a narrower coastal plain. All along the coast are sandy beaches, often with coastal dunes (up to a few meters high; Zerboni et al., 2020). The composition of coastal sands depends largely on the regional geology and are therefore predominantly carbonate with little quartz and few dark mineral fragments along the southern coast (McLachlan et al., 1998). Research on a similar site on the southeastern coast of Oman revealed sediment composition dominated by terrigenous minerals including quartz (25–65%) and feldspars (10–40%), as well as calcite (10–30%), halite (0–15%), dolomite (0–5%) that likely had lacustrine origin (e.g., shells, increased evaporation and concentration, influenced by seawater). Trace amounts of clay minerals (chlorite, illite, smectite, kaolinite, and palygorskite) were present and were likely eroded and transported from the regional soils and sediments (Lézine et al., 2010). Beachrock outcrops up to 3–4 m asl are common along the coastal environments, as well as estuaries or lagoons with mangroves (qurms) and without mangroves (khors). These often form where major wadis drain into the Arabian Sea (Hoorn & Cremaschi, 2004; Zerboni et al., 2020). Openings of estuaries change frequently, mainly due to the Indian Ocean monsoon (Hoorn & Cremaschi, 2004). The SW summer winds cause erosion of the beach and sand barriers, while the NE winter winds strike the coast from an oblique direction resulting in longshore sediment transport and sand barrier accumulation (Hoorn & Cremaschi, 2004).

4.2.2 Khor Al Balid and Khor Rori

Khor Al Balid is a T-shaped coastal lagoon located at a central point along the coast plains of southern Oman (Figure 4.1). The lagoon has low salinity, receiving fresh groundwater from the Wadi Garziz drainage system and minimal marine water due to the large sand barrier along the coast (Pavan & Visconti, 2023).

Though the lagoon is thought to have once surrounded the city of al-Balīd on three sides, forming a rectangular island with the Arabian Sea (Costa, 1979; Pavan & Visconti, 2023), the lagoon is currently largely silted in.

Khor Rori, ∼32 km east of Khor Al Balid (Figure 4.1), is a coastal estuary deeply cut into a marine erosive terrace (∼40 m amsl; (Cremaschi & Negrino, 2002). It is fed by Wadi Darbat and local karst springs. Wadi Darbat is currently blocked by a travertine dam (∼70 m high). The lower/coastal side of Wadi Darbat is often dry; however, the upper part is a perennial lake that can form a water fall during the higher precipitation monsoon seasons (Hoorn & Cremaschi, 2004). The entrance of Khor Rori is characterised by beachrock on both sides (5 m asl) and is often closed by a sand barrier, resulting in low salinity of the estuary (2.5 km long, up to 400 m wide, and 2.5–5 m deep; Hoorn & Cremaschi, 2004). Fine coastal sediments and gravel have accumulated in the estuary throughout the Holocene. Vegetation currently surrounding the estuary consists of coastal plain taxa, though there is evidence that khor vegetation was present between ∼250 BCE and ∼270 CE when higher rainfall and lake levels provided increased water supply to the khor (Cremaschi & Negrino, 2002).

4.3 Materials and methods

4.3.1 Sample collection & radiocarbon dating

In 1995, six sediment cores (ALB1–ABL6) were collected from both land and underwater sites throughout the coastal lagoons at Al Balid and four sediment cores (ROR1, ROR2, ROR3, and ROR5) were collected from Khor Rori lagoon (Figure 4.1). Material was collected using a piston corer or a vibracorer (Smith, 1987, 1998) and underwater samples were collected via SCUBA. Cores were split, described, and subsampled at 1- to 5-cm intervals.

Radiocarbon (14C) dating on organic matter and mollusk shell samples was performed at Beta-Analytical (Miami FL, USA) and IsoTrace Laboratories (University of Toronto ON, CA) through Accelerated Mass Spectrometry. Radiocarbon ages of organic matter samples were calibrated with IntCal20 (Reimer et al., 2020).

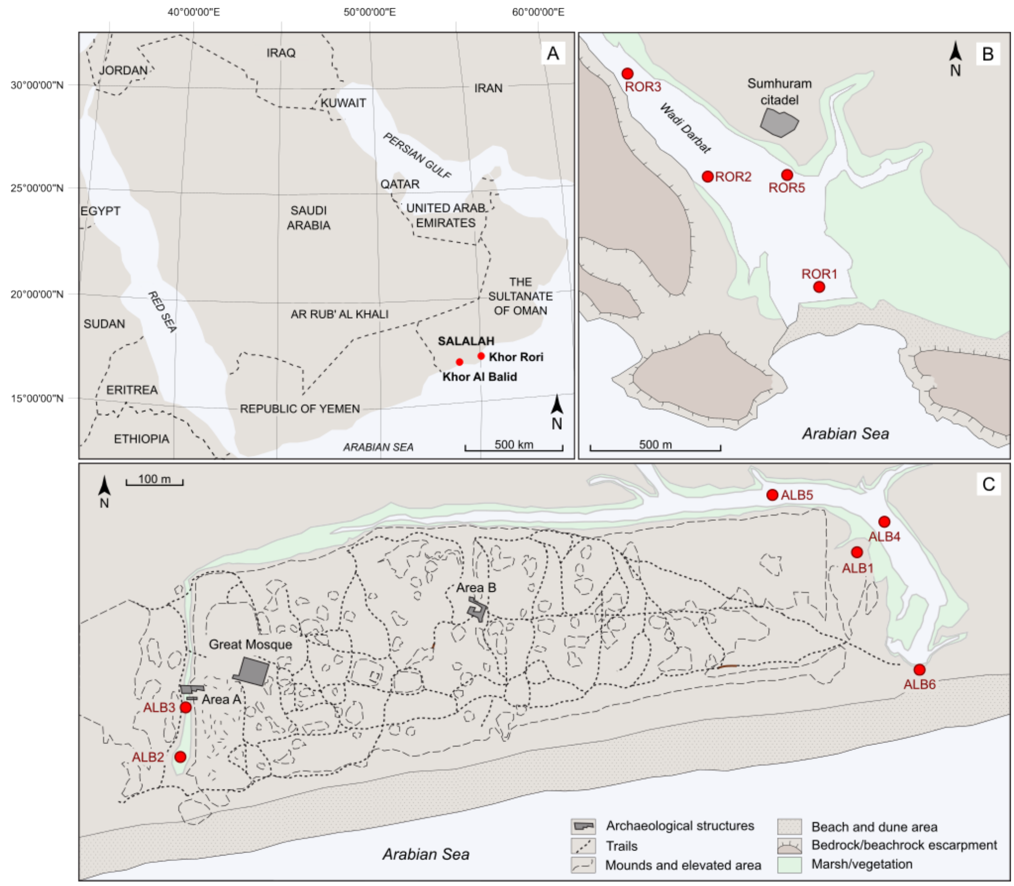

FIGURE 4.1: (A) The location of Khor Al Balid and Khor Rori within The Sultanate of Oman. (B) The location of Khor Rori cores ROR1, ROR2, ROR3, and ROR5, and (C) the Khor Al Balid cores ALB1–6. The map of Khor Al-Balid is based on Costa (1979).

Ages of shell samples were calibrated with Marine20 (Heaton et al., 2020) using a local marine reservoir correction of 45±67 (the average of 10 nearest data points to the Oman coast; http://calib.org/marine/).

4.3.2 Microfossils analysis

Subsamples of Khor Al Balid and Khor Rori cores ALB1 (n=10), ALB2 (n=13), ALB3 (n=6), ALB4 (n=13), ALB5 (n=14), ROR3 (n=8), ROR5 (n=9) were analyzed for foraminifera and testate amoebae content using standard methodologies as described by (Scott et al., 2001). Specimens were identified using well-illustrated references including Hottinger et al. (1993). Results from Khor Al Balid and Khor Rori were separately statistically grouped using Ward's minimum variance clustering method (Ward, 1963).

4.3.3 Geochemical analysis

Subsamples from the Khor Al Balid cores ALB1 (n=5), ALB2 (n=21), ALB3 (n=6), ALB4 (n=15), ALB5 (n=18), and ALB6 (n=8) and the Khor Rori cores ROR1 (n=29), ROR2 (n=20), ROR3 (n=36), and ROR5 (n=40) were analyzed by the Cox Analytical ITRAX X-Ray Fluorescence Core Scanner (μXRF) at the McMaster University Core Scanning Laboratory (MUSC Lab) using a sequential sample reservoir (Gregory et al., 2017). Analysis was performed with the Molybdenum X-Ray source, 30 kV, 30 mA, 15 second exposure time at 500 μm resolution. Elements of interest for this study include calcium (Ca), iron (Fe), potassium (K), silica (Si), strontium (Sr), and titanium (Ti), which are useful environmental proxies for past fluctuations in sea level and rainfall (Krywy-Janzen et al., 2019; McNeill-Jewer et al., 2019). A major source of Sr is from marine organisms with aragonitic skeletons, as well as from limestone weathering (Marshall & McCulloch, 2002; Wood & Macpherson, 2005). Sources of Ca in the Dhofar region include weathering of the limestone platform and the marine carbonate sands and shells (McLachlan et al., 1998). Si is mainly sourced from terrestrial weathering, with some from biogenic silica and from coastal quartz sands (Lézine et al., 2010; Peinerud, 2000). Values of Ca/Si were therefore used to indicate relative proportions of marine carbonate sands and shells compared to fluvial/terrestrial and marine silica sands. Ti, Fe, and K are also products of terrestrial weathering, particularly mud-sized grains; thus, Ti+Fe+K/Ca values can be used an indicator for variations in fluvial/terrestrial input compared to marine sands and shells (e.g., Adegbie et al., 2003; Bahr et al., 2005; Rothwell & Croudace, 2015; Tjallingii et al., 2010). The Incoherent/Coherent scatter (Inc/Coh) values obtained during μXRF analysis can provide an indication of organic matter content throughout a sedimentary sequence, with higher values relating to lower density, increased porosity, and/or increased water content, as well as lower average atomic mass within sediments (Chawchai et al., 2016; Rothwell & Croudace, 2015).

Samples with statistically similar geochemical composition were identified by constrained cluster analysis of the μXRF results. Geochemical clustering was conducted separately for Khor Al Balid and Khor Rori samples due to the variability in geological settings. In addition to the main elements of interest (Ca, Fe, K, Si, Sr, and Ti), additional elements (Cr, Pb, Cu, S, Zn, Ba, Zr, Rb, Ni, and Mn; Huang et al., 2016; Rothwell & Croudace, 2015) were included in the chemofacies analyses to help distinguish between geochemically distinct periods of deposition. Data was row-centered (mean = 0, sd = 1) and then grouped using a Self-Organizing Map (SOM; "SOMbrero" package, Olteanu & Villa-Vialaneix, 2015). Ward's hierarchical clustering was used to group samples, which were then further grouped into higher order superclusters.

4.4 Results

4.4.1 Core lithology and chronology results

The cores collected from Khor Al Balid record a transition from sandy sediments to grey mud. Within the grey mud, some cores contain a peat/OM layer (in ALB1 between 37–39 cm, ALB2 between 27–30 cm, ALB4 between 23–26 cm, 21–22 cm, and 11.5–20 cm, and ALB5 between 15–21 cm) and/or an upper sand layer (in ALB1 between 39–55 cm, ALB3 between 10–12 cm, ALB4 between 6–9 cm, and ALB5 between 8–9.5 cm and 5–7 cm. ALB6 is entirely composed of sand. Pebbles were observed within the lower sand units of ALB1 (100–127 cm) and ALB3 (15–20 cm). Cores collected from Khor Rori mainly consist of grey mud with lower sand units in ROR1 (59.5–68 cm, and 14.5–56.5 cm) and ROR3 (65–72 cm, 61–64 cm, and 55–60 cm) and upper sand units in ROR1 (14.5–56.5 cm) and ROR5 (30.5–37 cm). Sediments at Khor Rori were relatively poorly sorted, with sandy mud at the top of ROR1 (7.5–14.5 cm) and silty/muddy sand throughout the bottom of ROR1 (92–107 cm) and the bottom (37–105 cm) and top (0–30.5 cm) of ROR5. Pebbles were observed throughout the bottom portions of all four cores, and large boulders with barnacle were present at the bottom of ROR2.

Based on radiocarbon results (Table 4.1), the basal sandy sediments across Khor Al Balid span several thousand years (5634–5204 BCE to 20 BCE–471 CE).

These sands transition to grey mud around 1229–1430 CE at the western side of the lagoon and around 774–1169 CE at the eastern side of the lagoon. The upper sandy sediments that were observed in almost all cores were dated to the 18th–19th century, based on the date obtained from ROR3 (1525–1950 CE), as well as the upper age range for the underlying sediments in ALB5 (1299–1632 CE; Table 4.1).

Table 4.1: Radiocarbon results for Khor Al Balid (ALB) and Khor Rori (ROR) samples.

Core	Description	Depth (cm)	C14 Age (yr BP)	Error ±	Modelled Calibrated Age (yr BP)	Modelled Calibrated Age (BCE/CE)
ALB1	Gastropods	31	1710	50	1274 – 841*	677 – 1110*
ALB1	Organic material	71	1290	60	1301 – 969	649 – 982
ALB2	Organic material	27 – 30	690	40	722 – 521	1229 – 1430
ALB2	Bivalve fragment	32 – 35	2330	50	1969 – 1480*	-20 – 471*
ALB4	Organic material	24	1100	50	1177 – 782	774 – 1169
ALB5	Organic material	18	530	50	652 – 319	1299 – 1632
ALB5	Bivalve	30 – 31	7120	70	7586 – 7155*	-5635 – -5204*
ROR2	Oyster	41	130	60	-2 – -17*(!)	1953 – 1968*(!)
ROR2	Barnacle	41	210	40	109 – -2*(!)	1841 – 1953*(!)
ROR2	Barnacle	41	270	40	116 – -2*(!)	1835 – 1953*(!)
ROR3	Organic material	60	220	40	425 – 1(!)	1525 – 1950(!)
ROR3	Wood	20	Modern	-	Modern	Modern

* Calibrated with Marine20, local marine reservoir correction = 45±67 (http://calib.org/marine/)

(!) Date probably out of range

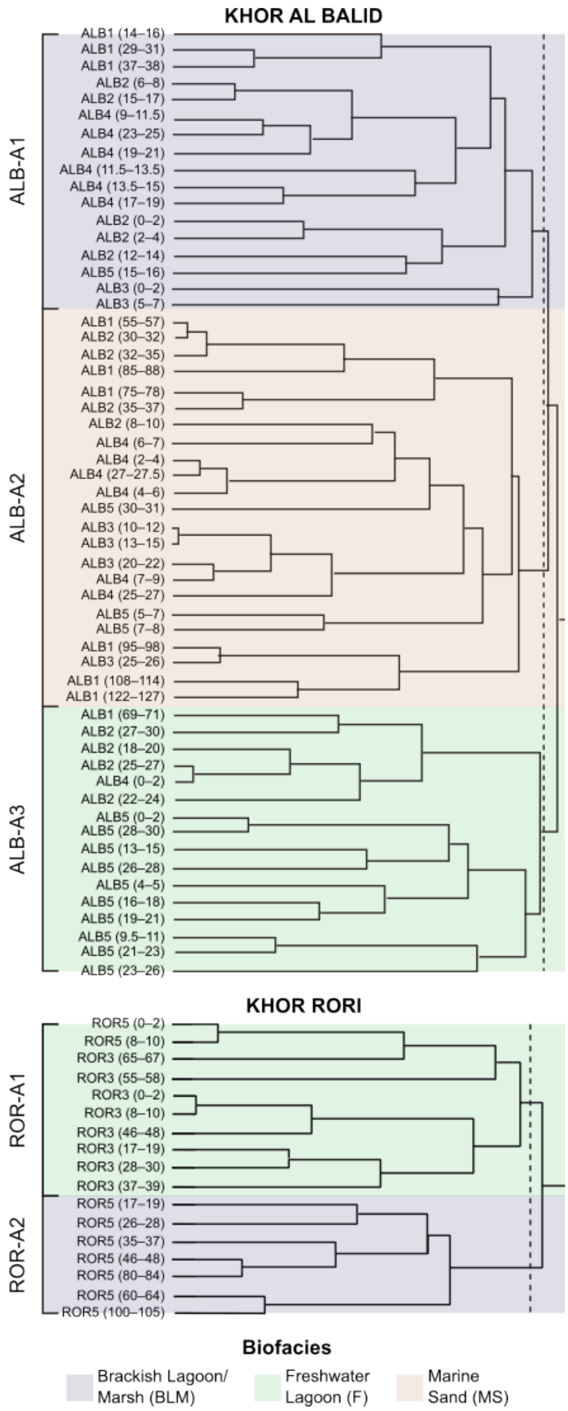

FIGURE 4.2: Khor Al Balid & Khor Rori microfossil cluster results showing assemblages ALB-A1–ALB-A3, ROR-A1, and ROR-A2 which correspond to Brackish Lagoon and Marsh, Marine Sand, and Freshwater Lagoon biofacies.

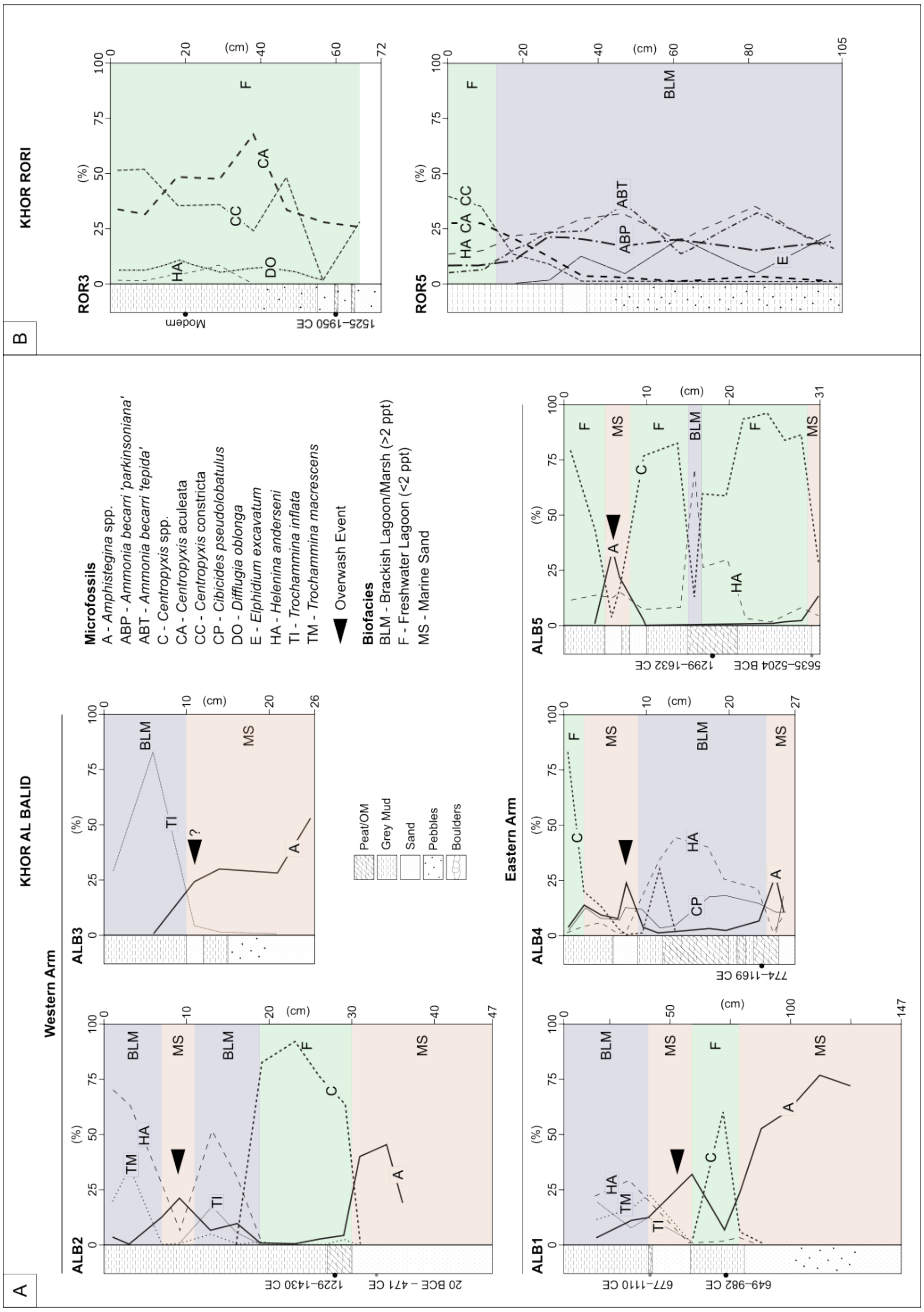

FIGURE 4.3: Relative abundances (%) of dominant microfossils in A) Khor Al Balid cores ALB1–5 and B) Khor Rori cores ROR3 and ROR5, with biofacies results (see Figure 4.2).

4.4.2 Microfossil results

Twenty-one foraminifera taxa and three testate amoebae taxa were identified in Khor Al Balid, while eleven foraminifera taxa and six testate amoebae taxa were observed in Khor Rori samples (Appendix C1, C2, and C3). Microfossil concentrations were relatively low in Khor Rori cores (ROR3 avg = 100, range = 2–238; ROR5 avg = 299, range = 184–415) compared to Khor Al Balid (Appendix C1 and C2). Concentrations were slightly higher in the western arm of Khor Al Balid (ALB2 avg = 585, range = 154–1926; ALB3 avg = 598, range = 114–1519) compared to the eastern arm (ALB1 avg = 551; range = 178–977; ALB4 avg = 332, range = 9–4291; ALB5 avg = 373, range = 118–892). Average SDI (Shannon Diversity Index) values are relatively consistent across Khor Al Balid (ALB1 avg = 1.6; ALB2 avg = 1.3; ALB3 avg = 1.5; ALB4 avg = 1.7; ALB5 avg = 1.0; Appendix C1).

Clustering results revealed three assemblages at Khor Al Balid (ALB-A1, ALB-A2, and ALB-A3) and two assemblages at Khor Rori (ROR-A1 and ROR-A2; Figure 4.2 and 4.3). These assemblages were identified as belonging to three main biofacies based on relative abundances of marine and fresh/brackish microfossil species: Marine Sand (MS), Brackish and Lagoon/Marsh (BLM), and Freshwater Lagoon (F).

4.4.2.1 Marine Sand (MS) biofacies

MS biofacies make up the bottom sandy sediments of all analyzed Khor Al Balid cores as well as a thin upper layer within ALB1, ALB2, ALB4, and ALB5 (Figure 4.3). The dominant microfossils within assemblage ALB-A2 (MS biofacies) include the foraminifera taxa *Amphistegina* spp. (4.7–77.1 %), *C. pseudolobatulus* (0–18.3 %), *Elphidium lebatum* (0.5–11.3 %), and *H. andersoni* (0–15.0 %). Planktic foraminifera were observed in ALB4, with highest abundances (18.2–32.9 %).

4.4.2.2 Brackish Lagoon/Marsh (BLM) biofacies

In the western arm of Khor Al Balid, the top half of cores ALB2 and ALB3 belong to BLM biofacies, with the exception of the thin MS unit in ALB2 (Figure

4.3). In the eastern arm, the top third of ALB1, the middle of ALB4, and a very thin unit in the middle of ALB5 belong to BLM biofacies. ROR5 is predominantly BLM with the exception of a relatively thin F biofacies unit at the top of the core (Figure 4.3). Assemblage ALB-A1 (BLM biofacies) is dominated by foraminifera taxa *Amphistegina* spp. (0.2–12.9 %), *Cibicides pseudolobatulus* (0–15.2 %), *Discorinopsis aquayoi* (0–20.0 %), *Elphidium transluscens* (0–19.8 %), *Helenina andersoni* (0–70.4 %), *Quinqueloculina seminulum* (0–24.6 %), *Trochammina macrescens* (0–35.2 %), and *Trochammina inflata* (0–83.1 %; Appendix C1). ROR-A2 (BLM biofacies) is dominated by the foraminifera *Ammonia becarri "parkinsoniana"* (9.9–21.1 %), *Ammonia bercarri "tepida"* (13.3–36.4 %), *Elphidium excavatum* (1.6–22.8 %), *H. andersoni* (13.6–34.9 %), and the testate amobae *C. aculeata* (0–20.2 %).

4.4.2.3 Freshwater Lagoon (F) biofacies

F biofacies directly following the basal MS units in ALB1, ALB5, and ALB3. In ALB4, only the topmost sediments belong to F biofacies. The majority of ALB5 is belongs to F, with the exception of the basal and upper MS and the thin BLM unit mid-core. At Khor Rori, the samples from ROR3 belong entirely to F, as well as a relatively thin unit at the very top of the core. Assemblage ALB-A3 (F biofacies) is dominated by testate amoebae taxa *Arcella vulgaris* (0–10.2 %), *Centropyxis constricta* (1.5–68.5 %) and *Centropyxis aculeata* (14.4–93.6 %), with some observations of the foraminifer *H. andersoni* (0–13.5 %). The dominant species within ROR-A1 (F biofacies) include the testate amoebae *A. vulgaris* (0–72.2 %), *C. constricta* (0–54.4 %) and *C. aculeata* (22.8–68.5 %), as well as the foraminfera *H. andersoni* (1.7–14.1 %; Appendix C2).

4.4.3 Geochemistry results

The elemental data from Khor Al Balid was grouped into seven superclusters (MS-1, and LM-2 to LM-7; Figure 4.4 and 4.5; Appendix C4 and C5) that correspond well with lithology and with the biofacies results. The samples analyzed from the basal sand units of Al Balid cores all belong to MS-1. ALB1, ALB4, and ALB5 also contain an upper MS-1 chemofacies that corresponds to the upper sand units within the cores. This chemofacies was identified as Marine Sand due to the highest Ca/Si values (avg = 1349±403) and the lowest Ti+Fe+K/Ca (avg = 0.031±0.031) and Inc/Coh values (avg = 3.93±0.24; Table 4.2). The six other superclusters (LM-2 to LM-7) mostly correspond to grey mud and peat/OM units within the Al Balid cores (Figure 4.5). Though these superclusters vary slightly in composition (Figure 4.4), they were all identified as Lagoon/Marsh chemofacies in order to more clearly define/identify the transition from open estuary (i.e., marine sand) to lagoon settings across the study sites. All six of the LM chemofacies contain distinctly lower Ca/Si (avg = 663±433), higher Ti+Fe+K/Ca (avg = 0.679±0.654), and higher Inc/Coh (avg = 4.96±0.55) values compared to the MS chemofacies (Figure 4.5, Table 4.2).

The elemental data from Khor Rori was grouped into seven superclusters (LM-1 to LM-6, and MS-7; Figure 4.6 and 4.7). Similarly to Khor Al Balid, LM-1 to LM-6 at Khor Rori were identified as Lagoon/Marsh chemofacies because of distinctly lower Ca/Si values (avg = 425±393) and higher Ti+Fe+K/Ca (avg = 1.848±3.859) and Inc/Coh values (avg = 4.49±0.48) compared to the Marine Sand chemofacies (MS-7; Ca/Si avg = 1127±428; Ti+Fe+K/Ca avg=0.094±0.105; Inc/Coh avg = 3.90±0.18; Table 4.2). In ROR2 and ROR3, LM chemofacies correspond well with the grey mud and peat/OM units while the MS chemofacies corresponds with sand (Figure 4.7). These trends are also apparent in ROR1 and ROR5, except for the upper sand unit in ROR1 which belonged to LM. The units with mixed grain sizes (e.g., the top of ROR5) show some alternating between chemofacies (Figure 4.7).

TABLE 4.2: Average Ca/Si, Ti+Fe+K/Ca, and Inc/Coh values, with standard deviations (sd), for Marine Sand and Lagoon/Marsh chemofacies in Khor Al Balid and Khor Rori samples.

Location	**Chemofacies**	**Ca/Si**	**±sd**	**Ti+Fe+K/Ca**	**±sd**	**Inc/Coh**	**±sd**
Khor Al Balid	Marine Sand (MS-1)	1349	403	0.031	0.031	3.93	0.24
	Lagoon/Marsh (LM-2–7)	663	433	0.679	0.654	4.96	0.55
Khor Rori	Marine Sand (MS-7)	1127	428	0.094	0.105	3.90	0.18
	Lagoon/Marsh (LM-1–6)	425	393	1.848	3.859	4.49	0.48

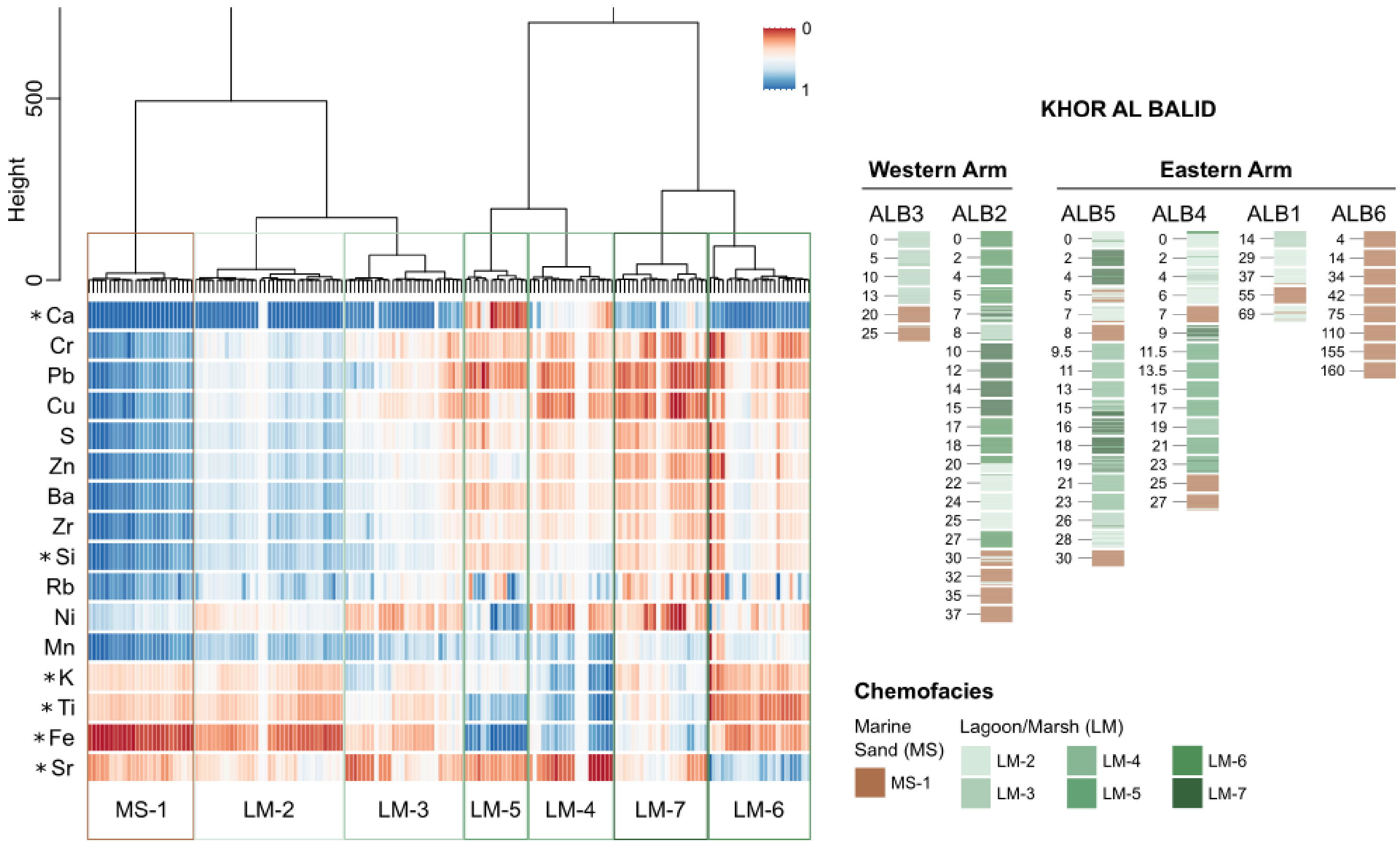

FIGURE 4.4: Elemental clustering results showing the heatmap of relative proportions of elements within superclusters ALB-C1–ALB-C7, the distribution of superclusters within Khor Al Balid cores ALB1–ALB6, and the corresponding Brackish Lagoon and Marsh, Freshwater Lagoon, and Marine Sand chemofacies. Cores are listed in order of increasing proximity to the coast. *Denotes elements of interest (see Methods section 4.3.3).

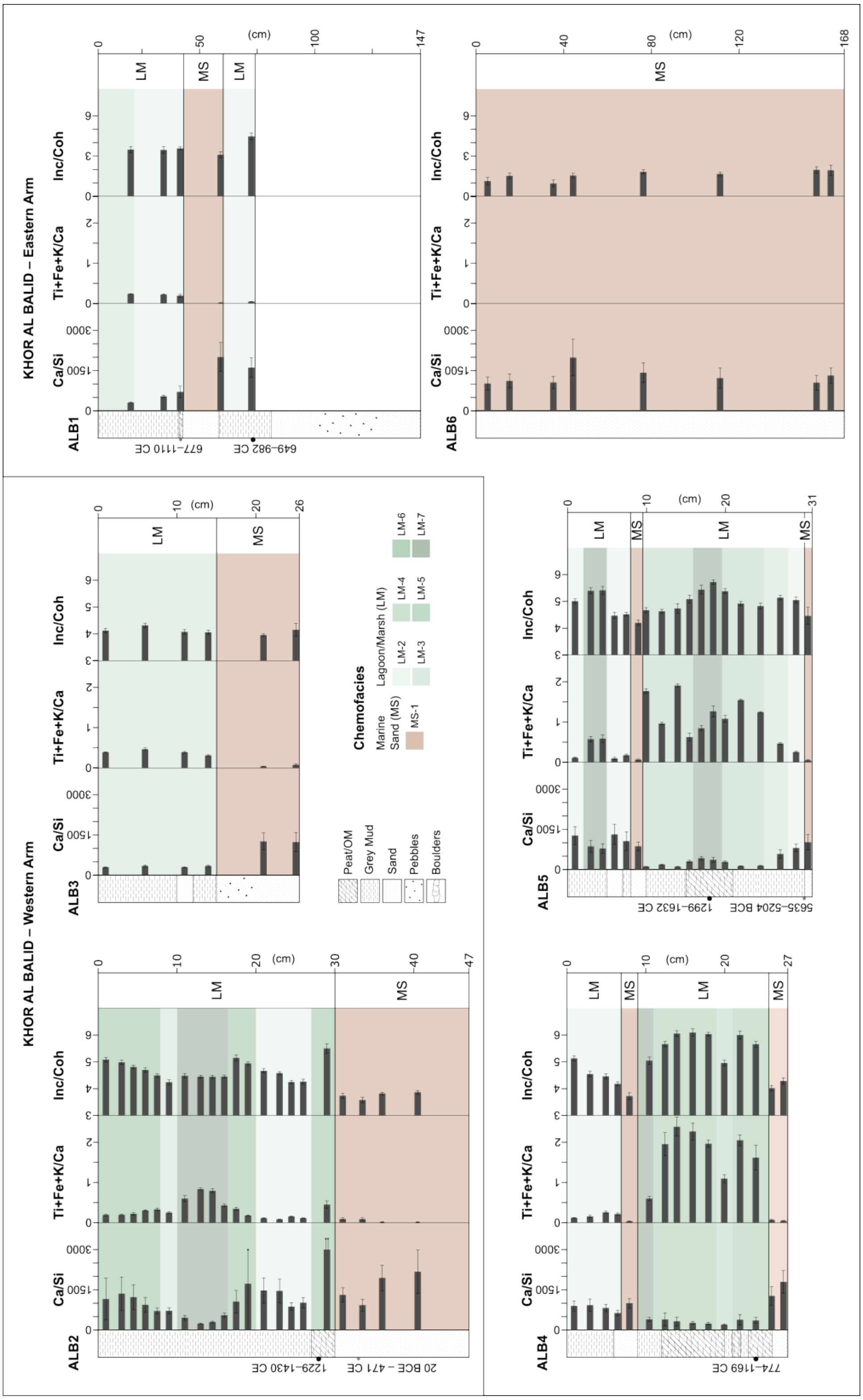

FIGURE 4.5: Elemental ratio results for Khor Al Balid cores ALB1–6 with lithology, radiocarbon dating, and chemofacies results (see Figure 4.4).

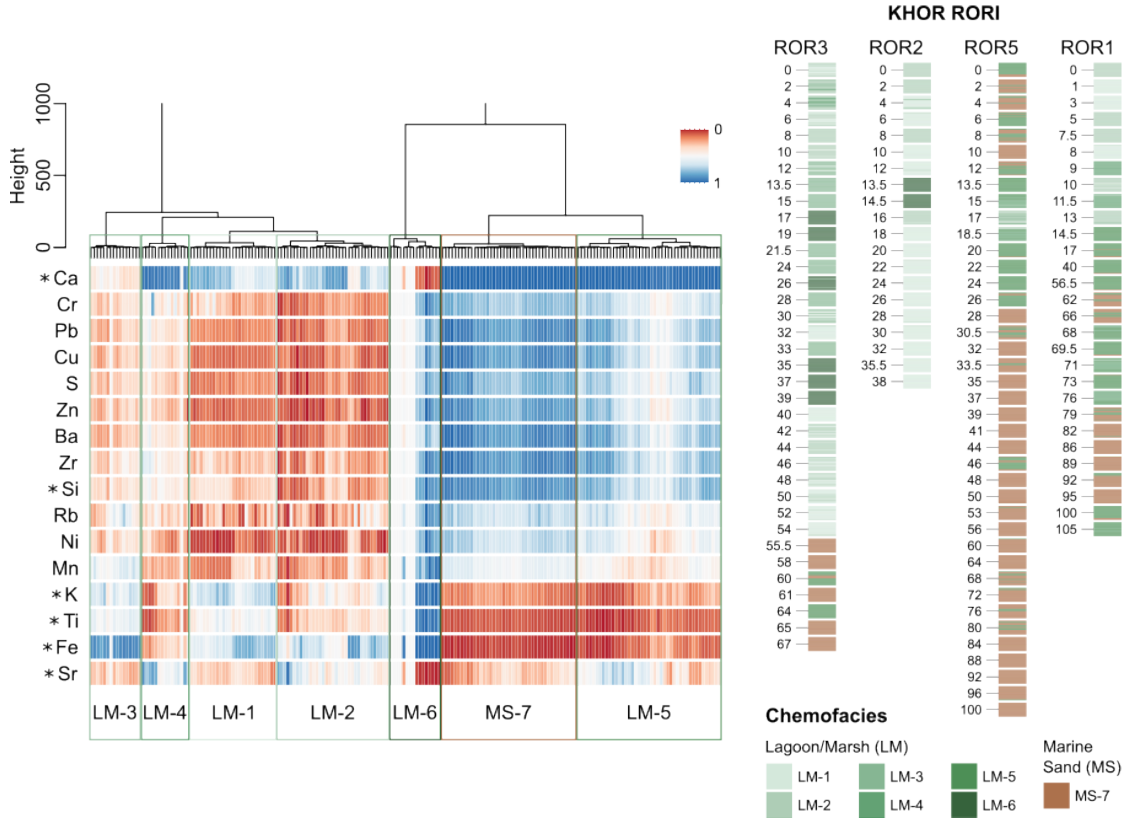

FIGURE 4.6: Elemental clustering results showing the heatmap of relative proportions of elements within superclusters ROR-C1–ROR-C7, the distribution of superclusters within Khor Rori cores ROR1–ROR3 and ROR5, and the corresponding Brackish Lagoon and Marsh, Freshwater Lagoon, and Marine Sand chemofacies. Cores are listed in order of increasing proximity the coast. *Denotes elements of interest (see Methods section 4.3.3).

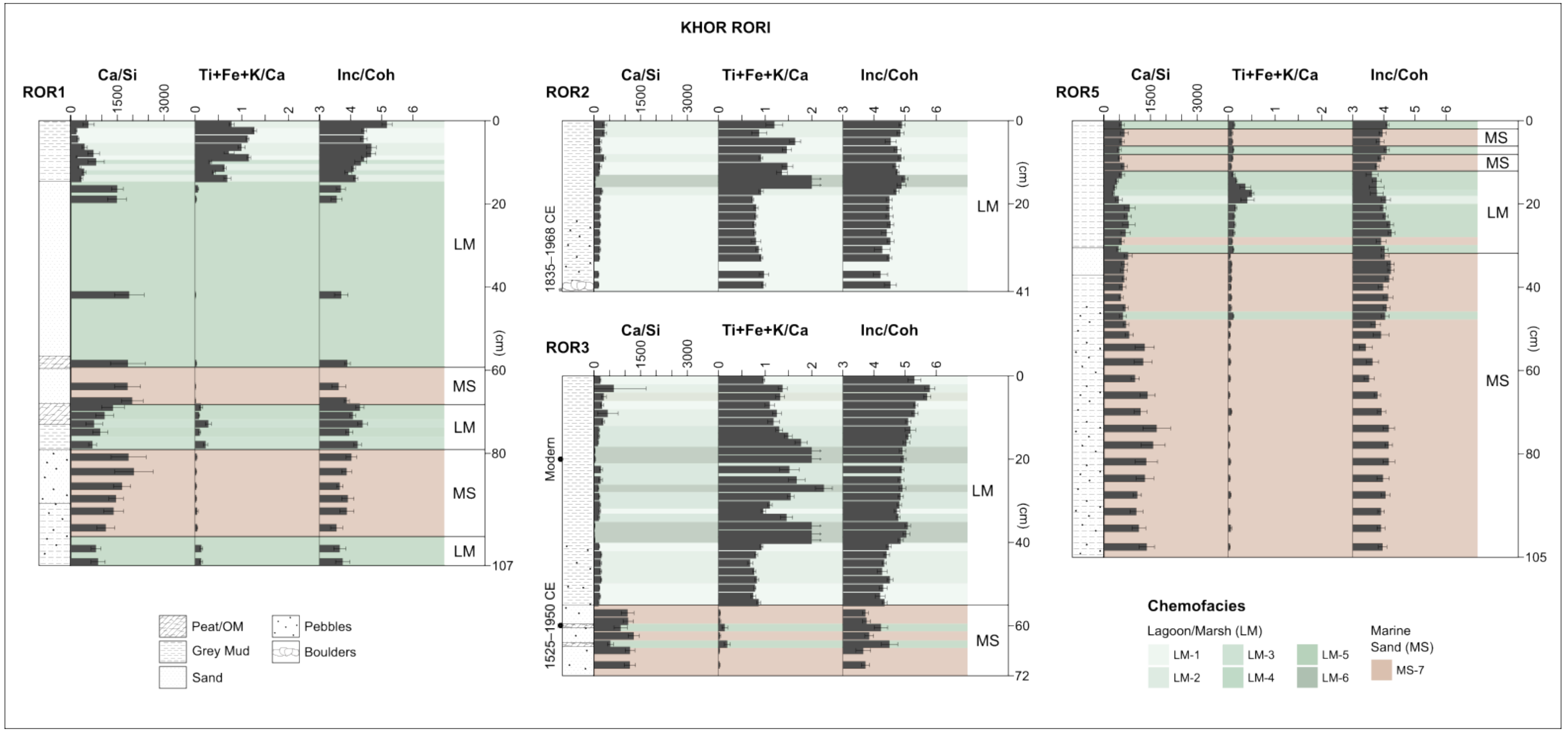

FIGURE 4.7: Elemental ratio results for Khor Rori cores ROR1–ROR3, and ROR5 with lithology, radiocarbon dating, and chemofacies results (see Figure 4.6).

4.5 Discussion

4.5.1 Changes in coastal geomorphology

The transition from open estuary to lagoon conditions is recorded in the lithology, biofacies, and chemofacies of cores ALB1–ALB5 collected from Khor Al Balid (Figure 4.8). The shift from sands to mud or peat/OM in all five cores suggests a decrease in depositional energy that took place by around 1169 CE (ALB4: 774–1169 CE) in the eastern arm and by around 1430 CE (ALB2: 1229–1430 CE) in the western arm. Benthic foraminifera assemblages indicate that conditions within the Khor were saline prior to this shift, with increased presence of shallow marine shelf taxa (*Amphistegina* spp., *C. pseudolobatulus*, and *Elphidium* spp.; Figure 4.3; Murray, 2014). Following this shift in conditions, the khor was dominated by more brackish tolerant foraminifera species that are typical of lagoons, salt marshes, and/or intertidal environments (e.g., *A. becarri 'parkinsoniana'*, *A. becarri 'tepida'*, *H. andersoni*, *T. macrescens*, and *T. inflata*; Debenay et al., 2002; Gennari et al., 2011; Horton & Edwards, 2006; Murray, 2014; Verlaak & Collins, 2021). The high abundance of testate amoebae (∼60–90 % *C. constricta* and/or *C. aculeata*) in sediments immediately following the shift from sand to mud and peat/OM indicates that salinity was low enough to support these fresh to brackish tolerant species (Figure 4.3; Vázquez Riveiros et al., 2007). The transition from high-energy marine to low-energy fresh/brackish conditions was recorded quite abruptly in all of the Khor Al Balid cores suggesting that the sand barriers at the eastern and western mouths the of estuary had formed completely at that point in time. Dredging activities were likely not taking place after this transition as conditions remain fresh/brackish throughout time, with the exception of one upper MS facies in all five cores (see Discussion 5.2). Following sand barrier formation, sedimentation, shoaling, and evaporation would have occurred over time, leading to the brackish conditions reflected in the biofacies of all the three shallowest cores (ALB1, ALB2, and ALB3). The freshwater conditions reflected in the uppermost biofacies of ALB4 and ALB5 reflect the input of freshwater from Wadi Garziz drainage system into the khor (Pavan & Visconti, 2023). The chemofacies show variable conditions in lagoon deposits over time (LM1–LM7), which may represent changes in sediment sources and/or reworking of deposits (e.g., through erosion, storms, human activity, etc). Higher Ca/Si values, for instance, correspond with sandy sediments, reflecting increased shell content and/or marine sand compared to fluvial sands; however, values also peak and/or increase in sediments over time (e.g., ALB2, ALB4, and ALB5; Figure 4.5), which may indicate relatively lower fluvial input over time due to increasingly arid conditions and/or an increase in site degradation and wind-blown carbonate sands from the nearby coast. Despite these complex variations, the LM chemofacies clearly demonstrates changing conditions following the closure of the estuary to the sea and supports the biofacies and lithological results; thus, LM-1 to LM-7 were dealt with as one group for the purposes of this study.

The cores collected from Khor Rori seem to contain sediments deposited after the formation of the coastal sand barrier (Figure 4.9). The records, however, appear to have undergone multiple erosive events through wave erosion and through wadi flow. Because the elevation of Khor Rori is higher than the flat coastal plain at Khor Al Balid, the amount of erosion and reworking is higher, and the sediment records are slightly less coherent. The sand units at the base of ROR1, ROR3, and RO5 may represent the same depositional event as the upper sand units observed in Khor Al Balid (see Discussion 5.2), due to the relatively young ages obtained from the sediments (1525–1950 CE to modern; Table 4.1). The biofacies suggest that conditions at Khor Rori have been fresh to brackish since around the 16th century CE but were maybe more marine for short periods with partial breaching of the sand barrier. The presence of sand units and/or MS chemofacies at the top of ROR5 and ROR1, which are in closest proximity to the coast, may indicate a breach in, or redeposition of, the coastal sand barrier. Breaching of the coastal sand barriers along this region of the coast are known to occur (Hoorn & Cremaschi, 2004), usually in association with large storm events such as tropical cyclones. Cyclone Mekuno in 2018, for instance, caused coastal flooding and the formation of a channel through the barrier at the mouth of Khor Al Balid (Andreou et al., 2022).

Previous research on palynological changes at Khor Al Balid and Khor Rori suggests that the estuaries were surrounded by khor taxa, received abundant freshwater from the wadis, and were open to the sea prior to at least 270–420 CE (Hoorn & Cremaschi, 2004; Lippi et al., 2011). Results from our study further constrain the timing to the 12th to 15th century CE at Khor Al Balid (Figure 4.10). The closure of the wadi mouths likely resulted from a combination of longshore drift, a slight drop in sea-level, and reduced storm/flooding events. Khor Rori appears to have alternated between open and closed at least until the 19th–20th century and appears to be largely closed until the present. Seasonal accumulation and erosion of sand barriers occurs naturally along the southeast Oman coast, due to monsoonal wind directions and longshore drift (Hoorn & Cremaschi, 2004; Shammas & Jacks, 2007). Land levels have been relatively stable since the mid-Holocene (i.e., no tectonic uplift/subsidence; Hoffmann et al., 2013c); however, the possible $\sim$1 m drop in sea-level in the past 1000 years along the southeast coast of the Arabian Peninsula (Khanna et al., 2021) has likely contributed to reduced erosion of sand barriers and increased accumulation of coastal sands. The regional climate has become increasingly arid since the mid-Holocene (Burns et al., 1998; Cremaschi et al., 2015; Cremaschi & Negrino, 2005; Fleitmann et al., 2003, 2007). Decreased precipitation, along with relatively lower wadi water levels and fewer flooding events compared to more humid climate periods means that the sand barriers were not being eroded/removed from the mouths of estuaries as frequently as they may have been in the past.

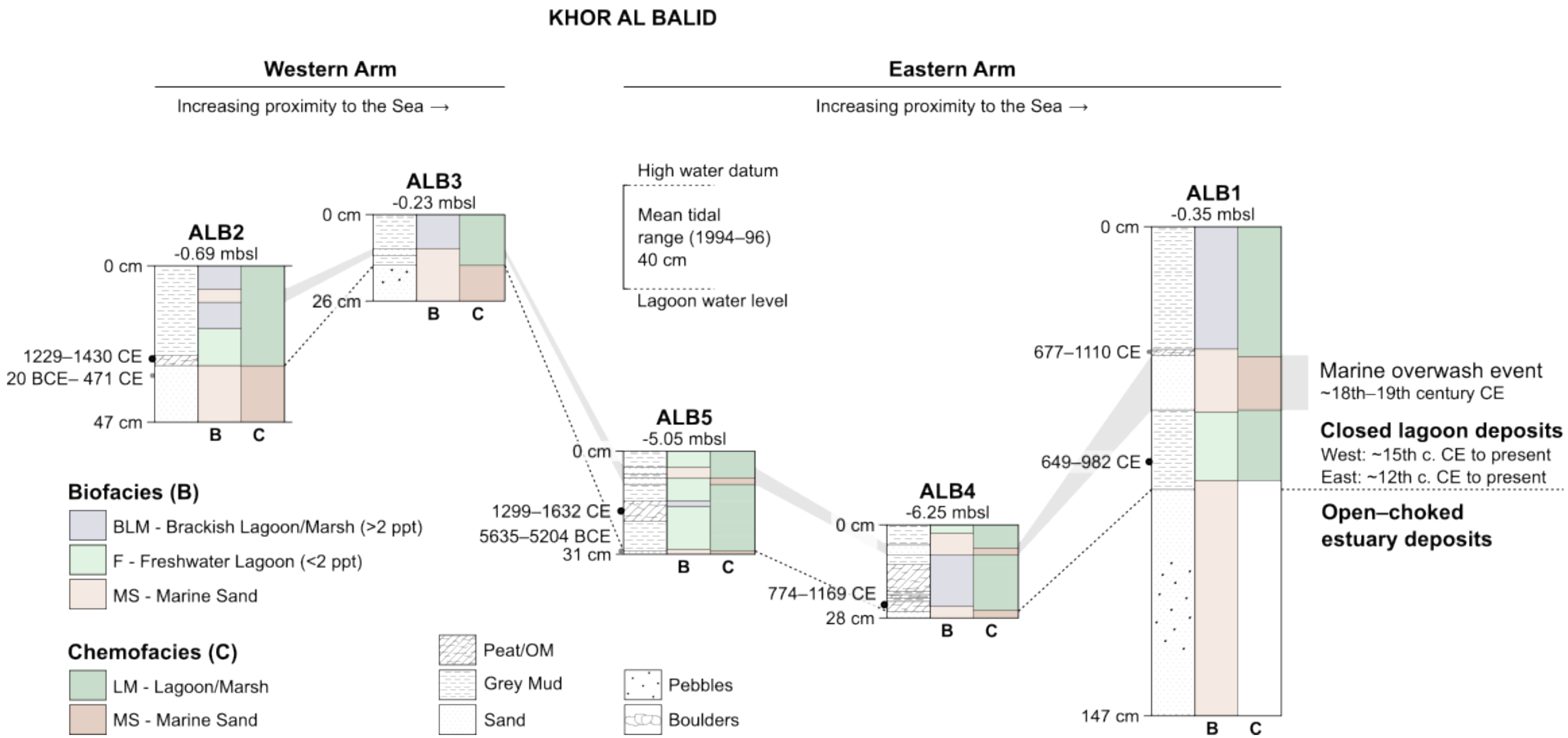

FIGURE 4.8: Correlation between cores collected from Khor Al Balid based on lithology, biofacies (B), chemofacies (C), and radiocarbon dating results. Black circles represent dates obtained from organic matter; smaller grey circles represent dates obtained from shell samples.

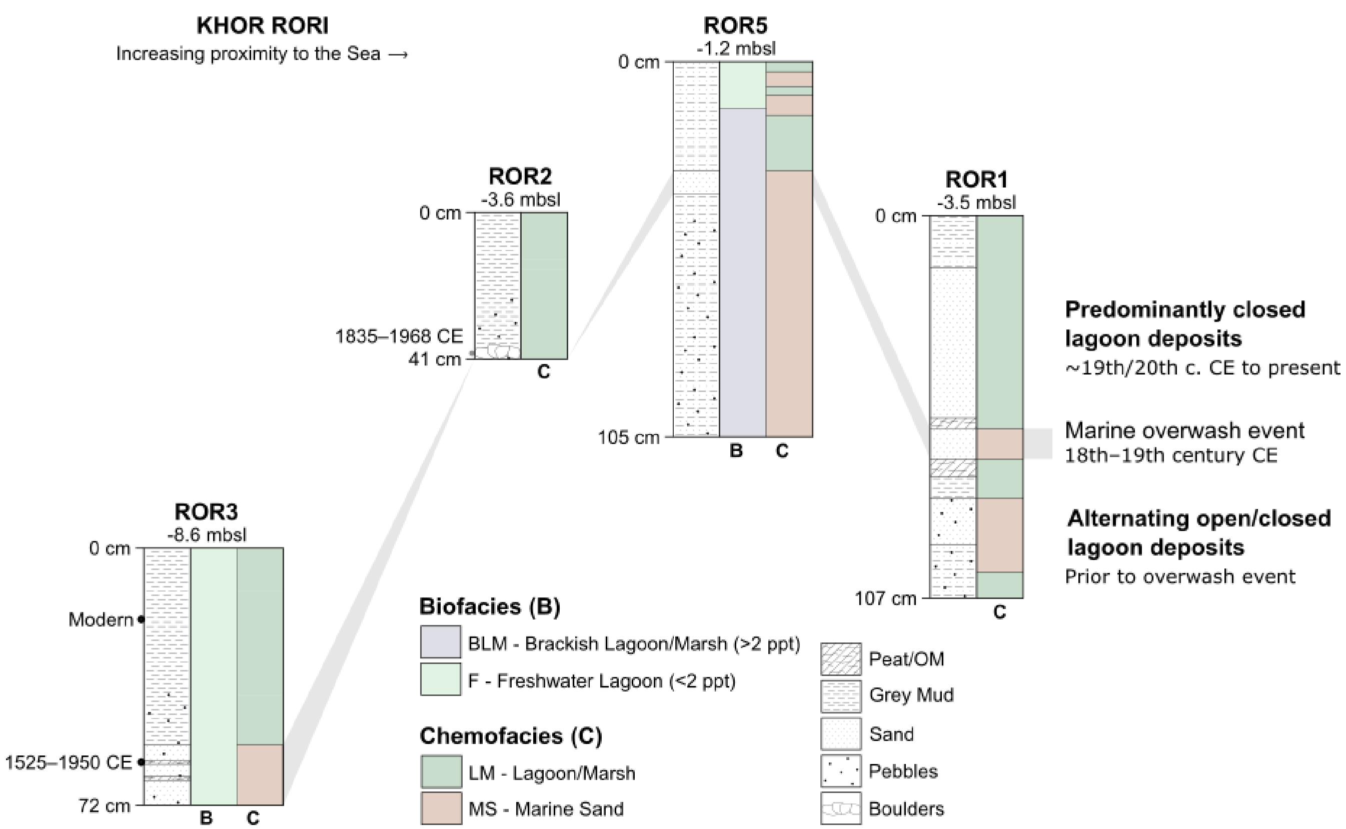

FIGURE 4.9: Correlation between cores collected from Khor Rori based on lithology, biofacies (B), chemofacies (C), and radiocarbon dating results. Black circles represent dates obtained from organic matter; smaller grey circles represent dates obtained from shell samples.

FIGURE 4.10: Model of environmental changes at Khor Al Balid and Khor Rori spanning the past ~2000 years.

4.5.2 Large overwash event

Cores from both Khor Al Balid and Kohr Rori record a large overwash event that took place relatively recently (Figure 4.8 and 4.9). Marine proxies including the presence of sand units, MS biofacies, and/or MS chemofacies in the upper portions of ALB1–5 suggest that coastal conditions became more saline for a period of time (i.e., the lagoon barriers were breached) or that an extreme wave event occurred across the entire coastal region. The peaks in relative abundance of *Amphistegina* spp. in these layers within ALB1, ALB2, ALB4, and ALB5 is especially indicative of marine intrusion, as this large, robust taxon is typical of reefs and other marine shelf habitats (Langer & Mouanga, 2016; Murray, 2014; Uthicke & Nobes, 2008; Weinmann et al., 2013). The increase in Ca/Si and distinct decrease in Ti+Fe+K/Ca and Inc/Coh values in cores ALB1, ALB4, and ALB5 in the upper sand units also provide strong evidence for the event. Though the deposits from Khor Rori are somewhat less coherent, they also provide supportive evidence for the event. The barnacles and oyster fragments on the rock at the bottom of ROR2 date from 1835–1968, suggesting that estuary conditions were open again for a period of time around the 19th–20th century. The grey mud and Lagoon facies (freshwater microfossils, relatively low Ca/Si values, etc.) that characterize most of the sediments at Khor Rori were likely deposited following this extreme wave event, when the sand barrier remained largely closed. Considering the date obtained from the bottom alternating sand/peat of ROR3 (1525–1950 CE) assumed to be deposited around this event and the age of the underlying lagoon deposits from ALB5 (∼1632 CE), a reasonable estimate for the extreme wave event is the 18th–19th century CE.

A flooding event was observed in the palynological study by (Hoorn & Cremaschi (2004), within the top 40 cm of a core from the eastern arm of Khor Al Balid. Though their event was not dated, it may represent the same extreme wave event observed in our cores. Extreme wave events in the Arabian sea have occurred throughout the Holocene, generated by Indian Ocean cyclones and tsunamis (Fritz et al., 2010; Hoffmann et al., 2015; Hoffmann et al., 2013a; Hoffmann et al., 2013b; Shah-hosseini et al., 2011). Catastrophic storms are rare in the Arabian Sea (three in the past 1200 years; Blount et al., 2010). Most storms are small and dissipate quickly (Fritz et al., 2010), though even cyclonic storms can cause significant watershed inundation and wadi flooding along the Dhofar coast (Al Ruheili et al., 2019). The Dhofar coast is highly vulnerable to tropical cyclones, which strike the region every five to seven years (Al Ruheili & Radke, 2020; Andreou et al., 2022; Mansour, 2019). The most recent cyclone, Mekunu in 2018, had a 5–8 m storm surge and caused high precipitation (∼600 mm), coastal flooding, and erosion (Al Ruheili et al., 2019; Andreou et al., 2022). The storm highly impacted the site at Khor Al Balid, causing a breach in the sand barrier at the mouth of the eastern estuary and patches of flooding approximately 100 m inland (Andreou et al., 2022). During the overwash event observed in our cores, marine material (e.g., sand and *Amphistegina* spp.) was transported at least 250 m inland (ALB3) and at least 550 m upstream into Khor Al Balid (ALB5). Because marine material was deposited much further inland and in both eastern and western arms of the lagoon, it is possible that the sand barriers on both sides were breached and that the event was of much larger magnitude than the recent storm Mekunu. Detailed instrumental and historical records of tropical cyclones prior to the 1900s are limited (Dibajnia et al., 2010; Membery, 2001, 2002). Written accounts and reviews of historical cyclone tracks provide information on past events, including a rare cyclone in the Gulf of Aden in 1885 (Membery, 2002) and a severe tropical storm that hit the southern Oman coast in 1898 (Dibajnia et al., 2010). Even relatively distant tropical cyclones (e.g., 370 away) can bring in tropical air over the Dhofar mountains, resulting in extreme rainfall and flooding of the Salalah plain (Membery, 2002). These nearby events, or more likely an unrecorded tropical cyclone during the 18th–19th centuries CE, could potentially have been large enough to cause the observed impacts at Khor Al Balid and Khor Rori.

Extreme waves generated by a tsunami is another probable cause for the observed overwash event. Three main sources for tsunamis in southern Oman include the Makran Subduction Zone (MSZ; between the Arabian/Eurasian Plates), the Sunda-Sumatra subduction zone (between the Indian/Australian Plates), and the Owen Fracture Zone (OFZ; a strike-slip boundary between the Arabian/Indian Plates; (Browning & Thomas, 2016; Hoffmann et al., 2020; Sieh, 2007). The MSZ can generate very large earthquakes (e.g., Mw>8.5; Hoffmann et al., 2020), generating tsunamis that directly impact the northern coast of Oman (Donato et al., 2008; Hoffmann et al., 2013b; Pilarczyk & Reinhardt, 2012). Large historical earthquakes from the MSZ have been documented in 1765, 1851, and 1945 (Mokhtari et al., 2019; Okal & Synolakis, 2008). The 1765 or the 1851 event could have caused the overwash observed in our cores; however, the southern coast of Oman is not in a direct path of impact from the MSZ, and the risk to the Dhofar coast from this source has been deemed very low (Rashidi et al., 2020). A tsunami generated from the Sunda-Sumatra subduction zone near Indoneasia, however, could highly impact this area of the coast (Browning & Thomas, 2016). Underwater earthquakes generated from the Sunda megathrust fault have been documented in 1797, 1833, 1861, 1907, 1935, 2000, 2002, 2004 and 2005 (Sieh, 2007). The 2004 tsunami generating event was well-recorded and caused a maximum runup (altitude of inland penetration) of only 3.3 m in Salalah (Okal et al., 2006). Historical tsunami events, however, are more difficult to track and estimate the magnitude of, including the 1797 and 1833 events which are recorded in corals (Sieh, 2007). Other evidence suggests that the last giant tsunami before the 2004 Indian Ocean tsunami occurred ∼2900 BP (Rubin et al., 2017) or were confined to the northeast Indian Ocean (Malik et al., 2019). Though the Indonesian subduction zone is relatively far from the southern Oman coast, it is possible that the 1797 or the 1833 earthquake events were large enough to cause our observed event on southern coast of Oman. Closest in proximity to the Dhofar coast, the 800 km long OFZ system, is theoretically possible of producing significant tsunamis of unknown potential, through strike slip or vertical block motions (Fournier et al., 2011; Tanioka & Satake, 1996). The Owen Ridge, a submarine feature ∼300–400 km from the southern Oman coast near the OFZ, contains evidence of several mass failure events (Rodriguez et al., 2013). These events could have triggered a tsunami; however, they likely date back to the Miocene or Pleistocene (Bache et al., 2011). Though there is no evidence (historical accounts, sediment deposits) of a OFZ tsunami (Rodriguez et al., 2013), the OFZ is a likely source if our event was the result of a tsunami.

The settlement at Khor Rori is thought to be abandoned well in advance of the 18th century CE (Degli Esposti & Pavan, 2020), therefore this event does not have much bearing on the history of the site. The port city at Khor Al Balid, however, may still have been occupied when this potential large cyclone or tsunami struck the coast. Along with the political, economic, and military issues towards the end of the 16th and 17th centuries CE (Fusaro, 2020; Pavan, 2021), this extreme wave event may have contributed to the decline and abandonment of the city at Khor Al Balid. Whether the sites were abandoned or not, this event, as well as other similarly destructive large storms and wave events, has archeological implications for site conservation. This is demonstrated by the damage observed to the site at Khor Al Balid following Mekunu in 2018 (D'Andrea, 2021; Pavan, 2021).

4.5.3 Implications for harbour activity

Changes in coastal morphology due to increased aridity and a decrease in sea level were likely occurring at both Khor Rori and Khor Al Balid simultaneously, though the slightly upstream location of Sumhuram likely lead to its decline earlier than al-Balīd. The progressive accumulation of coastal sediments and decreased input from the wadi ∼270–420 CE (Hoorn & Cremaschi, 2004) would have made it difficult for ships to enter to Khor Rori and conduct maritime trade activities at the port city ∼1 km upstream, even if the barrier was often open or partially open until very recently. As previously speculated, this likely contributed to abandonment of Sumhuram by the 5th century CE (Degli Esposti & Pavan, 2020; Hoorn & Cremaschi, 2004). Environmental changes may not have affected maritime activity at al-Balīd until several centuries later due to its location adjacent to the coast. Archaeological evidence and documented descriptions have provided information on the original harbour layout at al-Balīd. The presence of marine sand and aquatic organisms (testate amoebae and foraminifera) in ALB2 and ALB3 supports previous evidence that the site was surrounded on all four sides by water (Costa, 1979; D'Andrea, 2021). Our cores suggest that the eastern arm of Khor Al Balid closed off from the sea during the 12th century, but the western side was open until the 15th c. CE. The estimated founding of al-Balīd is around the 10th century CE, when harbour structures including jetties, breakwaters, and gates were built along the southern (seaside) city wall (Newton & Zarins, 2014). Additional harbour structures that would have supported horse exporting activities (paddocks, check dam and sluices for water supply, canopies, a stone quay, jetties, dry dock structures, and loading platforms on the eastern side of the lagoon) have been linked to the height of horse trade in the region (mid 14th to mid 16th centuries; Newton & Zarins, 2014). The coastal sand barriers were likely fully established by this time, suggesting that maritime trade activities were able to proceed without sea access into the eastern or western arms of the estuary. Recent archaeological excavations have suggested that the city did not have a substantial harbor (Ghidoni & Pavan, 2022; Pavan & Visconti, 2023). Instead, small boats (sambuqs or kambaris) used large stone anchors in a roadstead (sheltered body of water) to transport trade goods to and from larger ships anchored offshore (Newton & Zarins, 2019; Pavan

& Visconti, 2023). The recent discovery of sand-covered blocks south of the breakwater that extend ∼50 m offshore (D'Andrea et al., 2022) also provide evidence for anchoring structures and a potential wooden pier used load/unload goods such as horses (Ghidoni & Pavan, 2022). These archaeological findings agree with our results. Shipping activities were likely able to proceed for several centuries until significant amounts of sand had accumulated along the coast, increasing the width of the shoreline (i.e., beach is currently at least 120 m wide) and decreasing the feasibility of transporting goods.

Another possibility is that the dates of sediments obtained here are slightly older than estimated due to the incorporation of older, reworked organic matter into sediments (through erosion and redeposition; Strunk et al., 2020). If this is the case, the formation of sand barriers at Khor Al Balid may have occurred closer towards the founding of al-Balīd. In any case, the estuary entrances that once formed natural harbours were likely becoming choked with sand, and may have been frequently dredged to keep the openings clear (Newton & Zarins, 2019). The eventual formation of sand barriers along the shore of Khor Al Balid through a drop in sea level and an increasingly arid climate greatly changed the morphology of the coast. These environmental changes, alongside political/military pressures and bans on major exports (D'Andrea, 2021; Fusaro, 2020) likely had a significant impact on harbor activity and the nearby population.

4.6 Conclusion

Accumulations of sands have naturally built up along the southern coast of Oman over the past ∼1500 years as a result of decreased sea level (∼1 m in the past 1 ka) and an increasingly arid climate, allowing longshore drift to choke and close the wadi entrances (Decker et al., 2020; Hoorn & Cremaschi, 2004; Khanna et al., 2021). Lithological, microfossil (foraminifera and testate amoebae), and geochemical (μXRF) records within sediment cores from Khor Rori and Khor Al Balid were analyzed here. Results indicate that the eastern arm of Khor Al Balid closed off from the sea around the 12th century CE, while the western arm closed around the 15th century CE. Results align well with previous archaeological findings of site chronology and maritime trade structures at the site's ancient port city of al-Balīd. Our results suggest that the sand barriers had accumulated and formed the lagoon at Khor Al Balid by the time maritime trade activity reached its peak at the site. Harbour activity at al-Balīd is thought to have mainly involved jetties, breakwaters, and the transport of goods between smaller boats and larger ships anchored offshore instead of substantial harbour structures (Ghidoni & Pavan, 2022; Pavan & Visconti, 2023). This would mean that maritime trade was possible even after closure of the natural harbours of the estuary. Over time, however, shipping activities were likely increasingly difficult as sand continued to accumulate and widen the beach along the coastline. Evidence of a large overwash event dating around the 18th–19th century is recorded in almost all cores across Khor Al Balid and Khor Rori. This event may have been the result of a very large tropical cyclone or tsunami, though further research is required to determine the cause. This event, and the progressive environmental changes along the coast likely had a significant impact on the population near Khor Al Balid and may have contributed towards abandonment of the city. Results from this study provide an important paleoenvironmental perspective towards the overall understanding of site development and decline at Khor Rori and Khor Al Balid.

Acknowledgments

This field work was conducted in 1995, with the Transarabia Coastal Survey. This was part of the Transarabia Expedition, an ongoing regional survey of Dhofar sponsored by His Majesty, Sultan Qaboos and the Ministry of Information. We greatly appreciated the support of Dr. Abdul Aziz bin Mohammed Al-Rowas, Minister of Information and his staff. Various corporate sponsors including British Petroleum, DHL Worldwide Express, Nortech Surveys Ltd., Airwork Ltd., OUA-Inchcape Middle East, Holiday Inn and the InterContinental Hotels offered substantial logistical support. The Expedition was directed by Dr. Juris Zarins of Southwest Missouri State University and Jana Owens of UCLA.

References

Adegbie, A. T., Schneider, R. R., Röhl, U., & Wefer, G. (2003). Glacial millennial-scale fluctuations in central African precipitation recorded in terrigenous sediment supply and freshwater signals offshore Cameroon. Palaeogeogr. ,Palaeoclimatol., Palaeoecol., 197(3–4), 323–333. https://doi.org/10.1016/S0031-0182(03)00474-7.

Al-Kindi, K. M., Al Nadhairi, R., & Al Akhzami, S. (2023). Dynamic Change in Normalised Vegetation Index (NDVI) from 2015 to 2021 in Dhofar, Southern Oman in Response to the Climate Change. Agriculture, 13(3), 592. https://doi.org/10.3390/agriculture13030592.

Al Ruheili, A., Dahm, R., & Radke, J. (2019). Wadi flood impact assessment of the 2002 cyclonic storm in Dhofar, Oman under present and future sea level conditions. Journal of Arid Environments, 165(March), 73–80. https://doi.org/10.1016/j.jaridenv.2019.04.002.

Al Ruheili, A., & Radke, J. (2020). Visualization of 2002 storm surge along the coast of Dhofar, case study of Oman. Environment, Development and Sustainability, 22(1), 501–517. https://doi.org/10.1007/s10668-018-0186-z.

Amato, V., Aiello, G., Barra, D., Caporaso, L., Caruso, T., Giaccio, B., Parisi, R., & Rossi, A. (2020). Holocene paleogeographic evolution of an ancient port city of the central Mediterranean area: Natural and anthropogenic modifications from Salerno city, southern Italy. Geoarchaeology, 35(3), 366–383. https://doi.org/10.1002/gea.21774.

Andreou, G. M., Westley, K., Huigens, H. O., & Blue, L. (2022). Exploring the Impact of Tropical Cyclones on Oman's Maritime Cultural Heritage Through the Lens of Al-Baleed, Salalah (Dhofar Governorate). Journal of Maritime Archaeology, 17(3), 465–486. https://doi.org/10.1007/s11457-022-09333-4.

Bache, F., Leroy, S., Baurion, C., Robinet, J., Gorini, C., Lucazeau, F., Razin, P., D'Acremont, E., & Al-Toubi, K. (2011). Post-rift uplift of the Dhofar margin (Gulf of Aden). Terra Nova, 23(1), 11–18. https://doi.org/10.1111/j.1365-3121.2010.00975.x.

Bahr, A., Lamy, F., Arz, H., Kuhlmann, H., & Wefer, G. (2005). Late glacial to Holocene climate and sedimentation history in the NW Black Sea. Marine Geology, 214(4), 309–322. https://doi.org/10.1016/j.margeo.2004.11.013.

Blount, C., Fritz, H. M., & Al-Harthy, A. H. M. (2010). Coastal vulnerability assessment based on historic tropical cyclones in the Arabian Sea. In Y.

Charabi (Ed.), Indian Ocean Tropical Cyclones and Climate Change. Springer Science+Business Media.

Browning, J., & Thomas, N. (2016). An assessment of the tsunami risk in Muscat and Salalah, Oman, based on estimations of probable maximum loss. International Journal of Disaster Risk Reduction, 16, 75–87. https://doi.org/10.1016/j.ijdrr.2016.02.002.

Burns, S. J., Matter, A., Frank, N., & Mangini, A. (1998). Speleothem-based paleoclimate record from northern Oman. Geology, 26(6), 499. https://doi.org/10.1130/0091-7613(1998)026<0499:SBPRFN>2.3.CO;2.

Cazenave, A. (2018). Global sea-level budget 1993 – present. Earth Syst. Sci. Data, 10, 1551–1590.

Charman, D. J., Gehrels, W. R., Manning, C., & Sharma, C. (2010). Reconstruction of recent sea-level change using testate amoebae. Quat. Res., 73(2), 208–219. https://doi.org/10.1016/j.yqres.2009.11.009.

Chawchai, S., Kylander, M. E., Chabangborn, A., Löwemark, L., & Wohlfarth, B. (2016). Testing commonly used X-ray fluorescence core scanning-based proxies for organic-rich lake sediments and peat. Boreas, 45(1), 180–189. https://doi.org/10.1111/bor.12145.

Connan, J., Ghidoni, A., Mezzatesta, E., Joliot, C., Mathe, C., Vosmer, T., Gley, R., Bihannic, I., Pavan, A., Engel, M. H., & Zumberge, A. (2023). Geochemical study of the luting and coating of medieval watercraft from the ship timbers discovered in the citadel of al-Balīd, Oman: Composition and origin. J. Archaeol. Sci.: Rep., 49(January), 104051. https://doi.org/10.1016/j.jasrep.2023.104051.

Costa, P. M. (1979). The Study of the city of Zafār (al-Balīd). Journal of Oman Studies, 5, 111–150.

Cremaschi, M., & Negrino, F. (2002). The frankincense road of Sumhuram: paleoenvironmental and prehistorical background. In Khor Rori Report 1 (pp. 325–384).

Cremaschi, M., & Negrino, F. (2005). Evidence for an abrupt climatic change at 870014C yr B.P. in rockshelters and caves of Gebel Qara (Dhofar-Oman): Palaeoenvironmental implications. Geoarchaeology, 20(6), 559–579. https://doi.org/10.1002/gea.20068.

Cremaschi, M., Zerboni, A., Charpentier, V., Crassard, R., Isola, I., Regattieri, E., & Zanchetta, G. (2015). Early–Middle Holocene environmental changes and pre-Neolithic human occupations as recorded in the cavities of Jebel Qara (Dhofar, southern Sultanate of Oman). Quaternary International, 382, 264–276. https://doi.org/10.1016/j.quaint.2014.12.058.

D'Andrea, A. (2021). Reconsidering the Topography of al-Balīd (Oman): A Preliminary Review of the Graphical Documentation. Annali Sezione Orientale, 81(1–2), 39–50. https://doi.org/10.1163/24685631-12340110.

D'Andrea, A., Giunta, R., Pavan, A., & Valentini, R. (2022). New activities at the archaeological site of al-Balid (December 2021-January 2022). International Association for the Study of Arabia Bulletin, 28.

D'Andrea, A., Guinta, R., Pavan, A., & Valentini, R. (2021). Introduction. In A. D'Andrea, R. Guinta, A. Pavan, & R. Valentini (Eds.), The site of Zafar/al-Balid (Sultanate of Oman): Archaeological investigations between past and present. Centro Interdipartimentale di Servizi di Archeologia (CISA).

Debenay, A. J.-P., & Guillou, J.-J. (2002). Ecological Transitions Indicated by Foraminiferal Assemblages in Paralic Environments. Estuaries, 25(6), 1107–1120.

Decker, V., Falkenroth, M., Lindauer, S., Landgraf, J., Al-Lawati, Z., Al-Rahbi, H., Franz, S. O., & Hoffmann, G. (2020). Collapse of Holocene mangrove ecosystems along the coastline of Oman. Quaternary Research, 100, 52–76. https://doi.org/10.1017/qua.2020.96.

Degli Esposti, M., & Pavan, A. (2020). Water and power in South Arabia: the excavation of "Monumental Building 1" (MB1) at Sumhuram (Sultanate of Oman). Arabian Archaeology and Epigraphy, 31(2), 393–421. https://doi.org/10.1111/aae.12159.

Dibajnia, M., Soltanpour, M., Nairn, R., & Allahyar, M. (2010). Cyclone Gonu: the most intense tropical cyclone on record in the Arabian Sea. In Y. Charabi (Ed.), Indian Ocean Tropical Cyclones and Climate Change (pp. 149–157). Springer Science+Business Media.

Dieng, H. B., Cazenave, A., Meyssignac, B., & Ablain, M. (2017). New estimate of the current rate of sea level rise from a sea level budget approach. Geophysical Research Letters, 44(8), 3744–3751. https://doi.org/10.1002/2017GL073308.

Donato, S. V., Reinhardt, E. G., Boyce, J. I., Rothaus, R., & Vosmer, T. (2008). Identifying tsunami deposits using bivalve shell taphonomy. Geology, 36(3), 199–202. https://doi.org/10.1130/G24554A.1.

Finkler, C., Fischer, P., Baika, K., Rigakou, D., Metallinou, G., Hadler, H., & Vött, A. (2018). Tracing the Alkinoos Harbor of ancient Kerkyra, Greece, and reconstructing its paleotsunami history. Geoarchaeology, 33(1), 24–42. https://doi.org/10.1002/gea.21609.

Fleitmann, D., Burns, S. J., Mangini, A., Mudelsee, M., Kramers, J., Villa, I., Neff, U., Al-Subbary, A. A., Buettner, A., Hippler, D., & Matter, A. (2007). Holocene ITCZ and Indian monsoon dynamics recorded in stalagmites from Oman and Yemen (Socotra). Quaternary Science Reviews, 26(1–2), 170–188. https://doi.org/10.1016/j.quascirev.2006.04.012.

Fleitmann, D., Burns, S. J., Mudelsee, M., Neff, U., Kramers, J., Mangini, A., & Matter, A. (2003). Holocene Forcing of the Indian Monsoon Recorded in a Stalagmite from Southern Oman. Science, 300(5626), 1737–1739. https://doi.org/10.1126/science.1083130.

Fleitmann, D., Burns, S. J., Neff, U., Mudelsee, M., Mangini, A., & Matter, A. (2004). Palaeoclimatic interpretation of high-resolution oxygen isotope profiles derived from annually laminated speleothems from Southern Oman. Quat. Sci. Rev., 23, 935–945. https://doi.org/10.1016/j.quascirev.2003.06.019.

Fournier, M., Chamot-Rooke, N., Rodriguez, M., Huchon, P., Petit, C., Beslier, M. O., & Zaragosi, S. (2011). Owen Fracture Zone: The Arabia–India plate boundary unveiled. Earth and Planetary Science Letters, 302(1–2), 247–252. https://doi.org/10.1016/j.epsl.2010.12.027.

Fritz, H. M., Blount, C. D., Albusaidi, F. B., & Al-Harthy, A. H. M. (2010). Cyclone Gonu storm surge in Oman. Estuarine, Coastal and Shelf Science, 86(1), 102–106. https://doi.org/10.1016/j.ecss.2009.10.019.

Fusaro, A. (2019). New project on Islamic ceramics from al-Balid: Chronology, technology, tradition, and provenance. Proceedings of the Seminar for Arabian Studies, 49, 129–146.

Fusaro, A. (2020). The Islamic Port of al-Balīd (Oman), between Land and Sea: Place of Trade, Exchange, Diversity, and Coexistence. Journal of Material Cultures in the Muslim World, 1(1–2), 67–95. https://doi.org/10.1163/26666286-12340003.

Galletti, C. S., Turner, B. L., & Myint, S. W. (2016). Land changes and their drivers in the cloud forest and coastal zone of Dhofar, Oman, between 1988 and 2013. Regional Environmental Change, 16(7), 2141–2153. https://doi.org/10.1007/s10113-016-0942-2.

Gasse, F., & Van Campo, E. (1994). Abrupt post-glacial climate events in West Asia and North Africa monsoon domains. Earth and Planetary Science Letters, 126(4), 435–456. https://doi.org/10.1016/0012-821X(94)90123-6.

Gehrels, W. R. (2006). DISTRIBUTION OF TESTATE AMOEBAE IN SALT MARSHES ALONG THE NORTH AMERICAN EAST COAST. The Journal of Foraminiferal Research, 36(3), 201–214. https://doi.org/10.2113/gsjfr.36.3.201.

Gennari, G., Rosenberg, T., Spezzaferri, S., Berger, J.-P., Fleitmann, D., Preusser, F., Al-Shanti, M., & Matter, A. (2011). FAUNAL EVIDENCE OF A HOLOCENE PLUVIAL PHASE IN SOUTHERN ARABIA WITH REMARKS ON THE MORPHOLOGICAL VARIABILITY OF HELENINA ANDERSENI. The Journal of Foraminiferal Research, 41(3), 248–259. https://doi.org/10.2113/gsjfr.41.3.248.

Ghidoni, A., & Pavan, A. (2022). Boats, horses, and moorings: maritime activities at al-Balīd in the medieval period. Proceedings of the Seminar for Arabian Studies, 51, 169–182.

Goodman, B. N., Reinhardt, E. G., Dey, H. W., Boyce, J. I., Schwarcz, H. P., Sahoğlu, V., Erkanal, H., & Artzy, M. (2009). Multi-proxy geoarchaeological study redefines understanding of the paleocoastlines and ancient harbours of Liman Tepe (Iskele, Turkey). Terra Nova, 21(2), 97–104. https://doi.org/10.1111/j.1365-3121.2008.00861.x.

Gregory, B. R. B., Reinhardt, E. G., Macumber, A. L., Nasser, N. A., Patterson, R. T., Kovacs, S. E., & Galloway, J. M. (2017). Sequential sample reservoirs for Itrax-XRF analysis of discrete samples. J. Paleolimnol., 57(3), 287–293. https://doi.org/10.1007/s10933-017-9944-4.

Heaton, T. J., Köhler, P., Butzin, M., Bard, E., Reimer, R. W., Austin, W. E. N., Bronk Ramsey, C., Grootes, P. M., Hughen, K. A., Kromer, B., Reimer, P. J., Adkins, J., Burke, A., Cook, M. S., Olsen, J., & Skinner, L. C. (2020). Marine20—The Marine Radiocarbon Age Calibration Curve (0–55,000 cal BP). Radiocarbon, 62(4), 779–820. https://doi.org/10.1017/RDC.2020.68.

Hoffmann, G., Grützner, C., Reicherter, K., & Preusser, F. (2015). Geo-archaeological evidence for a Holocene extreme flooding event within the Arabian Sea (Ras al Hadd, Oman). Quaternary Science Reviews, 113, 123–133. https://doi.org/10.1016/j.quascirev.2014.09.033.

Hoffmann, G., Grützner, C., Schneider, B., Preusser, F., & Reicherter, K. (2020). Large Holocene tsunamis in the northern Arabian Sea. Marine Geology, 419 (September 2019), 106068. https://doi.org/10.1016/j.margeo.2019.106068.

Hoffmann, G., Reicherter, K., Wiatr, T., Grützner, C., & Rausch, T. (2013a). Block and boulder accumulations along the coastline between Fins and Sur (Sultanate of Oman): tsunamigenic remains? Natural Hazards, 65(1), 851–873. https://doi.org/10.1007/s11069-012-0399-7.

Hoffmann, G., Rupprechter, M., Balushi, N. Al, Grützner, C., & Reicherter, K. (2013b). The impact of the 1945 Makran tsunami along the coastlines of the Arabian Sea (Northern Indian Ocean) - a review. Zeitschrift Für Geomorphologie, Supplementary Issues, 57(4), 257–277. https://doi.org/10.1127/0372-8854/2013/S-00134.

Hoffmann, G., Rupprechter, M., & Mayrhofer, C. (2013c). Review of the long-term coastal evolution of North Oman – subsidence versus uplift. Z. Dt. Ges. Geowiss., 164(2), 237–252. https://doi.org/10.1127/1860-1804/2013/0002.

Hoorn, C., & Cremaschi, M. (2004). Late Holocene palaeoenvironmental history of Khawr Rawri and Khawr Al Balid (Dhofar, Sultanate of Oman). Palaeogeography, Palaeoclimatology, Palaeoecology, 213(1–2), 1–36. https://doi.org/10.1016/j.palaeo.2004.03.014.

Horton, B. P., & Edwards, R. J. (2006). Quantifying Holocene sea-level change using intertidal foraminifera: lessons from the British Isles. Anuário Do Instituto de Geociências, 29(1), 541–542. https://doi.org/10.11137/2006_1_541-542.

Hottinger, L., Halicz, E., & Reiss, Z. (1993). Recent foraminiferida from the Gulf of Aqaba, Red Sea. Slovenska Akademija Znanosti in Umetnosti.

Huang, J., Löwemark, L., Chang, Q., Lin, T., Chen, H., Song, S., & Wei, K. (2016). Choosing optimal exposure times for XRF core-scanning: Suggestions based on the analysis of geological reference materials. Geochemistry, Geophysics, Geosystems, 17(4), 1558–1566. https://doi.org/10.1002/2016GC006256.

Khanna, P., Petrovic, A., Ramdani, A. I., Homewood, P., Mettraux, M., & Vahrenkamp, V. (2021). Mid-Holocene to present circum-Arabian sea level database: Investigating future coastal ocean inundation risk along the Arabian plate shorelines. Quat. Sci. Rev., 261, 106959. https://doi.org/10.1016/j.quascirev.2021.106959.

Krywy-Janzen, A., Reinhardt, E. G., McNeill-Jewer, C., Coutino, A., Waltham, B., Stastna, M., Rissolo, D., Meacham, S., & van Hengstum, P. (2019). Water-level change recorded in Lake Pac Chen Quintana Roo, Mexico infers connection with the aquifer and response to Holocene sea-level rise and Classic Maya droughts. J. Paleolimnol., 62(4), 373–388. https://doi.org/10.1007/s10933-019-00094-0.

Kwarteng, A. Y., Dorvlo, A. S., & Vijaya Kumar, G. T. (2009). Analysis of a 27-year rainfall data (1977-2003) in the Sultanate of Oman. International Journal of Climatology, 29(4), 605–617. https://doi.org/10.1002/joc.1727.

Lambeck, K., Purcell, A., Flemming, N. C., Vita-Finzi, C., Alsharekh, A. M., & Bailey, G. N. (2011). Sea level and shoreline reconstructions for the Red Sea: Isostatic and tectonic considerations and implications for hominin migration out of Africa. Quaternary Science Reviews, 30(25–26), 3542–3574. https://doi.org/10.1016/j.quascirev.2011.08.008.

Langer, M. R., & Mouanga, G. H. (2016). Invasion of amphisteginid foraminifera in the Adriatic Sea. Biol. Invasions, 18(5), 1335–1349. https://doi.org/10.1007/s10530-016-1070-0.

Lézine, A.-M., Robert, C., Cleuziou, S., Inizan, M.-L., Braemer, F., Saliège, J.-F., Sylvestre, F., Tiercelin, J.-J., Crassard, R., Méry, S., Charpentier, V., & Steimer-Herbet, T. (2010). Climate change and human occupation in the Southern Arabian lowlands during the last deglaciation and the Holocene. Global and Planetary Change, 72(4), 412–428. https://doi.org/10.1016/j.gloplacha.2010.01.016.

Lézine, A.-M., Saliège, J., Mathieu, R., Tagliatela, T., Mery, S., Charpentier, V., Cleuziou, S., & History, S. V. (2002). Mangroves of Oman during the late Holocene: climatic implications and impact on human settlements. Veget. Hist. Archaeobot., 11, 221–232.

Lippi, M. M., Bellini, C., Benvenuti, M., & Fedi, M. (2011). Palaeoenvironmental signals in ancient urban setting: The heavy rainfall record in Sumhuram, a pre-Islamic archaeological site of Dhofar (S Oman). The Holocene, 21(6), 951–965. https://doi.org/10.1177/0959683611400203.

Lischi, S., Pavan, A., & Fusaro, A. (2020). Preliminary investigations on the local pottery in Dhofar (southern Oman) from the Iron Age to the Islamic period. International Association for the Study of Arabia (IASA) News and Research by Country, 25, 15–17.

Lückge, A., Doose-Rolinski, H., Khan, A. ., Schulz, H., & von Rad, U. (2001). Monsoonal variability in the northeastern Arabian Sea during the past 5000 years: geochemical evidence from laminated sediments. Palaeogeography, Palaeoclimatology, Palaeoecology, 167(3–4), 273–286. https://doi.org/10.1016/S0031-0182(00)00241-8.

Machado, M. J., Pérez-González, A., & Benito, G. (1998). Paleoenvironmental Changes during the Last 4000 yr in the Tigray, Northern Ethiopia. Quaternary Research, 49(3), 312–321. https://doi.org/10.1006/qres.1998.1965.

Malik, J. N., Johnson, F. C., Khan, A., Sahoo, S., Irshad, R., Paul, D., Arora, S., Baghel, P. K., & Chopra, S. (2019). Tsunami records of the last 8000 years in the Andaman Island, India, from mega and large earthquakes: Insights on recurrence interval. Scientific Reports, 9(1), 18463. https://doi.org/10.1038/s41598-019-54750-6.

Mansour, S. (2019). Geospatial modelling of tropical cyclone risks to the southern Oman coasts. International Journal of Disaster Risk Reduction, 40(January), 101151. https://doi.org/10.1016/j.ijdrr.2019.101151.

Marriner, N., & Morhange, C. (2007). Geoscience of ancient Mediterranean harbours. Earth-Sci. Rev., 80(3–4), 137–194. https://doi.org/10.1016/j.earscirev.2006.10.003.

Marshall, J. F., & McCulloch, M. T. (2002). An assessment of the Sr/Ca ratio in shallow water hermatypic corals as a proxy for sea surface temperature. Geochim. Cosmochim. Acta, 66(18), 3263–3280. https://doi.org/10.1016/S0016-7037(02)00926-2.

McLachlan, A., Fisher, M., Al-Habsi, H. N., Al-Shukairi, S. S., & Al-Habsi, A. M. (1998). Ecology of sandy beaches in Oman. Journal of Coastal Conservation, 4(2), 181–190. https://doi.org/10.1007/BF02806510.

McNeill-Jewer, C. A., Reinhardt, E. G., Collins, S., Kovacs, S., Chan, W. M., Devos, F., & LeMaillot, C. (2019). The effect of seasonal rainfall on nutrient input and biological productivity in the Yax Chen cave system (Ox Bel Ha), Mexico, and implications for μXRF core studies of paleohydrology. Palaeogeogr. ,Palaeoclimatol., Palaeoecol., 534(July), 109289. https://doi.org/10.1016/j.palaeo.2019.109289.

Membery, D. (2001). Monsoon tropical cyclones: Part 1. Weather, 56, 431–438. https://doi.org/10.1002/wea.3402.

Membery, D. (2002). Monsoon tropical cyclones: Part 2. Weather, 57, 246–255. https://doi.org/10.1002/wea.3402.

Milne, G. A., & Mitrovica, J. X. (2008). Searching for eustasy in deglacial sea-level histories. Quat. Sci. Rev., 27(25–26), 2292–2302. https://doi.org/10.1016/j.quascirev.2008.08.018.

Mokhtari, M., Ala Amjadi, A., Mahshadnia, L., & Rafizadeh, M. (2019). A review of the seismotectonics of the Makran Subduction Zone as a baseline for Tsunami Hazard Assessments. Geoscience Letters, 6(1), 13. https://doi.org/10.1186/s40562-019-0143-1.

Moraetis, D., Mattern, F., Scharf, A., Frijia, G., Kusky, T. M., Yuan, Y., & El-Hussain, I. (2018). Neogene to Quaternary uplift history along the passive margin of the northeastern Arabian Peninsula, eastern Al Hajar Mountains, Oman. Quaternary Research (United States), 90(2), 418–434. https://doi.org/10.1017/qua.2018.51.

Murray, J. W. (2014). Ecology and Palaeoecology of Benthic Foraminifera. Routledge. https://doi.org/10.4324/9781315846101.

Newton, L. S., & Zarins, J. (2014). A possible Indian quarter at al-Baleed in the fourteenth-seventeenth centuries AD? Proceedings of the Seminar for Arabian Studies, 44(July 2013), 257–276.

Newton, L. S., & Zarins, J. (2019). The archaeological heritage of Oman, Vol 1. Dhofar through the ages: an ecological, archaeological, and historical landscape. Archaeopress Publishing LTD.

Okal, E. A., Fritz, H. M., Raad, P. E., Synolakis, C., Al-Shijbi, Y., & Al-Saifi, M. (2006). Oman Field Survey after the December 2004 Indian Ocean Tsunami. Earthquake Spectra, 22(3_suppl), 203–218. https://doi.org/10.1193/1.2202647.

Okal, E. A., & Synolakis, C. E. (2008). Far-field tsunami hazard from mega-thrust earthquakes in the Indian Ocean. Geophysical Journal International, 172(3), 995–1015. https://doi.org/10.1111/j.1365-246X.2007.03674.x.

Olteanu, M., & Villa-Vialaneix, N. (2015). On-line relational and multiple relational SOM. Neurocomputing, 147(1), 15–30. https://doi.org/10.1016/j.neucom.2013.11.047.

Pavan, A. (2021). A sentinel on the Indian Ocean: The Citadel of Al-Balid (Excavations 2016–2020). In A. D'Andrea, R. Guinta, A. Pavan, & R. Valentini

(Eds.), The site of Zafar/al-Balid (Sultanate of Oman): Archaeological investigations between past and present (Vol. 12, pp. 23–46). Centro Interdipartimentale di Servizi di Archeologia (CISA).

Pavan, A., & Al Kathiri, A. (2021). The objects from al-Balid at the museum of the Frankincense Land, Salalah, Sultanate of Oman. In A. D'Andrea, R. Guinta, A. Pavan, & R. Valentini (Eds.), The site of Zafar/al-Balid (Sultanate of Oman): Archaeological investigations between past and present (Vol. 12, pp. 127–136). Centro Interdipartimentale di Servizi di Archeologia (CISA).

Pavan, A., & Visconti, C. (2023). Looking for connections between Arabia and East Asia: diplomatic gifts, luxury vessels and utilitarian wares unearthed at the city port of al-Balīd, Sultanate of Oman. Egitto e Vicino Oriente, 205–227. https://doi.org/10.12871/978883339777114.

Peinerud, E. K. (2000). Interpretation of Si concentrations in lake sediments: three case studies. Environ. Geol., 40(1), 64–72.

Pilarczyk, J. E., & Reinhardt, E. G. (2012). Testing foraminiferal taphonomy as a tsunami indicator in a shallow arid system lagoon: Sur, Sultanate of Oman. Marine Geology, 295–298(November 1945), 128–136. https://doi.org/10.1016/j.margeo.2011.12.002.

Pint, A., Seeliger, M., Frenzel, P., Feuser, S., Erkul, E., Berndt, C., Klein, C., Pirson, F., & Brückner, H. (2015). The environs of Elaia's ancient open harbour – a reconstruction based on microfaunal evidence. J. Archaeol. Sci., 54, 340–355. https://doi.org/10.1016/j.jas.2014.06.011.

Poag, C. W. (2015). Benthic Foraminifera of the Gulf of Mexico: Distribution, Ecology, Paleoecology. Texas A&M University Press.

Rashidi, A., Dutykh, D., Shomali, Z. H., Keshavarz Farajkhah, N., & Nouri, M. (2020). A Review of Tsunami Hazards in the Makran Subduction Zone. Geosciences, 10(9), 372. https://doi.org/10.3390/geosciences10090372.

Reimer, P. J., Austin, W. E. N., Bard, E., Bayliss, A., Blackwell, P. G., Bronk Ramsey, C., Butzin, M., Cheng, H., Edwards, R. L., Friedrich, M., Grootes, P. M., Guilderson, T. P., Hajdas, I., Heaton, T. J., Hogg, A. G., Hughen, K. A., Kromer, B., Manning, S. W., Muscheler, R., ... Talamo, S. (2020). The IntCal20 Northern Hemisphere Radiocarbon Age Calibration Curve (0–55 cal kBP). Radiocarb., 62(4), 725–757. https://doi.org/10.1017/RDC.2020.41.

Reinhardt, E. G. (2000). Al Balid Harbor Site Formation: Evolution of the Ancient Harbor at Al Balid, Oman. Sedimentological and Micropaleontological Evidence. [Unpublished Report, McMaster Univserity].

Reinhardt, E. G., Patterson, R. T., & Schroeder-Adams, C. J. (1994). Geoarchaeology of the ancient harbor site of Caesarea Maritima, Israel; evidence from sedimentology and paleoecology of benthic foraminifera. J. Foraminiferal Res., 24(1), 37–48. https://doi.org/10.2113/gsjfr.24.1.37.

Ribechini, E., Pérez-Arantegui, J., Pavan, A., Degano, I., Zanaboni, M., & Colombini, M. P. (2016). First evidence of purple pigment production and dyeing in southern Arabia (Sumhuram, Sultanate of Oman) revealed by mass spectrometric and chromatographic techniques. Journal of Cultural Heritage, 19, 486–491. https://doi.org/10.1016/j.culher.2015.11.006.

Riddick, N. L., Boyce, J. I., Krezoski, G. M., Şahoğlu, V., Erkanal, H., Tuğcu, İ., Alkan, Y., Gabriel, J. J., Reinhardt, E. G., & Goodman-Tchernov, B. N. (2022a). Palaeoshoreline reconstruction and underwater archaeological potential of Liman Tepe: A long-occupied coastal prehistoric settlement in western Anatolia, Turkey. Quat. Sci. Rev., 276, 107293. https://doi.org/10.1016/j.quascirev.2021.107293.

Riddick, N. L., Boyce, J. I., Reinhardt, E. G., Rothaus, R. M., Chomicki, K. M., & McCarthy, F. M. G. (2021). Multi-proxy palaeoenvironmental record of coastal tectonic uplift and abandonment (ca. 6th c. CE) of Lechaion's inner harbour, ancient Corinth, Greece. Quat. Sci. Rev., 267, 107080. https://doi.org/10.1016/j.quascirev.2021.107080.

Riddick, N. L., Boyce, J. I., Şahoğlu, V., Erkanal, H., Tuğcu, İ., Alkan, Y., Reinhardt, E. G., & Goodman-Tchernov, B. N. (2022b). Coastal palaeoenvironmental record of Late Bronze to Iron Age harbour development at Liman Tepe-Clazomenae, western Anatolia, Turkey. Mar. Geol., 450(June), 106842. https://doi.org/10.1016/j.margeo.2022.106842.

Rietti-shati, A. M., Shemesh, A., & Karlen, W. (1998). A 3000-Year Climatic Record from Biogenic Silica Oxygen Isotopes in an Equatorial High- Altitude Lake. Science, 281(5379), 980–982.

Rodriguez, M., Chamot-Rooke, N., Hébert, H., Fournier, M., & Huchon, P. (2013). Owen Ridge deep-water submarine landslides: implications for tsunami hazard along the Oman coast. Natural Hazards and Earth System Sciences, 13(2), 417–424. https://doi.org/10.5194/nhess-13-417-2013.

Rothwell, R. G., & Croudace, I. W. (2015). Twenty Years of XRF Core Scanning Marine Sediments: What Do Geochemical Proxies Tell Us? In I. W. Croudace & R. G. Rothwell (Eds.), Micro-XRF Studies of Sediment Cores: Applications of a Non-destructive Tool for the Environmental Sciences (Vol. 17, pp. 25–102). Springer Netherlands. https://doi.org/10.1007/978-94-017-9849-5.

Rubin, C. M., Horton, B. P., Sieh, K., Pilarczyk, J. E., Daly, P., Ismail, N., & Parnell, A. C. (2017). Highly variable recurrence of tsunamis in the 7,400 years before the 2004 Indian Ocean tsunami. Nature Communications, 8(1), 16019. https://doi.org/10.1038/ncomms16019.

Scott, D. B., Medioli, F. S., & Schafer, C. T. (2001). Chapter 2: Methodological Considerations. In Monitoring in Coastal Environments Using Foraminifera and Thecamoebian Indicators (pp. 10–27). Cambridge University Press. https://doi.org/10.1017/CBO9780511546020.

Shah-hosseini, M., Morhange, C., Naderi Beni, A., Marriner, N., Lahijani, H., Hamzeh, M., & Sabatier, F. (2011). Coastal boulders as evidence for high-energy waves on the Iranian coast of Makran. Marine Geology, 290(1–4), 17–28. https://doi.org/10.1016/j.margeo.2011.10.003.

Shammas, M. I., & Jacks, G. (2007). Seawater intrusion in the Salalah plain aquifer, Oman. Environ. Geol., 53(3), 575–587. https://doi.org/10.1007/s00254-007-0673-2.

Sieh, K. (2007). The Sunda Megathrust — Past Present and Future. Journal of Earthquake and Tsunami, 01(01), 1–19. https://doi.org/10.1142/S179343110700002X.

Smith, D. G. (1987). A Mini-Vibracoring System. Journal of Sedimentary Petrology, 57(4), 757–794.

Smith, D. G. (1998). Vibracoring: a new method for coring deep lakes. Palaeogeography, Palaeoclimatology, Palaeoecology, 140(1–4), 433–440. https://doi.org/10.1016/S0031-0182(98)00031-5.

Stock, F., Knipping, M., Pint, A., Ladstätter, S., Delile, H., Heiss, A. G., Laermanns, H., Mitchell, P. D., Ployer, R., Steskal, M., Thanheiser, U., Urz, R., Wennrich, V., & Brückner, H. (2016). Human impact on Holocene sediment dynamics in the Eastern Mediterranean - the example of the Roman harbour of Ephesus. Earth Surf. Process. Landf., 41(7), 980–996. https://doi.org/10.1002/esp.3914.

Stock, F., Pint, A., Horejs, B., Ladstätter, S., & Brückner, H. (2013). In search of the harbours: New evidence of Late Roman and Byzantine harbours of Ephesus. Quat. Int., 312, 57–69. https://doi.org/10.1016/j.quaint.2013.03.002.

Strunk, A., Olsen, J., Sanei, H., Rudra, A., & Larsen, N. K. (2020). Improving the reliability of bulk sediment radiocarbon dating. Quat. Sci. Rev., 242, 106442. https://doi.org/10.1016/j.quascirev.2020.106442.

Tanioka, Y., & Satake, K. (1996). Tsunami generation by horizontal displacement of ocean bottom. Geophysical Research Letters, 23(8), 861–864. https://doi.org/10.1029/96GL00736.

Tjallingii, R., Stattegger, K., Wetzel, A., & Van Phach, P. (2010). Infilling and flooding of the Mekong River incised valley during deglacial sea-level rise. Quaternary Science Reviews, 29(11–12), 1432–1444. https://doi.org/10.1016/j.quascirev.2010.02.022.

Uthicke, S., & Nobes, K. (2008). Benthic Foraminifera as ecological indicators for water quality on the Great Barrier Reef. Estuar. Coast. Shelf Sci., 78(4), 763–773. https://doi.org/10.1016/j.ecss.2008.02.014.

Vázquez Riveiros, N., Babalola, A. O., Boudreau, R. E. A., Patterson, R. T., Roe, H. M., & Doherty, C. (2007). Modern distribution of salt marsh foraminifera and thecamoebians in the Seymour–Belize Inlet Complex, British Columbia, Canada. Mar. Geol., 242(1–3), 39–63. https://doi.org/10.1016/j.margeo.2006.08.009.

Verlaak, Z. R. F., & Collins, L. S. (2021). Environmental Controls on the Distribution of Modern Benthic Foraminifera in the Florida Everglades and Their Use as Paleoenvironmental Indicators. Journal of Foraminiferal Research, 51(3), 182–209. https://doi.org/10.2113/gsjfr.51.3.182.

Ward, J. H. (1963). Hierarchical Grouping to Optimize an Objective Function. J. Am. Stat. Assoc., 58(301), 236–244. https://doi.org/10.1080/01621459.1963.10500845.

Weinmann, A. E., Rödder, D., Lötters, S., & Langer, M. R. (2013). Traveling through time: The past, present and future biogeographic range of the invasive foraminifera Amphistegina spp. in the Mediterranean Sea. Mar. Micropaleontol., 105, 30–39. https://doi.org/10.1016/j.marmicro.2013.10.002.

Wood, H. K., & Macpherson, G. L. (2005). Sources of Sr and implications for weathering of limestone under tallgrass prairie, northeastern Kansas. Applied

Geochemistry, 20(12), 2325–2342. https://doi.org/10.1016/j.apgeochem.2005.08.002.

Woor, S., Buckland, C., Parton, A., & Thomas, D. S. G. (2022). Assessing the robustness of geochronological records from the Arabian Peninsula: A new synthesis of the last 20 ka. Global and Planetary Change, 209, 103748. https://doi.org/10.1016/j.gloplacha.2022.103748.

Zarins, J. (2007). Aspects of recent archaeological work at al-Balīd (Zafār), Sultanate of Oman. Proceedings of the Seminar for Arabian Studies, 37(July 2006), 309–324.

Zerboni, A., Perego, A., Mariani, G. S., Brandolini, F., Al Kindi, M., Regattieri, E., Zanchetta, G., Borgi, F., Charpentier, V., & Cremaschi, M. (2020). Geomorphology of the Jebel Qara and coastal plain of Salalah (Dhofar, southern Sultanate of Oman). Journal of Maps, 16(2), 187–198. https://doi.org/10.1080/17445647.2019.1708488.

Chapter 5

Summary and Conclusions

Microfossils and μXRF core scanning results are important additions to multi-proxy geoarchaeological studies, and their uses and applications in this field are still being developed. Diatoms and testate amoebae, as well as elemental results obtained through μXRF core scanning, have rarely been applied as proxies in coastal geoarchaeological studies. This research advances the use of these proxies while investigating paleoenvironmental changes in regions with well-known maritime trade histories.

In the first of the three studies, a multiproxy approach was used to investigate the formation of wetlands surrounding Muyil, a Classic Maya maritime trading port. Microfossil (foraminifera, diatoms), μXRF, pollen, carbon stable isotope, and radiocarbon dating methods were applied to sediments collected from Boca Paila cave. This study included the first assessment of diatom species found within the sampled cave system and demonstrated the advantage of underwater cave systems as a source of undisturbed environmental proxies. Results indicate that shallow wetlands began to form with sea-level rise between $\sim$1157 BCE and 312 CE, which corresponds well with the estimated founding of Muyil $\sim$350 BCE (Witschey, 1993). The canoe-accessible channel connecting the port site to the coast would not have been navigable prior to wetland development. The formation of deeper lagoons after $\sim$312 CE (facilitating access to the port site) corresponds with a population increase and the construction of additional structures built at the site, as well as an increase in maritime trade activity along the eastern coast of the Yucatán Peninsula (Andrews, 1993; Witschey, 1993). Further research on maritime port sites along the coast can confirm the link between changes in coastal morphology and an increase in maritime trade activity in the region.

The research conducted at the coast of Caesarea was the first study to investigate the use of epiphytic foraminifera as biostratigraphic indicators in geoarchaeological studies. The foraminifera assemblages demonstrated that *Pararotalia calcariformata* was an especially abundant epiphytic foraminifer that proved to be a useful biomarker of anthropogenic hard structure emplacement on the sandy coastline. The significant increase of this species only occurred as a result of the altered substrate conditions following construction of Sebastos harbour around 2000 years ago. The presence of *P. calcariformata* in sediments dating to the Santorini event bed (1630–1550 BCE) confirms that it did not arrive in the Mediterranean following the opening of the Suez Canal in 1869 as previously thought (Schmidt et al., 2015; Zenetos et al., 2012), which has implications for future ecological assessments in the region. μXRF and magnetic susceptibility results showed that harbour material (e.g., heavy minerals from within the volcanic ash component, kurkar particles) was transported offshore over time, especially during erosive events related to tsunamis. The findings of this study demonstrate novel applications of foraminifera in sandy, nearshore harbour settings, highlight long-term impacts of anthropogenic coastal development on ecological communities, and may provide a tracer for sand transport on clastic shelves.

The third study revealed information on the development of sand barriers and lagoons at two archaeological sites with a previously limited paleoenvironmental perspective. Palynological work conducted in 2004 suggested that the lagoons were open estuaries prior to ∼420 CE (Hoorn & Cremaschi, 2004). The authors speculated that an increasingly arid climate resulted in decreased fluvial output and progressive siltation of the estuaries. Foraminifera, testate amoebae, μXRF, and radiocarbon dating results from this third study indicated that sand barriers accumulated and closed off the eastern arm of Khor Al Balid from the Arabian Sea during the 12th century CE, while the western arm closed during the 15th century CE. Previous archaeological results indicate that shipping involved the transport of goods on smaller boats to and from larger ships anchored offshore (Ghidoni & Pavan, 2022; Pavan & Visconti, 2023), meaning that maritime trade was still possible after lagoon formation. Continuous accumulation of sands along the coast would have progressively widened the beach (currently at least 120 m) likely making it increasingly difficult to conduct shipping. Evidence of an extreme wave event (e.g., a tsunami or large tropical cyclone) occurring around the 18th–19th century is observed in most cores across Khor Al Balid and Khor Rori. This extreme wave event and the progressive coastal morphological changes were likely major contributing factors towards the decline and eventual abandonment of the city. The extreme wave event also has implications for the preservation of archaeological sites along the coast.

This dissertation provides important new coastal morphological data in three archaeological settings, allowing for a more comprehensive understanding of site development in each case. The results contribute to the advancement of geoarchaeological research through the use of under-utilized sources of sediment records (i.e., underwater cave systems) and a new application of benthic foraminifera data, which can be applied in future studies.

References

Aiello, G., Amato, V., Barra, D., Caporaso, L., Caruso, T., Giaccio, B., Parisi, R., & Rossi, A. (2020). Late Quaternary benthic foraminiferal and ostracod response to palaeoenvironmental changes in a Mediterranean coastal area, Port of Salerno, Tyrrhenian Sea. Reg. Stud. Mar. Sci., 40, 101498. https://doi.org/10.1016/j.rsma.2020.101498.

Algan, O., Yalçın, M. N., Özdoğan, M., Yılmaz, Y., Sarı, E., Kırcı-Elmas, E., Yılmaz, İ., Bulkan, Ö., Ongan, D., Gazioğlu, C., Nazik, A., Polat, M. A., & Meriç, E. (2011). Holocene coastal change in the ancient harbor of Yenikapı–İstanbul and its impact on cultural history. Quaternary Research, 76(1), 30–45. https://doi.org/10.1016/j.yqres.2011.04.002.

Amato, V., Aiello, G., Barra, D., Caporaso, L., Caruso, T., Giaccio, B., Parisi, R., & Rossi, A. (2020). Holocene paleogeographic evolution of an ancient port city of the central Mediterranean area: Natural and anthropogenic modifications from Salerno city, southern Italy. Geoarchaeology, 35(3), 366–383. https://doi.org/10.1002/gea.21774.

Andrews, A. P. (1993). Late Postclassic lowland Maya archaeology. J. World Prehist., 7(1), 35–69. https://doi.org/10.1007/BF00978220 Armstrong, H., & Brasier, M. (2005). Microfossils (Second). Blackwell Publishing Ltd.

Bony, G., Marriner, N., Morhange, C., Kaniewski, D., & Perinçek, D. (2012). A high-energy deposit in the Byzantine harbour of Yenikapı, Istanbul (Turkey). Quaternary International, 266, 117–130. https://doi.org/10.1016/j.quaint.2011.03.031.

Brush, G. S. (2001). Natural and anthropogenic changes in Chesapeake Bay during the last 1000 years. Human and Ecological Risk Assessment (HERA), 7(5), 1283–1296. https://doi.org/10.1080/20018091095005.

Charman, D. J., Gehrels, W. R., Manning, C., & Sharma, C. (2010). Reconstruction of recent sea-level change using testate amoebae. Quat. Res., 73(2), 208–219. https://doi.org/10.1016/j.yqres.2009.11.009.

D'Andrea, A. (2021). Reconsidering the Topography of al-Balīd (Oman): A Preliminary Review of the Graphical Documentation. Annali Sezione Orientale, 81(1–2), 39–50. https://doi.org/10.1163/24685631-12340110.

Daniel, T., Ansorge, J., Schmölcke, U., & Frenzel, P. (2019). Multiproxy palaeontological investigations of Holocene sediments in the harbour area of the Hanseatic town Stralsund, North-Eastern Germany, southern Baltic Sea coast. Quaternary International, 511(December 2017), 22–42. https://doi.org/10.1016/j.quaint.2018.05.017.

Di Bella, L., Bellotti, P., Frezza, V., Bergamin, L., & Carboni, M. G. (2011). Benthic foraminiferal assemblages of the imperial harbor of Claudius (Rome): Further paleoenvironmental and geoarcheological evidences. The Holocene, 21(8), 1245–1259. https://doi.org/10.1177/0959683611405239.

Finkler, C., Fischer, P., Baika, K., Rigakou, D., Metallinou, G., Hadler, H., & Vött, A. (2018). Tracing the Alkinoos Harbor of ancient Kerkyra, Greece, and reconstructing its paleotsunami history. Geoarchaeology, 33(1), 24–42. https://doi.org/10.1002/gea.21609.

Ghidoni, A., & Pavan, A. (2022). Boats, horses, and moorings: maritime activities at al-Balīd in the medieval period. Proceedings of the Seminar for Arabian Studies, 51, 169–182.

Giaime, M., Jol, H. M., Salmon, Y., López, G. I., Hamid, A. abu, Bergevin, L., Bauman, P., McClymont, A., Sailer-Haugland, E., & Artzy, M. (2021).

Using a multi-proxy approach to locate the elusive Phoenician/Persian anchorage of Tel Akko (Israel). Quaternary International, 602(June), 66–81. https://doi.org/10.1016/j.quaint.2021.06.008.

Goiran, J.-P., Chan, W. M., Benech, C., Vitale, Q., Riddick, N., Delile, H., Salomon, F., Chapkanski, S., Oberlin, C., Brocard, G., Lisé-Pronovost, A., & Vittori, C. (2022). Developments in Geoarchaeological Research, Methodologies and Applications in Harbour Maritime Archaeology. Seasides of Byzantium: Harbours and Anchorages of a Mediterranean Empire, 21, 109–129.

Goiran, J.-P., Salomon, F., Mazzini, I., Bravard, J.-P., Pleuger, E., Vittori, C., Boetto, G., Christiansen, J., Arnaud, P., Pellegrino, A., Pepe, C., & Sadori, L. (2014). Geoarchaeology confirms location of the ancient harbour basin of Ostia (Italy). Journal of Archaeological Science, 41, 389–398. https://doi.org/10.1016/j.jas.2013.08.019.

Goldberg, P., & Macphail, R. I. (2006). Practical and Theoretical Geoarchaeology. Blackwell Science Ltd.

Goodman, B. N., Reinhardt, E. G., Dey, H. W., Boyce, J. I., Schwarcz, H. P., Sahoğlu, V., Erkanal, H., & Artzy, M. (2009). Multi-proxy geoarchaeological study redefines understanding of the paleocoastlines and ancient harbours of Liman Tepe (Iskele, Turkey). Terra Nova, 21(2), 97–104. https://doi.org/10.1111/j.1365-3121.2008.00861.x.

Hoorn, C., & Cremaschi, M. (2004). Late Holocene palaeoenvironmental history of Khawr Rawri and Khawr Al Balid (Dhofar, Sultanate of Oman). Palaeogeography, Palaeoclimatology, Palaeoecology, 213(1–2), 1–36. https://doi.org/10.1016/j.palaeo.2004.03.014.

Jaijel, R., Glover, J. B., Rissolo, D., Beddows, P. A., Smith, D., Ben-Avraham, Z., & Goodman-Tchernov, B. (2018). Coastal reconstruction of Vista Alegre, an ancient maritime Maya settlement. Palaeogeogr. ,Palaeoclimatol., Palaeoecol., 497(May 2017), 25–36. https://doi.org/10.1016/j.palaeo.2018.02.003.

Kraft, J. C., Rapp, G., Kayan, I., & Luce, J. V. (2003). Harbor areas at ancient Troy: Sedimentology and geomorphology complement Homer's Iliad. Geology, 31(2), 163. https://doi.org/10.1130/0091-7613(2003)031<0163:HAAATS>2.0.CO;2.

Marriner, N., & Morhange, C. (2006). The 'Ancient Harbour Parasequence': Anthropogenic forcing of the stratigraphic highstand record. Sediment. Geol., 186(1–2), 13–17. https://doi.org/10.1016/j.sedgeo.2005.12.001.

Marriner, N., & Morhange, C. (2007). Geoscience of ancient Mediterranean harbours. Earth-Sci. Rev., 80(3–4), 137–194. https://doi.org/10.1016/j.earscirev.2006.10.003.

Marriner, N., Morhange, C., Boudagher-Fadel, M., Bourcier, M., & Carbonel, P. (2005). Geoarchaeology of Tyre's ancient northern harbour, Phoenicia. J. Archaeol. Sci., 32(9), 1302–1327. https://doi.org/10.1016/j.jas.2005.03.019.

Marriner, N., Morhange, C., & Goiran, J. P. (2010). Coastal and ancient harbour geoarchaeology. Geology Today, 26(1), 21–27. https://doi.org/10.1111/j.1365-2451.2010.00740.x.

Mazzini, I., Faranda, C., Giardini, M., Giraudi, C., & Sadori, L. (2011). Late Holocene palaeoenvironmental evolution of the Roman harbour of Portus, Italy. Journal of Paleolimnology, 46(2), 243–256. https://doi.org/10.1007/s10933-011-9536-7.

Mcgowran, B. (2005). Biostratigraphy: microfossils and geological time. Cambridge University Press. https://doi.org/10.5860/CHOICE.44-0941.

Morhange, C., Blanc, F., Schmitt-Mercury, S., Bourcier, M., Carbonel, P., Oberlin, C., Prone, A., Vivent, D., & Hesnard, A. (2003). Stratigraphy of late-Holocene deposits of the ancient harbour of Marseilles, southern France. The Holocene, 13(4), 593–604. https://doi.org/10.1191/0959683603hl619rr.

Morhange, C., & Marriner, N. (2015). Chapter 9: Archeological and biological relative sea-level indicators. In Handbook of Sea Level Research (pp. 146–156). John Wiley & Sons, Ltd.

Murray, J. W. (2006). Ecology and Applications of Benthic Foraminifera. In Ecology and Applications of Benthic Foraminifera. Cambridge University Press. https://doi.org/10.1017/CBO9780511535529.

Pavan, A., & Visconti, C. (2023). Looking for connections between Arabia and East Asia: diplomatic gifts, luxury vessels and utilitarian wares unearthed at the city port of al-Balīd, Sultanate of Oman. Egitto e Vicino Oriente, 205–227. https://doi.org/10.12871/978883339777114.

Pint, A., Seeliger, M., Frenzel, P., Feuser, S., Erkul, E., Berndt, C., Klein, C., Pirson, F., & Brückner, H. (2015). The environs of Elaia's ancient open harbour – a reconstruction based on microfaunal evidence. J. Archaeol. Sci., 54, 340–355. https://doi.org/10.1016/j.jas.2014.06.011.

Rapp, G. J. (1987). Geoarchaeology. Annual Review of Earth and Planetary Science, 15, 97–113.

Reinhardt, E. G., Patterson, R. T., & Schroeder-Adams, C. J. (1994). Geoarchaeology of the ancient harbor site of Caesarea Maritima, Israel; evidence from sedimentology and paleoecology of benthic foraminifera. J. Foraminiferal Res., 24(1), 37–48. https://doi.org/10.2113/gsjfr.24.1.37.

Reinhardt, E. G., & Raban, A. (1999). Destruction of Herod the Great's harbor at Caesarea Maritima, Israel—Geoarchaeological evidence. Geology, 27(9), 811. https://doi.org/10.1130/0091-7613(1999)027<0811:DOHTGS>2.3.CO;2.

Riddick, N. L., Boyce, J. I., Krezoski, G. M., Şahoğlu, V., Erkanal, H., Tuğcu, İ., Alkan, Y., Gabriel, J. J., Reinhardt, E. G., & Goodman-Tchernov, B. N. (2022). Palaeoshoreline reconstruction and underwater archaeological potential of Liman Tepe: A long-occupied coastal prehistoric settlement in western Anatolia, Turkey. Quat. Sci. Rev., 276, 107293. https://doi.org/10.1016/j.quascirev.2021.107293.

Riddick, N. L., Boyce, J. I., Reinhardt, E. G., Rothaus, R. M., Chomicki, K. M., & McCarthy, F. M. G. (2021). Multi-proxy palaeoenvironmental record of coastal tectonic uplift and abandonment (ca. 6th c. CE) of Lechaion's inner harbour, ancient Corinth, Greece. Quat. Sci. Rev., 267, 107080. https://doi.org/10.1016/j.quascirev.2021.107080.

Riddick, N. L., Boyce, J. I., Şahoğlu, V., Erkanal, H., Tuğcu, İ., Alkan, Y., Reinhardt, E. G., & Goodman-Tchernov, B. N. (2022). Coastal palaeoenvironmental record of Late Bronze to Iron Age harbour development at Liman Tepe-Clazomenae, western Anatolia, Turkey. Mar. Geol., 450(June), 106842. https://doi.org/10.1016/j.margeo.2022.106842.

Rothwell, R. G., & Croudace, I. W. (2015). Twenty Years of XRF Core Scanning Marine Sediments: What Do Geochemical Proxies Tell Us? In I. W. Croudace & R. G. Rothwell (Eds.), Micro-XRF Studies of Sediment Cores: Applications of a Non-destructive Tool for the Environmental Sciences (Vol. 17, pp. 25–102). Springer Netherlands. https://doi.org/10.1007/978-94-017-9849-5.

Salomon, F., Keay, S., Carayon, N., & Goiran, J.-P. (2016). The Development and Characteristics of Ancient Harbours—Applying the PADM Chart to the Case Studies of Ostia and Portus. PLOS ONE, 11(9), e0162587. https://doi.org/10.1371/journal.pone.0162587.

Schmidt, C., Morard, R., Almogi-Labin, A., Weinmann, A. E., Titelboim, D., Abramovich, S., & Kucera, M. (2015). Recent Invasion of the Symbiont-Bearing Foraminifera Pararotalia into the Eastern Mediterranean Facilitated by the Ongoing Warming Trend. PLOS ONE, 10(8), e0132917. https://doi.org/10.1371/journal.pone.0132917.

Seeliger, M., Bartz, M., Erkul, E., Feuser, S., Kelterbaum, D., Klein, C., Pirson, F., Vött, A., & Brückner, H. (2013). Taken from the sea, reclaimed by the sea: The fate of the closed harbour of Elaia, the maritime satellite city of Pergamum (Turkey). Quaternary International, 312, 70–83. https://doi.org/10.1016/j.quaint.2013.03.004.

Seeliger, M., Brill, D., Feuser, S., Bartz, M., Erkul, E., Kelterbaum, D., Vött, A., Klein, C., Pirson, F., & Brückner, H. (2014). The Purpose and Age of Underwater Walls in the Bay of Elaia of Western Turkey: A Multidisciplinary Approach. Geoarchaeology, 29(2), 138–155. https://doi.org/10.1002/gea.21471.

Stock, F., Knipping, M., Pint, A., Ladstätter, S., Delile, H., Heiss, A. G., Laermanns, H., Mitchell, P. D., Ployer, R., Steskal, M., Thanheiser, U., Urz, R., Wennrich, V., & Brückner, H. (2016). Human impact on Holocene sediment dynamics in the Eastern Mediterranean - the example of the Roman harbour of Ephesus. Earth Surf. Process. Landf., 41(7), 980–996. https://doi.org/10.1002/esp.3914.

Stock, F., Pint, A., Horejs, B., Ladstätter, S., & Brückner, H. (2013). In search of the harbours: New evidence of Late Roman and Byzantine harbours of Ephesus. Quat. Int., 312, 57–69. https://doi.org/10.1016/j.quaint.2013.03.002.

Véron, A., Goiran, J. P., Morhange, C., Marriner, N., & Empereur, J. Y. (2006). Pollutant lead reveals the pre-Hellenistic occupation and ancient growth of Alexandria, Egypt. Geophysical Research Letters, 33(6), L06409. https://doi.org/10.1029/2006GL025824.

Vött, A., Schriever, A., Handl, M., & Brückner, H. (2007). Holocene palaeogeographies of the central Acheloos River delta (NW Greece) in the vicinity of the ancient seaport Oiniadai. Geodinamica Acta, 20(4), 241–256. https://doi.org/10.3166/ga.20.241-256.

Witschey, W. R. T. (1993). The archaeology of Muyil, Quintana Roo, Mexico: A maya site on the east coast of the Yucatan Peninsula. Tulane University.

Zenetos, A., Gofas, S., Morri, C., Rosso, A., Violanti, D., Garcia Raso, J. E., Cinar, M. E., Almogi-Labin, A., Ates, A. S., Azzurro, E., Ballesteros, E., Bianchi, C. N., Bilecenoglu, M., Gambi, M. C., Giangrande, A., Gravili, C., Hyams-Kaphzan, O., Karachile, P. K., Katsanevakis, S., … Veriaque, M. (2012). Alien species in the Mediterranean Sea by 2012. A contribution to the application of European Union's Marine Strategy Framework Directive (MSFD). Part 2. Introduction trends and pathways. Mediterr. Mar. Sci., 13(2), 328. https://doi.org/10.12681/mms.327

Appendix

APPENDIX A1: Chapter 2 Supplementary Data 1 -
Table of organic geochemistry results for 34 samples from BP2.

Depth (cm)	$\delta^{13}C$	$\delta^{15}N$	%C	%N	C/N
0	-22.366	9.191	29.3	3.2	9.2
2	-21.784	9.049	27.8	3	9.2
4	-21.963	9.385	29.2	3.2	9.1
6	-21.842	8.857	23.9	2.6	9.2
8	-20.767	7.994	28	3.1	9.2
11	-20.996	7.655	29.4	3.1	9.6
13	-20.166	7.329	28.9	3.1	9.3
15	-21.35	7.267	29.8	2.9	10.2
17	-22.069	7.728	31.1	3.2	9.8
19	-21.086	7.325	31.2	3.2	9.9
22	-22.338	8.291	25	2.4	10.5
24	-26.12	8.605	8.4	0.8	10
26	-25.129	9.007	3.8	0.4	8.6
28	-22.989	8.842	14	1.4	9.7
31	-26.221	8.444	30.1	2.5	12.1
33	-25.075	6.498	6.2	0.5	12.6
35	-26.288	7.525	16.7	1.4	11.8
37	-26.246	6.402	13.2	1	12.8
39	-27.889	7.539	12.7	1.2	10.2
42	-26.985	7.124	33.9	3.4	10.1
44	-26.983	7.269	40.1	4	10.1
46	-26.917	6.957	41.6	4.1	10.2
48	-27.191	7.038	43.8	4.3	10.1
50	-26.909	7.072	45	4.3	10.4
52	-26.848	7.078	47.7	4.5	10.7
55	-26.673	7.186	45.6	4.3	10.6
57	-27.385	7.783	43.2	4.5	9.6
59	-27.6	7.48	44.4	4.4	10.2
61	-27.211	6.944	43.3	4.1	10.5
63	-27.474	7.644	46.5	4.5	10.4
65	-27.697	7.664	44	4.3	10.3
67	-27.294	6.973	46.7	4.2	11
70	-28.232	8.116	48	4.5	10.7
72	-26.222	8.359	44.6	3.3	13.3

APPENDIX A2: Chapter 2 Supplementary Data 2 - Table of foraminifera concentrations, Shannon diversity index (SDI), and relative abundances (%) in 12 samples from core BP2.

Depth (cm)	**1**	**7**	**16**	**26**	**29**	**32**	**35**	**40**	**49**	**59**	**64**	**70**
Individuals/cc	749	1365	497	307	224	88	125	19	30	38	80	9
SDI	1.70	2.42	3.29	2.15	1.72	0.37	0.43	0.33	0.56	0.49	0.67	0.25
Agglutinated taxa	0.36	-	0.54	-	-	-	0.53	100.00	71.11	59.65	65.00	92.59
Ammodiscus spp.	0.71	0.39	0.54	21.52	54.46	92.80	94.15	-	28.89	36.84	33.33	7.41
Ammonia tepida	6.41	9.38	2.01	2.61	4.17	0.38	-	-	-	-	-	-
Ammonia parkinsoniana	15.66	5.47	3.62	6.74	11.01	2.65	-	-	-	-	-	-
Bolivina pseudopunctada	2.49	0.98	6.43	2.39	1.19	0.38	-	-	-	-	-	-
Bolivina variabilis	6.41	8.01	13.40	6.30	3.87	-	-	-	-	-	-	-
Bolivina spp.	-	0.20	1.21	0.22	0.60	-	-	-	-	-	-	-
Elphidium spp.	19.93	15.43	3.22	11.74	12.20	-	-	-	-	-	-	-
Nonionella spp.	-	3.13	1.61	-	-	-	-	-	-	-	-	-
Physalidia simplex	-	-	1.07	1.09	0.30	-	-	-	-	-	-	-
Patellina corrugata	-	0.20	-	0.43	4.17	3.79	5.32	-	-	1.75	0.83	-
Reophax scottii	-	-	5.76	-	0.89	-	-	-	-	-	0.83	-
Rosalina spp.	41.99	38.09	33.11	0.65	4.76	-	-	-	-	-	-	-
Rosalina subauracana	3.91	4.10	2.28	1.74	1.19	-	-	-	-	-	-	-
Siphonina reticulata	-	-	-	0.87	-	-	-	-	-	-	-	-
Triloculina oblonga	0.36	0.98	9.79	-	-	-	-	-	-	-	-	-
Triloculina bermudezi	0.36	1.17	5.76	2.39	-	-	-	-	-	-	-	-
Ostracods	1.42	12.50	9.65	41.30	1.19	-	-	-	-	1.75	-	-

APPENDIX A3: Chapter 2 Supplementary Data 3 - Table of diatom concentrations, Shannon diversity index (SDI), and relative abundances (%) in 23 samples from core BP2.

Depth (cm)	**0**	**3**	**6**	**9**	**12**	**15**	**18**	**21**	**24**	**27**	**30**	**33**	**36**	**39**	**42**	**45**	**48**	**51**	**57**	**60**	**63**	**66**	**72**
Individuals/cc	$3.1x10^7$	$1.4x10^6$	$1.7x10^6$	$9.1x10^5$	$7.1x10^5$	$7.2x10^5$	$5.8x10^5$	$4.1x10^5$	$4.4x10^4$	$3.8x10^4$	$5.0x10^2$	$5.6x10^2$	$5.7x10^2$	-	-	-	-	-	-	-	-	-	-
Shannon Diversity Index	2.60	3.03	2.77	3.25	3.24	3.04	3.24	3.07	0.92	0.1	0.03	0.02	0.02	0	0	0	0	0	0	0	0	0	0
Achnanthes sp.	2.11	2.02	0.25	0.71	0.95	0.49	3.70	4.34	1.35	-	-	-	-	-	-	-	-	-	-	-	-	-	-
Amphora arenaria	3.01	2.02	3.74	5.18	4.53	2.22	2.47	3.06	1.35	-	-	-	-	-	-	-	-	-	-	-	-	-	-
Amphora bigibba	2.71	2.78	2.00	0.24	0.24	1.23	0.25	1.02	-	-	-	-	-	-	-	-	-	-	-	-	-	-	-
Amphora coffeaformis	3.92	6.06	2.24	1.18	2.39	1.72	1.48	1.02	-	-	-	-	-	-	-	-	-	-	-	-	-	-	-
Amphora immarginata	3.92	5.81	1.50	6.82	7.64	7.64	7.65	10.97	2.70	-	-	-	-	-	-	-	-	-	-	-	-	-	-
Amphora ostrearia	4.22	1.26	1.25	3.53	3.82	1.72	2.72	3.32	5.41	-	-	-	-	-	-	-	-	-	-	-	-	-	-
Amphora proteus	1.51	3.03	2.99	5.18	5.97	6.16	7.90	9.44	12.16	16.67	-	-	-	-	-	-	-	-	-	-	-	-	-
Amphora sp.	5.72	11.62	3.49	3.76	4.77	2.22	2.96	1.28	2.70	-	-	-	-	-	-	-	-	-	-	-	-	-	-
Cocconeis placentula	0.30	0.25	0.50	0.24	0.95	2.22	2.72	1.28	-	16.67	-	-	100.00	-	-	-	-	-	-	-	-	-	-
Craticula spp.	17.77	20.96	18.45	13.41	18.14	17.73	10.62	9.18	8.11	-	-	-	-	-	-	-	-	-	-	-	-	-	-
Cyclotella meneghiniana	24.40	12.37	31.17	22.35	3.10	20.20	13.83	10.71	12.16	-	50.00	-	-	-	-	-	-	-	-	-	-	-	-
Diploneis spp.	0.30	0.25	0.50	0.71	1.67	1.72	1.48	0.77	-	-	-	-	-	-	-	-	-	-	-	-	-	-	-
Diploneis suborbicularis	-	1.01	1.00	3.53	0.72	1.48	1.48	2.55	4.05	-	-	-	-	-	-	-	-	-	-	-	-	-	-
Fragilaria spp.	1.20	1.52	0.75	1.18	0.48	0.25	0.99	1.02	-	-	-	-	-	-	-	-	-	-	-	-	-	-	-
Frustulia rhomboides	-	0.51	0.50	1.41	0.72	0.49	0.25	-	-	-	-	-	-	-	-	-	-	-	-	-	-	-	-
Gramatophora spp.	0.90	0.76	0.75	4.71	8.11	8.62	7.16	9.18	13.51	16.67	-	-	-	-	-	-	-	-	-	-	-	-	-
Hyalosynedra laevigata	8.13	8.33	9.48	4.00	5.49	1.97	2.96	1.53	1.35	-	-	-	-	-	-	-	-	-	-	-	-	-	-
Mastogloia erythraea	0.30	1.26	2.49	0.71	1.67	2.71	-	-	1.35	16.67	-	-	-	-	-	-	-	-	-	-	-	-	-
Mastogloia spp.	7.83	6.31	4.49	3.29	3.34	3.20	1.48	1.28	2.70	-	-	-	-	-	-	-	-	-	-	-	-	-	-
Navicula digitoradiata	0.30	1.01	0.75	0.24	0.48	0.49	0.49	0.26	1.35	-	-	-	-	-	-	-	-	-	-	-	-	-	-
Navicula oblonga	0.90	1.52	2.49	1.18	1.43	1.72	0.49	0.26	1.35	-	-	-	-	-	-	-	-	-	-	-	-	-	-
Navicula spp.	1.51	3.28	1.75	1.65	0.48	0.49	1.23	0.51	-	-	-	-	-	-	-	-	-	-	-	-	-	-	-
Neidium spp.	1.51	1.01	1.00	1.41	1.43	0.25	0.74	2.04	1.35	-	-	-	-	-	-	-	-	-	-	-	-	-	-
Nitzschia spp.	0.60	0.76	0.50	0.94	1.19	1.72	0.49	0.26	1.35	-	-	-	-	-	-	-	-	-	-	-	-	-	-
Oestrupia powellii	1.51	0.76	1.50	3.76	1.91	1.72	3.46	3.57	2.70	-	-	-	-	-	-	-	-	-	-	-	-	-	-
Pleurosigma sp.	2.71	0.51	0.50	0.71	1.43	0.49	1.23	1.02	-	-	-	-	-	-	-	-	-	-	-	-	-	-	-
Rhopaloidia gibberula	0.60	-	-	-	0.24	0.25	0.99	1.28	-	-	-	-	-	-	-	-	-	-	-	-	-	-	-
Staurosirella sp.	0.60	0.25	1.25	2.35	0.72	0.25	5.68	2.81	1.35	-	-	100.00	-	-	-	-	-	-	-	-	-	-	-
Phytoliths	1.51	2.78	2.74	5.65	15.99	8.62	13.09	16.07	21.62	33.33	50.00	-	-	-	-	-	-	-	-	-	-	-	-

APPENDIX A4: Chapter 2 Supplementary Data 4 - Table of foraminifera and diatom taxa identified in core BP2, with documented salinity and habitat preferences.

Taxon	Salinity Preference	Additional Ecological Information (life mode; recorded habitats)	References
Foraminifera			
Ammodiscus spp.	M	Bathyal and abyssal, anchialine cave, and lagoon	(1; 2)
Ammonia parkinsoniana (d'Orbigny, 1839) *Ammonia tepida* (Cushman, 1926)	M/B (10–31 ppt)	*Ammonia* spp.: Infaunal, free, muddy sand; marsh to subtidal, brackish to hypersaline lagoon, and inner marine shelf; can tolerate high salinity (up to 50 ppt) and low oxygen	(1; 2; 3)
Bolivina pseudopunctada Höglund, 1947 *Bolivina variabilis* (Williamson, 1858) *Bolivina* spp.	M	*Bolivina* spp.: Infaunal and epifaunal, free-living, mud; inner shelf to bathyal, anchialine cave, and lagoon	(1; 2)
Elphidium spp.	M/B (0–70 ppt)	Epifaunal and infaunal, free, mud/sand; brackish marsh to hypersaline lagoon, inner shelf, reef, anchialine cave	(1; 2; 3)
Jadamina macrescens (Brady, 1870)	M/B/F (0–50 ppt)	Epifaunal and infaunal, free, mud/silt; high/mid marsh	(1; 3)
Nonionella spp.	M	Infaunal, free, mud; shelf to upper bathyal areas, rare in deeper water	(1; 3)
Physalidia simplex Heron-Allen & Earland, 1915	M		(4)
Patellina corrugata Williamson, 1858	M	*Patellina* spp.: epifaunal, clinging or attached, firm substrates; inner shelf, reef, and lagoon	(2; 3; 5)
Reophax scottii Chaster, 1892	M	*Reophax* spp.: Infaunal, free, mud/sand; shelf to bathyal, anchialine cave, and lagoon	(2; 3)
Rosalina spp. *Rosalina subauracana* (Cushman, 1922)	M	Epifaunal, free, clinging or attached, hard substrates; outer/mid/inner shelf, reef, lagoon, and anchialine cave	(1; 2; 3)
Siphonina reticulata (Czjzek, 1848)	M	Anchialine cave, reef, and lagoon	(2)
Triloculina bermudezi Acosta, 1940 *Triloculina oblonga* (Montagu, 1803)	M (32–55 ppt)	*Triloculina* spp.: Epifaunal, free or clinging, mud/sand/plants; inner shelf, lagoon, hypersaline lagoon, mangrove, reef, and anchialine cave	(1; 2; 3)
Trochammina inflata (Montagu, 1808)	M/B/F (0–60 ppt)	Epifaunal and infaunal, free; intertidal to abyssal, high/mid marsh, mangrove, and swamp	(1; 2; 3)
Diatoms (Bacillariophyceae)			
Achnanthes sp.	F/B/M	Benthic, planktic, or epiphytic; often marine bay/nearshore; often polyhalobe (18–30 ppt)	(1; 2; 3; 7; 8; 9)
Amphora arenaria Donkin, 1858	M (18–30 ppt)	Benthic; bay/nearshore	(6; 7; 8; 10; 11)
Amphora bigibba Grunow ex A. Schmidt, 1875	M (18–30 ppt)	Tychopelagic; nearshore	(6; 8; 10; 11)

APPENDIX A4: Chapter 2 Supplementary Data 4 - Continued.

Taxon	Salinity Preference	Additional Ecological Information (life mode; recorded habitats)	References
Amphora coffeaformis (C. Agardh) Kützing, 1844	M/B	Benthic; also found in some coastal freshwater areas	(8; 9; 11)
Amphora immarginata Nagumo, 2003	M	Benthic; nearshore	(8; 11)
Amphora ostrearia Hendey, 1964	M (18–30 ppt)	Tychopelagic; nearshore	(8; 10; 11)
Amphora proteus Gregory, 1857	M/B (18–30/5–18 ppt)	Benthic; marine bay/nearshore	(6; 7; 8; 10; 11)
Amphora sp.	F/B/M	Typically benthic; shallow marine, estuary, or mangrove swamp	(10)
Cocconeis placentula Ehrenberg, 1838	F/B	Benthic or epibiotic; also found in marine bay/nearshore; *Cocconeis* spp. are often associated with mangrove assemblages	(6; 7; 8; 9; 10; 11)
Craticula spp.	F/B	Often observed in mesohaline conditions (3–22 ppt)	(7; 10)
Cyclotella meneghiniana Kützing, 1844	F/B	Benthic or planktic; shallow, nutrient-rich waters; often associated with mangrove assemblages	(6; 7; 9; 10; 11)
Diploneis spp.	F/B/M (18–30 ppt)	Often associated with mangrove assemblages	(7; 8; 10; 11)
Diploneis suborbicularis (Gregory) Cleve, 1894	M	Nearshore	(6; 8; 11)
Fragilaria spp.	F/B	Benthic; known to tolerate broad environmental gradients and environmental instability	(6; 7; 8; 9; 10; 11)
Frustulia rhomboides (Ehrenberg) De Toni, 1891	M	Benthic or planktic; bay/nearshore	(6; 8)
Gramatophora spp.	M (18–30/5–18 ppt)	Benthic or planktic; marine bay, nearshore, or oceanic surface/epipelagic	(6; 8; 9; 10; 11)
Hyalosynedra laevigata (Grunow) D. M. Williams & Round, 1986	M/B (18–30 ppt)	Planktic; marine bay, nearshore and coastal mangrove swamp	(6; 8; 10; 11)
Mastogloia erythraea	F/B/M	Benthic or planktic; often bay/nearshore	(6; 7; 11)
Mastogloia spp.	F/B/M	Marine nearshore, shallow marine estuary, or mangrove swamp; often polyhalobe (18–30 ppt) to mesohalobe (5–18 ppt)	(7; 8; 10)
Navicula digitoradiata (Gregory) Ralfs, 1861	F	Benthic	(6; 8; 9)
Navicula oblonga	F/B		(11)
Navicula spp.	F/B/M	Benthic; often associated with mangrove assemblages	(7; 9; 10; 11)
Neidium spp.	F	Benthic	(6; 9)
Nitzschia spp.	F/B/M	Benthic, epilithic, or tychopelagic; euryhaline; often associated with mangrove assemblages	(6; 7; 8; 10; 11)
Oestrupia powellii (Lewis) Heiden ex. Hustedt, 1935	M	Planktic or tychoplanktic; bay/nearshore	(6; 8; 10)
Pleurosigma spp.	F/B/M (5–18 ppt)	Benthic, tychoplanktic; marine bay/nearshore	(7; 8; 9; 10)
Rhopaloidia gibberula (Ehrenberg) O. F. Müller, 1899	M/B (18–30/5–18 ppt)	Benthic; bay/nearshore, soft substrates; *Rhopalodia* spp. are often associated with mangrove assemblages	(6; 8; 10)
Staurosirella spp.	F	Benthic; some species also found in marine bay/nearshore	(6; 8; 10; 11)

APPENDIX A4 - References:

1. Poag, C. W. (2015). Benthic Foraminifera of the Gulf of Mexico: Distribution, Ecology, Paleoecology. Texas A&M University Press.

2. van Hengstum, P. J., Scott, D. B., & Javaux, E. J. (2009). Foraminifera in elevated Bermudian caves provide further evidence for +21 m eustatic sea level during Marine Isotope Stage 11. Quat. Sci. Rev., 28(19–20), 1850–1860. https://doi.org/10.1016/j.quascirev.2009.05.017.

3. Murray, J. W. (2006). Ecology and Applications of Benthic Foraminifera. In Ecology and Applications of Benthic Foraminifera. Cambridge University Press. https://doi.org/10.1017/CBO9780511535529.

4. van Hengstum, P. J., Reinhardt, E. G., Beddows, P. A., & Gabriel, J. J. (2010). Linkages between Holocene paleoclimate and paleohydrogeology preserved in a Yucatan underwater cave. Quat. Sci. Rev., 29(19–20), 2788–2798. https://doi.org/10.1016/j.quascirev.2010.06.034 5. Myers, E. H. (1935). The life history of Patellina Corrugata Williamson, a foraminifer (pp. 355–392).

6. Krayesky, D., del Castillo, E. M., Zamudio, M. E., Norris, J. N., & Fredericq, S. (2009). Diatoms (Bacillariophyta) of the Gulf of Mexico. In D. L. Felder & D. K. Camp (Eds.), Gulf of Mexico–Origin, Waters, and Biota. Biodiversity. Texas A&M University Press.

7. Licea, S., Moreno-Ruiz, J. L., & Luna, R. (2016). Checklist of Diatoms (Bacillariophyceae) from the Southern Gulf of Mexico: Data-Base (1979-2010) and New Records. J. Biodivers. Endanger. Species, 04(03). https://doi.org/10.4172/2332-2543.1000174.

8. Lopez-Fuerte, F. O., Siqueiros-Beltrones, D. A., & Navarro, J. N. (2010). Benthic diatoms associated with mangrove enviroments in the northwest region of México (V. P. e Imprenta (ed.)).

9. Sánchez, M., Alcocer, J., Escobar, E., & Lugo, A. (2002). Phytoplankton of cenotes and anchialine caves along a distance gradient from the northeastern coast of Quintana Roo, Yucatan Peninsula. Hydrobiologia, 467, 79–89. https://doi.org/10.1023/A:1014936714964.

10. Smol, J. P., & Stoermer, E. F. (2010). The Diatoms (J. P. Smol & E. F. Stoermer (eds.); Second). Cambridge University Press. https://doi.org/10.1017/CBO9780511763175.

11. The Periphyton Group, F. I. U. (2022). Diatom Image Database. Florida Coastal Everglades LTER, Florida International University. https://fce-lter.fiu.edu/data/database/diatom/.

APPENDIX A5: Chapter 2 Supplementary Data 5 - Correspondance regarding an abnormal flow event near Cenote Akalche (Ox Bel Ha Cave System ∼20 km north of Boca Paila).

On Jan 29, 2020, at 9:19 AM, Cameron Russo <cameron_russo@icloud.com> wrote:

Hey Ed, let me know if this is what you need, and if you have any questions or want further info?

Yesterday, 28-Jan-2020, Laszlo Cseh and I did a dive in Akalche. The dive finished at 2:09pm. Within a couple mins of surfacing, when we were still in the water on the surface just floating, de-kitting our tanks - the water level suddenly went up by approx. 1m in about 3 seconds. Stayed there for about 3 seconds. Dropped by about 1 or 2m, then continued with waves up and down about that height and gradually getting smaller for 15mins!!

The surface water of Akalche is always brown and bad viz, but as a result of the waves, there was much more jungle matter (leaves, mud, branches) in the cenote after, and the visibility was even worse than usual.

In the confusion and mild panic when the waves started Laszlo dropped and lost a side mount tank. I held on to the edge of the cenote for dear life and I would estimate we waited in the water for 15mins before we thought it safe enough to let go of the side, remove the rest of our equipment and exit the water.

After we finished packing up everything and were ready to head home, we had a last look at the cenote, there was mud and debris approx. 5m away (sideways, not up and down) from the edge of the pool of water (I would guess this would equate to the 1m rise).

We then went to look at the Coco Ha cenote (500m or 1km down the road), and there were no signs whatsoever of the water rising there. The ground was completely dry and 'clean' where it normally is, and the water was as clear as it usually is.

Thanks,
Cameron

Email: cameron_russo@yahoo.com.au
Mobile: +64 21 301 402

APPENDIX B1: Chapter 3 Supplementary Data 1 - Common minerals in offshore sands at Caesarea, with chemical compositions and major sources.

Minerals			Composition	Sources: Nile-derived sands, silts, & clays[1–9]	Kurkar & onshore terrain[2–12]	Aeolian dust[2, 13–16]	Marine productivity[3]	Sebastos harbour[17,18]: Seawater cement	Sebastos harbour[17,18]: Pozzolanic Aggregate	Sebastos harbour[17,18]: Non-Pozzolanic Aggregate
		Quartz	SiO_2	X	X	X				X
	Feldspars	Unspecified	$KAlSi_3O_8$ / $NaAlSi_3O_8$ / $CaAl_2Si_2O_8$	X	X	X				
	Feldspars	Sanidine	$(K,Na)AlSi_3O_8$						X	
	Unspecified iron oxides		$Fe_{2\text{–}3}O$	X	x	x				
	Carb-onates	Calcite	$CaCO_3$	x	X	X	X	X	X	X
	Carb-onates	Aragonite	$(Ca, Sr)CO_3$		X		X			
	Clays	Smectite	$[\sim Ca_{0.17}(Al, Fe, Mg)_2(Si, Al)_4O_{10}(OH)_2 \bullet nH_2O]$	X	x	X				
	Clays	Kaolinite	$[Al_2Si_2O_5(OH)_4]$	X	x	X				
	Clays	Illite	$[\sim K_{0.8}Al_2(Al_{0.8}Si_{3.2}(OH)_2]$	X	x	X				X
Heavy minerals	Amphi-boles	Hornblende	$(Na, K)_{0\text{–}1}Ca_2(Mg, Fe^{2+}, Fe^{3+}, Al)_5(Si, Al)_8O_{22}(OH)_2$	x	x					
Heavy minerals	Amphi-boles	Anthophyllite	$(Mg,Fe)_7Si_8O_{22}(OH)_2$							X
Heavy minerals	Clino-pyroxene	Unspecified	$(Ca,Mg,Fe,Na)(Mg,Fe,Al)(Si,Al)_2O_6$						X	
Heavy minerals	Clino-pyroxene	Augite	$(Ca, Mg, Fe^{2+}, Fe^{3+}, Al)_2(Si, Al)_2O_6$	x	x					
Heavy minerals		Biotite	$K(Mg, Fe)_3AlSi_3O_{10}(OH, F)_2$	x	x					
Heavy minerals	stable/ resistant	Zircon	$ZrSiO_4$	x	x					
Heavy minerals	stable/ resistant	Rutile	TiO_2	x	x					
Heavy minerals	stable/ resistant	Tourmaline	$Na(Mg, Fe, Li, Al)_3Al_6(Si_6O_{18})(BO_3)_3(OH, F)_4$	x	x					
Heavy minerals	meta-morphic	Sillimanite	$AlAlOSiO_4$	x						
Heavy minerals	meta-morphic	Staurolite	$Fe_2Al_9O_6[(Si, Al)O_4]_4(OH)_2$	x						
Heavy minerals	meta-morphic	Kyanite	$AlAlOSiO_4$	x						
Heavy minerals	opaque	Magnetite	$FeFe_2O_4$	x	x				X	
Heavy minerals	opaque	Hematite	Fe_2O_3	x						
Heavy minerals	opaque	Pyrite	FeS_2	x						
Heavy minerals	opaque	Garnet	$X_3Y_2(SiO_4)_3$	x	x					
	Zeolites	Phillipsite	$K_2(Ca, Na_2)Al_6Si_{10}O_{32} \bullet 12H_2O$					x	X	
	Zeolites	Chabazite	$Ca_2(Al_4Si_8)O_{24} \bullet 13H_2O$					x		
	Zeolites	Analcime	$Na(AlSi_2)O_6 \bullet H_2O$						X	
		Bassanite	$CaSO_4 \bullet 1/2H_2O$					x		
		Ettringite	$Ca_6Al_2(SO_4)_3(OH)_{12} \bullet 26H_2O$					x		
		Halite	$NaCl$					x		
		Sjogrenite	$Mg_6Fe^{3+}{}_2(CO_3)(OH)_{16} \bullet 4H_2O$					x		
		Tobermorite	$Ca_4Si_6O_{17}(H_2O)_2 \bullet (Ca \bullet 3H_2O)$					X		

APPENDIX B1 - References:

1. Goldsmith, S., Krom, M., Sandler, A., & Herut, B. (2001). Spatial trends in the chemical composition of sediments on the continental shelf and slope off the Mediterranean coast of Israel. Continental Shelf Research, 21(16–17), 1879–1900. https://doi.org/10.1016/S0278-4343(01)00027-9.

2. Inman, D. L., & Jenkins, S. A. (1984). The Nile Littoral Cell and Man's Impact on the Coastal Zone of the Southeastern Mediterranean. Coastal Engineering Proceedings, 1(19), 109. https://doi.org/10.9753/icce.v19.109.

3. Nir, Y. (1984). Recent sediments of the Israeli Mediterranean continental shelf and slope. University of Goteburg, Sweden.

4. Stanley, D. J. (1989). Sediment transport on the coast and shelf between the Nile delta and Israeli margin as determined by heavy minerals. Journal of Coastal Research, 5(4), 813–828.

5. Lin, I. J., Rohrlich, V., & Slatkine, A. (1974). Surface microtextures of heavy mineralsfrom the Mediterranean coast of Israel. Journal of Sedimentary Petrology, 44(4), 1281–1295.

6. Pomerancblum, M. (1966). The distributionof heavy minerals and their hydraulic equivalents in sediments of the Mediterranean continental shelf of Israel. Journal of Sedimentary Petrology, 36(1), 162–174.

7. Boenigk, W., & Neber, A. (2005). Temporal and Spatial Variations in the Heavy Mineral Spectra of Coastal Dunes Along the Israeli Coastal Plain. Journal of The Israel Prehistoric Society, 35, 19–43.

8. Almagor, G., Gill, D., & Perath, I. (2000). Marine Sand Resources Offshore Israel. Marine Georesources & Geotechnology, 18(1), 1–42.

9. Ronen, A. (2018). Quaternary sedimentology and prehistory on the Mediterranean coastal plain of Israel. Quaternary International, 464, 315–326. https://doi.org/10.1016/j.quaint.2017.10.027.

10. Morag, N., Avigad, D., Gerdes, A., Abbo, A. (2021) Detrital zircon and rutile U–Pb, Hf isotopes and heavy mineral assemblages of Israeli Miocene sands: Fingerprinting the Arabian provenance of the Levant. Basin Research, 33(3), 1967–1984. doi:10.1111/bre.12544.

11. Ilani, S., Shirav, M., Halicz, L., Yofa, O. (1992) Geochemistry of stream sediments in the mount Carmel area, Israel. Report GSI/15/92. Ministry of Energy and Infrastructure, Geological Survey of Israel, Israel.

12. Wasserman, R. I. (2021). Deterioration of Sandstone in the Historical and Contemporary Sea Walls upon the Impact of the Natural and Man-Made Hazards. Applied Sciences, 11(15), 6892. https://doi.org/10.3390/app11156892.

13. Kandler, K., Schneiders, K., Heuser, J., Waza, A., Aryasree, S., Althausen, D., Hofer, J., Abdullaev, S. F., Makhmudov, A. N. (2020) Differences and similarities of Central Asian, African, and Arctic dust composition from a single particle perspective. Atmosphere, 11(3), 269. doi:10.3390/atmos11030269.

14. Baldo, C., Formenti, P., Nowak, S., Chevaillier, S., Cazaunau, M., Pangui, E., Di Biagio, C., Doussin, J–F., Ignnatyev, K., Dagsson-Waldhauserova, P., Arnalds, O., MacKenzie, A. R., Shi, Z. (2020) Distinct chemical and mineralogical composition of Icelandic dust compared to northern African and Asian dust. Atmos. Chem., Phys., 20, 13521–13539. https://doi.org/10.5194/acp-20-13521-2020.

15. Jeong, G. Y. (2008) Bulk and single-particle mineralogy of Asian dust and a comparison with its source soils. Journal of Geophysical Research, 113, D02208. doi:10.1029/2007JD008606. 16. Jeong, G. Y., Park, M. Y., Kandler, K., Nousiainen, T., Kemppinen, O. (2016) Mineralogical properties and internal structures of individual fine particles of Saharan dust. Atmos. Chem. Phys., 16, 12397–12410. doi:10.5194/acp-16-12397-2016.

17. Vola, G., Gotti, E., Brandon, C., Oleson, J. P., & Hohlfelder, R. L. (2011). Chemical, mineralogical and petrographic characterization of Roman ancient hydraulic concretes cores from Santa Liberata, Italy, and Caesarea Palestinae, Israel. Periodico Di Mineralogia, 80(2), 317–338. https://doi.org/10.2451/2011PM0023.

18. Boyce, J. I., Reinhardt, E. G., & Goodman, B. N. (2009). Magnetic detection of ship ballast deposits and anchorage sites in King Herod's Roman harbour, Caesarea Maritima, Israel. J. Archaeol. Sci., 36(7), 1516–1526. https://doi.org/10.1016/j.jas.2009.03.007.

APPENDIX B2: Chapter 3 Supplementary Data 2 - μXRF average counts for elements of interest in W, C1, C2, HC (hydraulic concrete; COF), and K (kurkar; COF).

Core/ Area	Depth (cm)	Zr	SD	Ca	SD	Si	SD	Ti	SD	Fe	SD	Sr	SD	Zr+Ti/ Ca	SD	Zr+Ti/ Si	SD	Sr/Ca	SD
	0–5	397	±143	172119	±24522	17657	±3460	2970	±837	5573	±885	2109	±138	0.020	±0.004	0.195	±0.049	0.012	±0.002
	70–75	1017	±305	209938	±29846	23810	±1098	6974	±3459	6167	±1097	2346	±175	0.039	±0.016	0.339	±0.157	0.011	±0.002
	110–115	329	±115	189258	±27153	21272	±1217	5681	±4857	6118	±1071	2253	±147	0.032	±0.025	0.278	±0.214	0.012	±0.002
W	130–135	646	±341	255620	±40964	22266	±1533	3794	±1454	6136	±1199	2404	±137	0.018	±0.008	0.199	±0.069	0.010	±0.002
	150–155	430	±160	297180	±29974	21090	±929	3826	±3243	5001	±727	2520	±178	0.015	±0.012	0.202	±0.150	0.009	±0.001
	152–157	837	±197	195907	±30622	20725	±1055	4795	±1740	6288	±704	2174	±122	0.029	±0.008	0.272	±0.085	0.011	±0.002
	180–185	609	±216	229867	±39636	22493	±2125	5451	±3130	4898	±737	2482	±167	0.028	±0.017	0.274	±0.157	0.011	±0.002
	0–1	743	±190	170971	±20778	15771	±1072	10250	±3017	11158	±1640	2252	±176	0.064	±0.017	0.705	±0.219	0.013	±0.002
	12–13	763	±256	161029	±21841	17333	±883	5571	±3203	7089	±1056	2048	±128	0.041	±0.026	0.362	±0.173	0.013	±0.002
	26–27	524	±248	247453	±28267	16178	±1205	5980	±2586	7208	±1183	2598	±185	0.027	±0.012	0.403	±0.163	0.011	±0.001
	28–29	522	±317	233598	±29330	16424	±973	6060	±2493	7417	±991	2477	±181	0.029	±0.013	0.400	±0.151	0.011	±0.001
	30–31	653	±269	274475	±54847	6834	±633	5703	±1986	7780	±1007	2384	±152	0.024	±0.009	0.943	±0.336	0.009	±0.002
	38–39	373	±207	174316	±18349	17032	±1308	6243	±2514	7455	±738	2044	±199	0.038	±0.016	0.386	±0.141	0.012	±0.002
	42–43	303	±158	185727	±33586	16850	±1048	4077	±655	6362	±552	2114	±158	0.024	±0.004	0.261	±0.046	0.012	±0.002
	44–45	234	±114	162698	±22674	17149	±962	5044	±1709	6409	±864	2055	±99	0.033	±0.013	0.308	±0.100	0.013	±0.002
	46–47	333	±118	194626	±23728	18335	±1076	5503	±1966	7581	±849	2001	±138	0.030	±0.011	0.318	±0.104	0.010	±0.001
C1	70–71	260	±129	182743	±23164	18332	±984	4153	±694	6429	±961	2124	±107	0.025	±0.005	0.242	±0.042	0.012	±0.002
	80–81	233	±129	206776	±44149	16798	±965	4733	±1637	6885	±884	2139	±169	0.025	±0.010	0.296	±0.101	0.011	±0.002
	82–83	218	±119	194139	±24482	14542	±812	4696	±929	7260	±890	2212	±189	0.026	±0.007	0.338	±0.063	0.012	±0.002
	84–85	228	±72	185088	±27404	14573	±964	4380	±972	6860	±945	2367	±256	0.025	±0.006	0.319	±0.079	0.013	±0.003
	86–87	277	±117	183679	±25342	17326	±877	4679	±1532	7148	±719	2374	±161	0.027	±0.009	0.289	±0.105	0.013	±0.002
	88–89	278	±111	210125	±34981	15628	±987	4265	±547	7066	±627	2537	±275	0.022	±0.006	0.291	±0.033	0.012	±0.002
	94–95	261	±74	196520	±26212	16673	±1943	4149	±609	8076	±697	2199	±183	0.023	±0.005	0.268	±0.047	0.011	±0.002
	96–97	339	±204	187000	±25123	19034	±1573	4630	±1283	7152	±695	2295	±125	0.027	±0.005	0.265	±0.081	0.013	±0.002
	98–98	274	±123	184881	±26762	17098	±1445	4716	±1344	7552	±860	2252	±138	0.028	±0.009	0.294	±0.080	0.012	±0.002
	126–127	470	±148	193731	±21380	15254	±683	10316	±2133	14044	±1177	2143	±210	0.056	±0.012	0.711	±0.164	0.011	±0.002
	2–3	554	±249	246148	±67472	19488	±1800	7428	±2420	9562	±1385	2397	±454	0.035	±0.016	0.410	±0.118	0.010	±0.002
	22–23	788	±293	184647	±23646	22392	±1435	8198	±3546	9337	±1071	2512	±236	0.050	±0.023	0.399	±0.151	0.014	±0.003
	24–25	391	±164	172407	±18621	18544	±1604	7979	±2466	10268	±1171	2053	±152	0.049	±0.015	0.453	±0.128	0.012	±0.002
	26–27	445	±135	177748	±16276	18045	±891	8403	±2893	10934	±820	2065	±150	0.050	±0.017	0.488	±0.151	0.012	±0.002
	43–44	461	±142	183428	±24293	16651	±771	8037	±2244	11413	±1155	2074	±149	0.047	±0.012	0.514	±0.153	0.011	±0.002
	63–64	326	±128	208323	±39292	14953	±1610	6689	±1430	8966	±697	2147	±185	0.034	±0.006	0.477	±0.123	0.011	±0.002
C2	82–83	391	±161	174952	±28503	18404	±818	7053	±1668	9317	±817	2051	±142	0.043	±0.013	0.406	±0.102	0.012	±0.002
	123–124	323	±114	183301	±22625	11252	±677	14698	±874	20045	±1030	2187	±169	0.083	±0.011	1.339	±0.109	0.012	±0.002
	126–127	266	±83	180654	±18451	11056	±690	12917	±3255	15846	±1835	2138	±156	0.073	±0.017	1.200	±0.328	0.012	±0.002
	129–130	388	±156	174019	±23797	7066	±925	9387	±1546	14234	±1884	2165	±137	0.058	±0.014	1.405	±0.289	0.013	±0.002
	137–138	360	±162	183343	±25014	11180	±2610	8081	±2484	10891	±1238	2222	±162	0.046	±0.012	0.781	±0.269	0.012	±0.002
	139–140	361	±123	209582	±22096	16659	±993	9381	±3241	11051	±861	2253	±176	0.047	±0.016	0.585	±0.196	0.011	±0.002
	141–142	458	±233	202596	±26839	17350	±1195	11953	±3562	13298	±1318	2091	±154	0.063	±0.021	0.715	±0.195	0.010	±0.002
	161–162	457	±98	196603	±16689	13169	±1125	14087	±3100	18122	±1185	2133	±181	0.075	±0.018	1.116	±0.272	0.011	±0.001
HC	-	2517	±800	167214	±140398	10003	±1445	17757	±3819	37205	±8636	3002	±578	0.187	±0.105	2.024	±0.362	0.025	±0.012
K	-	204	±135	849757	±132336	4494	±1459	1691	±1569	4738	±2471	4376	±1259	0.002	±0.002	1.265	±4.605	0.006	±0.005

APPENDIX B3: Chapter 3 Supplementary Data 3 - Relative abundances (%) of foraminifera taxa observed in W, C1, and C2.

Core	Depth (cm)	Specimens per cubic centimeter	Biofacies Assemblage	*Ammonia inflata*	*Ammonia parkinsoniana*	*Ammonia tepida*	*Buccella* spp.	*Elphidium* spp.	*Pararotalia calcariformata*	*Porosononion* spp.	*Textularia bocki*	*Tretomphalus bulloides*	Miliolids	Planktics	Other Rotalids	Other taxa
W	0–5	22.9	A1	-	19.77	-	-	5.23	51.74	4.07	0.58	-	15.12	3.49	-	-
	70–75	27.3	A1	0.98	21.46	0.49	0.49	2.44	43.90	6.83	0.49	0.49	15.12	2.44	2.44	2.44
	110–115	16.5	A2	3.23	62.10	-	1.61	4.84	4.03	-	-	0.81	20.16	0.81	1.61	0.81
	130–135	87.5	A2	0.91	51.68	4.88	1.37	4.73	1.22	12.04	-	-	18.75	3.20	-	1.22
	150–155	22.4	A2	1.19	45.83	7.14	0.60	8.93	-	8.93	0.60	-	22.02	1.19	0.60	2.98
	152–157	70.1	A2	2.09	68.25	0.57	-	1.33	0.38	1.90	-	0.38	18.25	3.42	2.47	0.95
C1	0–1	20.0	A1	0.67	4.67	1.33	1.33	1.33	55.33	5.33	-	0.67	18.00	2.00	3.33	6.00
	12–13	23.1	A1	-	13.87	1.16	1.73	0.58	42.77	4.05	0.58	-	20.23	10.40	1.16	3.47
	26–27	190.0	A1	0.38	2.63	0.75	0.38	0.38	73.68	0.75	1.13	-	12.78	2.63	1.13	3.38
	30–31	272.2	A1	0.41	12.24	0.82	0.41	0.82	60.41	2.04	0.41	-	17.14	0.82	2.04	2.45
	30–37	61.1	A1	0.43	9.91	0.86	-	-	56.90	2.59	2.16	0.43	15.95	3.88	3.88	3.02
	38–39	35.4	A3	0.51	15.15	0.51	0.51	4.55	19.19	1.52	0.51	2.02	41.92	6.06	5.05	2.53
	46–47	14.7	A4	0.91	23.18	0.91	3.64	4.09	0.91	7.73	-	3.64	45.45	1.36	4.09	4.09
	70–71	36.3	A4	1.45	25.36	2.17	0.72	-	15.94	11.59	-	-	28.26	10.14	0.72	3.62
	80–81	36.0	A4	1.48	34.07	0.74	1.85	1.85	-	12.59	-	-	41.48	3.33	-	2.59
	84–85	27.3	A4	1.46	43.41	0.98	0.98	-	-	13.17	-	-	37.07	0.49	-	2.44
	85–93	38.5	A4	1.38	33.91	0.69	0.69	2.77	-	11.42	-	-	39.10	7.96	-	2.08
	94–95	48.0	A4	0.56	43.61	0.83	-	3.33	-	7.50	-	-	31.39	9.17	-	3.61
	96–97	38.3	A3	1.05	19.16	1.05	-	3.48	-	10.80	-	-	55.75	6.27	-	2.44
	126–127	23.5	A4	2.84	28.41	1.14	2.27	1.70	-	15.34	-	-	31.82	7.39	5.11	3.98
C2	2–3	12.4	A3	2.15	4.30	3.23	-	2.15	18.28	3.23	3.23	1.08	50.54	2.15	6.45	3.23
	22–23	15.5	A3	-	9.05	-	2.59	-	6.90	2.16	-	4.74	68.53	0.86	2.16	3.02
	24–25	19.9	A4	2.01	35.57	1.34	-	3.69	6.38	1.01	1.01	-	39.60	7.05	2.35	-
	26–27	34.1	A4	1.95	31.25	1.95	0.39	0.78	6.25	2.34	1.17	5.47	46.48	1.56	0.39	-
	28–35	33.3	A4	3.20	31.20	0.80	-	4.00	10.80	2.00	0.40	-	39.20	6.80	1.60	-
	35–38	18.6	A4	1.79	29.75	0.72	0.72	2.15	20.79	1.43	0.72	-	37.99	1.43	2.15	0.36
	38–42	13.9	A3	1.92	23.08	0.48	0.48	5.29	6.73	3.37	0.48	-	57.21	0.96	-	-
	43–44	8.8	A4	0.76	38.64	1.52	0.76	5.30	-	3.03	-	-	43.18	3.79	3.03	-
	63–64	15.7	A3	3.39	16.10	3.39	0.85	3.39	-	8.47	-	-	58.47	5.08	-	0.85
	82–83	23.1	A3	1.16	15.03	4.62	0.58	5.78	-	3.47	1.16	-	61.85	6.36	-	-
	126–127	33.6	A4	-	32.94	4.37	-	4.76	1.19	12.70	0.79	-	29.37	6.75	3.17	3.97
	129–130	41.3	A4	0.65	36.13	3.55	-	8.71	-	11.94	-	-	32.26	3.23	0.97	2.58
	131–137	60.0	A4	-	33.33	2.84	2.84	3.90	0.71	17.02	1.06	-	20.57	14.54	1.06	2.13
	139–140	110.3	A2	0.24	51.63	4.59	1.09	3.39	-	18.50	0.24	-	17.90	1.21	-	1.21
	141–142	165.5	A2	0.16	69.95	0.79	0.79	0.79	-	11.61	-	-	11.61	4.29	-	-
	161–162	29.6	A4	1.35	20.27	0.90	1.35	3.60	-	14.41	-	-	41.44	12.16	1.80	2.70

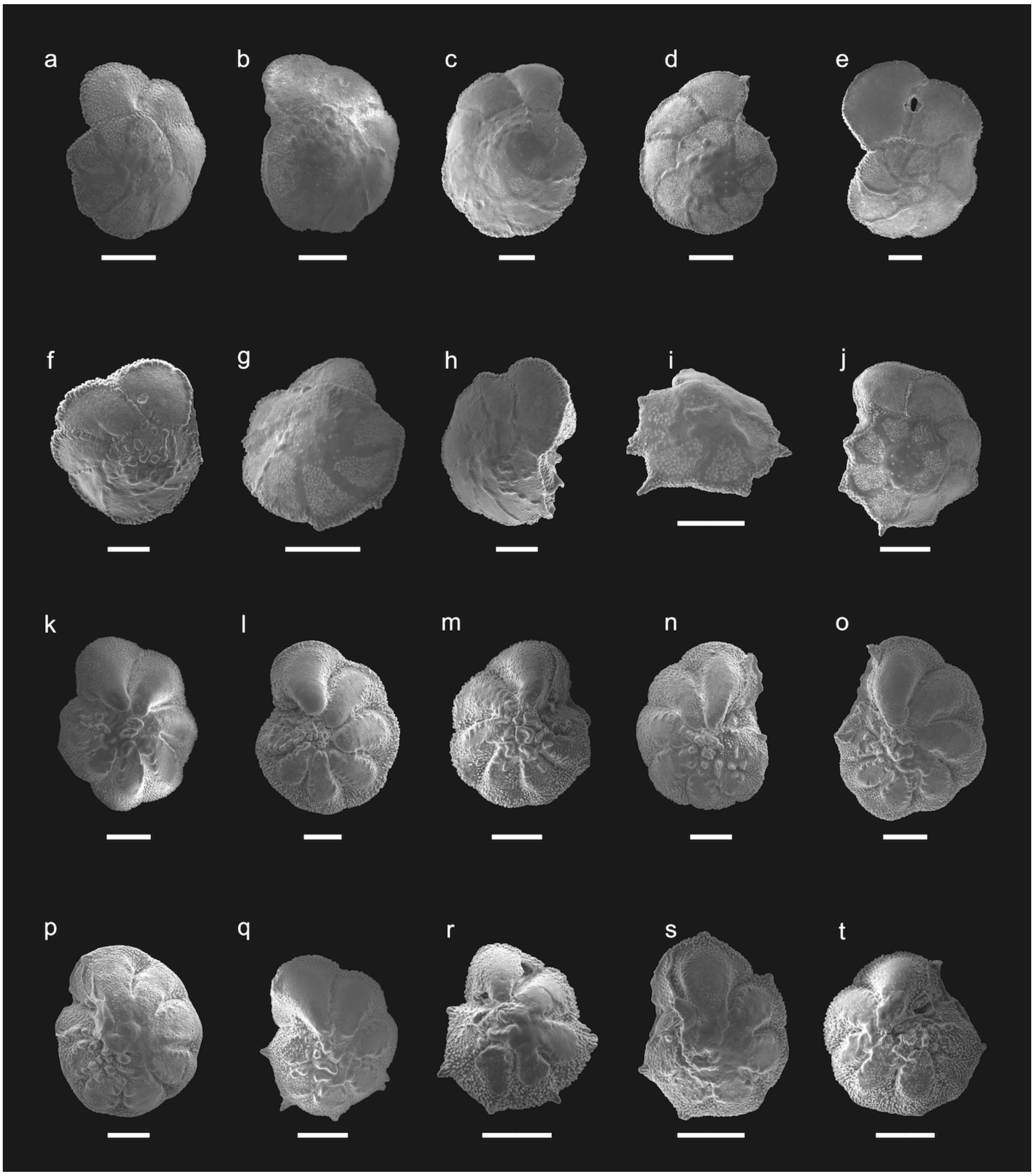

APPENDIX B4: Chapter 3 Supplementary Data 4 - SEM images of *Pararotalia calcariformata* from C1 (12–13 cm) a–j: spiral view. k–t: umbilical view. Scale bars represent 100 μm.

APPENDIX C1: Chapter 4 Supplementary Data 1 - Table of relative abundances (%) of foraminifera and testate amoebae in Khor Al Balid samples, with concentration (specimens/cc), Shannon Diversity Index (SDI), and biofacies (see Figure 4.2; BLM=Brackish marsh/lagoon, MS=Marine sand, F=Freshwater).

Core	**ALB1**	**ALB1**	**ALB1**	**ALB1**	**ALB1**	**ALB1**	**ALB1**	**ALB1**	**ALB1**	**ALB1**
Sample depth (cm)	**14–16**	**29–31**	**37–38**	**55–57**	**69–71**	**75–78**	**85–88**	**95–98**	**108–114**	**122–127**
Specimens/cc	595	368	393	436	537	827	643	552	178	977
SDI	2.0	2.1	2.0	1.7	1.5	2.1	1.5	1.4	0.9	1.0
Biofacies	ALB-A1	ALB-A1	ALB-A1	ALB-A2	ALB-A3	ALB-A2	ALB-A2	ALB-A2	ALB-A2	ALB-A2
Foraminifera taxa										
Ammonia beccarii "parkinsoniana"	0.8	3.2	1.2	3.8	2.6	3.5	2.6	4.3	1.4	1.7
Amphistegina spp.	3.6	11.0	12.7	32.3	7.1	23.9	52.6	60.3	77.1	72.1
Assilina ammonoides	0.4	-	-	1.6	0.4	0.6	4.1	-	5.0	7.3
Borelis schlumbergeri	-	-	0.6	0.5	-	2.0	2.6	2.1	0.5	3.2
Brebina sp.	-	-	-	3.3	0.4	2.0	5.9	2.6	2.3	1.5
Cibicides pseudolobatulus	2.0	3.2	7.9	6.5	4.0	11.5	1.5	4.3	0.5	-
Discorinopsis aquayoi	20.0	7.8	1.2	-	0.9	0.6	-	-	-	-
Elphidium craticulatum	1.2	1.9	0.6	4.3	1.8	1.7	2.2	1.7	2.3	0.7
Elphidium excavatum	0.8	0.6	-	-	-	-	-	-	-	-
Elphidium limbatum	2.0	2.6	6.1	7.6	1.8	6.9	5.9	5.2	1.8	3.9
Elphidium translucens	1.6	1.9	0.6	0.5	-	-	-	-	-	-
Helenina andersoni	22.4	28.5	21.2	1.6	0.9	3.8	-	0.4	-	-
Miliolinella semicostata	0.4	2.6	0.6	-	-	4.3	0.4	-	-	-
Nonion subturgidum	-	-	-	-	0.4	0.3	-	-	-	-
Pararotalia spinigera	-	1.3	-	0.5	0.4	0.6	0.4	0.4	-	-
Quinqueloculina seminulum	0.8	-	-	-	0.4	0.6	-	-	-	-
Rosalina columbiensis	-	-	-	-	-	-	-	-	-	-
Trochammina inflata	19.6	7.8	12.7	1.6	-	-	-	-	-	-
Trochammina macrescens	12.0	16.8	23.0	0.5	0.4	-	-	-	-	-
Eroded specs	7.6	5.8	8.5	20.2	5.3	18.7	14.8	10.7	7.2	6.6
Planktic taxa	-	-	-	-	-	-	-	-	-	-
Testate amoebae taxa										
Arcella vulgaris	-	-	-	-	10.2	1.1	-	-	-	-
Centropyxis constricta	-	-	-	-	50.5	2.9	-	-	-	-
Centropyxis aculeata	-	-	-	-	9.7	3.2	-	-	-	-

APPENDIX C1: Chapter 4 Supplementary Data 1 - Continued.

Core	**ALB2**	**ALB2**	**ALB2**	**ALB2**	**ALB2**	**ALB2**	**ALB2**	**ALB2**	**ALB2**	**ALB2**	**ALB2**	**ALB2**	**ALB2**
Sample depth (cm)	**0–2**	**2–4**	**6–8**	**8–10**	**12–14**	**15–17**	**18–20**	**22–24**	**25–27**	**27–30**	**30–32**	**32–35**	**35–37**
Specimens/cc	221	1926	221	702	232	489	522	934	382	154	380	610	830
SDI	0.9	0.7	2.0	2.0	1.7	2.0	0.5	0.2	0.8	1.0	1.7	1.4	1.7
Biofacies	ALB-A1	ALB-A1	ALB-A1	ALB-A2	ALB-A1	ALB-A1	ALB-A3	ALB-A3	ALB-A3	ALB-A3	ALB-A2	ALB-A2	ALB-A2
Foraminifera taxa													
Ammonia beccarii "parkinsoniana"	0.5	-	7.3	3.6	0.3	1.8	-	-	3.8	1.2	4.7	1.0	5.5
Amphistegina spp.	3.8	0.5	12.9	20.8	6.7	10.0	-	0.6	2.8	4.6	40.2	45.7	19.3
Assilina ammonoides	-	-	-	-	0.3	1.1	-	-	-	-	1.6	0.5	-
Borelis schlumbergeri	0.5	-	2.4	1.0	0.3	0.7	-	-	-	-	2.0	1.5	0.4
Brebina sp. 1	-	-	-	5.1	1.0	2.2	-	-	-	-	4.7	2.5	1.1
Cibicides pseudolobatulus	0.5	-	12.1	18.3	1.8	10.3	-	-	-	1.2	9.4	6.0	17.1
Discorinopsis aquayoi	-	0.3	1.6	1.0	3.9	1.1	-	-	1.0	-	1.2	-	-
Elphidium craticulatum	1.6	-	3.3	4.1	1.8	3.3	-	-	-	1.2	1.6	2.0	3.7
Elphidium excavatum	-	-	0.8	-	0.5	-	-	-	-	-	-	-	-
Elphidium limbatum	-	-	2.4	6.1	1.0	2.6	-	-	-	-	3.9	6.5	10.6
Elphidium translucens	-	-	2.4	0.5	0.8	0.4	-	-	1.8	-	-	-	-
Helenina andersoni	70.3	63.4	25.9	6.6	51.3	31.0	-	-	-	-	-	-	-
Miliolinella semicostata	-	-	0.8	3.0	0.3	1.5	-	-	-	-	1.2	1.0	2.9
Nonion subturgidum	-	-	-	-	-	-	-	-	-	-	-	-	-
Pararotalia spinigera	-	-	-	1.5	-	2.2	-	-	-	-	1.2	-	1.5
Quinqueloculina seminulum	0.5	-	1.6	-	0.8	0.7	-	-	1.0	-	0.8	-	-
Rosalina columbiensis	-	-	-	-	-	-	-	-	-	-	-	-	-
Trochammina inflata	0.5	-	-	0.5	17.3	5.8	-	-	-	-	0.4	0.5	-
Trochammina macrescens	20.2	35.2	0.8	1.0	5.4	0.4	1.3	-	-	2.4	-	-	-
Eroded specs.	1.1	-	17.8	15.7	4.9	15.0	2.8	1.3	6.5	22.0	16.1	16.9	24.1
Planktic taxa	-	-	-	-	-	-	-	-	-	-	-	-	-
Testate amoebae taxa													
Arcella vulgaris	-	-	-	-	-	-	5.5	0.6	-	-	-	-	-
Centropyxis constricta	-	-	-	-	-	-	68.5	55.4	55.2	47.6	-	-	-
Centropyxis aculeata	-	-	-	-	-	-	14.4	37.1	21.4	16.2	-	-	-

APPENDIX C1: Chapter 4 Supplementary Data 1 - Continued.

Core	**ALB3**	**ALB3**	**ALB3**	**ALB3**	**ALB3**	**ALB3**
Sample depth (cm)	**0–2**	**5–7**	**10–12**	**13–15**	**20–22**	**25–26**
Specimens/cc	1519	255	115	114	866	719
SDI	1.3	0.7	1.9	1.8	1.8	1.5
Biofacies	ALB-A1	ALB-A1	ALB-A2	ALB-A2	ALB-A2	ALB-A2
Foraminifera taxa						
Ammonia beccarii "parkinsoniana"		0.2	2.1	2.5	4.7	3.3
Amphistegina spp.	0.2	0.4	24.3	30.3	28.3	53.4
Assilina ammonoides	-	-	3.5	1.8	2.2	0.3
Borelis schlumbergeri	-	-	3.9	1.1	2.7	1.0
Brebina sp.	-	0.4	0.9	3.9	2.7	1.3
Cibicides pseudolobatulus	0.2	0.8	5.6	4.9	5.2	5.6
Discorinopsis aquayoi	0.6	-		-	-	-
Elphidium craticulatum	-	-	2.1	1.4	3.3	3.0
Elphidium excavatum	8.0	-	-	-	-	0.7
Elphidium limbatum	-	-	6.1	6.4	5.2	6.0
Elphidium translucens	19.8	0.2	1.3	0.4	-	1.7
Helenina andersoni	-	1.9	0.4	0.4	-	0.3
Miliolinella semicostata	-	-	-	1.8	4.4	1.0
Nonion subturgidum	-	-	-	-	-	-
Pararotalia spinigera	-	-	3.5	0.7	3.0	0.3
Quinqueloculina seminulum	24.6	7.7	1.7	2.1	0.5	0.3
Rosalina columbiensis	-	-	-	-	-	-
Trochammina inflata	29.7	83.1	4.8	2.1	-	-
Trochammina macrescens	-	1.4	-	0.4	-	-
Eroded specs.	-	3.9	33.4	29.9	23.1	19.8
Planktic taxa	-	-	-	-	-	-
Testate amoebae taxa						
Arcella vulgaris	-	-	-	-	-	-
Centropyxis constricta	-	-	-	-	-	-
Centropyxis aculeata	-	-	-	-	-	-

APPENDIX C1: Chapter 4 Supplementary Data 1 - Continued.

Core	**ALB4**	**ALB4**	**ALB4**	**ALB4**	**ALB4**	**ALB4**	**ALB4**	**ALB4**	**ALB4**	**ALB4**	**ALB4**	**ALB4**	**ALB4**
Sample depth (cm)	**0–2**	**2–4**	**4–6**	**6–7**	**7–9**	**9–11.5**	**11.5–13.5**	**13.5–15**	**17–19**	**19–21**	**23–25**	**25–27**	**27–27.5**
Specimens/cc	601	862	1277	4291	718	790	18	13	8	14	44	460	319
SDI	0.5	1.9	2.0	2.0	1.8	2.0	1.6	1.5	1.5	1.9	1.9	1.5	1.9
Biofacies	ALB-A3	ALB-A2	ALB-A2	ALB-A2	ALB-A2	ALB-A1	ALB-A1	ALB-A1	ALB-A1	ALB-A1	ALB-A1	ALB-A2	ALB-A2
Foraminifera taxa													
Ammonia beccarii "parkinsoniana"	-	2.8	2.3	2.3	2.5	2.8	0.6	-	-	2.2	6.0	6.1	4.9
Amphistegina spp.	3.2	11.9	7.9	4.7	22.3	2.8	0.6	0.8	2.5	1.5	6.4	26.9	8.4
Assilina ammonoides	-	1.4	0.9	0.3	1.3	0.8	-	-	-	-	-	0.9	0.4
Borelis schlumbergeri	-	0.3	0.9	-	0.4	-	-	-	-	-	-	-	-
Brebina sp.	-	-	0.5	0.3	0.8	0.4	-	-	-	-	-	-	-
Cibicides pseudolobatulus	1.2	11.2	6.9	4.1	12.3	10.6	1.8	3.3	15.2	13.9	14.2	10.0	9.1
Discorinopsis aquayoi	-	-	5.6	5.8	0.4	4.5	-	2.5	-	3.7	-	-	-
Elphidium craticulatum	-	1.0	0.9	-	1.7	0.4	0.6	-	-	0.7	1.6	0.9	0.4
Elphidium excavatum	-	-	-	-	-	-	-	1.7	-	0.7	0.9	-	-
Elphidium limbatum	0.4	4.2	0.5	0.6	6.3	2.0	1.2	-	-	0.7	12.8	11.3	6.5
Elphidium translucens	-	-	-	-	-	1.6	2.4	4.1	2.5	2.9	1.1	0.4	0.4
Helenina andersoni	5.2	3.8	7.0	0.4	-	19.5	30.0	42.2	39.3	23.4	25.0	-	13.4
Miliolinella semicostata	-	4.2	5.6	4.9	5.9	1.2	-	-	-	-	0.2	-	0.7
Nonion subturgidum	-	1.0	1.8	2.6	0.8	5.3	4.9	15.7	16.5	11.4	5.2	-	0.7
Pararotalia spinigera	-	-	0.5	0.9	0.8	0.4	-	-	-	-	-	0.4	-
Quinqueloculina seminulum	-	-	-	2.0	-	1.6	0.6	0.8	1.3	0.7	-	-	0.4
Rosalina columbiensis	-	-	-	7.3	1.3	3.3	-	-	2.5	-	-	-	-
Trochammina inflata	-	-	-	-	-	0.8	1.2	0.8	-	-	-	-	0.7
Trochammina macrescens	-	-	0.5	0.3	-	-	0.6	-	-	-	-	-	-
Eroded specs.	5.2	24.6	22.6	14.5	24.5	19.6	6.1	7.5	5.1	13.1	22.5	41.3	28.8
Planktic taxa	-	10.5	14.3	32.9	5.5	8.1	24.4	18.2	13.9	22	3.6	-	6.5
Testate amoebae taxa													
Arcella vulgaris	-	-	-	-	-	-	-	-	-	-	-	-	-
Centropyxis constricta	62.2	4.9	2.7	0.3	-	-	3.0	-	-	-	-	-	3.7
Centropyxis aculeata	21.0	12.7	8.7	1.5	-	-	20.1	-	-	-	-	-	12.5

APPENDIX C1: Chapter 4 Supplementary Data 1 - Continued.

Core	**ALB5**	**ALB5**	**ALB5**	**ALB5**	**ALB5**	**ALB5**	**ALB5**	**ALB5**	**ALB5**	**ALB5**	**ALB5**	**ALB5**	**ALB5**	**ALB5**
Sample depth (cm)	**0–2**	**4–5**	**5–7**	**7–8**	**9.5–11**	**13–15**	**15–16**	**16–18**	**19–21**	**21–23**	**23–26**	**26–28**	**28–30**	**30–31**
Specimens/cc	892	316	478	274	118	126	271	309	177	122	187	548	701	762
SDI	0.7	0.9	1.9	2.0	1.0	0.7	1.1	1.1	1.1	0.3	0.2	0.7	0.6	1.7
Biofacies	ALB-A3	ALB-A3	ALB-A2	ALB-A2	ALB-A3	ALB-A3	ALB-A1	ALB-A3	ALB-A3	ALB-A3	ALB-A3	ALB-A3	ALB-A3	ALB-A2
Foraminifera taxa														
Ammonia beccarii "parkinsoniana"	-	-	9.0	5.9	-	0.5	0.9	-	-	-	-	1.3	0.5	3.7
Amphistegina spp.	-	0.7	33.9	21.5	0.5	1.5	1.7	-	-	-	-	1.4	1.1	12.7
Assilina ammonoides	-	-	0.4	0.7	-	-	-	-	-	-	-	-	-	-
Borelis schlumbergeri	-	-	-	0.7	-	-	-	-	-	-	-	-	-	-
Brebina sp.	-	-	-	-	-	-	-	-	-	-	-	-	-	-
Cibicides pseudolobatulus	-	-	13.1	7.8	-	-	0.9	-	0.9	-	-	4.6	1.1	4.3
Discorinopsis aquayoi	-	-	-	-	1.5	-	2.7	1.5	0.9	-	-	0.7	0.5	0.5
Elphidium craticulatum	-	-	1.9	-	-	-	-	-	-	-	-	-	-	0.9
Elphidium excavatum	-	-	-	-	2.0	-	-	-	-	-	-	-	-	-
Elphidium limbatum	-	-	8.2	5.9	0.5	-	0.9	-	-	-	-	0.7	-	3.7
Elphidium translucens	-	-	-	-	4.0	-	1.8	1.5	3.6	0.5	0.6	-	-	0.5
Helenina andersoni	11.2	13.5	11.9	15.0	6.5	7.6	70.4	26.2	29.7	2.5	0.6	3.3	7.1	4.3
Miliolinella semicostata	-	-	0.4	-	-	-	-	-	-	-	-	-	-	-
Nonion subturgidum	-	-	-	-	-	-	-	-	-	-	-	-	-	-
Pararotalia spinigera	-	-	0.7	0.7	-	-	-	-	-	-	-	-	-	-
Quinqueloculina seminulum	-	-	-	-	0.5	-	0.4	-	-	-	-	-	-	-
Rosalina columbiensis	-	-	-	-	-	-	-	-	-	-	-	-	-	-
Trochammina inflata	-	-	-	-	2.0	-	2.3	1.5	0.9	-	-	-	-	-
Trochammina macrescens	-	-	-	1.3	-	0.5	-	3.8	-	-	-	-	-	-
Eroded specs.	8.0	8.3	14.6	20.8	4.0	1.9	3.1	1.5	1.8	-	-	3.9	2.6	38.5
Planktic taxa	-	-	-	-	-	-	-	-	-	-	-	-	-	-
Testate amoebae taxa														
Arcella vulgaris	1.6	0.7	-	0.7	1.5	4.3	0.9	1.5	1.8	2.5	2.0	-	-	2.8
Centropyxis constricta	32.8	14.3	-	3.3	3.5	1.5	0.9	13.9	5.4	7.4	2.6	12.4	28.0	3.7
Centropyxis aculeata	46.4	28.6	3.4	13.7	73.3	81.2	12.0	45.4	53.1	86.1	93.6	71.0	58.0	24.4

APPENDIX C2: Chapter 4 Supplementary Data 2 - Table of relative abundances (%) of foraminifera and testate amoebae in Khor Rori samples, with concentration (specimens/cc), and biofacies (see Figure 4.2; BLM=Brackish marsh/lagoon, MS=Marine sand, F=Freshwater).

Core	**ROR3**	**ROR3**	**ROR3**	**ROR3**	**ROR3**	**ROR3**	**ROR3**	**ROR3**
Sample depth (cm)	**0–2**	**8–10**	**17–19**	**28–30**	**37–39**	**46–48**	**55.5–58**	**65–67**
Specimens/cc	182	238	144	100	78	49	2	5
Biofacies	ROR-A1	ROR-A1	ROR-A1	ROR-A1	ROR-A1	ROR-A1	ROR-A1	ROR-A1
Foraminifera taxa								
Ammonia beccarii "parkinsoniana"	-	-	-	-	-	-	-	-
Ammonia beccarii "tepida"	-	-	-	-	-	-	-	-
Amphistegina spp.	-	-	-	-	-	-	-	-
Brizalina striatula	-	-	-	-	-	-	-	-
Cibicides pseudolobatulus	-	-	-	-	-	-	-	-
Discorinopsis aquayoi	-	-	-	-	-	-	-	-
Elphidium craticulatum	-	-	-	-	-	-	-	-
Elphidium crispum	-	-	-	-	-	-	-	-
Elphidium excavatum	-	-	-	-	-	-	-	-
Helenina andersoni	1.8	1.7	4.3	8.4	-	-	-	-
Nonionella opima	-	-	-	-	-	-	-	-
Testate amoebae taxa								
Arcella vulgaris	6.0	5.0	3.2	4.2	4.4	9.8	72.2	43.5
Centropyxis aculeata	33.9	31.9	49.0	47.9	68.5	33.6	22.8	26.1
Centropyxis constricta	51.3	54.4	29.7	33.9	21.0	46.7	-	30.4
Cucurbitella tricuspis		1.0	4.0	1.4		4.5	-	-
Difflugia oblonga	5.3	5.0	9.7	4.2	6.2	5.3	-	-
Difflugia urceolata	1.8	1.0	-	-	-	-	-	-

APPENDIX C2: Chapter 4 Supplementary Data 2 - Continued.

Core	**ROR5**	**ROR5**	**ROR5**	**ROR5**	**ROR5**	**ROR5**	**ROR5**	**ROR5**	**ROR5**
Sample depth (cm)	**0–2**	**8–10**	**17–18.5**	**26–28**	**35–37**	**46–48**	**60–64**	**80–84**	**100–105**
Specimens/cc	196	184	203	308	277	390	331	415	390
Biofacies	ROR-A1	ROR-A1	ROR-A2	ROR-A2	ROR-A2	ROR-A2	ROR-A2	ROR-A2	ROR-A2
Foraminifera taxa									
Ammonia beccarii "parkinsoniana"	7.7	7.6	9.9	21.1	19.9	16.7	19.8	14.5	19.0
Ammonia beccarii "tepida"	4.1	5.4	14.8	22.7	23.5	36.4	13.3	31.8	15.4
Amphistegina spp.	1.0	-	-	1.6	1.1	1.0	3.9	1.2	3.9
Brizalina striatula	-	-	-	-	-	-	0.6	0.5	3.3
Cibicides pseudolobatulus	-	1.1	8.9	2.9	5.1	3.3	6.2	4.8	4.4
Discorinopsis aquayoi	-	1.1	2.0	1.0	1.4	0.8	2.1	0.5	2.6
Elphidium craticulatum	1.0	2.2	3.0	3.3	2.2	1.3	2.7	2.4	2.6
Elphidium crispum	2.0	3.3	3.9	1.0	2.5	2.1	6.8	1.7	9.7
Elphidium excavatum	-	-	-	1.6	12.6	4.4	20.4	4.8	22.8
Helenina andersoni	12.8	14.1	21.2	22.7	29.2	31.5	19.2	34.9	13.6
Nonionella opima	-	-	-	-	-	-	2.1	-	2.1
Testate amoebae taxa									
Arcella vulgaris	-	-	-	-	-	-	-	-	-
Centropyxis aculeata	27.0	27.2	20.2	11.4	2.5	2.1	-	2.7	-
Centropyxis constricta	21.4	17.9	9.9	5.5	-	-	-	-	-
Cucurbitella tricuspis	5.1	3.3	3.5	1.6	-	-	-	-	-
Difflugia oblonga	-	-	-	-	-	-	-	-	-
Difflugia urceolata	-	-	-	-	-	-	-	-	-

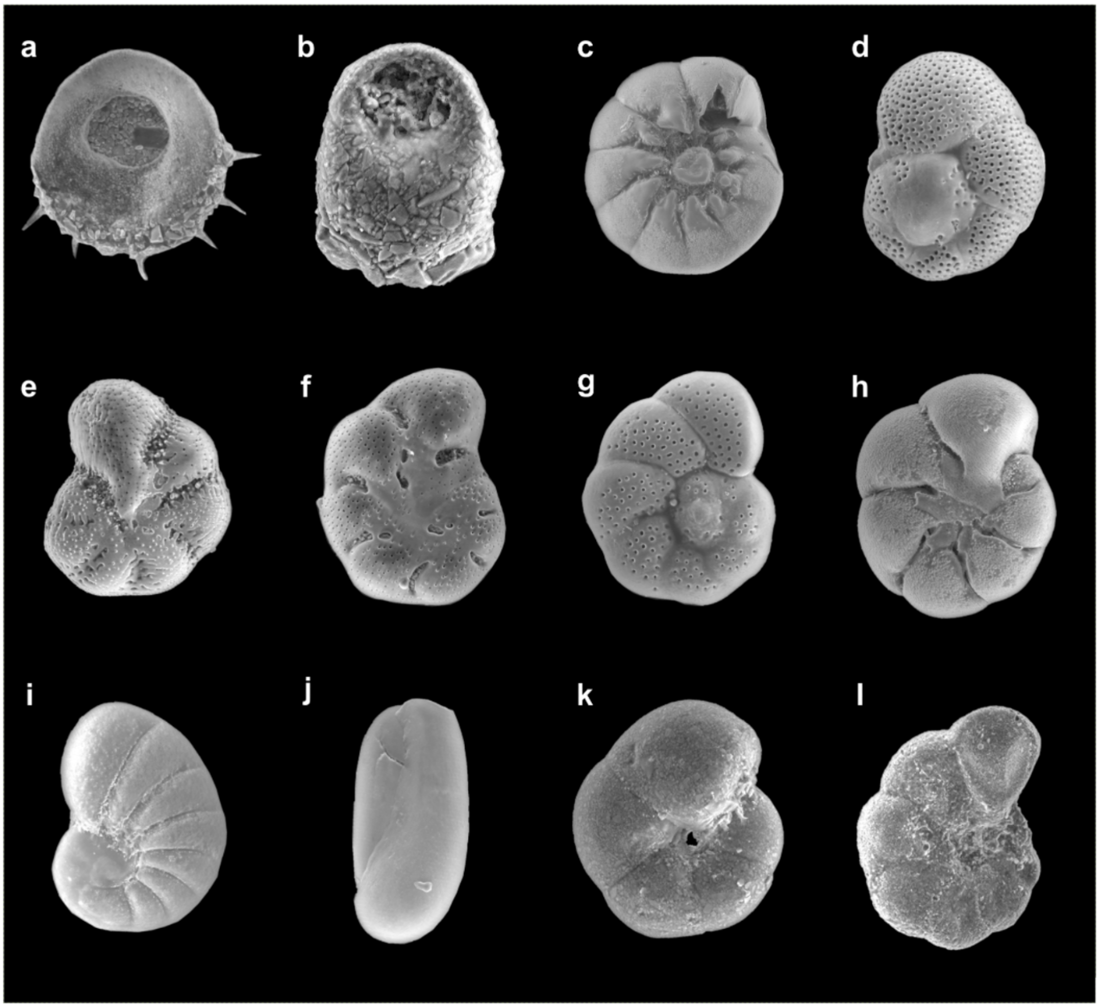

APPENDIX C3: Chapter 4 Supplementary Data 3 - SEM images of selected microfossils within Khor Al Balid and Khor Rori. Note: scales unavailable. Testate amoebae: a. *Centropyxis aculeata*, b. *Centropyxis constricta.* Foraminifera: c. *Ammonia beccarii*, d. *Discorinopsis aquayoi*, e. *Elphidium translucens* – dorsal view, f. *Elphidium translucens* – ventral view, g. *Elphidium* sp., h. *Helenina andersoni*, i. *Nonionella depressula*, j. *Quinqueloculina seminulum*, k. *Trochammina inflata*, l. *Trochammina macrescens.*

APPENDIX C4: Chapter 4 Supplementary Data 4 - Table of μXRF counts for elements of interest in Khor Al Balid cores ALB1–ALB6.

Core	Sample (cm)	Chemo-facies	Ca ± sd	Fe ± sd	K ± sd	Si ± sd	Sr ± sd	Ti ± sd	Ca/Si ± sd	Ti+Fe+K/Ca ± sd	Inc/Coh ± sd
	14–16	LM-3	122576 ±3460	27383 ±940	1469 ±80	406 ±25	17670 ±800	930 ±91	303 ±21	0.245 ±0.008	4.25 ±0.11
	29–31	LM-2	143601 ±13028	29557 ±1956	1693 ±157	268 ±28	15007 ±1180	1150 ±172	538 ±46	0.227 ±0.015	4.23 ±0.13
ALB1	37–38	LM-2	134341 ±10611	24072 ±3451	1315 ±251	202 ±41	15316 ±887	917 ±202	704 ±211	0.198 ±0.035	4.29 ±0.06
	55–57	MS-1	143601 ±17295	29557 ±565	1693 ±107	268 ±28	15007 ±1779	1150 ±25	1997 ±535	0.018 ±0.004	4.05 ±0.12
	69–71	LM-2	171854 ±6742	7750 ±326	311 ±88	111 ±21	25160 ±835	190 ±61	1607 ±363	0.048 ±0.003	4.74 ±0.12
	0–2	LM-6	61964 ±4054	10955 ±509	787 ±71	65 ±22	15517 ±648	264 ±60	1154 ±770	0.195 ±0.016	5.49 ±0.10
	2–4	LM-6	69899 ±6598	12956 ±997	414 ±70	60 ±22	16668 ±878	290 ±104	1354 ±617	0.196 ±0.017	5.37 ±0.09
	4–5	LM-6	83141 ±9775	17451 ±1857	542 ±96	75 ±23	17873 ±973	414 ±88	1224 ±456	0.223 ±0.029	5.16 ±0.08
	5–7	LM-6	88934 ±8418	25674 ±2099	834 ±136	101 ±26	17306 ±1017	719 ±122	938 ±279	0.307 ±0.019	5.03 ±0.10
	7–8	LM-6	98331 ±11834	30267 ±1528	1140 ±142	142 ±25	17093 ±1121	1001 ±218	705 ±108	0.333 ±0.032	4.78 ±0.07
	8–10	LM-3	119344 ±12338	27644 ±2499	1271 ±171	171 ±33	17366 ±1701	1025 ±182	716 ±107	0.252 ±0.023	4.48 ±0.11
	10–12	LM-7	82475 ±10952	45715 ±2310	1638 ±145	187 ±44	13964 ±1259	1538 ±196	457 ±90	0.602 ±0.078	4.77 ±0.10
	12–14	LM-7	81724 ±3657	63566 ±1678	2491 ±164	352 ±37	11122 ±459	2307 ±153	234 ±21	0.838 ±0.028	4.73 ±0.07
	14–15	LM-7	80185 ±3038	59544 ±2453	2208 ±161	273 ±30	11603 ±362	2067 ±154	297 ±33	0.797 ±0.051	4.72 ±0.07
	15–17	LM-7	91030 ±6755	36444 ±1366	1355 ±103	168 ±22	15120 ±820	1230 ±146	551 ±81	0.431 ±0.035	4.73 ±0.07
ALB2	17–18	LM-6	51530 ±5721	16933 ±1264	443 ±105	55 ±18	11506 ±442	383 ±78	1058 ±416	0.348 ±0.040	5.57 ±0.13
	18–20	LM-6	64080 ±6703	10787 ±655	402 ±63	55 ±21	13079 ±493	224 ±61	1724 ±2023	0.180 ±0.017	5.32 ±0.07
	20–22	LM-2	94260 ±16155	10145 ±814	312 ±58	68 ±18	15100 ±702	233 ±72	1475 ±470	0.115 ±0.013	4.99 ±0.10
	22–24	LM-2	110508 ±14658	8867 ±646	245 ±68	82 ±24	16133 ±709	210 ±98	1457 ±434	0.085 ±0.009	4.88 ±0.07
	24–25	LM-2	141974 ±10285	20727 ±1294	853 ±157	167 ±28	18308 ±823	674 ±129	872 ±148	0.157 ±0.007	4.49 ±0.07
	25–27	LM-2	151787 ±6910	16560 ±779	741 ±92	154 ±28	20901 ±556	567 ±210	1016 ±198	0.118 ±0.005	4.51 ±0.11
	27–30	LM-6	34681 ±13687	14092 ±2648	229 ±88	43 ±20	8278 ±914	287 ±85	876 ±510	0.453 ±0.090	5.99 ±0.21
	30–32	MS-1	160495 ±17693	13878 ±4786	473 ±132	128 ±29	16510 ±1482	390 ±181	1306 ±265	0.093 ±0.034	3.88 ±0.12
	32–35	MS-1	200477 ±23370	16085 ±4965	868 ±323	229 ±61	16928 ±1883	594 ±203	925 ±223	0.089 ±0.032	3.68 ±0.12
	35–37	MS-1	181548 ±28280	1503 ±256	30 ±49	99 ±28	16367 ±1529	10 ±47	1940 ±476	0.009 ±0.002	3.97 ±0.05
	37–44	MS-1	178263 ±32469	890 ±204	0 ±0	91 ±33	16019 ±1458	20 ±58	2171 ±807	0.005 ±0.002	4.03 ±0.08
	0–2	LM-3	155051 ±9290	55938 ±2977	3149 ±264	523 ±57	6222 ±290	1917 ±110	298 ±19	0.394 ±0.005	4.12 ±0.09
	5–7	LM-3	119279 ±14481	51014 ±4408	2412 ±297	353 ±71	8458 ±653	1958 ±259	345 ±39	0.467 ±0.032	4.32 ±0.08
	10–12	LM-3	145235 ±7949	51799 ±2289	2973 ±236	486 ±50	8894 ±606	2177 ±136	300 ±20	0.393 ±0.019	4.08 ±0.08
ALB3	13–15	LM-3	153630 ±8467	43142 ±1149	2743 ±169	448 ±44	8498 ±633	1854 ±127	345 ±27	0.311 ±0.016	4.06 ±0.08
	20–22	MS-1	178187 ±17731	5926 ±828	328 ±212	150 ±39	17029 ±1313	155 ±85	1262 ±312	0.036 ±0.005	3.96 ±0.05
	25–26	MS-1	144218 ±15891	10091 ±2138	309 ±112	128 ±49	12149 ±1607	268 ±82	1237 ±360	0.076 ±0.021	4.15 ±0.24

APPENDIX C4: Chapter 4 Supplementary Data 4 - Continued.

Core	Sample (cm)	Chemo-facies	Ca ± sd	Fe ± sd	K ± sd	Si ± sd	Sr ± sd	Ti ± sd	Ca/Si ± sd	Ti+Fe+K/Ca ± sd	Inc/Coh ± sd
	0–2	LM-2	98297 ±12128	11314 ±1281	382 ±108	113 ±25	15415 ±776	305 ±76	901 ±189	0.122 ±0.006	5.12 ±0.09
	2–4	LM-2	116269 ±13816	16667 ±1660	544 ±105	131 ±30	14885 ±884	524 ±128	928 ±229	0.155 ±0.026	4.54 ±0.09
	4–6	LM-2	111536 ±9001	26530 ±2311	880 ±145	139 ±27	14076 ±793	894 ±208	823 ±138	0.255 ±0.029	4.46 ±0.10
	6–7	LM-2	139329 ±14086	27012 ±1836	1184 ±145	224 ±41	14341 ±1025	1020 ±195	635 ±99	0.212 ±0.029	4.18 ±0.07
	7–9	MS-1	198024 ±13775	6214 ±905	366 ±221	204 ±44	16712 ±1347	275 ±186	1001 ±164	0.035 ±0.005	3.73 ±0.12
	9–11.5	LM-7	64888 ±6221	35995 ±2581	1132 ±137	170 ±39	8494 ±626	1385 ±204	396 ±70	0.597 ±0.053	5.04 ±0.13
	11.5–13.5	C5	28169 ±5558	50969 ±3218	966 ±162	84 ±29	4562 ±365	1386 ±147	394 ±245	1.942 ±0.283	5.64 ±0.10
ALB4	13.5–15	C5	22554 ±2118	51011 ±4255	873 ±104	77 ±20	3830 ±174	1346 ±144	325 ±161	2.373 ±0.233	6.03 ±0.10
	15–17	C5	22310 ±3075	47886 ±5365	864 ±134	88 ±22	3660 ±283	1323 ±164	264 ±52	2.261 ±0.212	6.07 ±0.13
	17–19	C5	29694 ±2577	54941 ±3574	1246 ±137	129 ±30	3174 ±178	1664 ±169	240 ±46	1.953 ±0.088	6.01 ±0.06
	19–21	C4	68372 ±7039	69026 ±3307	2392 ±242	353 ±68	4852 ±469	2583 ±212	199 ±30	1.091 ±0.097	4.95 ±0.10
	21–23	C5	23038 ±2194	44724 ±1986	762 ±119	71 ±25	4530 ±247	1229 ±147	385 ±198	2.039 ±0.133	5.98 ±0.14
	23–25	C5	33679 ±6531	49853 ±4024	1041 ±162	102 ±31	4857 ±440	1490 ±235	356 ±110	1.609 ±0.310	5.64 ±0.11
	25–27	MS-1	175589 ±12171	10554 ±1798	490 ±160	148 ±43	16860 ±1206	466 ±161	1273 ±341	0.066 ±0.013	4.02 ±0.10
	27–27.5	MS-1	155766 ±15125	6615 ±843	201 ±97	91 ±21	16715 ±1218	136 ±69	1797 ±417	0.045 ±0.009	4.29 ±0.12
	0–2	LM-2	115727 ±6228	12211 ±848	324 ±73	96 ±21	18903 ±532	299 ±65	1271 ±336	0.111 ±0.012	5.00 ±0.08
	2–4	LM-7	60669 ±6953	32721 ±2107	734 ±104	74 ±19	9315 ±544	875 ±100	864 ±214	0.573 ±0.070	5.38 ±0.11
	4–5	LM-7	58724 ±6705	32299 ±2795	684 ±102	77 ±15	8538 ±589	930 ±166	786 ±178	0.586 ±0.092	5.40 ±0.15
	5–7	LM-2	107967 ±18793	9599 ±1866	221 ±89	87 ±23	12639 ±1035	234 ±92	1312 ±371	0.096 ±0.029	4.46 ±0.11
	7–8	LM-2	125275 ±18733	20105 ±2187	696 ±173	129 ±45	12357 ±910	619 ±94	1063 ±346	0.174 ±0.028	4.51 ±0.07
	8–9.5	MS-1	234523 ±16492	13743 ±3158	600 ±191	278 ±48	13558 ±899	420 ±165	868 ±167	0.063 ±0.015	4.19 ±0.10
	9.5–11	LM-4	67946 ±2344	112303 ±2293	3957 ±125	610 ±32	3530 ±178	3777 ±156	112 ±5	1.768 ±0.059	4.66 ±0.09
	11–13	LM-4	86811 ±2608	77454 ±2336	3060 ±136	466 ±40	6140 ±436	2876 ±217	188 ±16	0.961 ±0.032	4.62 ±0.07
ALB5	13–15	LM-4	65212 ±2930	116136 ±5716	4102 ±230	619 ±61	3171 ±144	3936 ±225	106 ±11	1.904 ±0.036	4.73 ±0.18
	15–16	LM-4	78593 ±7616	45228 ±4596	1757 ±244	258 ±45	6480 ±232	1608 ±242	309 ±35	0.624 ±0.095	5.07 ±0.15
	16–18	LM-7	60581 ±4045	47897 ±2448	1401 ±109	146 ±23	5561 ±184	1572 ±127	424 ±64	0.843 ±0.067	5.42 ±0.16
	18–19	LM-7	40085 ±5734	47401 ±3242	1102 ±162	116 ±31	4245 ±212	1480 ±225	365 ±97	1.264 ±0.140	5.70 ±0.09
	19–21	LM-4	58571 ±4959	59066 ±2462	1786 ±169	209 ±35	4415 ±157	1958 ±129	286 ±39	1.079 ±0.088	5.36 ±0.09
	21–23	LM-4	70400 ±2343	101712 ±3419	3373 ±143	536 ±36	2915 ±134	3582 ±136	134 ±9	1.544 ±0.021	4.91 ±0.07
	23–26	LM-4	80251 ±3504	93077 ±4021	3495 ±230	561 ±40	3309 ±101	3237 ±182	144 ±7	1.244 ±0.014	4.81 ±0.11
	26–28	LM-3	81801 ±6497	35616 ±2394	1144 ±187	151 ±43	8024 ±387	1067 ±149	582 ±164	0.463 ±0.026	5.12 ±0.08
	28–30	LM-2	93837 ±6462	22308 ±1844	737 ±103	120 ±25	9275 ±1143	725 ±121	805 ±141	0.254 ±0.022	5.04 ±0.11
	30–31	MS-1	185252 ±33745	8137 ±1613	335 ±94	193 ±62	12648 ±1630	274 ±177	1021 ±289	0.049 ±0.013	4.45 ±0.31
	4–7	MS-1	312591 ±21141	1316 ±248	33 ±83	323 ±72	17343 ±1368	6 ±23	1018 ±245	0.004 ±0.001	3.56 ±0.13
	14–17	MS-1	293648 ±20311	1250 ±319	38 ±115	275 ±59	17858 ±1278	12 ±45	1116 ±261	0.004 ±0.001	3.75 ±0.10
	34–37	MS-1	293336 ±16096	1522 ±452	31 ±53	291 ±68	17700 ±1040	0 ±0	1057 ±234	0.005 ±0.002	3.47 ±0.13
ALB6	42–48	MS-1	274413 ±18630	1164 ±366	5 ±17	159 ±67	18178 ±1713	12 ±32	1987 ±682	0.004 ±0.001	3.77 ±0.08
	75–78	MS-1	295532 ±21504	1160 ±194	17 ±84	222 ±61	16720 ±1700	39 ±148	1423 ±373	0.004 ±0.001	3.90 ±0.08
	110–113	MS-1	303852 ±226688	1369 ±417	38 ±97	270 ±74	16414 ±1759	3 ±10	1218 ±376	0.005 ±0.001	3.82 ±0.07
	155–156	MS-1	288955 ±19608	2100 ±335	27 ±55	292 ±75	18464 ±1132	34 ±129	1052 ±274	0.008 ±0.002	3.98 ±0.12
	160–164	MS-1	299118 ±14412	1434 ±256	21 ±64	238 ±54	21235 ±1058	20 ±39	1317 ±288	0.005 ±0.001	3.96 ±0.19

APPENDIX C5: Chapter 4 Supplementary Data 5 - Table of μXRF counts for elements of interest in Khor Rori cores ROR1–ROR3, and ROR5.

Core	Sample (cm)	Chemo-facies	**Ca** ± sd	**Fe** ± sd	**K** ± sd	**Si** ± sd	**Sr** ± sd	Ti ± sd	**Ca/Si** ± sd	**Ti+Fe+K/Ca** ± sd	**Inc/Coh** ± sd
	0–1	LM-2	61128 ±7819	45091 ±3860	1123 ±161	115 ±32	9621 ±514	1254 ±134	575 ±185	0.781 ±0.056	5.17 ±0.16
	1–3	LM-1	75443 ±5905	89293 ±4796	3130 ±280	414 ±70	6630 ±510	3341 ±253	186 ±27	1.272 ±0.043	4.44 ±0.08
	3–5	LM-1	77848 ±3301	82060 ±2867	2828 ±235	331 ±52	5457 ±270	2946 ±169	240 ±34	1.129 ±0.032	4.42 ±0.11
	5–7.5	LM-2	66103 ±7418	61931 ±3107	1604 ±171	152 ±37	8051 ±362	1791 ±150	453 ±85	0.996 ±0.079	4.67 ±0.15
	7.5–8	LM-2	70681 ±12140	47650 ±3812	1135 ±192	101 ±28	10145 ±910	1307 ±167	737 ±189	0.725 ±0.107	4.66 ±0.15
	8–9	LM-1	81431 ±3200	87531 ±2436	3144 ±139	410 ±44	5797 ±304	3093 ±160	200 ±18	1.152 ±0.037	4.44 ±0.09
	9–10	LM-4	105465 ±12962	32214 ±3623	1128 ±274	140 ±46	13559 ±725	1151 ±219	823 ±257	0.329 ±0.030	4.33 ±0.19
	10–11.5	LM-2	112549 ±8483	65591 ±3875	2725 ±267	401 ±67	8680 ±430	2508 ±224	286 ±39	0.631 ±0.033	4.10 ±0.06
	11.5–13	LM-4	128065 ±8662	47365 ±2498	2034 ±167	297 ±42	12214 ±860	1943 ±224	437 ±55	0.402 ±0.032	3.93 ±0.11
	13–14.5	LM-2	100061 ±8147	64059 ±2237	2127 ±140	288 ±25	12331 ±687	2327 ±164	349 ±37	0.690 ±0.075	4.17 ±0.07
	14.5–17	LM-5	170876 ±17865	9740 ±2167	356 ±125	115 ±15	16950 ±1149	273 ±118	1501 ±187	0.062 ±0.020	3.69 ±0.14
	17–20	LM-5	209546 ±39232	4725 ±750	133 ±113	148 ±49	17554 ±1431	63 ±48	1489 ±306	0.024 ±0.007	3.55 ±0.18
	40–43	LM-5	181655 ±31130	1878 ±372	8 ±19	101 ±26	18086 ±1326	3 ±11	1884 ±473	0.011 ±0.002	3.70 ±0.22
	56.5–59.5	LM-5	183444 ±33874	4898 ±1264	77 ±122	110 ±40	16490 ±1555	61 ±43	1843 ±566	0.028 ±0.009	3.90 ±0.09
ROR1	62–65	MS-7	247701 ±29411	2157 ±401	1 ±3	143 ±38	17569 ±1301	0 ±0	1833 ±412	0.009 ±0.002	3.62 ±0.23
	66–68	MS-7	257858 ±37646	1647 ±507	8 ±34	134 ±32	16988 ±1363	0 ±0	1980 ±346	0.007 ±0.002	3.88 ±0.08
	68–69.5	LM-5	135681 ±17748	16053 ±3577	384 ±114	107 ±38	15058 ±1170	477 ±194	1362 ±366	0.128 ±0.039	4.30 ±0.13
	69.5–71.5	LM-5	162752 ±30486	12532 ±1672	448 ±198	162 ±67	16175 ±784	469 ±256	1093 ±288	0.084 ±0.015	4.07 ±0.09
	71.2–73	LM-4	106272 ±19147	27856 ±4548	798 ±232	157 ±62	12204 ±766	962 ±335	755 ±271	0.286 ±0.065	4.39 ±0.16
	73–76	LM-5	165670 ±28849	15076 ±2707	578 ±226	188 ±68	14120 ±1285	578 ±273	952 ±242	0.100 ±0.022	3.96 ±0.12
	76–79	LM-4	120867 ±20115	24931 ±3678	913 ±171	177 ±41	15485 ±1102	910 ±239	704 ±127	0.227 ±0.048	4.23 ±0.12
	79–82	MS-7	149545 ±37700	4630 ±1042	45 ±58	85 ±24	8908 ±1606	56 ±34	1863 ±561	0.033 ±0.010	4.03 ±0.17
	82–86	MS-7	200715 ±49778	4630 ±1449	20 ±40	107 ±39	9281 ±2781	45 ±57	2037 ±614	0.025 ±0.010	3.87 ±0.16
	86–89	MS-7	220441 ±43943	5142 ±1552	86 ±70	137 ±40	6119 ±1879	61 ±58	1655 ±276	0.025 ±0.009	3.65 ±0.10
	89–92	MS-7	226341 ±48587	5605 ±1469	116 ±115	159 ±44	6921 ±2164	92 ±41	1460 ±230	0.026 ±0.007	3.91 ±0.20
	92–95	MS-7	217454 ±56928	8126 ±3291	186 ±113	160 ±45	9958 ±3413	216 ±126	1383 ±315	0.043 ±0.023	3.88 ±0.23
	95–100	MS-7	240715 ±51832	10045 ±2148	427 ±158	223 ±65	10878 ±2841	330 ±98	1132 ±286	0.046 ±0.012	3.55 ±0.19
	100–105	LM-5	185137 ±50998	22275 ±4135	959 ±304	241 ±99	12059 ±2137	846 ±214	817 ±153	0.136 ±0.030	3.65 ±0.19
	105–107	LM-5	147629 ±25742	17565 ±3184	733 ±173	176 ±49	13334 ±2985	614 ±158	884 ±225	0.131 ±0.030	3.75 ±0.23

APPENDIX C5: Chapter 4 Supplementary Data 5 - Continued.

Core	Sample (cm)	Chemo-facies	**Ca** ± sd	**Fe** ± sd	**K** ± sd	**Si** ± sd	**Sr** ± sd	Ti ± sd	**Ca/Si** ± sd	**Ti+Fe+K/Ca** ± sd	**Inc/Coh**	± sd
	0–2	LM-2	60848 ±13757	66534 ±5972	1695 ±319	185 ±83	8459 ±691	2097 ±308	354 ±70	1.190 ±0.179	4.90	±0.10
	2–4	LM-2	74462 ±14382	58941 ±6153	1694 ±284	223 ±69	8510 ±419	1945 ±273	349 ±65	0.866 ±0.163	4.85	±0.12
	4–6	LM-1	60709 ±6262	92924 ±5826	2590 ±310	304 ±69	6849 ±401	3015 ±230	206 ±36	1.632 ±0.117	4.54	±0.18
	6–8	LM-1	59994 ±4857	81691 ±3867	2352 ±156	281 ±48	6840 ±405	2815 ±168	217 ±29	1.454 ±0.100	4.76	±0.11
	8–10	LM-2	72957 ±7432	61990 ±5224	1855 ±192	227 ±39	8327 ±631	2014 ±167	328 ±48	0.905 ±0.039	4.88	±0.09
	10–12	LM-1	62440 ±6381	85315 ±5499	2524 ±274	322 ±84	6454 ±361	3192 ±304	204 ±46	1.466 ±0.115	4.71	±0.11
	12–13.5	LM-1	69621 ±5337	87132 ±3040	2857 ±233	429 ±64	6268 ±391	3424 ±235	165 ±23	1.349 ±0.114	4.77	±0.05
	13.5–14.5	LM-6	23352 ±1952	155882 ±6655	3841 ±246	567 ±52	2904 ±211	5309 ±252	41 ±3	7.096 ±0.414	5.00	±0.10
	14.5–16	LM-6	25241 ±1663	147830 ±7547	3968 ±267	655 ±71	2453 ±174	5692 ±377	39 ±3	6.248 ±0.208	4.89	±0.15
	16–18	LM-2	84363 ±6810	71378 ±3542	2341 ±206	329 ±58	8038 ±340	2540 ±245	261 ±34	0.907 ±0.044	4.72	±0.08
ROR2	18–20	LM-1	99160 ±5127	66256 ±3394	2902 ±189	508 ±59	7498 ±366	2975 ±225	197 ±17	0.728 ±0.017	4.50	±0.09
	20–22	LM-1	96354 ±6866	71058 ±3704	2942 ±229	505 ±71	7408 ±444	3073 ±260	193 ±19	0.802 ±0.042	4.49	±0.09
	22–24	LM-1	97274 ±8280	71146 ±4404	3022 ±302	507 ±93	7394 ±344	3084 ±292	196 ±27	0.796 ±0.028	4.50	±0.12
	24–26	LM-1	98340 ±6508	69237 ±4523	3010 ±310	492 ±63	7344 ±533	3042 ±283	202 ±22	0.766 ±0.031	4.53	±0.10
	26–28	LM-1	104132 ±6009	73600 ±4334	3308 ±204	568 ±67	8295 ±932	3384 ±284	185 ±16	0.771 ±0.025	4.41	±0.17
	28–30	LM-1	95208 ±12454	68807 ±3291	2936 ±191	490 ±51	6384 ±504	3045 ±252	194 ±16	0.797 ±0.100	4.53	±0.11
	30–32	LM-1	97302 ±14363	76348 ±7412	3105 ±454	517 ±129	6809 ±589	3218 ±393	194 ±26	0.857 ±0.062	4.27	±0.25
	32–35.5	LM-1	91911 ±6220	77156 ±4311	3170 ±201	530 ±55	6974 ±403	3302 ±216	175 ±13	0.911 ±0.036	4.50	±0.07
	35.5–38	LM-1	93373 ±9119	82520 ±7396	3501 ±354	620 ±83	6860 ±554	3845 ±496	152 ±15	0.968 ±0.101	4.21	±0.23
	38–41	LM-1	91846 ±8882	80756 ±5519	3473 ±319	603 ±73	6780 ±323	3526 ±319	153 ±10	0.958 ±0.039	4.53	±0.19

APPENDIX C5: Chapter 4 Supplementary Data 5 - Continued.

Core	Sample (cm)	Chemo-facies	**Ca** ± sd	**Fe** ± sd	**K** ± sd	**Si** ± sd	**Sr** ± sd	Ti ± sd	**Ca/Si** ± sd	**Ti+Fe+K/Ca** ± sd	**Inc/Coh** ± sd
	0–2	LM-1	56280 ±4308	76766 ±4342	2070 ±179	274 ±39	7368 ±397	2406 ±166	208 ±21	1.446 ±0.042	5.29 ±0.21
	2–4	LM-2	35207 ±4944	68444 ±6220	1433 ±174	109 ±43	6135 ±352	1891 ±240	638 ±1032	2.054 ±0.144	5.79 ±0.17
	4–6	LM-3	40498 ±4555	75919 ±4532	1622 ±211	139 ±51	6081 ±446	2117 ±202	316 ±78	1.979 ±0.141	5.70 ±0.12
	6–8	LM-1	50706 ±6696	78291 ±5461	1906 ±272	203 ±57	6869 ±249	2312 ±270	263 ±53	1.644 ±0.152	5.33 ±0.07
	8–10	LM-2	37518 ±6126	66394 ±6630	1251 ±223	100 ±31	7819 ±439	1770 ±250	443 ±330	1.871 ±0.146	5.31 ±0.11
	10–12	LM-2	46360 ±7327	76801 ±7310	1720 ±288	158 ±41	7956 ±433	2162 ±302	301 ±41	1.765 ±0.191	5.09 ±0.09
	12–13.5	LM-3	48022 ±4993	88248 ±5289	2243 ±227	310 ±56	7026 ±512	2631 ±229	158 ±17	1.949 ±0.112	5.16 ±0.16
	13.5–15	LM-3	47537 ±3158	100542 ±3437	2527 ±153	307 ±50	5753 ±212	2961 ±113	158 ±22	2.237 ±0.120	5.10 ±0.07
	15–17	LM-3	42467 ±4116	105988 ±4790	2652 ±241	325 ±43	5559 ±253	3158 ±213	132 ±11	2.649 ±0.198	5.04 ±0.10
	17–19	LM-6	19548 ±876	177223 ±5035	4149 ±222	565 ±72	2159 ±137	5359 ±199	35 ±4	9.566 ±0.410	4.91 ±0.10
	19–21.5	LM-6	24540 ±1262	159635 ±6681	4163 ±251	568 ±54	2131 ±149	5245 ±316	43 ±3	6.892 ±0.109	4.95 ±0.08
	21.5–24	LM-3	43290 ±6388	91871 ±6929	2134 ±306	202 ±51	5878 ±252	2762 ±293	224 ±48	2.276 ±0.316	4.89 ±0.06
	24–26	LM-3	38914 ±5732	91973 ±9387	1963 ±309	190 ±42	5698 ±403	2646 ±377	214 ±55	2.510 ±0.266	4.86 ±0.09
	26–28	LM-6	34302 ±4601	109371 ±8953	2438 ±324	244 ±53	5043 ±238	3173 ±347	144 ±18	3.383 ±0.270	4.91 ±0.10
	28–30	LM-3	47487 ±4744	103687 ±6613	2702 ±309	280 ±55	5061 ±211	3097 ±272	174 ±24	2.315 ±0.104	4.85 ±0.09
	30–32	LM-3	60250 ±6778	93536 ±7768	2632 ±315	322 ±60	6722 ±398	2725 ±254	190 ±21	1.647 ±0.070	4.81 ±0.07
	32–33	LM-1	68665 ±6801	92371 ±6131	2960 ±351	372 ±64	4214 ±227	2911 ±261	187 ±20	1.436 ±0.069	4.73 ±0.08
ROR3	33–35	LM-3	49195 ±6890	100733 ±8477	2642 ±380	314 ±73	5696 ±389	2970 ±339	161 ±27	2.184 ±0.194	4.77 ±0.06
	35–37	LM-6	11430 ±1068	173493 ±4876	3791 ±144	445 ±26	2403 ±164	5463 ±204	26 ±3	16.125 ±1.593	5.08 ±0.09
	37–39	LM-6	6775 ±336	188988 ±6174	4385 ±208	633 ±75	1696 ±107	6290 ±249	11 ±1	29.538 ±1.689	5.03 ±0.11
	39–40	LM-6	20511 ±1427	158270 ±8705	4046 ±290	617 ±68	2018 ±151	5642 ±354	33 ±2	8.201 ±0.257	4.85 ±0.09
	40–42	LM-1	71405 ±5838	91866 ±4600	3048 ±260	430 ±71	7658 ±335	3428 ±238	168 ±14	1.381 ±0.048	4.47 ±0.08
	42–44	LM-2	76370 ±6649	85993 ±5368	2782 ±285	324 ±48	8298 ±350	2745 ±214	239 ±22	1.201 ±0.045	4.40 ±0.09
	44–46	LM-2	88365 ±9934	83071 ±5166	2995 ±314	412 ±73	9351 ±668	2697 ±245	218 ±25	1.012 ±0.086	4.32 ±0.07
	46–48	LM-2	86980 ±7181	93063 ±4204	3256 ±295	402 ±65	9297 ±315	2940 ±180	220 ±31	1.145 ±0.053	4.25 ±0.16
	48–50	LM-2	76228 ±5476	87757 ±4930	2921 ±247	328 ±46	8267 ±294	2763 ±205	235 ±23	1.229 ±0.062	4.50 ±0.09
	50–52	LM-1	87156 ±4871	95425 ±4100	3438 ±222	488 ±42	8466 ±243	3023 ±225	179 ±10	1.170 ±0.031	4.29 ±0.13
	52–54	LM-1	88016 ±6137	91324 ±4345	3256 ±225	460 ±61	6827 ±360	3084 ±225	194 ±21	1.113 ±0.070	4.19 ±0.15
	54–55	LM-1	81264 ±3880	97360 ±3625	3753 ±196	538 ±67	4926 ±301	3400 ±180	153 ±16	1.288 ±0.063	4.33 ±0.08
	55.5–58	MS-7	255380 ±21232	11587 ±2610	576 ±170	243 ±44	6517 ±1125	374 ±116	1081 ±201	0.049 ±0.010	3.72 ±0.09
	58–60	MS-7	270492 ±31245	11497 ±4113	530 ±193	251 ±43	6148 ±617	349 ±162	1099 ±165	0.047 ±0.019	3.75 ±0.13
	60–61	LM-5	197821 ±33265	35066 ±10241	982 ±217	237 ±36	8430 ±1146	981 ±294	857 ±212	0.200 ±0.090	4.22 ±0.21
	61–64	MS-7	263337 ±26028	10513 ±5116	385 ±193	209 ±29	7445 ±1296	282 ±181	1279 ±177	0.043 ±0.021	3.84 ±0.14
	64–65	LM-5	170742 ±31976	42451 ±7168	1420 ±236	325 ±47	7357 ±2267	1334 ±337	529 ±98	0.280 ±0.091	4.49 ±0.26
	65–67	MS-7	294659 ±24866	7500 ±1135	324 ±97	258 ±39	5116 ±615	215 ±73	1159 ±154	0.027 ±0.005	3.65 ±0.24
	67–72	MS-7	286133 ±21810	8603 ±1753	396 ±240	253 ±37	6263 ±966	224 ±79	1155 ±180	0.033 ±0.008	3.72 ±0.13

APPENDIX C5: Chapter 4 Supplementary Data 5 - Continued.

Core	Sample (cm)	Chemo-facies	Ca ± sd	Fe ± sd	K ± sd	Si ± sd	Sr ± sd	Ti ± sd	Ca/Si ± sd	Ti+Fe+K/Ca ± sd	Inc/Coh ± sd
	0–2	LM-5	193189 ±27858	22105 ±2032	1316 ±185	338 ±66	12984 ±1187	1024 ±206	582 ±77	0.128 ±0.018	4.12 ±0.05
	2–4	MS-7	229292 ±17340	16707 ±2778	1014 ±189	358 ±76	12952 ±1242	729 ±159	665 ±123	0.081 ±0.014	3.96 ±0.12
	4–6	MS-7	223950 ±28189	17081 ±1136	1077 ±156	382 ±41	12179 ±1158	781 ±125	589 ±73	0.086 ±0.011	3.88 ±0.12
	6–8	LM-5	213257 ±15464	21665 ±2723	1326 ±225	429 ±54	13809 ±1276	924 ±224	502 ±55	0.113 ±0.016	4.10 ±0.09
	8–10	MS-7	228711 ±29188	19723 ±2874	1252 ±199	448 ±68	13682 ±1538	846 ±209	515 ±56	0.096 ±0.012	3.92 ±0.11
	10–12	MS-7	257992 ±20291	14788 ±1496	935 ±172	398 ±61	12288 ±1180	598 ±114	661 ±96	0.064 ±0.007	3.78 ±0.06
	12–13.5	LM-5	223431 ±23460	22651 ±5157	1328 ±311	393 ±91	14001 ±2299	911 ±219	586 ±87	0.112 ±0.027	3.62 ±0.20
	13.5–15	LM-5	205233 ±19419	33008 ±3644	1952 ±231	484 ±68	13324 ±1133	1481 ±238	428 ±40	0.178 ±0.017	3.78 ±0.15
	15–17	LM-5	155515 ±20832	50878 ±10660	2309 ±325	434 ±67	11631 ±992	2050 ±431	361 ±37	0.368 ±0.111	3.77 ±0.24
	17–18.5	LM-2	128863 ±12715	60142 ±3758	2703 ±262	416 ±61	11706 ±992	2478 ±322	312 ±24	0.510 ±0.045	3.78 ±0.21
	18.5–20	LM-1	138160 ±23431	49955 ±6775	2028 ±261	292 ±59	11872 ±1645	1868 ±228	484 ±102	0.411 ±0.145	4.07 ±0.15
	20–22	LM-5	154377 ±20273	22544 ±1693	1055 ±139	193 ±51	13800 ±1209	908 ±192	835 ±170	0.161 ±0.024	3.98 ±0.08
	22–24	LM-5	174808 ±17972	20568 ±2044	1165 ±174	230 ±32	15048 ±1394	889 ±213	772 ±115	0.131 ±0.020	4.07 ±0.08
	24–26	LM-5	164573 ±13727	21122 ±2856	1138 ±212	217 ±59	15795 ±1012	886 ±173	805 ±197	0.141 ±0.015	4.21 ±0.11
	26–28	LM-5	182060 ±19569	20046 ±3557	1151 ±228	273 ±71	13585 ±1237	870 ±203	702 ±153	0.123 ±0.025	4.25 ±0.10
	28–30.5	MS-7	249137 ±20685	19062 ±2292	1218 ±191	435 ±66	12565 ±2405	886 ±251	581 ±65	0.085 ±0.007	3.91 ±0.16
	30.5–32	LM-5	231072 ±21444	23034 ±2972	1504 ±210	491 ±63	11891 ±955	1104 ±178	476 ±56	0.112 ±0.016	4.03 ±0.12
	32–33.5	MS-7	272414 ±20605	9366 ±1554	584 ±284	354 ±50	12653 ±1877	365 ±119	783 ±126	0.038 ±0.008	4.03 ±0.13
	33.5–35	MS-7	230478 ±18861	15387 ±2016	927 ±183	353 ±71	12220 ±2520	682 ±137	670 ±98	0.074 ±0.010	4.23 ±0.11
ROR5	35–37	MS-7	232285 ±25849	12926 ±1660	884 ±130	365 ±64	12113 ±1149	606 ±114	651 ±112	0.062 ±0.008	4.23 ±0.10
	37–39	MS-7	228599 ±14394	13970 ±1779	998 ±183	351 ±46	11159 ±1095	728 ±147	659 ±72	0.069 ±0.007	4.18 ±0.12
	39–41	MS-7	251127 ±22206	13060 ±1269	982 ±149	424 ±92	12217 ±1631	612 ±100	610 ±98	0.059 ±0.005	3.98 ±0.16
	41–44	MS-7	243688 ±21852	14670 ±2367	1083 ±235	447 ±72	10739 ±1013	686 ±180	553 ±66	0.067 ±0.010	4.14 ±0.15
	44–46	MS-7	243199 ±28914	12967 ±2462	813 ±162	355 ±72	11246 ±1513	587 ±175	698 ±83	0.060 ±0.012	4.10 ±0.10
	46–48	LM-5	201272 ±18472	19263 ±1483	1274 ±142	339 ±84	12935 ±911	1087 ±224	616 ±107	0.108 ±0.014	4.05 ±0.12
	48–50	MS-7	261044 ±18121	11848 ±2233	793 ±125	369 ±53	12368 ±1254	453 ±77	718 ±85	0.050 ±0.009	3.74 ±0.16
	50–53	MS-7	279171 ±27253	9095 ±1814	614 ±204	349 ±60	11456 ±1355	340 ±92	818 ±133	0.036 ±0.007	3.91 ±0.26
	53–56	MS-7	212200 ±29003	8793 ±1160	1316 ±185	172 ±52	11876 ±1198	318 ±101	1318 ±306	0.128 ±0.018	4.12 ±0.05
	56–60	MS-7	222737 ±42220	8980 ±3253	1014 ±189	187 ±65	12071 ±2556	322 ±145	1268 ±285	0.081 ±0.014	3.96 ±0.12
	60–64	MS-7	245485 ±39802	9150 ±1860	1077 ±156	248 ±50	11416 ±1757	399 ±118	1007 ±138	0.086 ±0.011	3.88 ±0.12
	64–68	MS-7	244166 ±20135	6665 ±1243	1326 ±225	180 ±44	11348 ±1785	212 ±74	1409 ±246	0.113 ±0.016	4.10 ±0.09
	68–72	MS-7	190672 ±31791	12043 ±2110	1252 ±199	168 ±53	11747 ±1354	561 ±225	1184 ±201	0.096 ±0.012	3.92 ±0.11
	72–76	MS-7	185779 ±19148	5705 ±1030	935 ±172	116 ±31	10538 ±2066	155 ±85	1701 ±445	0.064 ±0.007	3.78 ±0.06
	76–80	MS-7	208454 ±43232	5324 ±1334	1328 ±311	141 ±49	11319 ±2251	150 ±86	1587 ±386	0.112 ±0.027	3.62 ±0.20
	80–84	MS-7	198158 ±36068	7689 ±1500	1952 ±231	154 ±48	11925 ±2715	241 ±66	1368 ±356	0.178 ±0.017	3.78 ±0.15
	84–88	MS-7	215093 ±40411	7169 ±1049	2309 ±325	170 ±51	10512 ±1915	232 ±87	1323 ±281	0.368 ±0.111	3.77 ±0.24
	88–92	MS-7	217561 ±31719	10258 ±1342	2703 ±262	205 ±41	11381 ±2394	450 ±112	1079 ±132	0.510 ±0.045	3.78 ±0.21
	92–96	MS-7	259436 ±21691	8108 ±3070	2028 ±261	258 ±58	10725 ±1285	315 ±172	1049 ±208	0.411 ±0.145	4.07 ±0.15
	96–100	MS-7	209867 ±24654	10369 ±3454	1055 ±139	193 ±45	12375 ±1748	460 ±207	1129 ±217	0.161 ±0.024	3.98 ±0.08
	100–105	MS-7	231713 ±29110	7451 ±1549	1165 ±174	173 ±37	9998 ±1570	223 ±80	1383 ±247	0.131 ±0.020	4.07 ±0.08